Technische Universität München
Institut für Energietechnik

Lehrstuhl für Thermodynamik

A Moments Model for the Numerical Simulation of Bubble Column Flows

Thomas Acher

Vollständiger Abdruck der von der Fakultät für Maschinenwesen der Technischen Universität München zur Erlangung des akademischen Grades eines

Doktor – Ingenieurs

genehmigten Dissertation.

Vorsitzende:

Univ.-Prof. Dr. rer. nat. Sonja Berensmeier

Prüfer der Dissertation:

1. Univ.-Prof. Wolfgang Polifke, Ph. D.
2. Univ.-Prof. Dr.-Ing. Kai-Olaf Hinrichsen

Die Dissertation wurde am 16.09.2014 bei der Technischen Universität München eingereicht und durch die Fakultät für Maschinenwesen am 26.02.2015 angenommen.

Acknowledgements

This thesis was created during my work as a doctoral candidate at Linde AG, Engineering Division, from 2011 to 2014. Within the CFD group of Linde Engineering, the focus of my work was associated with the research effort to enhance the modeling of bubble column flows. Furthermore, I was given the chance to gain experience in the numerical simulation of a variety of fluid dynamic phenomena in the field of process and chemical engineering, specifically related to multiphase flows.

First of all, I would like to thank Prof. Polifke for the academic supervision of this work, for many fruitful discussions and for his vivid interest in the advance of this project at all times. Further, I thank Prof. Sonja Berensmeier for kindly accepting to chair the examination process and Prof. Kai-Olaf Hinrichsen for his participation in the defense committee as second referee.

My special gratitude goes to Dr. Stefan Lenz and Dr. Christian Gobert. I do not only appreciate their technical guidance throughout the course of this work and the reviewing of this thesis, but also their competent support, even beyond this project. I also want to thank my colleagues Dr. Hans-Jörg Zander, Dr. Karl-Heinz Hofmann, Gregor Bloch, Thibaut Monnin and Paul Heinz for sharing their technical expertise in many discussions. Further, the helpful scientific exchange with Patrick Dems, Gary Jasor and several other researchers at the Chair of Thermodynamics is much acknowledged. I am also very thankful to Dr. Frieda Pattenden and Samantha Cass for proofreading of my work.

Last but not least, I would like to say thank you to my parents, who set me on the road, to my friends, who kept me going, and especially to My Thanh Tran, who accompanied me through this journey with her strength, patience and support.

Contents

List of Figures

List of Tables

Nomenclature

Latin Characters

a	Volume-specific bubble surface	m^{-1}
$\boldsymbol{a}$	Acceleration	$\mathrm{m\,s}^{-2}$
A	Area	m^2
$\mathcal{A}$	Aspect ratio	
b	Population balance birth term	$\mathrm{m}^{-4}\,\mathrm{s}^{-1}$
$\boldsymbol{b}$	Mass-specific body force	$\mathrm{m\,s}^{-2}$
C	Model constant	
d	Population balance death term	$\mathrm{m}^{-4}\,\mathrm{s}^{-1}$
D	Diameter	m
$\mathcal{D}$	Diffusion coefficient	$\mathrm{m}^2\,\mathrm{s}^{-1}$
E	Drag multiplying factor	
$\mathbb{E}$	Activation energy	$\mathrm{J\,mol}^{-1}$
f	Bubble volume ratio	
F	Breakup frequency	s^{-1}
$\boldsymbol{F}$	Interfacial force	N
g	Gravitational acceleration	$\mathrm{m\,s}^{-2}$
G	Filter kernel function	
$\boldsymbol{G}$	Diffusive flux	$\mathrm{kg\,m}^{-2}\,\mathrm{s}^{-1}$
h	Discontinuous events source term	
$\mathcal{H}$	Dimensionless Henry coefficient	
j	Stoichiometric coefficient	
$\boldsymbol{J}$	Generic molecular flux	
$\mathcal{J}$	Jacobian matrix	

k	Turbulent kinetic energy	$\mathrm{m^2\,s^{-2}}$
$\mathcal{K}$	Mass transfer coefficient	$\mathrm{m\,s^{-1}}$
l	Length scale	m
$\dot{m}$	Mass flux	$\mathrm{kg\,m^{-2}\,s^{-1}}$
$M^{(k)}$	Function moment of order k	$\mathrm{m^{k-3}}$
$\boldsymbol{M}$	Momentum flux	$\mathrm{kg\,m^{-2}\,s^{-2}}$
$\mathbb{M}$	Molecular mass	$\mathrm{g\,mol^{-1}}$
n	Number density function	
$\boldsymbol{n}$	Normal vector	
N	Volume-specific particle number	$\mathrm{m^{-3}}$
$\mathcal{O}$	Order	
p	Pressure	Pa
P	Probability density function	
$\mathcal{P}$	Breakup or coalescence probability	
r	Coalescence kernel function	$\mathrm{m^{-3}\,s^{-1}}$
R	Radius	m
$\mathbb{R}$	Gas constant	$\mathrm{J\,mol^{-1}\,K^{-1}}$
$\boldsymbol{S}$	Strain-rate tensor	$\mathrm{s^{-1}}$
$\mathbb{S}$	Stoichiometric concentration ratio	
t	Time	s
T	Temperature	K
$\boldsymbol{T}$	Stress tensor	$\mathrm{kg\,m^{-1}\,s^{-2}}$
$\boldsymbol{u}$	Velocity vector	$\mathrm{m\,s^{-1}}$
V	Volume	$\mathrm{m^3}$
w	Quadrature weight	$\mathrm{m^{-3}}$
$\boldsymbol{x}$	Position vector	
X	Phase indicator function	
Y	Mass concentration	

Z	Scalar transport parameter	

Greek Characters

α	Volume fraction	
β	Daughter bubble size distribution	m
γ	Breakup and coalescence size parameter	m
Γ	Interfacial mass transfer	$\mathrm{kg\,m^{-3}\,s^{-1}}$
$\mathit{\Gamma}$	Gamma function	
δ	Dirac delta function	
Δ	Spatial discretization	m
ϵ	Turbulent dissipation	$\mathrm{m^2\,s^{-3}}$
ζ	Internal coordinate	
$\boldsymbol{\zeta}$	Internal coordinate vector	
$\boldsymbol{\eta}$	Relative position vector	
Θ	Breakup and coalescence volume parameter	$\mathrm{m^3}$
κ	Curvature	$\mathrm{m^{-1}}$
λ	Reaction rate constant	
Λ	Eigenvalue	
μ	Dynamic viscosity	$\mathrm{Pa\,s}$
ν	Kinematic viscosity	$\mathrm{m^2\,s^{-1}}$
ξ	Mixture fraction	
ϖ	Size group volume fraction	
ρ	Density	$\mathrm{kg\,m^{-3}}$
σ	Surface tension	$\mathrm{N\,m^{-1}}$
$\boldsymbol{\varsigma}$	Surface force	$\mathrm{N\,m^{-2}}$
τ	Time scale	s
$\boldsymbol{\tau}$	Relaxation time	s
ϑ	Bubble size ratio	

$\boldsymbol{\tau}$	Shear stress tensor	$\mathrm{kg\,m^{-1}\,s^{-2}}$
Υ	Interfacial chemical production rate	$\mathrm{kg\,m^{-2}\,s^{-1}}$
ϕ	Turbulence eddy size	m
Φ	Generic source term	
ψ	Generic fluid property	
Ψ	Volumetric chemical production rate	$\mathrm{s^{-1}}$
ω	Coalescence collision frequency	$\mathrm{m^3\,s^{-1}}$
Ω	Breakup collision frequency	$\mathrm{m^{-2}\,s^{-1}}$

Abbreviations

BNDM	Bubble Number Density Model
CFD	Computational Fluid Dynamics
CQMOM	Conditional Quadrature Method of Moments
DNS	Direct Numerical Simulation
DQMOM	Direct Quadrature Method of Moments
EDM	Eddy Dissipation Model
EELES	Euler-Euler Large Eddy Simulation
EQMOM	Extended Quadrature Method of Moments
FDF	Filtered Density Function
GPBE	Generalized Population Balance Equation
GSL	Gnu Scientific Library
IATE	Interfacial Area Transport Equation
IMV	Identical Moment Velocities
LEPDF	Large Eddy Probability Density Function
LES	Large Eddy Simulation
MOM	Method of Moments
MTE	Moment Transport Equation
MUSIG	Multiple-size Group Model

NDF	Number Density Function
PBE	Population Balance Equation
PD	Product Difference
PDF	Probability Density Function
PMOM	Presumed Function Method of Moments
QMOM	Quadrature Method of Moments
RANS	Reynolds-Averaged Navier-Stokes
RSM	Reynolds Stress Model
RTA	Relaxation Time Approach
SGS	Sub-Grid Scale
VLES	Very Large Eddy Simulation
VOF	Volume of Fluid

Dimensionless Numbers

Da	Damköhler number
Eo	Eötvös number
Mo	Morton number
Nu	Nusselt number
Pr	Prandtl number
Re	Reynolds number
Sc	Schmidt number
Sh	Sherwood number
We	Weber number

Subscripts

A	Arrhenius model
B	Batchelor scale

$\mathcal{B}$	Breakup
c	Continuous phase
$chem$	Chemical reaction
$cont$	Contact
C	Control volume or area
$\mathcal{C}$	Coalescence
d	Dispersed phase
$drain$	Drainage
D	Drag
$\hat{D}$	Quadrature abscissa
EDM	Eddy dissipation model
GD	Generalized drag
h	Horizontal
I	Interface
k	Phase indicator
L	Lift
mol	Molecular
min	Minimum
mix	Turbulent mixing
n	Number density function
p	Particle
P	Projection
rel	Relative
res	Mean residence
s	Largest scales
sf	Superficial
st	Stoichiometric
S	Smagorinsky model

SGS	Sub-grid scale
ter	Terminal state
tur	Turbulence
TD	Turbulent dispersion
v	Vertical
VM	Virtual mass
w	Quadrature weight
Z	Generic interfacial force
Γ	Interfacial mass transfer
$\mathit{\Gamma}$	Gamma function
η	Kolmogorov scale

Superscripts

A	Exemplary chemical reactant
B	Exemplary chemical reactant
C	Exemplary chemical product
(k)	Generic order of moment
P	Generic chemical product
R	Generic chemical reactant
$\mathcal{T}$	Transpose
X	Generic chemical species

1 Introduction

1.1 Bubble column reactors

Bubble columns are employed as chemical reactors or contactors in which gas is dispersed in the form of bubbles into a continuous liquid phase to effect an intensive interfacial contacting. The resulting two-phase flow accounts for the excellent heat and mass transfer characteristics of this type of apparatus. Due to these favorable properties, bubble columns are intensively applied in chemical, biochemical, petrochemical, pharmaceutical and metallurgical industries for a variety of processes, i.e. oxidation, hydrogenation, chlorination, numerous biochemical processes [110], etc. Additional advantages of these apparatuses are their compactness, simple construction without moving parts and low operating and maintenance costs. Industrial high tonnage bubble columns are built in a wide range of sizes, from devices with a capacity of $100\,\mathrm{m}^3 - 200\,\mathrm{m}^3$ to large reactors with $3000\,\mathrm{m}^3$. Units for waste water treatment may even exceed these dimensions and reach a capacity of up to $20\,000\,\mathrm{m}^3$ [56].

A conventional bubble column is constituted of a cylindrical vessel holding the liquid with a gas distributor at its bottom. Various types are commonly used for the distributor design, including perforated plates, sintered plates or different jet configurations. A basic bubble column setup is sketched in figure 1.1. Gas is sparged into the column, in which ascending bubbles interact with the liquid phase and induce a dynamic two-phase flow. Depending on the intensity of mass transfer phenomena, a corresponding proportion of the gaseous phase is absorbed in the liquid, while the remaining gas escapes through the upper surface. The off-gas is either recovered and fed back to the gas inlet or is released.

Bubble column designs have been modified and adapted over the years to a wide range of configurations. The insertion of internals into the two-phase flow region is very common in industrial reactors to prevent an excessive maldistribution of the gaseous phase, attenuate large recirculation zones

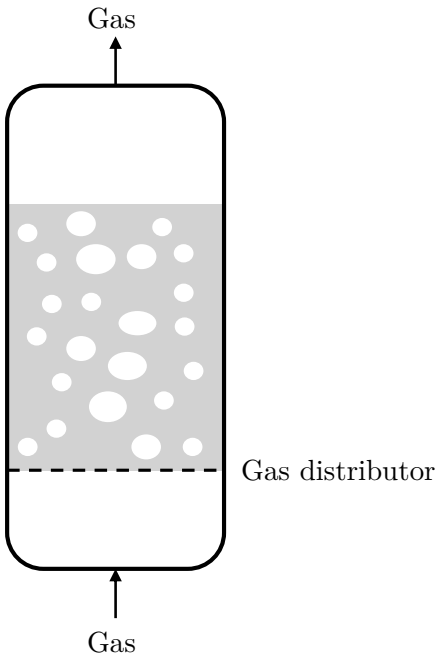

Figure 1.1: Sketch of a simple bubble column configuration

or adjust the reactor temperature level via integral heat exchange devices. Horizontally arranged internal perforated plates create a multistage cascade, which intensifies mass transfer, while installed packings or static mixers promote a uniform gas flow throughout the column. In bubble column loop reactors, the recirculation of the liquid phase is directed through internal or external loops. In this way, a high gas throughput can be achieved, retaining a homogenous two-phase flow zone [105]. Slurry bubble columns are three-phase reactors or contactors characterized by the suspension of particles in the liquid phase. This type of apparatus allows for an intimate and homogeneous contacting of solid catalysts with the gas-liquid flow.

Although the gas is distributed homogeneously over the entire cross-section in conventional bubble columns, the dispersed gaseous phase predominantly rises through the center of the column, specifically larger bubbles. By entraining the surrounding liquid, the ascending gas phase causes a recirculating fluid motion of the liquid phase. The liquid moves downwards in the near-wall regions, partially transporting a certain amount of bubbles with it. Depending on the column geometry and the gas throughput, this pattern is eventually superimposed by radial, meandering or spiral motions of the gas-liquid flow. The resulting complex hydrodynamic behavior determines

the two-phase flow characteristics, including dispersed and continuous phase velocities, gas phase distribution and bubble sizes.

The core of chemical reactor design can be subdivided into the modeling of chemical reactions and flow dynamics. While there is an emphasis on using very detailed approaches for the reaction kinetics, strongly simplifying assumptions are often applied concerning the occurring pattern of fluid motion. Due to this prioritization, the insufficient understanding of prevailing fluid dynamics often is a major source of uncertainty in the reactor design (see figure 1.2).

This correlation is particularly relevant for bubble column reactors, since the gas-liquid interaction determines heat and mass transfer effects, which govern the functionality and efficiency of the apparatus. In most cases, empirical correlations and deductions from oversimplified considerations are used for the evaluation of hydrodynamic characteristics, mass and heat transfer phenomena, and dispersion processes in bubble columns [188]. These approaches do not capture the complexity of interacting phenomena and their results are limited in accuracy and scope of application. For a more detailed representation of the hydrodynamic, thermodynamic and chemical processes of the gas-liquid flow, analysis methods based on *computational fluid dynamics* (CFD) have been promoted in recent years.

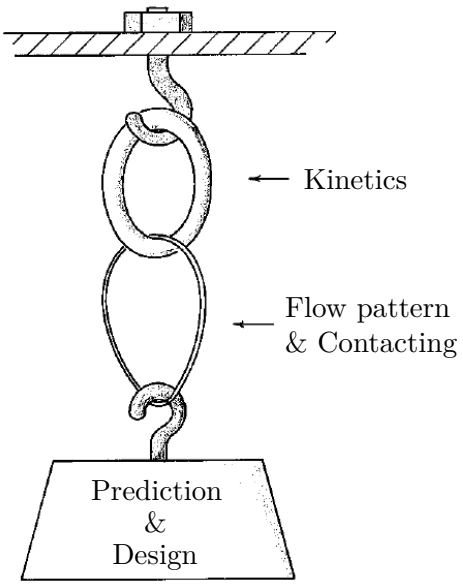

Figure 1.2: The role of fluid dynamics and kinetics in chemical reactor design [127]

The development and enhancement of CFD methods for multiphase flows has been a field of activity for numerous researchers over the last two to three decades. Most of these research activities can be assigned to one of three general simulation techniques, which differ in their modeling approach, their focus of investigation and their computational demands [177] [223] (see section 2.1). All of these fundamental multiphase CFD methods have been applied to turbulent gas-liquid flows in numerous studies. Nevertheless, the representation of various aspects of gas-liquid flow dynamics with conventional CFD approaches is associated with considerable uncertainties, bound to specific hydrodynamic conditions or requires a disproportional computational effort. Specifically focusing on the enhancement of CFD models for industrial scale bubble column hydrodynamics, the present work contributes to the continuing research effort in the respective field.

1.2 Objectives and outline

The aim of this work is the development of a numerically efficient simulation model for the comprehensive representation of bubble column flows in industrial scale applications. To accurately capture the complex two-phase hydrodynamics, the modeling approach is required to reproduce the transient character of these flows in a three-dimensional domain. These constraints necessitate the application of a computationally efficient method with an associated discretization of the flow field.

The approach at hand resolves the fluid dynamics to a large extent, while non-resolved phenomena are accounted for by corresponding model formulations. Besides the abstracted consideration of interfacial phenomena, e.g., mass and momentum transfer effects, the allowance of fluid particle interaction, i.e. breakup and coalescence, represents the major part of this modeling effort. In contrast to the majority of related studies, the energy containing scales of fluid turbulence are resolved in this approach, while only small scale turbulent phenomena are considered in the form of model formulations. This procedure gives a detailed representation of turbulence in the flow field and its influence on fluid dynamics and bubble interaction.

As the consideration of different fluid particle sizes, i.e. *polydispersity*, is potentially associated with a substantially increased computational demand

of the respective CFD method for multiphase flows, its numerically efficient incorporation in the current model is a core part of this study. Fluid particle dimensions are decisive for the accurate determination of the gas phase flow dynamics and its interaction with the continuous phase. Depending on the hydrodynamic and geometrical conditions, a broad spectrum of bubble sizes may occur in a bubble column reactor.

A subdivision of the fluid particle size spectrum is commonly used to incorporate polydispersity in related multiphase CFD approaches. This direct consideration of the entire size range prevents the analysis of gas-liquid flows in large domains with reasonable computational effort. Since this work specifically aims at the simulation of industrial scale applications, local bubble size spectra are represented in an abstracted manner by using only specific characteristics of the associated size distribution function (i.e. the mathematical moments). This procedure significantly reduces the computational demand for the resolution of fluid particle polydispersity.

The present approach for the abstracted representation of local fluid particle dimensions necessitates an adaption of bubble breakup and coalescence formulations to suit this modeling framework. Based on the characteristics of this conversion process, additional constraints affect the selection and incorporation of fluid particle interaction formulations. The novel configuration of models in this work is established on the premise of not only providing accuracy in the description of breakup and coalescence phenomena, but also retaining efficiency in its numerical realization. In contrast to common variants of the considered modeling framework, the current method is able to comprehensively describe the polydisperse character of industrial scale bubble column hydrodynamics with reasonable computational effort.

Besides the influence of breakup and coalescence phenomena on local bubble size distributions, the respective population balance is also affected by non-uniformities in local fluid particle motion. An incorporation of model functionalities for the evaluation of individual bubble velocities contradicts the superimposed modeling concept and is impracticable for bubble column flows of the considered scale. With the current restriction to locally size-dependent bubble dynamics, a numerically efficient evaluation of resulting implications on bubble size relations is ensured. Although this concept of size-specific fluid particle motion, i.e. *polycelerity*, generally represents

a simplification, it is specifically favorable for bubbly flows, where the dispersed phase flow is governed by interfacial interaction rather than by particle inertia. While the assumption of locally uniform bubble velocities is commonly made in alternative studies, the present model configuration captures polydisperse gas phase motion more accurately. As a novel application, the current work exhibits the representation of polycelerity in the simulation of complex bubble column hydrodynamics.

Using experimental data from well-studied test cases, the current numerical model is validated by a comparison of pilot scale bubble column flow characteristics. Besides fluid dynamic properties including dispersed and continuous phase velocities as well as characteristics of turbulence, local bubble size distributions and gas fractions are analyzed and contrasted. In a further study, the transport and interfacial exchange of chemical species is analyzed numerically.

In chapter 2 of this thesis, the general mathematical correlations for the description of multiphase flows are derived in conjunction with the introduction of corresponding modeling approaches. Subsequently, fundamentals for the applied gas-liquid flow modeling concept are discussed further, with an emphasis on turbulence considerations and interfacial exchange formulations. The chapter is completed by a brief outline of modeling approaches for chemical reaction phenomena within a CFD framework, associated with a discussion on their accurate scope of application.

The principles of population balance theory are presented in chapter 3, accompanied by the derivation of corresponding governing equations. While the central part of this section focuses on the consideration of breakup and coalescence phenomena, the incorporation of population balance equations into a CFD framework is exemplified. The introduction of the configuration used in this study concludes the chapter.

With reference to the introduction of general modeling concepts in the preceding sections, the methodical details of the approach employed in the current study are specified in chapter 4. To this end, the adaptions and extensions of prevalent theories, which have been developed in the scope of this work, are explicated and formally derived. An outline of the model implementation into an existing CFD framework represents the final part of this segment.

The validation studies of the developed model are presented in chapter 5. Besides the comparison of current simulation results concerning hydrodynamic properties with equivalent data from experimental and numerical studies, this part consists of an investigation of different local particle velocity evaluation approaches. As a final point, the depiction of absorption processes with the current numerical framework is analyzed.

2 Gas-liquid flow modeling

2.1 Modeling approaches

Caused by the dynamic interaction between the dispersed and the continuous phase, bubble column hydrodynamics are characterized by a broad spectrum of fluid dynamic time and length scales. These length scales encompass several orders of magnitude, ranging from large-scale liquid circulations of up to several meters down to the smallest scales of turbulence. Due to the width of the spatial and temporal range of gas-liquid motion, a direct numerical representation of all hydrodynamic phenomena in industrial bubble columns is not feasible. Therefore, different multiphase CFD methods have been developed, resolving specific scales of the gas-liquid flow field, while representing unresolved hydrodynamic effects through appropriate model formulations.

Table 2.1 provides an overview of the available CFD methods for dispersed gas-liquid flows, including their considered length scales and potential applications. This categorization of approaches subject to the level of spatial resolution is also referred to as *hierarchy of models* [199] [54]. Every numerical approach is tailored to investigate specific hydrodynamic characteristics, which eventually can be transferred to the coarser-resolving CFD approach in the form of subscale model formulations. This interrelated multilevel modeling allows for the numerical investigation of gas-liquid flow phenomena of almost the entire spectrum of length and time scales [211]. Yet, every level of numerical gas-liquid flow modeling is accompanied by a considerable effort of model development and validation. Subsequently, the three general CFD methods for the simulation of dispersed gas-liquid flows will be introduced in more detail.

Interface resolving methods

Interface tracking or capturing methods resolve the position and dynamic behavior of the phase boundaries. Hence, these approaches are preferably used for the simulation of segregated gas-liquid and

Model	Equations	Spacial resolution	Applicability
Interface resolving methods	Navier-Stokes equation for both phases; advanced interface tracking or capturing scheme	High $\Delta \ll D_p$	Small systems; $\mathcal{O}(10^2)$ bubbles
Euler-Lagrange model	Equation of motion for each bubble; volume averaged mass-and momentum conservation equation for liquid phase	Medium $\Delta \approx D_p$	Lab-scale bubble columns, bubble plumes
Euler-Euler model	Averaged mass and momentum conservation equations for both phases	Low $\Delta \gg D_p$	Full size reactor

Table 2.1: Overview of general modeling techniques for dispersed gas-liquid flows (adapted from [59])

liquid-liquid flows or detailed studies of dispersed flows with a small number of fluid particles. The fluid dynamics of the phases and their interfacial coupling is described directly by the Navier-Stokes equations with respective phase-specific properties. No cross-phase averaging procedure is applied, accompanied by modeling assumptions for unresolved multiphase flow conditions. Due to their very high computational demand, these methods are not suitable for the simulation of dispersed two-phase flows in industrial scale applications, e.g., bubble column hydrodynamics.

Interface tracking and capturing approaches differ in the way phase boundaries are accounted for. Commonly, interface tracking techniques are based on a moving mesh approach, in which the interface coincides with a set of conforming cell faces. Alternatively, a dynamic surface mesh or Lagrangian particles are employed to depict the phase boundaries relative to a fixed Eulerian mesh. These approaches are commonly referred to as front-tracking methods [208] [204]. While the representation of the interface is very accurate, strong topology changes of bubbles such as breakup and coalescence require additional model modifications.

In contrast, the interface capturing method is typically based on a purely Eulerian description of the two-phase flow field. With this approach, the Navier-Stokes equation is supplemented by an advection equation for a marker field, indicating the position of fluid interfaces.

In this way, even major transformations of the phase boundaries can be depicted, provided that advanced numerical schemes are used to optimally ensure the conservativity of both phases. The two most commonly applied variants of the interface capturing approach are the *Level-Set method* [166] [187] and the *Volume-of-Fluid (VOF) method* [98].

Euler-Lagrange method

This approach is applicable exclusively to the simulation of dispersed multiphase flows. The primary phase is described as a continuum in an Eulerian context, while the particles of the dispersed phase are tracked individually in a Lagrangian manner. Interfacial coupling is the crucial part of the Euler-Lagrange method and various corresponding approaches, representing different levels of modeling complexity, can be applied. Although several techniques have been developed to average particle conditions or define representative particles, the computational costs of this method prevent the adequate depiction of the multiphase flow dynamics in industrial applications with a large number of dispersed particles.

If a one-way coupling approach is applied, the influence of the dispersed phase on the continuous phase is neglected, whereas the fluid particle motion is mainly governed by the primary phase velocity. In contrast, a two-way coupling technique considers the interdependency of gas-liquid phase motion, including the back-coupling of bubble presence and dynamics on the continuous phase. By additionally depicting particle-particle interaction in the flow field, the four-way coupling approach provides the most comprehensive representation of the two-phase flow dynamics. Although its application is accompanied by a substantial increase in computational effort, this coupling procedure is essential for the accurate representation of bubble column flows with moderate to high gas throughput.

The dispersed phase volume fraction α_d is a rough indicator of which coupling approach is most appropriate for the concerned gas-liquid flow. One-way coupling may be used for marginal gas content $\alpha < 10^{-6}$, while the two-way coupling approach is suitable for gas volume fractions of up to $\alpha \approx 10^{-3}$. For higher values of the dispersed

phase volume fraction, a four-way coupling technique should be used [191] [74] [218].

Euler-Euler method

Both the dispersed as well as the continuous phase are considered as interpenetrating continua with this approach. Instead of resolving interfacial surfaces, the phase volume fraction indicates local phase proportions. The representation of the two-phase flow on the corresponding large scale level necessitates the incorporation of model formulations for the description of phase interaction phenomena. Using this approach, it is possible to simulate the multiphase hydrodynamics of industrial applications with their large dimensions and numerous dispersed phase particles.

The governing equations for the Euler-Euler method can be derived from different averaging techniques of the fluid dynamic conservation equations (see section 2.2), implicating the consideration of unresolved flow phenomena through respective models. Formulations for the interfacial exchange of mass, momentum or heat may be derived empirically, numerically or analytically. Based on simplifying assumptions concerning the kinetic exchange between the phases and the interfacial velocity difference respectively, a number of simplistic two-phase flow models have been developed (e.g., *homogeneous equilibrium model* [101], *drift flux model* [230], *diffusion model* [207]). Since their scope of application is limited and excludes the detailed description of complex bubble column flows, these approaches will not be discussed further in this work.

With the incorporation of a population balance equation (PBE), local bubble size distributions can be considered in the Euler-Euler framework. In addition, this configuration allows for the inclusion of breakup and coalescence phenomena to give a profound representation of polydisperse gas-liquid flows.

The Euler-Euler method is taken as the basis for the numerical simulation model introduced in this work. Through comprehensive adaptions and extensions, an adequate method for the description of bubble column hydrodynamics of industrial relevance is developed. The theoretical foundation

of this approach is outlined in the subsequent section, followed by the explication of complementing and exceeding model formulations.

2.2 Eulerian governing equations

The governing equations for multiphase flows in an Eulerian context with a focus on the formulations for dispersed gas-liquid flows are derived in this section. The starting point for this process is the local instantaneous formulation of a general balance equation in an incompressible and isothermal multiphase environment. With a short overview of conventional averaging procedures (time averaging, volume averaging, ensemble averaging), the volume fraction is introduced as the indicator function for the phases. Subsequently, the volume averaged continuous field transport equations of mass, momentum and chemical species are deduced in a phase-specific context.

The following derivation of two-phase flow governing equations is restricted to the concept of a continuous field description of the phases in an Eulerian context. Although the deduction of interface tracking and capturing methods is closely related to the outlined procedure, merely distinct in the scale of averaging, these approaches are not discussed in further detail in this work. In contrast to more general concepts, which allow for numerous dispersed phases, or include a potential size-specific classification of fluid particles in the equation derivation (i.e. *multifluid model*), the following explications differentiate between two phases only (i.e. *two-fluid model*). For more generic approaches in the derivation of mathematical formulations for Eulerian multiphase models, the reader is referred to respective literature by Drew & Passman [70], Ishii & Hibiki [103], Prosperetti & Tryggvason [177] or Kolev [113].

2.2.1 Local instantaneous formulation

The discussion of local instantaneous governing equations in a multiphase system is predicated on the consideration of a spatially fixed control volume V_C which is occupied by two separated time-dependent subregions $V_1(t)$ and $V_2(t)$ associated with different physical phases (see figure 2.1):

$$V_C = V_1(t) \cup V_2(t) = \bigcup_k V_k(t) \quad \text{with} \quad k = 1, 2. \tag{2.1}$$

The region boundaries are denoted as A_C and $A_k(t)$ respectively, with $A_I(t) = A_1(t) \cap A_2(t)$ as the phase separating interface which is considered as surface of infinitesimal thickness. The delimitation A_C of the domain V_C is comprised of subregion boundaries sections:

$$A_C = A_{1,C}(t) \cup A_{2,C}(t) = \bigcup_k A_{k,C}(t) \quad \text{with} \quad A_{k,C} \subseteq A_k. \tag{2.2}$$

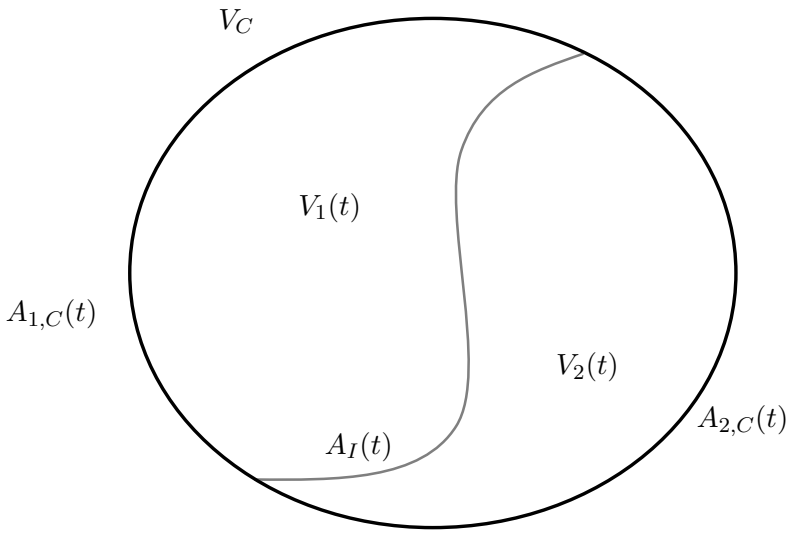

Figure 2.1: Eulerian control volume V_C and subdomains $V_1(t)$, $V_2(t)$ for two-fluid balance equations

This simple reference environment is the basis for the subsequent derivation of a balance equation for the generic phase-specific extensive fluid property ψ_k. The respective mathematical conversion is applied in a comparable manner for the more general multifluid approach by, e.g., Hjertager [99] or Buffo [27].

Assuming the validity of the continuum hypothesis, the integral balance formulation for ψ on V_C results in

$$\frac{\mathrm{d}}{\mathrm{d}t}\int_{V_C}\rho\psi\,\mathrm{d}V = \underbrace{\sum_k\left(\frac{\mathrm{d}}{\mathrm{d}t}\int_{V_k(t)}\rho_k\psi_k\,\mathrm{d}V\right)}_{\text{accumulation}} = \\ \underbrace{-\sum_k\int_{A_{k,C}(t)}\rho_k\psi_k\left(\boldsymbol{u}_k\cdot\boldsymbol{n}_k\right)\,\mathrm{d}A}_{\text{net convective flux}} \underbrace{-\sum_k\int_{A_{k,C}(t)}\left(\boldsymbol{J}_k\cdot\boldsymbol{n}_k\right)\,\mathrm{d}A}_{\text{net diffusive flux}} \\ + \underbrace{\int_{A_I(t)}\Phi_I\,\mathrm{d}A}_{\text{interfacial source term}} + \underbrace{\sum_k\int_{V_k(t)}\rho_k\Phi_k\,\mathrm{d}V}_{\text{volumetric source term}}, \tag{2.3}$$

where ρ_k, $\boldsymbol{u}_k$ and $\boldsymbol{J}_k$ are the density, velocity and molecular flux of phase k, $\boldsymbol{n}_k$ denotes the normal vector of $A_k(t)$ in outward direction, and Φ_I and Φ_k are the interfacial and volumetric source term.

With the introduction of an interface velocity $\boldsymbol{u}_I$, the terms of equation (2.3) representing accumulation, net convective flux and net diffusive flux are transformed by making use of Leibniz and Gauss' theorems:

$$\frac{\mathrm{d}}{\mathrm{d}t}\int_{V_k(t)}\rho_k\psi_k\,\mathrm{d}V = \int_{V_k(t)}\frac{\partial}{\partial t}\rho_k\psi_k\,\mathrm{d}V + \int_{A_I(t)}\rho_k\psi_k\left(\boldsymbol{u}_I\cdot\boldsymbol{n}_{k,I}\right)\,\mathrm{d}A, \tag{2.4}$$

$$\int_{A_{k,C}(t)}\rho_k\psi_k\left(\boldsymbol{u}_k\cdot\boldsymbol{n}_k\right)\,\mathrm{d}A = \int_{V_k(t)}\nabla\cdot\left(\rho_k\psi_k\boldsymbol{u}_k\right)\,\mathrm{d}V - \int_{A_I(t)}\rho_k\psi_k\left(\boldsymbol{u}_I\cdot\boldsymbol{n}_{k,I}\right)\,\mathrm{d}A, \tag{2.5}$$

$$\int_{A_{k,C}(t)}\left(\boldsymbol{J}_k\cdot\boldsymbol{n}_k\right)\,\mathrm{d}A = \int_{V_k(t)}\nabla\cdot\boldsymbol{J}_k\,\mathrm{d}V - \int_{A_I(t)}\left(\boldsymbol{J}_k\cdot\boldsymbol{n}_{k,I}\right)\,\mathrm{d}A, \tag{2.6}$$

where $\boldsymbol{n}_{k,I}$ represents $\boldsymbol{n}_k$ exclusively on the phase boundary to denote the direction of interfacial exchange associated with k.

The combination of equations (2.3) to (2.6) yields

$$\sum_k\int_{V_k(t)}\left[\frac{\partial}{\partial t}\rho_k\psi_k + \nabla\cdot\left(\rho_k\psi_k\boldsymbol{u}_k\right) + \nabla\cdot\boldsymbol{J}_k - \rho_k\Phi_k\right]\,\mathrm{d}V = \\ \sum_k\int_{A_I(t)}\left[\dot{m}_{k,I}\psi_k + \left(\boldsymbol{J}_k\cdot\boldsymbol{n}_{k,I}\right)\right]\,\mathrm{d}A + \int_{A_I(t)}\Phi_I\,\mathrm{d}A, \tag{2.7}$$

with $\dot{m}_{k,I}$ representing the interfacial mass flux emanating from phase k, which in turn is defined as

$$\dot{m}_{k,I} = \rho_k \left(\boldsymbol{u}_k - \boldsymbol{u}_I \right) \cdot \boldsymbol{n}_{k,I}. \tag{2.8}$$

The generic choice of V_C implies a global validity of equation (2.7). Hence, the local instantaneous equation is deduced to

$$\frac{\partial}{\partial t} \rho_k \psi_k + \nabla \cdot \left(\rho_k \psi_k \boldsymbol{u}_k \right) + \nabla \cdot \boldsymbol{J}_k = \rho_k \Phi_k, \tag{2.9}$$

with the corresponding interfacial jump condition

$$\dot{m}_{1,I} \psi_1 + \dot{m}_{2,I} \psi_2 + \boldsymbol{J}_1 \cdot \boldsymbol{n}_{1,I} + \boldsymbol{J}_2 \cdot \boldsymbol{n}_{2,I} = -\Phi_I. \tag{2.10}$$

As a consequence of the physical phenomena considered in this work, the balance equations for mass, momentum and chemical species are formulated from the equations (2.9) and (2.10). The additional deduction of the energy balance equation in various forms is outlined by Jakobsen [105].

Mass balance equation $(\psi_k = 0)$

$$\frac{\partial}{\partial t} \rho_k + \nabla \cdot \left(\rho_k \boldsymbol{u}_k \right) = 0. \tag{2.11}$$

Interfacial jump condition

$$\dot{m}_{1,I} + \dot{m}_{2,I} = 0. \tag{2.12}$$

Momentum balance equation $(\psi_k = \boldsymbol{u}_k)$

$$\frac{\partial}{\partial t} \left(\rho_k \boldsymbol{u}_k \right) + \nabla \cdot \left(\rho_k \boldsymbol{u}_k \boldsymbol{u}_k \right) = \nabla \cdot \boldsymbol{T}_k + \rho_k \boldsymbol{b}_k. \tag{2.13}$$

Interfacial jump condition

$$\dot{m}_{1,I} \boldsymbol{u}_1 + \dot{m}_{2,I} \boldsymbol{u}_2 - \boldsymbol{T}_1 \cdot \boldsymbol{n}_{1,I} - \boldsymbol{T}_2 \cdot \boldsymbol{n}_{2,I} = \boldsymbol{\varsigma}_I. \tag{2.14}$$

The stress tensor $\boldsymbol{T}$ characterizes the diffusive transport of momentum. The unity of volumetric or body forces is represented by $\boldsymbol{b}_k$ and $\boldsymbol{\varsigma}_I$

denotes the area-specific surface force. With the assumption of a constant surface tension σ, $\boldsymbol{\varsigma}_I$ is defined as

$$\boldsymbol{\varsigma}_I = 2\kappa_I \sigma \boldsymbol{n}_{k,I}, \tag{2.15}$$

where κ_I represents the interface curvature [8].

Chemical species balance equation $(\psi_k = Y_k^{\mathrm{X}})$

$$\frac{\partial}{\partial t}\left(\rho_k Y_k^{\mathrm{X}}\right) + \nabla \cdot \left(\rho_k Y_k^{\mathrm{X}} \boldsymbol{u}_k\right) = -\nabla \cdot \boldsymbol{G}_k^{\mathrm{X}} + \rho_k \Psi_k^{\mathrm{X}}. \tag{2.16}$$

Interfacial jump condition

$$\dot{m}_{1,I} Y_1^{\mathrm{X}} + \dot{m}_{2,I} Y_2^{\mathrm{X}} + \boldsymbol{G}_1^{\mathrm{X}} \cdot \boldsymbol{n}_{1,I} + \boldsymbol{G}_2^{\mathrm{X}} \cdot \boldsymbol{n}_{2,I} = \Upsilon_I^{\mathrm{X}}. \tag{2.17}$$

$\boldsymbol{G}^{\mathrm{X}}$ denotes the diffusive flux of chemical species X according to Fick's law, while Ψ^{X} and Υ_I^{X} represent the net volumetric and interfacial production rate of X.

Equations (2.11) to (2.17) constitute the mathematical framework for a hydrodynamic and chemical depiction of an arbitrary gas-liquid system. For the adoption of these governing equations in a CFD simulation, a numerical discretization is required associated by a respective averaging of local fluid dynamic conditions. The scale of averaging determines the spectrum of hydrodynamic phenomena that are captured and signifies the computational demand. For the consideration of industrial scale apparatuses, comparably large scale averaging techniques are most suitable.

2.2.2 Averaging of governing equations

The numerical consideration of multiphase flow phenomena in an Euler-Euler context, associated with a respective spatially fixed discretization for both phases, implies the definition of averaged governing equations. Unresolved local multiphase flow conditions are accounted for by model formulations. Several techniques have been adopted for the derivation of averaged gas-liquid governing equations. These methods can be assigned to three fundamental approaches: *volume averaging* [164], *time averaging* [101] and *ensemble averaging* [68].

The separation of multiphase fluid dynamic phenomena into explicitly resolved and unresolved physical processes serves as a basic principle and is common to all of the mentioned procedures. For volume or time averaging, a continuous spatial domain or temporal interval is determined, while numerous discrete realizations are used to obtain a representative mean in the ensemble averaging method. Although the averaging domains differ in their dimension, these approaches are associated through the spatio-temporal correlation of fluid motion. For fluid dynamic investigations, be they of numerical, experimental or analytical nature, the ergodic hypothesis is commonly assumed valid. It states that for statistically stationary and homogeneous flows the volume, time and ensemble averages are identical [105]. Consequently, the resulting averaged governing equations are similar in the description of resolved flow phenomena and their mathematical structure is independent of the employed averaging approach.

In consideration of the spatial discretization of the multiphase flow domain with the application of CFD, the volume averaging approach appears most suitable. However, in the opinion of several researchers, the validity of averaged flow characteristics in an Euler-Euler formulation is predicated on the selection of an accurate averaging range. In this regard, Nigmatulin [164] argued that the considered domain should be "many times greater than the nonuniformities [...], but at the same time much less than the characteristic macrodimension of a problem". On the other hand, the properties of averaging procedures indicate that a different selection of the averaging scale does not implicate the invalidity of averaged flow quantities, but necessitates the reinterpretation of respective fluid dynamic characteristics and corresponding unclosed terms [21]. Even if the averaged quantities may not be exactly smooth, various numerical results (e.g., [227], [197], [163]) evince that a spatial discretization in range or slightly larger than the fluid particle size is sufficient for the adequate description of the dispersed phase as an Eulerian continuum. Additionally, an according resolution allows for an improved depiction of the continuous flow dynamics and hence may represent a favorable compromise. This correlation is further discussed in section 2.3 with regard to turbulence modeling. For a more detailed investigation of the connection between dispersed phase particle size and averaging domain, the reader is referred to respective discussions by Brennen [24] or Crowe et al. [49].

The volume averaging approach is used for the subsequent derivation of Euler-Euler gas-liquid flow governing equations. The interpretation of the averaging domain as a spatial filter is not only in line with the numerical discretization, but also agrees with the applied technique for turbulence modeling (see section 2.3.1). As a preliminary step, the characteristic or indicator function $X_k(\boldsymbol{x}, t)$ is introduced, depicting the position of phase k in the form of a Heavyside function:

$$X_k(\boldsymbol{x}, t) = \begin{cases} 1 & \text{if } \boldsymbol{x} \in V_k(t) \\ 0 & \text{otherwise} \end{cases}. \tag{2.18}$$

As the characteristic function can be interpreted as an extensive quantity analogous to the phase volume, a conservation equation is formulated, reading

$$\frac{\partial X_k}{\partial t} + \boldsymbol{u}_I \cdot \nabla X_k = 0. \tag{2.19}$$

Here, the gradient of the phase indicator function is defined as

$$\nabla X_k = \boldsymbol{n}_{k,I}\, \delta\left(\boldsymbol{x} - \boldsymbol{x}_I\right), \tag{2.20}$$

with $\delta\left(\boldsymbol{x} - \boldsymbol{x}_I, t\right)$ denoting the Dirac delta function for the identification of the interface associated with the respective position $\boldsymbol{x}_I$.

The consideration of the Eulerian control volume V_C with its internal location $\boldsymbol{x}$ is complemented by a relative position vector $\boldsymbol{\eta}$. This configuration allows for the representation of an arbitrary location in V_C by $\boldsymbol{x}' = \boldsymbol{x} + \boldsymbol{\eta}$. Hence, the mathematical operation of the volume averaging procedure of a generic quantity ψ is formulated as

$$\langle \psi \rangle = \frac{1}{V_C} \int_V \psi\left(\boldsymbol{x} + \boldsymbol{\eta}, t\right) \, \mathrm{d}\boldsymbol{x}'. \tag{2.21}$$

Applied to the characteristic function X_k, the volume averaging results in

$$\langle X_k \rangle = \frac{1}{V_C} \int_V X_k\left(\boldsymbol{x} + \boldsymbol{\eta}, t\right) \, \mathrm{d}\boldsymbol{x}' = \frac{V_k}{V_C} = \alpha_k. \tag{2.22}$$

This expression describes the volume fraction of phase k, where

$$\sum_k \alpha_k = \alpha_c + \alpha_d = 1. \tag{2.23}$$

As a prerequisite for the volumetric averaging of the conservation equations, Leibnitz and Gauss' rules for the temporal and convective term are defined as

$$\left\langle X_k \frac{\partial \psi_k}{\partial t} \right\rangle = \frac{\partial}{\partial t} \langle X_k \psi_k \rangle - \left\langle \psi_k \frac{\partial X_k}{\partial t} \right\rangle \overset{(2.19)}{=} \frac{\partial}{\partial t} \langle X_k \psi_k \rangle + \langle \psi_k \boldsymbol{u}_I \nabla \cdot X_k \rangle = \frac{\partial}{\partial t} \langle X_k \psi_k \rangle + \frac{1}{V_C} \int_{A_I(t)} \boldsymbol{n}_{k,I} \cdot \boldsymbol{u}_I \psi_k \left(\boldsymbol{x} + \boldsymbol{\eta}, t \right) \mathrm{d}A, \tag{2.24}$$

$$\langle X_k \nabla \psi_k \rangle = \nabla \langle X_k \psi_k \rangle - \langle \psi_k \nabla X_k \rangle = \nabla \langle X_k \psi_k \rangle - \frac{1}{V_C} \int_{A_I(t)} \boldsymbol{n}_{k,I} \psi_k \left(\boldsymbol{x} + \boldsymbol{\eta}, t \right) \mathrm{d}A. \tag{2.25}$$

By first multiplying the local instantaneous equation (2.9) with the characteristic function X_k, followed by the volumetric averaging procedure with respect to (2.24) and (2.25), the averaged balance equation for a generic phase-specific fluid variable ψ_k is obtained as

$$\frac{\partial}{\partial t} \langle X_k \rho_k \psi_k \rangle + \nabla \cdot \langle X_k \rho_k \psi_k \boldsymbol{u}_k \rangle + \nabla \cdot \langle X_k \boldsymbol{J}_k \rangle = \langle X_k \rho_k \Psi_k \rangle - \frac{1}{V_C} \int_{A_I} \left(\dot{m}_{k,I} \psi_k + \boldsymbol{J}_k \cdot \boldsymbol{n}_I \right) \mathrm{d}A. \tag{2.26}$$

The corresponding jump condition is formulated by multiplying (2.10) with the gradient of the indicator function ∇X_k prior to volume averaging. This limits the averaging domain to the phase boundaries and yields

$$\int_{A_I} \left(\dot{m}_{1,I} \psi_1 + \dot{m}_{2,I} \psi_2 + \boldsymbol{J}_1 \cdot \boldsymbol{n}_{1,I} + \boldsymbol{J}_2 \cdot \boldsymbol{n}_{2,I} \right) \mathrm{d}A = - \int_{A_I} \Phi_I \, \mathrm{d}A. \tag{2.27}$$

This derivation is restricted to isothermal and incompressible fluids only. Furthermore, the densities of both phases are assumed constant. Aiming at the formulation of the constitutive equations of the two-fluid model subject to volume averaged single fluid quantities, it is suitable to define a phasic averaging operator based on (2.21) as

$$\overline{\psi}_k = \frac{\langle X_k \psi_k \rangle}{\alpha_k}. \tag{2.28}$$

Given these prerequisites, equation (2.26) can be written in the form of

$$\frac{\partial}{\partial t}\left(\alpha_k \rho_k \overline{\psi}_k\right) + \nabla \cdot \left(\alpha_k \rho_k \overline{\psi}_k \overline{\boldsymbol{u}}_k\right) + \nabla \cdot \left[\alpha_k \left(\overline{\boldsymbol{J}_k} + \boldsymbol{J}_{k,tur}\right)\right] = \alpha_k \rho_k \overline{\Psi}_k - \frac{1}{V_C} \int_{A_I} \left(\dot{m}_{k,I} \psi_k + \boldsymbol{J}_k \cdot \boldsymbol{n}_I\right) \mathrm{d}A. \tag{2.29}$$

Denoting the unresolved scales of turbulence fluctuations, $\boldsymbol{J}_{k,tur}$ originates from the averaging of the advective term in the transport equation and is defined as

$$\boldsymbol{J}_{k,tur} = \rho_k \left(\overline{\psi_k \boldsymbol{u}_k} - \overline{\psi}_k \overline{\boldsymbol{u}}_k\right). \tag{2.30}$$

$\boldsymbol{J}_{k,tur}$ cannot be evaluated from averaged flow quantities and thus must be accounted for by a respective model formulation. The basic modeling approach as well as several methods for the determination of $\boldsymbol{J}_{k,tur}$ are explicated in the subsequent chapter.

With the specification of the generic variable ψ, the averaged two-fluid governing equations are derived, consisting of respective formulations for mass, momentum and chemical species.

Mass balance equation $(\overline{\psi}_k = 0)$

$$\frac{\partial}{\partial t}\left(\alpha_k \rho_k\right) + \nabla \cdot \left(\alpha_k \rho_k \overline{\boldsymbol{u}}_k\right) = \Gamma_k. \tag{2.31}$$

The source term Γ_k denotes the interfacial mass transfer, described as

$$\Gamma_k = -\frac{1}{V_C}\int_{A_I} \dot{m}_{k,I}\,\mathrm{d}A. \tag{2.32}$$

Interfacial jump condition

$$\int_{A_I} \left(\dot{m}_{1,I} + \dot{m}_{2,I}\right)\,\mathrm{d}A = \Gamma_1 + \Gamma_2 = 0. \tag{2.33}$$

Momentum balance equation $(\overline{\psi}_k = \overline{\boldsymbol{u}}_k)$

$$\frac{\partial}{\partial t}\left(\alpha_k\rho_k\overline{\boldsymbol{u}}_k\right) + \nabla\cdot\left(\alpha_k\rho_k\overline{\boldsymbol{u}}_k\overline{\boldsymbol{u}}_k\right) = \nabla\cdot\left[\alpha_k\left(\overline{\boldsymbol{T}}_k - \boldsymbol{T}_{k,tur}\right)\right] + \left(\alpha_k\rho_k\boldsymbol{g}\right) + \boldsymbol{M}_{k,\Gamma} + \boldsymbol{M}_{k,I}. \tag{2.34}$$

The residual stress tensor in virtue of unresolved turbulence is represented by $\boldsymbol{T}_{k,tur}$. $\boldsymbol{M}_{k,\Gamma}$ denotes the net variation of momentum due to interfacial mass transfer and is commonly approximated by

$$\boldsymbol{M}_{k,\Gamma} = -\frac{1}{V_C}\int_{A_I}\left(\dot{m}_{k,I}\boldsymbol{u}_k\right)\,\mathrm{d}A \approx \Gamma_k\overline{\boldsymbol{u}}_k, \tag{2.35}$$

while the interfacial flux of momentum is represented by $\boldsymbol{M}_{k,I}$, formulated as

$$\boldsymbol{M}_{k,I} = \frac{1}{V_C}\int_{A_I}\left(\boldsymbol{T}_k\cdot\boldsymbol{n}_{k,I}\right)\,\mathrm{d}A. \tag{2.36}$$

Interfacial jump condition

$$\int_{A_I}\left(\dot{m}_{1,I}\boldsymbol{u}_1 + \dot{m}_{2,I}\boldsymbol{u}_2 - \boldsymbol{T}_1\cdot\boldsymbol{n}_{1,I} - \boldsymbol{T}_2\cdot\boldsymbol{n}_{2,I}\right)\,\mathrm{d}A = -V_C\left(\boldsymbol{M}_{1,\Gamma} + \boldsymbol{M}_{2,\Gamma} + \boldsymbol{M}_{1,I} + \boldsymbol{M}_{2,I}\right) = \int_{A_I}\boldsymbol{m}_I^{\sigma}\,\mathrm{d}A. \tag{2.37}$$

Chemical species balance equation $(\overline{\psi}_k = \overline{Y}_k^{\mathrm{X}})$

$$\frac{\partial}{\partial t}\left(\alpha_k\rho_k\overline{Y}_k^{\mathrm{X}}\right) + \nabla\cdot\left(\alpha_k\rho_k\overline{Y}_k^{\mathrm{X}}\overline{\boldsymbol{u}}_k\right) = -\nabla\cdot\left[\alpha_k\left(\overline{\boldsymbol{G}}_k^{\mathrm{X}} + \boldsymbol{G}_{k,tur}^{\mathrm{X}}\right)\right] + \Gamma_k^{\mathrm{X}} + \left(\alpha_k\rho_k\overline{\Psi}_k^{\mathrm{X}}\right). \tag{2.38}$$

$\boldsymbol{G}_{k,tur}^{\mathrm{X}}$ describes the residual scalar flux caused by the unresolved flow turbulence. The unity of all interfacial mass fluxes of chemical species X in association with phase k is summarized in Γ_k^{X}, which is defined as

$$\Gamma_k^{\mathrm{X}} = -\frac{1}{V_C}\int_{A_I}\left(\dot{m}_{k,I}Y_k^{\mathrm{X}} + \boldsymbol{G}_k^{\mathrm{X}}\cdot\boldsymbol{n}_{k,I}\right)\mathrm{d}A. \tag{2.39}$$

Interfacial jump condition

$$\sum_k \Gamma_k^{\mathrm{X}} = \Gamma_1^{\mathrm{X}} + \Gamma_2^{\mathrm{X}} = -\frac{1}{V_C}\int_{A_I}\Upsilon_I^{\mathrm{X}}\,\mathrm{d}A. \tag{2.40}$$

The right hand side of equation (2.40) accounts for heterogeneous reactions, which occur on the interfacial boundary and affect the conservation of reacting species.

As opposed to numerous published derivations of volume averaged Euler-Euler governing equations, Prosperetti & Tryggvason [177] (referencing Harlow & Amsden [94]) pointed out that the diffusive term in the momentum equation (2.34) and $\boldsymbol{M}_{k,I}$ have to be considered in combination for further rigorous discussion on interfacial momentum exchange. This yields

$$\begin{aligned}\nabla\cdot\left(\alpha_k\overline{\boldsymbol{T}}_k\right)+\boldsymbol{M}_{k,I} &= -\nabla\left(\alpha_k\overline{p}_k\right)-\nabla\cdot\left(\alpha_k\overline{\boldsymbol{\tau}}_k\right)+p_{k,I}\nabla\alpha_k-\boldsymbol{\tau}_{k,I}\nabla\alpha_k+\boldsymbol{M}_{k,GD} = \\ &-\alpha_k\nabla\overline{p}_k-\nabla\cdot\left(\alpha_k\overline{\boldsymbol{\tau}}_k\right)+\left(p_{k,I}-\overline{p}_k\right)\nabla\alpha_k-\boldsymbol{\tau}_{k,I}\nabla\alpha_k+\boldsymbol{M}_{k,GD},\end{aligned} \tag{2.41}$$

where the averaged stress tensor $\overline{\boldsymbol{T}}$ has been split into a pressure term and the deviatoric stresses

$$\overline{\boldsymbol{T}} = -\left(\overline{p}\boldsymbol{I}+\overline{\boldsymbol{\tau}}\right). \tag{2.42}$$

The impact of all external forces on the phase boundaries of phase k is summarized in $\boldsymbol{M}_{k,GD}$, which is commonly referred to as *generalized drag term*. In contrast to the consideration of segregated flows, $\boldsymbol{\tau}_{k,I}\nabla\alpha_k$, the combined interfacial shear and volume fraction gradient effect, is neglected here since only dispersed flows are studied in this work [102]. Although several models have been developed accounting for the influence of an interfacial pressure difference $\left(p_{k,I}-\overline{p}_k\right)\nabla\alpha_k$ [121] [123], this term is generally assumed insignificant for incompressible fluids in an Euler-Euler context as argued by

Drew [68]. More detailed explications on the deduction of equation (2.41) can be found elsewhere (e.g., [177], [105], [151]).

The Newtonian strain stress relation (neglecting bulk viscosity) is assumed valid for both phases. Consequently, the shear stress tensor $\overline{\boldsymbol{\tau}}$ can be expressed in the form of

$$\overline{\boldsymbol{\tau}} = 2\mu_k \left(\frac{1}{3} \nabla \cdot \overline{\boldsymbol{u}}_k \boldsymbol{I} + \overline{\boldsymbol{S}}_k \right), \tag{2.43}$$

with the strain-rate tensor formulated as

$$\overline{\boldsymbol{S}}_k = \frac{1}{2} \left(\nabla \cdot \overline{\boldsymbol{u}}_k + (\nabla \cdot \overline{\boldsymbol{u}}_k)^{\mathcal{T}} \right). \tag{2.44}$$

Although local phase fractions and thermodynamic conditions potentially alter fluid viscosities in a gas-liquid environment, the dynamic viscosity μ_k of both phases is generally assumed to be constant. In this study, an isothermal two-phase flow environment is considered with relatively small local secondary phase fractions, which strengthens this assumption. The primary phase viscosity commonly corresponds to the respective molecular property ($\mu_c = \mu_{c,mol}$). A comparably unanimous method for the determination of the secondary phase viscosity μ_d has not been established so far. In several studies the laminar viscosity of the dispersed phase is equated with the molecular viscosity ($\mu_d = \mu_{d,mol}$) (e.g., [31]), while the respective property is neglected in alternative publications ($\mu_d = 0$) (e.g., [29]). In this work, the disperse phase viscosity is derived from the continuous phase equivalent including additional contributions from turbulence modeling. This procedure is in line with the majority of recent numerical investigations in this field (e.g., [229], [197]) and presented further in section 2.3.1.

In accordance with Fick's law, the diffusive flux of species X in phase k is defined as

$$\overline{\boldsymbol{G}}_k^{\mathrm{X}} = -\rho_k \mathcal{D}_k^{\mathrm{X}} \nabla \overline{Y}_k^{\mathrm{X}}, \tag{2.45}$$

where a constant phase-specific molecular diffusion coefficient $\mathcal{D}_k^{\mathrm{X}}$ is assumed.

With the application of the Euler-Euler method, local pressure differences between the phases caused by surface tension are generally neglected. Hence, the continuous as well as the dispersed phase share the identical pressure field:

$$\overline{p}_c = \overline{p}_d = \overline{p}. \tag{2.46}$$

2.3 Turbulence modeling

One of the major challenges in the numerical simulation of fluid dynamics is the consideration of turbulence. Since the numerical depiction of the entire spectrum of turbulence scales is still limited to academic investigations due to excessive computational demand, modeling approaches are inevitable in industrial CFD applications. The physics behind the generation, evolution and dissipation of turbulence is complex and still not fully understood. As a consequence, turbulence models are bound to certain prerequisites or have to be modified in virtue of the regarded fluid dynamic conditions, yet evoking considerable uncertainties in the simulation results. The severity of modeling deficiencies depends on the range of turbulent scales that are not numerically resolved, but have to be accounted for in an abstracted manner. Thus, it is suitable to strive for a compromise between the resolution of large turbulent eddies through affordable accuracy in the spacial discretization and adequate modeling of the residual turbulent scales.

Gas-liquid flows, specifically buoyancy driven bubbly flows, feature a wide range of turbulent scales. The size of turbulent eddies ranges from dimensions similar to the characteristic length of the mean flow down to the smallest turbulent scales (*Kolmogorov scales*) of motion. This broad spectrum in combination with its interrelation to fluid particle motion complicate the adequate description of turbulence in the numerical simulation of two-phase flows. Nevertheless, turbulent fluctuations in the flow field account for bubble coalescence and breakup phenomena, which

necessitates their accurate depiction in case fluid particle interaction is accounted for in the simulation.

If even the smallest scales of turbulence are resolved by the spatial discretization, the numerical approach is referred to as *direct numerical simulation* (DNS), emphasizing that no turbulence model is adopted. Regarding gas-liquid flows, this approach is ultimately accompanied by the application of an interface resolving method (see section 2.1) [206] [66]. Corresponding numerical studies assist the derivation or validation of model formulations for interfacial forces or multiphase turbulence, yet, the description of industrial scale engineering problems is not feasible.

The majority of existing gas-liquid flow turbulence models can be categorized as *Reynolds-averaged Navier-Stokes* (RANS) approaches deduced from single-phase flow formulations [132] [111]. Specifically adapted k-ϵ-models have been widely applied to the primary phase formulations in Eulerian-Eulerian simulations of gas-liquid flows (e.g., [172], [160], [183], [64]). Studies incorporating alternative RANS formulations, such as the k-ω-model [15] or the *Reynolds stress model* (RSM) [19] [37] are used far less frequently.

Due to the time-averaged representation of turbulence in RANS methods, this modeling approach is not able to accurately capture unsteady two-phase flow dynamics. The turbulent hydrodynamics are represented by a quasi steady-state approximation, which arguably is sufficient for the quantitative analysis of time-averaged mean flow patterns, but does not allow for the evaluation of instantaneous local flow phenomena or turbulence parameters [63]. Additionally, the assumption of an isotropic turbulence is made in the majority of RANS approaches. This does not coincide with the characteristics of turbulence in dispersed bubbly flows, where the large-scale velocity fluctuation amplitude in vertical direction is approximately double the respective value for horizontal directions [63]. The resulting deficient representation of the two-phase flow dynamics leads to an erroneous depiction of particle interaction phenomena and consequently to altered bubble size distributions. Due to this substantial influence, the adequate modeling of the two-phase flow turbulence is of major importance, specifically for bubble column flow simulations, which may be strongly affected by local bubble size relations.

Following this line of reasoning, a number of recent studies (e.g., [58], [22], [62], [197]) have incorporated the *large eddy simulation* (LES) approach for the Euler-Euler simulation of bubble column hydrodynamics. With the *Euler-Euler LES* (EELES) model, which is also referred to as *very large eddy simulation* (VLES), the large scale structures of turbulence, comprising most of the turbulent energy, are resolved while the residual scales are accounted for by a respective model formulation. In view of this, the LES approach can be characterized as a tradeoff between DNS and RANS, constituting a valuable compromise between accuracy in the depiction of turbulence and a numerically efficient representation, which allows for the consideration of large scale flows.

For the category of LES models considered in this study (see section 2.3.1), the distinguishing mark, which defines the minimum length of a resolved turbulent eddy, correlates with the numerical mesh size. LES governing equations are derived by a filtering operation, in which the spatial discretization defines the respective local filter width Δ_{tur}. Therefore, the modeling approaches for the residual spectrum of turbulence are commonly referred to as *sub-grid scale* (SGS) models. Further details on LES characteristics and fundamentals are explicated in the subsequent chapter.

By adopting the LES method for the simulation of dispersed gas-liquid flows, the interrelation of fluid particle sizes with the filter width of the turbulence spectrum has to be taken into consideration. To ensure LES model validity, Δ_{tur} must correspond to a methodical separation in the inertial subrange of turbulence energy. This necessitates a relatively fine spatial discretization in case of bubble column flows. On the other hand, a filter width smaller than the dispersed phase particle size deviates from the prerequisites for the averaged Euler-Euler governing equations (see section 2.2.2) and the potentially resolved scales of continuous phase fluid motion in proximity of fluid particles are resolved deficiently due to the absence of interface details. Furthermore, the derivation of conventional interfacial exchange terms is predicated on a spatial discretization according to an Eulerian conception.

By reference to the turbulent energy spectrum, figure 2.2 illustrates a configuration where the LES filter width Δ_{tur}, correlating to a cut-off wavenumber K of turbulence fluctuations in Fourier space, is smaller than

the fluid particle size D_p. The highlighted range of turbulence wavenumbers indicates the scale of eddies which are theoretically accounted for by the LES setup, although their accurate representation is not feasible in an Eulerian framework.

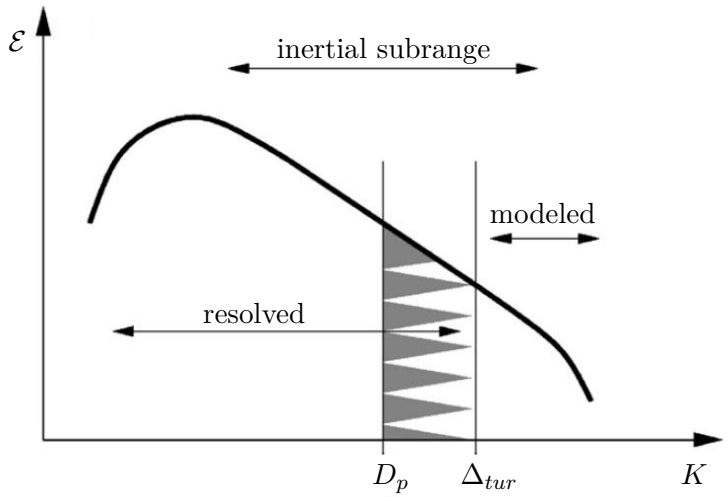

Figure 2.2: Turbulence energy spectrum in case $D_p > \Delta_{tur}$ (adapted from [161])

Milelli [153] performed a detailed systematic study investigating the relation between LES filter length and bubble size for the simulation of gas-liquid flows. His findings, which are summarized in [152], define a lower limit of the LES filter width by specifying

$$\frac{\Delta_{tur}}{D_p} \geq 1.5 \tag{2.47}$$

for an accurate representation of bubble affected turbulence in gas-liquid flows. A corresponding correlation is depicted in figure 2.3 in terms of the turbulence energy spectrum and in figure 2.4 illustrated as exemplary relation between bubble size and filter length, satisfying the Milelli criterion (2.47).

The application of LES methods for the Eulerian simulation of gas-liquid flows still represents a rather novel approach and its utilization for large scale engineering problems is still bound to the availability of high performance computing equipment. Thus, various fluid dynamic aspects related to turbulence modeling are still under investigation or subject to future

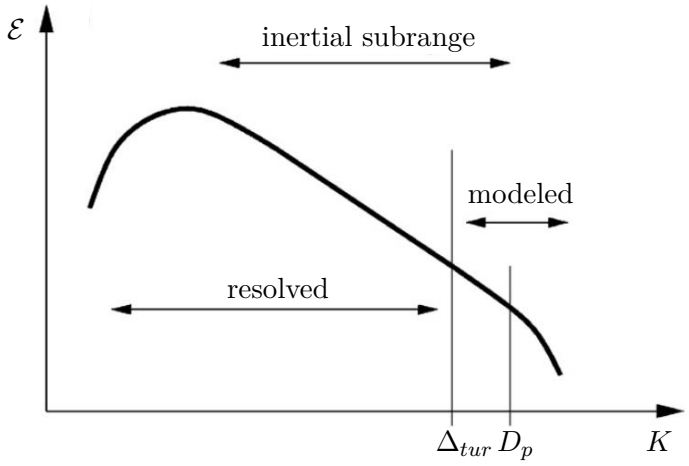

Figure 2.3: Turbulence energy spectrum in case $D_p < \Delta_{tur}$ (adapted from [161])

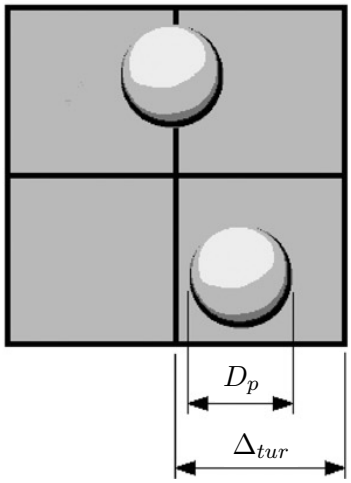

Figure 2.4: Illustration of the Milelli criterion [162]

studies. Nevertheless, this modeling approach is distinctly superior to RANS methods regarding the depiction of multiphase flow dynamics and turbulence characteristics. These advantages are of paramount importance for the proceeding investigation of dispersed phase particle interaction and ultimately for the analysis of heat and mass transfer phenomena. The following explanations on turbulence modeling are limited to the EELES approach. Further information on RANS modeling in particular for multiphase flow applications can be found elsewhere (e.g., [175], [217], [132], [111]).

2.3.1 LES fundamentals and eddy viscosity

Developed for the numerical simulation of single phase turbulent flows, the LES approach is based on a filtering procedure of the turbulent fluctuations of flow parameters, primarily the velocity components. This operation divides the turbulence spectrum into two parts. While larger eddies, containing most of the turbulent energy, are numerically resolved, turbulent scales below a certain spatial dimension have to be accounted for by a respective model. In view of the different properties of large and small scale turbulence eddies (see table 2.2), this differentiation is specifically favorable and yields a more generic validity of the turbulence modeling approach.

Large eddies	**Small scale eddies**
Produced by mean flow	Produced by large eddies
Depends on boundaries	Universal
Ordered	Random
Requires deterministic description	Can be modeled
Inhomogeneous	Homogeneous
Anisotropic	Isotropic
Long-lived	Short-lived
Diffusive	Dissipative
Difficult to model	Easier to model

Table 2.2: Comparison of properties of large scale and small scale turbulence eddies [114]

Generally, the cut-off filter size Δ_{tur} in physical space can be interpreted as a corresponding limiting wavenumber in Fourier space of turbulent fluctuations. Furthermore, several LES models are formulated in terms of a temporal filtering approach, which commonly relates to the spatial equivalent. The following explications solely refer to the spatial interpretation of LES filtering. Considering a generic flow quantity ψ, an arbitrary location in the flow domain $\boldsymbol{x}' = \boldsymbol{x} + \boldsymbol{\eta}$, and a spacial filter kernel function $G(\boldsymbol{x}, \boldsymbol{x}')$, the mathematical representation of the filtering operation is

$$\tilde{\psi}(\boldsymbol{x}) = \int G(\boldsymbol{x}, \boldsymbol{x}')\psi(\boldsymbol{x}')\,\mathrm{d}\boldsymbol{x}', \tag{2.48}$$

where the SGS turbulence fluctuations ψ' can be represented as

$$\psi' = \psi - \tilde{\psi}. \tag{2.49}$$

The derivation of the Euler-Euler governing equations for gas-liquid flows (2.29) is conducted by a volume averaging procedure, whose primary purpose is the simplified consideration of local two-phase flow conditions without interface details in the description of multiphase fluid dynamics. Besides this property, the deduction additionally prohibits the numerical resolution of turbulence fluctuations in the flow field with spatial dimensions below the averaging range. In this respect, the volume averaging procedure constitutes a spatial filtering operation to turbulence scales and consequently represents a specific form of the LES. Alternative derivations of

the two-fluid governing equations are based on the separation of averaging operations for local phasic conditions and turbulence fluctuations. This allows for the application of various LES configurations, but is accompanied by an increased complexity in the formal description. The current study is limited to the consideration of a volume averaging procedure which simultaneously represents an LES filtering operation. Hence, the specifics of the LES turbulence model are selected accordingly.

A so-called *box* or *top-hat* filter is applied, which is exclusively dependent on the selected spatial filter size Δ_{tur}:

$$G(\boldsymbol{x},\boldsymbol{x}') = \begin{cases} \frac{1}{\Delta_{tur}} & \text{if } |\boldsymbol{x}-\boldsymbol{x}'| \leq \frac{\Delta_{tur}}{2} \\ 0 & \text{otherwise} \end{cases} . \tag{2.50}$$

This type of filter kernel function can be categorized as homogeneous, which implies, without limitation,

- Consistency $\int_{-\infty}^{\infty} G(\boldsymbol{x},\boldsymbol{x}')\mathrm{d}\boldsymbol{x}'=1$,
- Linearity $\widetilde{\psi_1+\psi_2} = \tilde{\psi}_1 + \tilde{\psi}_2$.

Additionally, the filtering procedure in the considered form represents a Reynolds operator, which signifies $\widetilde{\tilde{\psi}\psi'} = 0$ and $\widetilde{\tilde{\psi}\psi} = \tilde{\psi}\tilde{\psi}$.

Since equivalence of volume averaging and LES filtering is assumed ($\overline{\psi} = \tilde{\psi}$), solely the notation for the former operation ($\overline{\psi}$) will be applied from now on.

In the generic Euler-Euler governing equation for gas-liquid flows (2.29), the averaging of the advective term yields the unclosed expression $\boldsymbol{J}_{k,tur}$ (see formulation (2.30)). With regard to the momentum balance equation, the respective term $\boldsymbol{J}_{k,tur}$ is generally referred to as *residual stress tensor* $\boldsymbol{T}_{k,tur}$. This parameter represents the spectrum of spatial turbulent velocity fluctuations which cannot be resolved by the selected averaging scale. In case of the continuous phase, the residual stress tensor is formulated as

$$\boldsymbol{T}_{c,tur} = \rho_c \left(\overline{\boldsymbol{u}_c\boldsymbol{u}_c} - \overline{\boldsymbol{u}}_c\overline{\boldsymbol{u}}_c\right) = \frac{2}{3}k_{c,tur}\boldsymbol{I} + \boldsymbol{\tau}_{c,tur}, \tag{2.51}$$

where $k_{c,tur}$ denotes the residual turbulent kinetic energy. The first term on the right hand side represents the isotropic part of the stress tensor whose definition in Einstein notation with indices i and j yields

$$\frac{2}{3}k_{c,tur}\boldsymbol{I} = \frac{1}{3}\rho_c\left(\overline{u_{c,i}u_{c,i}} - \overline{u}_{c,i}\overline{u}_{c,i}\right). \tag{2.52}$$

The deviatoric or anisotropic part $\boldsymbol{\tau}_{c,tur}$, which is also referred to as *SGS Reynolds stress tensor*, can consequently be described as

$$\boldsymbol{\tau}_{c,tur} = \rho_c\left(\overline{u_{c,i}u_{c,j}} - \overline{u}_{c,i}\overline{u}_{c,j}\right) - \frac{1}{3}\rho_c\left(\overline{u_{c,i}u_{c,i}} - \overline{u}_{c,i}\overline{u}_{c,i}\right). \tag{2.53}$$

Due to the occurrence of averages of velocity correlations (e.g., $\overline{u_{c,i}u_{c,j}}$) in equation (2.53), a direct evaluation of the Reynolds stress tensor $\boldsymbol{\tau}_{c,tur}$ is inaccessible. These terms are a function of unknown SGS velocity fluctuations and hence necessitate a model formulation to overcome this closure problem. Several approaches have been developed (e.g., [83] [224]) with the *Smagorinsky model* [192] being the most prevalent. It is based on the evaluation of the SGS Reynolds stress tensor by

$$\boldsymbol{\tau}_{c,tur} \equiv -2(C_S\Delta_{tur})^2\left|\overline{\boldsymbol{S}}_c\right|\overline{\boldsymbol{S}}_c, \tag{2.54}$$

with C_S representing the Smagorinsky coefficient and $\boldsymbol{S}_c$ denoting the strain-rate tensor introduced in equation (2.44). Although varying definitions are possible, the norm of the strain-rate tensor is formulated according to Pope [175] as

$$\left|\overline{\boldsymbol{S}}_c\right| \equiv \left(2\overline{\boldsymbol{S}}_c\overline{\boldsymbol{S}}_c\right)^{1/2}. \tag{2.55}$$

Derived from the fluid dynamic relations in laminar flow, the linear eddy viscosity model describes the Reynolds stress tensor $\boldsymbol{\tau}_{c,tur}$ in terms of the strain-rate tensor and a turbulent viscosity $\mu_{c,tur}$ [78]. The later expression is introduced to account for the unresolved turbulent velocity fluctuations in the form of an addition to viscous effects in the continuous phase flow. With regard to equation (2.54), the mathematical definition reads

$$\boldsymbol{\tau}_{c,tur} \equiv -2\mu_{c,tur}\overline{\boldsymbol{S}}_c, \tag{2.56}$$

with

$$\mu_{c,tur} = \rho_c(C_S\Delta_{tur})^2\left|\overline{\boldsymbol{S}}_c\right|. \tag{2.57}$$

For single phase high Reynolds number flows, Smagorinsky constant values of $C_S \approx 0.17$ are commonly specified, provided that the spatial filter width is within the inertial subrange of turbulence scales. Yet, the optimal value may vary in a wide range, from $C_S = 0.065$ [157] to $C_S = 0.25$ [109], depending on the local flow regime. Regarding the core part of a channel flow, for instance, optimal agreement to experimental findings is achieved with a Smagorinsky constant in the range of $0.065 < C_S < 0.1$ [79]. In case of the continuous phase turbulence in bubble column flows, a value of $C_S \approx 0.1$ is proposed by several respective studies (e.g., [227], [62]). Higher values for the Smagorinsky constant implicate a significant attenuation of the gas-liquid flow dynamics, which eventually results in a steady state solution [63]. The lack of an exact a priori specification for C_S represents a major disadvantage of the classical Smagorinsky model and initiates research towards dynamic C_S formulations or alternative LES approaches.

In a number of recent publications concerning the numerical simulation of gas-liquid flows, a further addition to the turbulent viscosity $\mu_{c,tur}$ due to bubble induced turbulence, is proposed [22] [182]. Since the relevance of this effect as well as its appropriate modeling approach (e.g., [184], [205]) is still under investigation, bubble induced turbulence is not taken into account in this work. This neglect is in line with the majority of numerical simulations of bubble column flows (e.g., [65], [53], [13]).

With the incorporation of the turbulence modeling formulations (2.54) to (2.57) into the volume averaged momentum equation (2.34), in conjunction with the discussion on phase-specific stress relations and interfacial momentum transfer (equations (2.41) to (2.44)), the Euler-Euler momentum equation for the continuous phase reads

$$\frac{\partial}{\partial t}\left(\alpha_c \rho_c \overline{\boldsymbol{u}}_c\right) + \nabla \cdot \left(\alpha_c \rho_c \overline{\boldsymbol{u}}_c \overline{\boldsymbol{u}}_c\right) = \nabla \cdot \left[\alpha_c \mu_{c,eff} \left(\nabla \cdot \overline{\boldsymbol{u}}_c + \left(\nabla \cdot \overline{\boldsymbol{u}}_c\right)^{\mathcal{T}} - \frac{2}{3}\overline{\boldsymbol{u}}_c \boldsymbol{I}\right)\right] - \alpha_c \nabla \overline{p} + \left(\alpha_c \rho_c \boldsymbol{g}\right) + \Gamma_c \overline{\boldsymbol{u}}_c + \boldsymbol{M}_{c,GD}, \tag{2.58}$$

with the effective dynamic viscosity $\mu_{c,eff}$ comprising a molecular and a turbulent contribution $\mu_{c,eff} = \mu_c + \mu_{c,tur}$.

There is no consent on the inclusion of a specific turbulence formulation in the Eulerian depiction of the dispersed phase. Several approaches have been proposed in the literature, ranging from the neglect of any representation of turbulence in the dispersed phase governing equations (e.g., [165]), over an evaluation analogous to the continuous phase formulation (e.g., [171]), to the derivation from continuous phase turbulence relations (e.g., [58]). The latter approach is also applied in this work, following the model of Jakobsen [106], where the primary phase effective viscosity $\mu_{c,eff}$ is scaled by the ratio of gas and liquid densities and transferred to the dispersed phase as

$$\mu_{d,eff} = \frac{\rho_d}{\rho_c} \mu_{c,eff}. \tag{2.59}$$

This definition allows for the formulation of the Euler-Euler dispersed phase momentum balance equation in analogy to the continuous phase expression (2.58) as

$$\frac{\partial}{\partial t}\left(\alpha_d \rho_d \overline{\boldsymbol{u}}_d\right) + \nabla \cdot \left(\alpha_d \rho_d \overline{\boldsymbol{u}}_d \overline{\boldsymbol{u}}_d\right) = \nabla \cdot \left[\alpha_d \mu_{d,eff} \left(\nabla \cdot \overline{\boldsymbol{u}}_d + \left(\nabla \cdot \overline{\boldsymbol{u}}_d\right)^{\mathcal{T}} - \frac{2}{3}\overline{\boldsymbol{u}}_d \boldsymbol{I}\right)\right] - \alpha_d \nabla \overline{p} + \left(\alpha_d \rho_d \boldsymbol{g}\right) + \Gamma_d \overline{\boldsymbol{u}}_d + \boldsymbol{M}_{d,GD}. \tag{2.60}$$

2.3.2 LES of the species transport equation

With regard to equation (2.30), the residual turbulent concentration fluctuations of a generic species X in phase k are given by

$$\boldsymbol{G}^{\mathrm{X}}_{k,tur} = \rho_k \left(\overline{Y^{\mathrm{X}}_k \boldsymbol{u}_k} - \overline{Y}^{\mathrm{X}}_k \overline{\boldsymbol{u}}_k \right). \tag{2.61}$$

Applying the gradient diffusion approach [72], $\boldsymbol{G}^{\mathrm{X}}_{k,tur}$ is modeled in the form of

$$\boldsymbol{G}^{\mathrm{X}}_{k,tur} = -\rho_k \mathcal{D}_{k,tur} \nabla \overline{Y}^{\mathrm{X}}_k, \tag{2.62}$$

where $\mathcal{D}_{k,tur}$ represents the phase-specific turbulent diffusion coefficient, which is evaluated in analogy to the Smagorinsky model [192] by

$$\mathcal{D}_{k,tur} = \frac{\mu_{k,tur}}{\mathrm{Sc}_{tur} \rho_k} = \frac{2 \left(C_S \Delta_{tur} \right)^2}{\mathrm{Sc}_{tur}} \left| \overline{\boldsymbol{S}}_k \right|. \tag{2.63}$$

As a consequence of the inherent relation of SGS diffusive momentum and species transport (see section 2.5.1), the turbulent Schmidt number Sc_{tur} is a model constant and determines the magnitude of the SGS species diffusion $\mathcal{D}_{k,tur}$. While a turbulent Schmidt number of $\mathrm{Sc}_{tur} = 0.7$ is common for RANS models, a value of $\mathrm{Sc}_{tur} = 0.4$ is generally set for LES approaches [173].

The introduced method for the evaluation of SGS diffusive transport, including the gradient diffusion approach (2.62) and the Smagorinsky model analogy (2.63), is not bound to the consideration of chemical species but commonly applied for the LES simulation of all passive scalar flow quantities. Specifically the SGS diffusion in the description of the fluid dynamic transport of enthalpy is modeled analogously, with the turbulent Prandtl number Pr_{tur} being the equivalent of the turbulent Schmidt number Sc_{tur}. In spite of the similar diffusive transport processes for heat and mass in single and multiphase fluid dynamics, variant specifications for Sc_{tur} and Pr_{tur} are conceivably used. In their LES simulation, Van der Hoeven et al. [210] suggest an SGS Prandtl number of $\mathrm{Pr}_{tur} = 0.7$ while specifying $\mathrm{Sc}_{tur} = 0.4$.

As discussed in the previous section, turbulence contributions are accounted for in the momentum equations of both the continuous and the dispersed phase. Following this concept, equation (2.62) is introduced as valid for

both phases in this work, although its application in case of the dispersed phase is avoided later on in the numerical studies of bubble column flows (see section 5). The way of incorporating diffusive terms in the dispersed phase species equations of an Euler-Euler model is controversial. Examples for alternative configurations can be found in the literature [229].

An adaption to the evaluation of the continuous phase diffusive transport as introduced in equations (2.62) and (2.63) is presented by Darmana et al. [55]. They determine the effective diffusion coefficient in their Euler-Lagrange LES of bubble column flows by

$$\mathcal{D}^{\mathrm{X}}_{c,eff} = \mathcal{D}^{\mathrm{X}}_{c} + \mathcal{D}_{c,tur} = \frac{\mu_{c,eff}}{\mathrm{Sc}^{\mathrm{X}}_{c}\rho_c}, \tag{2.64}$$

where $\mathrm{Sc}^{\mathrm{X}}_{c}$ denotes the (molecular) Schmidt number, which depicts the ratio between the diffusivity of momentum, i.e. viscosity, and the mass diffusivity as

$$\mathrm{Sc}^{\mathrm{X}}_{k} = \frac{\mu_{k,}}{\mathcal{D}^{\mathrm{X}}_{k,}\rho_k} \tag{2.65}$$

in the phase generic definition. The physical basis of this modified model is unclear. Thus, the determination of the turbulent diffusion coefficient in this work is deduced from the Smagorinsky model as presented above.

The introduced formulations regarding the LES modeling of species transport in association with the definition of the molecular diffusive flux according to Fick's law (2.45) yields an Euler-Euler transport equation for the generic species X in phase k in the form of

$$\frac{\partial}{\partial t}\left(\alpha_k\rho_k\overline{Y}^{\mathrm{X}}_{k}\right) + \nabla\cdot\left(\alpha_k\rho_k\overline{Y}^{\mathrm{X}}_{k}\overline{\boldsymbol{u}}_k\right) = \nabla\cdot\left(\alpha_k\mathcal{D}_{k,eff}\nabla\overline{Y}^{\mathrm{X}}_{k}\right) + \Gamma^{\mathrm{X}}_{k} + \left(\alpha_k\rho_k\overline{\Psi}^{\mathrm{X}}_{k}\right), \tag{2.66}$$

where the molecular and turbulent contributions to the species diffusion are summarized in $\mathcal{D}^{\mathrm{X}}_{k,eff} = \mathcal{D}^{\mathrm{X}}_{c} + \mathcal{D}_{c,tur}$. For high Schmidt number species, the SGS diffusivity outweighs the molecular equivalent which can thus be neglected. While this simplification generally is inapplicable for gaseous

flows (Sc $\approx$ 1), species diffusion in liquids can potentially be considered in that manner (Sc >> 1) [79].

2.4 Interfacial closure relations

As part of the deduction of volume averaged Euler-Euler governing equations, the interfacial interaction between the phases has been accounted for by the respective source terms $\boldsymbol{M}_{k,GD}$, Γ_k and Γ_k^{X} in the phase-specific conservation equations (see section 2.2.2). Model approaches for the interfacial exchange of momentum and mass, primarily suitable for bubbly flows, are introduced in the following subsections. This includes an explanation of the corresponding physical basis of the formulations and the presentation of several model variants.

2.4.1 Momentum transfer

As formulated in equation (2.41), $\boldsymbol{M}_{k,GD}$ denotes the contribution to the interfacial flux of momentum $\boldsymbol{M}_{k,I}$ which needs to be accounted for through a closure relation. This generalized drag term $\boldsymbol{M}_{k,GD}$ represents the unity of all external forces acting on the interfacial boundaries of phase k and is commonly expressed as a linear combination of various forces per unit two-phase flow volume. With the differentiation between continuous and dispersed phase, the consequent formulation reads

$$\boldsymbol{M}_{c,GD} = -\boldsymbol{M}_{d,GD} = \sum \boldsymbol{M}_Z = N \sum \boldsymbol{F}_Z, \tag{2.67}$$

where $\sum \boldsymbol{F}_Z$ represents the net force acting on a single particle and N denotes the number of fluid particles per two-phase mixture volume, evaluated as

$$N = \frac{6\alpha_d}{\pi D_p^3}, \tag{2.68}$$

with a mean diameter D_p of the dispersed phase. In the following section, interfacial forces of different nature are introduced contributing to

$$\sum \boldsymbol{F}_Z = \boldsymbol{F}_D + \boldsymbol{F}_L + \boldsymbol{F}_{VM} + \boldsymbol{F}_{TD}. \tag{2.69}$$

The considered forces account for the interfacial exchange of momentum due to drag, lift, virtual mass and turbulent dispersion (in order of their appearance in equation (2.69)). Beyond that, several additional interfacial forces for gas-liquid flows have been reported in literature. Since their effect is generally marginal, neglectable for bubble column flows or not yet comprehensively investigated, further contributions are not discussed in this work. The reader is referred to respective literature sources for information on Basset force [198], wall lubrication force [7] or wall deformation force [136].

2.4.1.1 Drag force

The drag force acting on a solid or fluid particle in a continuous flow field can be split into two components [18] [105]. The induced fluid stress normal to the interfacial boundary is described by the form drag, also referred to as pressure drag. The remaining shear stress components are accounted for by the friction drag. This separation is specifically prominent for analytical solutions of drag relations. In his pioneering work, Stokes [194] combined both contributions to analytically find the drag formulation for laminar flows around a rigid sphere

$$\boldsymbol{F}_D = 3\pi\mu_c D_p \left(\boldsymbol{u}_d - \boldsymbol{u}_c\right), \tag{2.70}$$

which is valid for very low particle Reynolds numbers $\mathrm{Re}_p < 1$, defined as

$$\mathrm{Re}_p = \frac{\rho_c D_p \left|\boldsymbol{u}_d - \boldsymbol{u}_c\right|}{\mu_c}. \tag{2.71}$$

In order to generalize the applicability of this approach, the standard formulation for the drag force is deduced from this considerations as

$$\boldsymbol{F}_D = \frac{1}{2} C_D \rho_c A_P \left|\boldsymbol{u}_d - \boldsymbol{u}_c\right| \left(\boldsymbol{u}_d - \boldsymbol{u}_c\right), \tag{2.72}$$

where A_P denotes the projection area of the particle to its relative velocity and the drag coefficient C_D accounts for the flow conditions. In the case of Stokes flow ($Re_p < 1$) around a sphere ($A_P = \frac{\pi}{4} D_p^2$), C_D can be derived from equation (2.70) as

$$C_D = \frac{24}{\mathrm{Re}_p}. \tag{2.73}$$

With expression (2.72), varying drag effects on rigid spheres for higher particle Reynolds numbers can be assigned to modified values of C_D. For $\mathrm{Re}_p > 1$, continuous phase flow inertial effects gain importance and with a further increase of Re_p, a vortex is formed behind the sphere. This contradicts the prerequisites of Stokes and equation (2.73) becomes invalid. The standard drag curve, shown in figure 2.5, illustrates the relation between the drag coefficient C_D and the particle Reynolds number Re_p for the flow around a sphere. To accurately capture this trend, several researchers have proposed drag coefficient correlations for particle Reynolds numbers exceeding the Stokes flow region, the most prominent were formulated by Schiller & Naumann [185] and Morsi & Alexander [159].

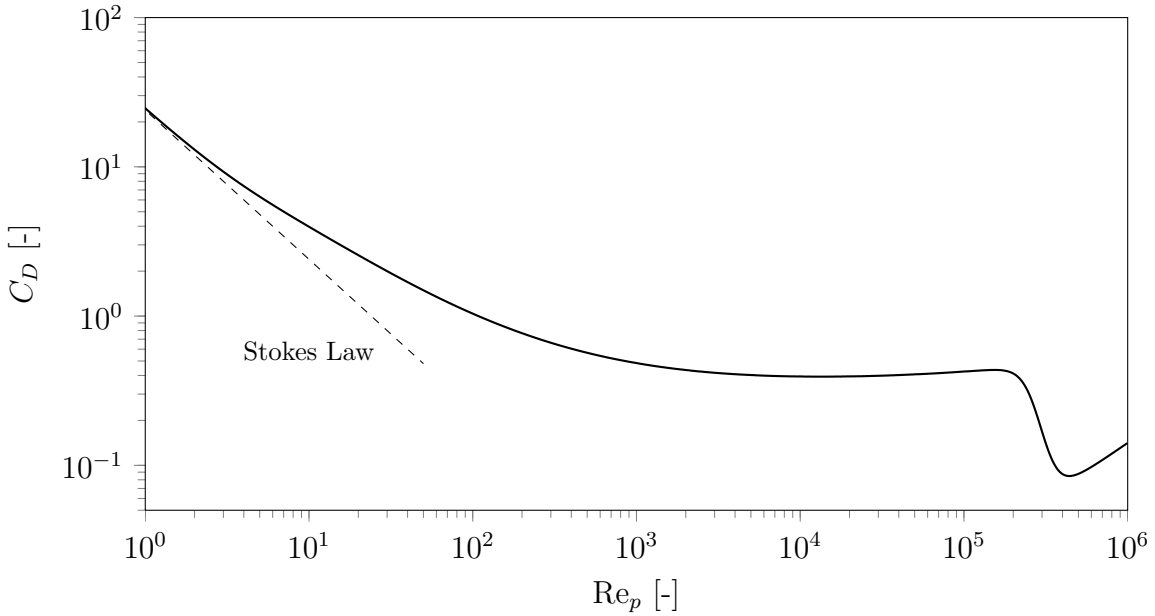

Figure 2.5: Standard drag curve: drag coefficient C_D of a sphere as a function of the particle Reynolds number Re_p (adapted from [44])

The description of interfacial forces on bubbles, or fluid particles in general, is substantially more complex than the consideration of rigid spheres.

Interfacial interaction may excite the deformation of the bubble, which alters the surrounding flow of the continuous phase. The modified fluid particle shape depends on the adjacent continuous phase flow pattern as well as on the physical properties of gas and liquid. This interrelation can be described by a group of dimensionless numbers. Besides the particle Reynolds number Re_p (2.71), the Eötvös number Eo

$$\mathrm{Eo} = \frac{g D_p^2 \left|\rho_c - \rho_d\right|}{\sigma} \tag{2.74}$$

and the Morton number Mo

$$\mathrm{Mo} = \frac{g \mu_c^4 \left|\rho_c - \rho_d\right|}{\rho_c^2 \sigma^3} \tag{2.75}$$

are of interest in this context. The shape regimes of single rising bubbles or falling drops, undisturbed by neighboring fluid particles or continuous phase fluid motion, are illustrated in figure 2.6.

Similar to the consideration of spherical particles, a vortex develops behind a rising bubble in case of higher particle Reynolds numbers. As a consequence of bubble deformation with a further increase of Re_p, the vortex may shed asymmetrically inducing a rocking bubble motion and bubble surface oscillations. Due to the complexity of gas-liquid flow phenomena, the formulation of a universally valid drag force model in an Euler-Euler context has not been achieved so far. Specifically for bubble column flows, numerous drag formulations have been published of which several will be introduced in the following.

The available drag force correlations for bubble column flows can be subdivided by their general approach. Formulations for the drag coefficient C_D as a function of the terminal rise velocity $u_{p,ter}$ of a bubble are applied in a small number of published simulations only (e.g., [22], [118]). From the consideration of a balance of forces for a single bubble rising in a stagnant fluid [89], the respective correlation is derived as

$$C_D = \frac{4}{3} \frac{\rho_c - \rho_d}{\rho_c} \frac{g D_p}{u_{p,ter}^2}. \tag{2.76}$$

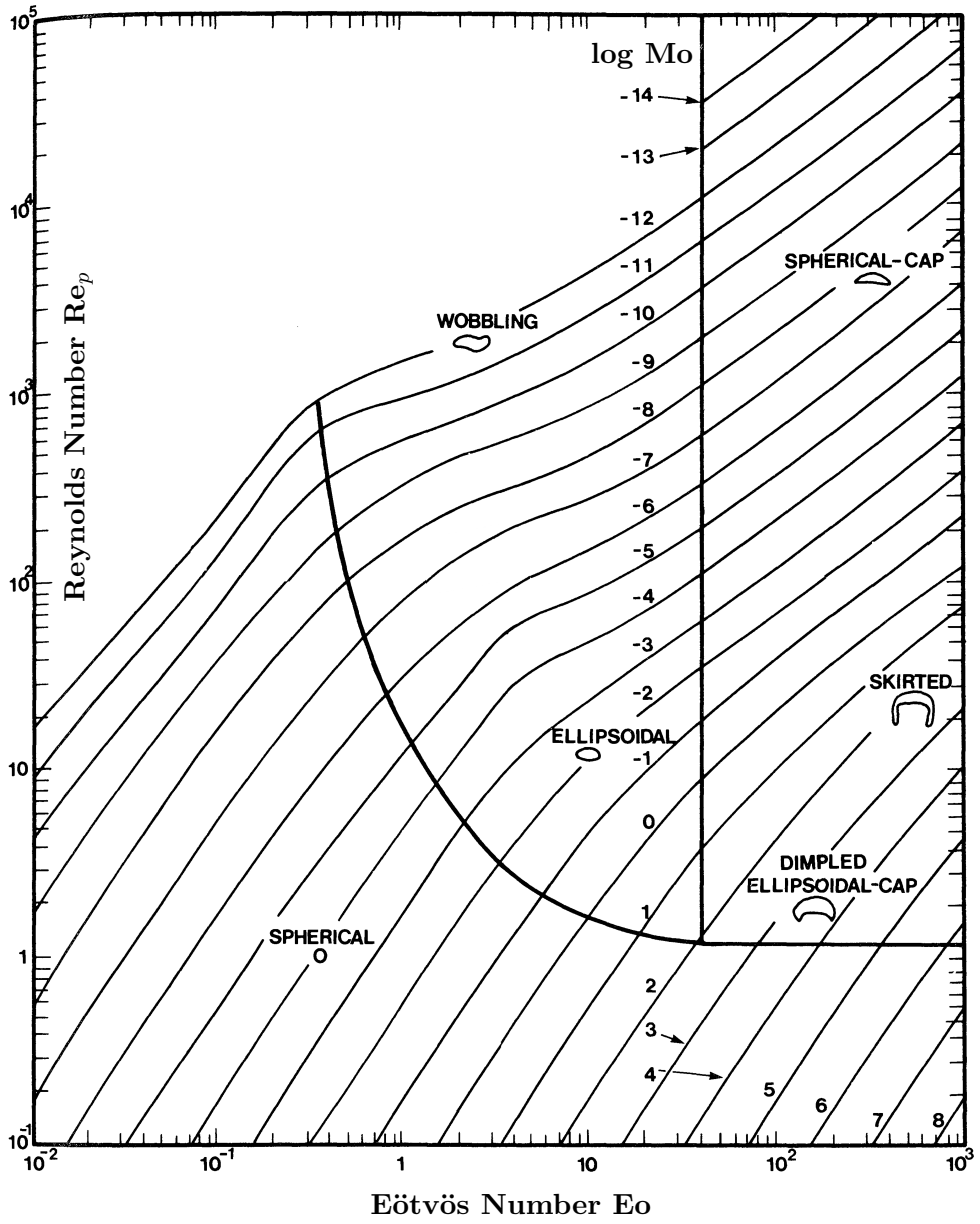

Figure 2.6: Grace diagram [88] for shape regimes of single rising bubbles or falling drops in liquid (adapted from [44])

This rather simplistic perception, which does not reflect the two-phase flow condition in bubble columns, may account for the rare use of this approach. Several researchers proposed different correlations to determine the bubble terminal velocity (e.g., [150], [45], [200]). Clift et al. [44] provide a comprehensive discussion of this topic including the analysis of various experimental results for air-water systems, illustrated in figure 2.7.

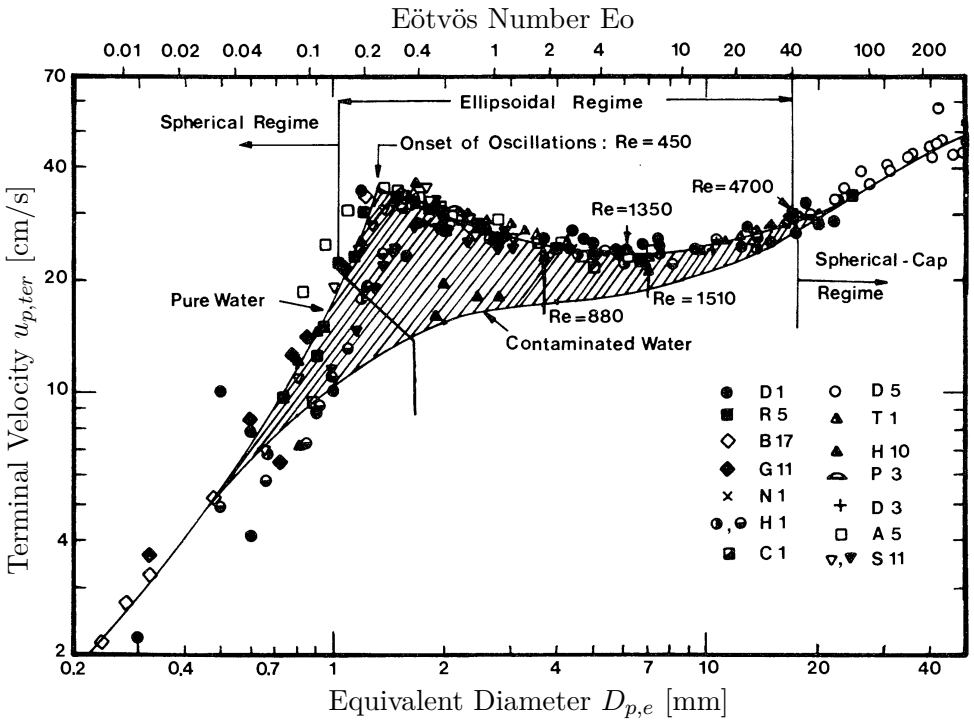

Figure 2.7: Terminal velocity of air bubbles in water at 20°C [44]

The majority of drag correlations for bubble column flows is formulated subject to one or multiple dimensionless numbers introduced above. Primarily the particle Reynolds number Re_p and the Eötvös number Eo are employed in this relation. Ishii & Zuber [104] established the arguably most prominent drag force model, a combination of several correlations valid for different bubble flow conditions. While they proposed adapted Stokes [194] and Schiller-Naumann [185] formulations in case of small Re_p values and undistorted spherical bubbles, novel correlations for the distorted bubble regime and churn-turbulent flow conditions were introduced, which are specifically relevant for bubble column flows:

- Distorted bubble regime

$$C_D = \frac{2}{3}\sqrt{\mathrm{Eo}}\,E, \tag{2.77}$$

with

$$E = \left(\frac{1 + 17.67 \alpha_c^{6/7}}{18.67 \alpha_c} \right)^2 . \tag{2.78}$$

- Churn-turbulent regime

$$C_D = \frac{8}{3} \alpha_c^2 . \tag{2.79}$$

In the vast majority of cases, the Ishii-Zuber model is applied in a simplified form. Here, solely the distorted bubble regime is considered, accompanied by the neglect of the multiplying factor E, which yields

$$C_D = \frac{2}{3} \sqrt{\mathrm{Eo}} . \tag{2.80}$$

For the two-phase flow conditions in industrial bubble columns with relatively high values for Eo and Re_p yet retaining moderate volumetric gas fractions, this simplification can be regarded as well justified.

Tomiyama et al. [201] [199] derived drag force formulations from detailed experiments analyzing single bubble motion of air-water systems. According to their model, the gas-liquid system has to be categorized subject to the level of contamination in order to select an adequate drag force expression. The following classification is proposed:

- Pure systems

$$C_D = \max \left[\min \left[\frac{16}{\mathrm{Re}_p} \left(1 + \mathrm{Re}_p^{0.687} \right), \frac{48}{\mathrm{Re}_p} \right], \frac{8}{3} \frac{\mathrm{Eo}}{\mathrm{Eo} + 4} \right] . \tag{2.81}$$

- Slightly contaminated systems

$$C_D = \max \left[\min \left[\frac{16}{\mathrm{Re}_p} \left(1 + \mathrm{Re}_p^{0.687} \right), \frac{72}{\mathrm{Re}_p} \right], \frac{8}{3} \frac{\mathrm{Eo}}{\mathrm{Eo} + 4} \right] . \tag{2.82}$$

- Fully contaminated systems

$$C_D = \max \left[\frac{16}{\mathrm{Re}_p} \left(1 + \mathrm{Re}_p^{0.687} \right), \frac{8}{3} \frac{\mathrm{Eo}}{\mathrm{Eo} + 4} \right] . \tag{2.83}$$

It is argued that recirculating gas motion inside the bubbles is induced in pure gas-liquid system flows, which decrease the viscous drag. This effect is either partially or entirely suppressed in case of contaminated systems due to the accumulation of impurities on the bubble surface. In the ultimate case, the interface can be regarded as rigid. [143]

The introduced drag closure relations are deduced from simplified two-phase flow considerations or unimpaired single bubble motion, neglecting the impact of neighboring fluid particles or swarm effects. These influences are taken into account in recent experimental and numerical investigations (e.g., [190], [124], [180]), potentially yielding drag force models which are inherently more suitable for the description of bubble column flow conditions.

2.4.1.2 Lift force

Similar to the derivation of Euler-Euler drag force models for gas-liquid flows, the theoretical principles for lift force correlations are based on investigations of laminar flow around spherical particles. In corresponding experimental investigations, the motion of a single rigid sphere perpendicular to the flow direction has been observed. The physical origin of this transversal migration has been denoted as lift force which is acting on the particle. This effect is induced by an asymmetric flow and pressure field around the particle position, caused either by particle rotation (Magnus lift force), shear flow conditions (Saffman lift force), or a combination of the two, respectively. From these considerations, a number of researchers (e.g., [10], [69]) derived the lift force formulation in an Eulerian context as

$$\boldsymbol{M}_L = C_L \alpha_d \rho_c \left(\boldsymbol{u}_d - \boldsymbol{u}_c\right) \times \nabla \times \boldsymbol{u}_c, \tag{2.84}$$

where C_L represents the lift coefficient which is evaluated according to model correlations. In case of spherical particles in an inviscid flow, a value of $C_L = 0.5$ has been determined, while Lahey [119] proposes values of the lift coefficient as small as $C_L = 0.01$ for viscous flows.

The investigation of lift forces acting on deformable fluid particles is accompanied by a considerable increase in complexity. Various experi-

mental studies of gas-liquid flows have indicated that the migration of bubbles normal to their direction of ascent does not only differ from the theoretical conclusions for rigid spheres, but may even be opposite in direction. Tomiyama et al. [199] [202] gave an explanation for this behavior, concluding from detailed experimental and numerical investigations of single bubble motion in simple shear flows. While the analyzed bubble motion is in line with the classical Saffman lift force theory for small Eötvös numbers, the bubble deformation is accompanied by a slanting of the adjacent vortex in case of higher Eötvös numbers. The resulting modified flow conditions may lead to an inversion of the net transversal forces.

Although this effect is not compatible with the concept of lift forces on spherical particles, Tomiyama et al. [202] quantify this phenomenon as part of a model formulation which is based on the classical lift force correlation (2.84). The parametrization yields a piecewise defined formulation[1] for the lift force coefficient in the form of

$$C_L = \begin{cases} \min\left[0.228\tanh\left(0.121\mathrm{Re}_p\right), f\left(\mathrm{Eo}_h\right)\right] & \text{if } \mathrm{Eo}_h < 4 \\ f\left(\mathrm{Eo}_h\right) & \text{if } 4 \leq \mathrm{Eo}_h \leq 10\,, \\ -0.27 & \text{if } \mathrm{Eo}_h > 10 \end{cases} \tag{2.85}$$

with

$$f\left(\mathrm{Eo}_h\right) = 0.00105\mathrm{Eo}_h^3 - 0.0159\mathrm{Eo}_h^2 - 0.0204\mathrm{Eo}_h + 0.474, \tag{2.86}$$

and Eo_h representing a modified Eötvös number with respect to the horizontal axis $D_{p,h}$ of the distorted bubble

$$\mathrm{Eo}_h = \frac{gD_{p,h}^2\left|\rho_c - \rho_d\right|}{\sigma}. \tag{2.87}$$

The bubble aspect ratio $\mathcal{A}$, representing the ratio between the vertical and horizontal dimension of the bubble, is determined according to Wellek et al. [215] as

[1] The present formulation is a slightly modified version of the original model, adapted by Frank et al. [81]

$$\mathcal{A} = \frac{D_{p,v}}{D_{p,h}} = \frac{1}{1 + 0.163\mathrm{Eo}^{0.757}}, \tag{2.88}$$

with a relation to the mean bubble diameter D_p in the form of

$$D_p = \left(D_{p,v} D_{p,h}^2\right)^{1/3}. \tag{2.89}$$

The diagram in figure 2.8 illustrates the relation between the lift coefficient C_L and the bubble diameter D_p according to the Tomiyama model for an air-water system at ambient conditions.

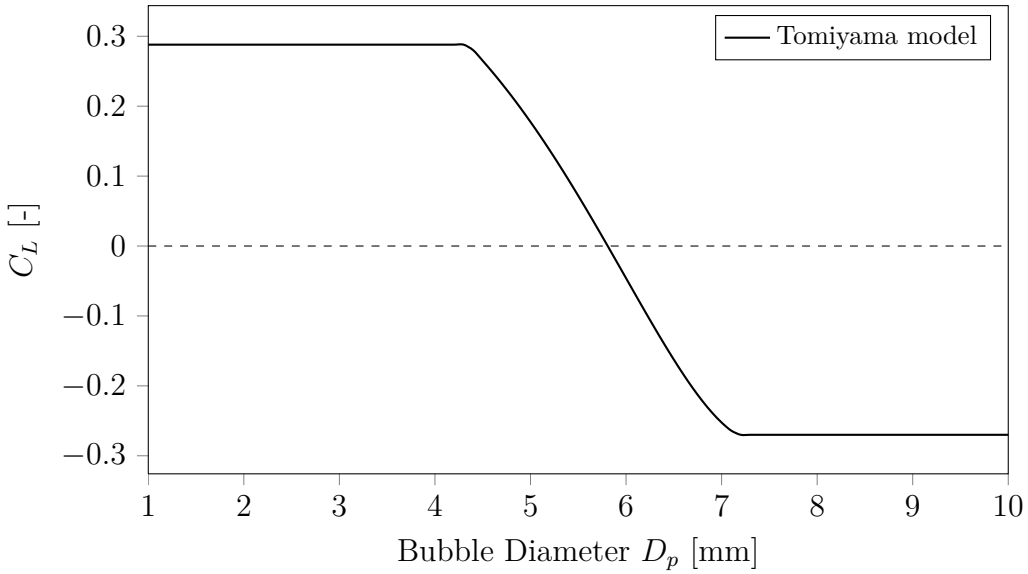

Figure 2.8: Lift force coefficient C_L according to the Tomiyama model for an air-water system ($|\boldsymbol{u}_d - \boldsymbol{u}_c| = 0.25\,\mathrm{m/s}$)

Alternative models for the lift force in bubbly flows can be found in a comprehensive overview by Hibiki & Ishii [96]. The lift force models published so far are derived from simplistic gas-liquid flow conditions, which also applies for the Tomiyama model. To further extend the respective considerations to more practical two-phase flows, a continuing research effort is required.

Following the results of several numerical investigations (e.g., [227], [93]), a lift force coefficient of $C_L = 0.5$ is applied in many recent bubble column flow simulations, specifically LES studies, superseding the former neglect of transversal forces. Latest publications on numerical investigations of

bubble column flows exhibit an increased application of more complex lift force correlations, particularly the Tomiyama model, without yielding a unanimous conclusion on the quality and suitability of model formulations.

2.4.1.3 Virtual mass force

An accelerating motion of a dispersed particle causes the continuous fluid in its vicinity to accelerate as well. As a consequence, a retaining force is acting on the particle, commonly referred to as virtual or added mass force. Drew et al. [69] [67] formulated an expression for the virtual mass force in an Eulerian framework as

$$\boldsymbol{M}_{VM} = C_{VM}\alpha_d\rho_c\left(\frac{\mathrm{D}\boldsymbol{u}_d}{\mathrm{D}t} - \frac{\mathrm{D}\boldsymbol{u}_c}{\mathrm{D}t}\right), \tag{2.90}$$

and derived a value of $C_{VM} = 0.5$ for the virtual mass coefficient in case of a spherical particle in potential flow. With this configuration, the acceleration of the particle is adapted as if half of the fluid mass it displaces were added to the particle mass.

Considering bubbly flows, Tomiyama [200] deduced a model expression for the virtual mass coefficient from experimental investigations. For ellipsoidal-shaped bubbles, he proposed the formulation of the virtual mass coefficient in the form of a diagonal tensor $\boldsymbol{C}_{VM}$ with different entries for the horizontal $C_{VM,h}$ and vertical direction $C_{VM,v}$, respectively. These expressions read

$$C_{VM,h} = \frac{\mathcal{A}\cos^{-1}\mathcal{A} - \sqrt{1-\mathcal{A}^2}}{\mathcal{A}^2\sqrt{1-\mathcal{A}^2} - \mathcal{A}\cos^{-1}\mathcal{A}}, \tag{2.91}$$

$$C_{VM,v} = \frac{\cos^{-1}\mathcal{A} - \mathcal{A}\sqrt{1-\mathcal{A}^2}}{\left(2\mathcal{A}^{-1} - \mathcal{A}\right)\sqrt{1-\mathcal{A}^2} - \cos^{-1}\mathcal{A}}. \tag{2.92}$$

So far, the introduced Tomiyama approach, as well as alternative models for virtual mass effects in bubbly gas-liquid flows (e.g., [84], [134]) have rarely been applied in published CFD simulations of bubble column hydrodynamics [227] [229]. Until now, the most frequently used virtual mass

correlation for respective Euler-Euler models is determined by the selection of $C_{VM} = 0.5$. Several comparative numerical studies (e.g., [58], [197]) indicate that virtual mass effects are of minor significance for gas-liquid flows in bubble columns, outweighed by the impact of lift, and primarily drag forces. Although their influence on the numerical results is arguably marginal, virtual mass correlations are frequently incorporated in recent corresponding publications, which may also be explained by beneficial effects on numerical stability.

2.4.1.4 Turbulent dispersion force

As discussed in section 2.3, the fluctuating motion of the dispersed phase is not or only partially resolved within an Euler-Euler framework for gas-liquid flows. Consequently, the dispersion of fluid particles due to unresolved turbulence is not depicted by the numerical model and various researchers propose the consideration of this effect in the form of an interfacial force, termed turbulent dispersion (or diffusion) force. A number of respective model formulations for the numerical incorporation of this force have been published. Moraga et al. [158] and Lucas et al. [135] give an overview of available models including their application in respective studies. The most prominent variant is based on a general expression of the turbulent dispersion force derived by analogy with molecular movement [120] as

$$\boldsymbol{M}_{TD} = C_{TD}\rho_c k_{c,tur}\nabla\alpha_d. \tag{2.93}$$

While the original model defined a constant value of $C_{TD} = 0.1$ for the turbulent dispersion coefficient, this approach was later extended by Lopez de Bertodano [133] who formulated a more general evaluation of C_{TD} subject to the particle Stokes number.

The introduced consideration of the dispersive transport of bubbles caused by gas-liquid turbulence in terms of an interfacial force is controversial, specifically with respect to a coincident modeling of the dispersed phase residual stress [99]. With the application of an LES approach, turbulent eddies down to the size range of the bubble diameter are accounted for by the numerical discretization (see section 2.3). Hence, depending on the bubble to grid size ratio, the justification for the incorporation of a turbulent

dispersion force model is limited or nonexistent. Generally, the turbulent dispersion force is neglected in LES simulations of bubble column flows, while latest studies pursue the adaption of existing formulations for the application in an LES context (e.g., [196]).

By studying published Euler-Euler model configurations for the simulation of bubble column hydrodynamics, it is evident that an unanimous setup for the modeling of interfacial forces has not been established yet, not in terms of considered phenomena nor in their respective model formulation. Several tabular reviews of bubble column flow simulation configurations (e.g., [197], [14], [91]) exhibit the variety of combinations with respect to interfacial momentum exchange closure relations. The main reason for the lack of definite knowledge in this field can be ascribed to the complexity of experimentally determining individual aspects of momentum exchange, particularly in polydisperse bubble swarms. Further numerical and experimental studies are necessary to clarify and quantify the interaction of interfacial forces. A similar conclusion is drawn by researchers like Ishii & Hibiki [103], who hereof reported: "In the present status of development, constitutive equations for some forces are based on speculation, and the applicable flow ranges are not given clearly. Thus, unlike the standard drag force, such lateral forces have not been well developed". In view of this, rather elementary configurations for the consideration of interfacial momentum exchange are applied in this work, coinciding with various numerical studies reported in the literature.

2.4.2 Mass transfer

In the Euler-Euler constitutive equations for gas-liquid flows (2.31) to (2.40), mass transfer phenomena are collectively accounted for by the source terms Γ_k and Γ_k^{X}. While both expressions are formulated with respect to the associated phase k, the latter exclusively represents the mass transfer of chemical species X. Consequently, the net mass transfer in association with phase k can be expressed as a combination of species-specific contributions by

$$\Gamma_k = \sum_X \Gamma_k^{\mathrm{X}}. \tag{2.94}$$

Mass transfer across the phase boundary in a gas-liquid environment may be effected by different thermodynamic and chemical phenomena, e.g., evaporation, condensation or absorption. Exclusively the latter effect is considered in this work and a brief explication of the respective physical basis is given in the subsequent segments. Although the remaining mass transfer phenomena originate from alternative physical processes, their impact on the conservation equations of mass, momentum and chemical species is commonly formulated similar to the correlation presented in chapter 2.2.2. As only a concise introduction to mass transfer theory is part of this section, the reader is referred to specialized literature for a detailed derivation of formulations and information on all physical aspects (e.g., [12], [50], [116]).

Mass transfer across the gas-liquid interface, specifically absorption, is driven by a local gradient in concentration of chemical species between the phases. The induced mass flux tends to counter the chemical imbalance until eventually a state of equilibrium is reached. While this process can be directly described if only diffusive transport is considered, turbulent convection necessitates the development of more complex concepts of formal representation. Several approaches have been developed to conceive this phenomenon.

The *penetration theory* was introduced by Higbie [97] and describes absorption from a bubble surface in terms of a reiterative transport of individual fluid elements that migrate to the interface, exchange mass while being in contact with the bubble and remigrate to the fluid bulk. Danckwerts [51] adapted this approach to establish the *surface renewal model* by defining a statistical evaluation approach for the contact time instead of the former assumption of a constant exposure time. As opposed to these approaches, the *boundary layer theory* considers the liquid fluid dynamics in the vicinity of the bubble by the constitutive equations. Yet, several simplifying assumptions have to be made in the derivation of practical formulations, which are outlined in respective literature sources (e.g., [18]).

A mass concentration profile from within a dispersed bubble across the phase boundary to the liquid bulk is illustrated in figure 2.9. This depiction exhibits the three types of resistance the mass flux between the phases has to overcome: the single phase transport to $\left(Y_d^{\mathrm{X}} \rightarrow Y_{d,I}^{\mathrm{X}}\right)$ and from the

interface $\left(Y_{c,I}^{\mathrm{X}} \rightarrow Y_{c}^{\mathrm{X}}\right)$, respectively, as well as the transfer resistance across the phase boundary $\left(Y_{d,I}^{\mathrm{X}} \rightarrow Y_{c,I}^{\mathrm{X}}\right)$.

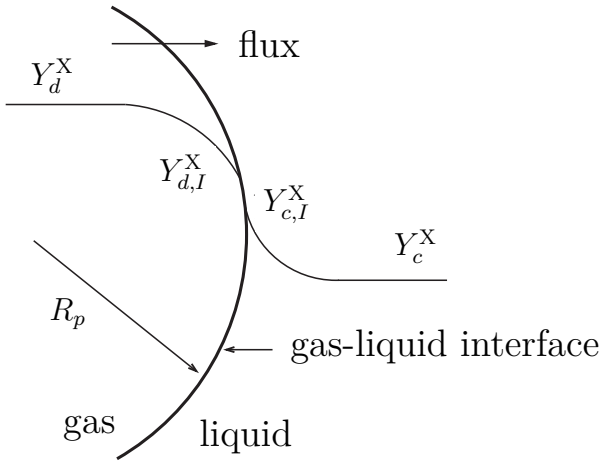

Figure 2.9: Illustration of mass concentration relations effecting mass transfer across the gas-liquid interface (adapted from [52])

Generally, the phase boundary is regarded as infinitesimally thin and thermodynamic equilibrium with respect to mass transfer is assumed at the interface. With the additional prerequisite of low solubility of a gaseous species X in liquid, which is generally well justified, the interfacial mass concentration relation can be represented by Henry's law as

$$Y_{c,I}^{\mathrm{X}} = \mathcal{H}^{\mathrm{X}} Y_{d,I}^{\mathrm{X}} \frac{\rho_d}{\rho_l}, \tag{2.95}$$

where the dependency of the dimensionless Henry coefficient $\mathcal{H}$ on temperature and pressure is neglected in this study. For bubbly flows, a homogeneous concentration of species throughout the bubble volume is commonly assumed ($Y_{d,I}^{\mathrm{X}} = Y_{d}^{\mathrm{X}}$) which yields

$$Y_{c,I}^{\mathrm{X}} = \mathcal{H}^{\mathrm{X}} Y_{d}^{\mathrm{X}} \frac{\rho_d}{\rho_c}. \tag{2.96}$$

The description of mass transfer between the phases can therefore be reduced to the consideration of the liquid side only. According to this concept, the interfacial mass flux of species X in volume-specific form is expressed as

$$\Gamma_c^{\mathrm{X}} = \mathcal{K}_c^{\mathrm{X}} a_p \rho_c \left(Y_{c,I}^{\mathrm{X}} - Y_c^{\mathrm{X}}\right) = \mathcal{K}_c^{\mathrm{X}} a_p \rho_c \left(\mathcal{H}^{\mathrm{X}} Y_d^{\mathrm{X}} \frac{\rho_d}{\rho_c} - Y_c^{\mathrm{X}}\right), \tag{2.97}$$

where $\mathcal{K}_c^{\mathrm{X}}$ is the volumetric mass transfer coefficient on the liquid side and a_p denotes the volume-specific net bubble surface. Various models for the determination of $\mathcal{K}_c^{\mathrm{X}}$ have been reported in the literature, deduced from the theoretical concepts of mass transfer introduced above. Expressions for the dimensionless Sherwood number, which represents the ratio between the effective absorption velocity and the molecular diffusivity as

$$\mathrm{Sh}^{\mathrm{X}} = \frac{\mathcal{K}_c^{\mathrm{X}} D_p}{\mathcal{D}_c^{\mathrm{X}}}, \tag{2.98}$$

are derived according to the boundary layer theory. These formulations correlate with equivalent Nusselt number (Nu) expressions for the related consideration of heat transfer, which is based on analogous physical transport processes. In case of spherical fluid particles, the correlation of Frössling is applicable, which reads

$$\mathrm{Sh}^{\mathrm{X}} = 2 + 0.6\,\mathrm{Re}_p^{1/2} \left(\mathrm{Sc}_c^{\mathrm{X}}\right)^{1/3}. \tag{2.99}$$

The dimensionless Schmidt number, adopted in this expression, is introduced above in equation (2.65). For bubble column flows, the correlation of Glaeser [86] is frequently applied. He proposes

$$\mathrm{Sh}^{\mathrm{X}} = 2 + 0.015\,\mathrm{Re}_p^{0.89} \left(\mathrm{Sc}_c^{\mathrm{X}}\right)^{0.7} \tag{2.100}$$

for deformable bubbles in turbulent flow [23] [216]. Deduced from penetration theory and surface renewal model, Lamont & Scott [122] developed a formulation for the mass transfer coefficient based on the consideration of local turbulence interaction with the interface

$$\mathcal{K}_c^{\mathrm{X}} = \frac{2}{\sqrt{\pi}} \left(\mathcal{D}_c^{\mathrm{X}}\right)^{0.5} \left(\frac{\epsilon_c \rho_c}{\mu_c}\right)^{0.25}, \tag{2.101}$$

where ϵ_c denotes turbulent dissipation in the liquid. The prefactor $\frac{2}{\sqrt{\pi}}$ has been adapted frequently, while the present form corresponds to the theoretical derivation [170].

In some literature sources, equation (2.97) is expanded by an additional factor, referred to as *enhancement factor*. It accounts for the influence of chemical reactions in the continuous phase on the absorption process. While the enhancement factor is unity for slow reactions, it is determined subject to reaction kinetics and local concentrations for fast chemical reactions [179]. Details on the categorization of chemical reactions with respect to reaction velocity are given in the subsequent section.

2.5 Depiction of chemical reaction

Due to the complexity of multi-component chemical interaction and the wide range of relevant time scales, specifically in relation to temporal dimensions of fluid dynamic transport, the consideration of chemical reactions in an Eulerian CFD framework is particularly challenging. This chapter outlines the theoretical basis of this topic in conjunction with a brief introduction of common modeling approaches. The thematic overview is of a rather general nature and not limited to the consideration of bubble column flows. A deduction of specific model correlations for bubbly flows is omitted as the representation of chemical reaction phenomena is not an integral part of the developed numerical model (see chapter 4).

The subsequent outline of chemical reaction modeling fundamentals is not bound to particular phasic conditions, yet the focus is shifted to multiphase reactive processes to the end of this section. Characteristics of hydrodynamic mixing processes are discussed at the beginning, as the relation between mixing time scales in the flow field and time scales of chemical reactions is of essential relevance for reaction modeling.

2.5.1 Mixing processes in turbulent flows

Scalar mixing processes in the flow are described in the form of convective and diffusive terms in corresponding transport equations. Regarding

chemical species, these effects are depicted as part of the local instantaneous species conservation equation (2.16), where $\nabla \cdot \left(\rho Y^{\mathrm{X}} \boldsymbol{u}\right)$ represents the convective transport and $\nabla \cdot \left(\rho \mathcal{D}^{\mathrm{X}} \nabla Y^{\mathrm{X}}\right)$ the diffusive component[2]. The interaction of both transport processes defines species mixing effects in turbulent flows:

- Turbulent convection induces a fluid dynamic engulfment of the species fields without molecular permeation. Assuming initially separated layers of chemical species in a turbulent flow, the convective transport is responsible for the deformation of species regions and elongation of the interface (see figure 2.10). Yet, there are no molecular mixing effects and discrete transitions between species regions persist. As a result of the convective transport, a complex structure of species fields develops, associated with a reduction of the respective characteristic length scales.

(a) $t = 0$ **(b)** $t > 0$

Figure 2.10: Illustration of fluid dynamic species mixing by turbulent convection [79]

- As opposed to turbulent convection, the mixing on a molecular level is described by the process of diffusion. Molecular diffusion effects the blurring of discrete interfaces between species fields and reduces local gradients of concentration (see figure 2.11). Deducible from its definition, the influence of molecular diffusion is intensified in regions of high concentration gradients and most effective in the smallest fluid dynamic length scales. The enhancement of molecular mixing properties in virtue of turbulence thus stems from the consequences

[2] Since this outline is limited to the consideration of reactive processes in a continuous flow field (also disregarding heterogeneous interfacial reactions ($\Upsilon_I^{\mathrm{X}} = 0$)), the phase indicating subscript is omitted in the remainder of this section (e.g., $\Psi_k^{\mathrm{X}} = \Psi_c^{\mathrm{X}} = \Psi^{\mathrm{X}}$).

of turbulent convection: a steepening of local concentration gradients and an increased exchange surface.

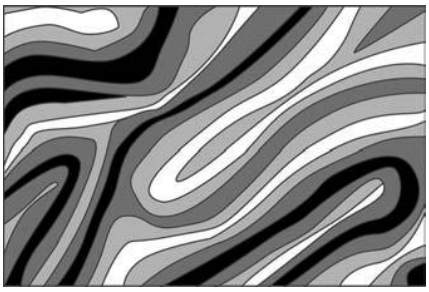

Figure 2.11: Illustration of fluid dynamic species mixing by turbulent convection and molecular diffusion [79]

Different characteristic length scales can be defined when studying turbulence, e.g., the *Kolmogorov microscale* l_η which represents the smallest spatial dimension of a turbulent eddy in the velocity field. Viscous effects prevent the formation of local velocity fluctuations below this scale. In analogy to this concept, a smallest length scale can also be defined for turbulent mixing processes where concentration gradients in smaller dimensions are leveled by diffusion. The relation between both microscales is defined by the Schmidt number Sc. In fluids, where Schmidt numbers are in the order of 100-1000 [11], the smallest length scale of mixing is referred to as *Batchelor scale* l_B, with

$$\frac{l_B}{l_\eta} = \mathrm{Sc}^{-1/2}. \tag{2.102}$$

Hence, the Batchelor microscale l_B is substantially smaller than the Kolmogorov length l_η in this environment. The evolution and behavior of velocity and species fluctuations are analogous for turbulent scales associated with the inertial subrange of the turbulence spectrum. Since turbulent fluctuations in the velocity field cease at spatial dimensions below the Kolmogorov microscales, the concentration fluctuations are spatially reduced by the strain field for the subjacent length spectrum. Ultimately, the Batchelor microscales are reached and the increasing influence of diffusive effects evens out remaining concentration gradients. A more detailed explanation of scalar and velocity turbulence interrelations is presented by Paul et al. [167].

2.5.2 Fundamentals of chemical reaction modeling

In section 2.2.1, the source term Ψ^{X} was introduced, a volume-specific net production rate, which describes the impact of chemical reactions on the species field. This expression is a function of the reaction rate constant λ and the concentrations of reacting species:

$$\Psi^{\mathrm{X}} = f\left(\lambda, Y^{\mathrm{A}}, Y^{\mathrm{B}}, \ldots, Y^{\mathrm{R}}\right). \tag{2.103}$$

If a simple chemical reaction of the form

$$\mathrm{A} + \mathrm{B} \longrightarrow \mathrm{C} \tag{2.104}$$

is considered, the related source terms are represented by

$$\Psi^{\mathrm{A}} = \Psi^{\mathrm{B}} = -\lambda Y^{\mathrm{A}} Y^{\mathrm{B}} \quad \text{and} \quad \Psi^{C} = \lambda Y^{\mathrm{A}} Y^{\mathrm{B}}. \tag{2.105}$$

In most cases, the reaction rate constant λ is strongly temperature-dependent, specifically in homogenous gas reactions. This aspect is commonly specified by the Arrhenius' equation

$$\lambda = C_A \exp\left(\frac{-\mathbb{E}}{\mathbb{R}T}\right), \tag{2.106}$$

which describes the interrelation of temperature T and activation energy $\mathbb{E}$ in chemical kinetics. The coefficients C_A and $\mathbb{R}$ represent the pre-exponential factor and the universal gas constant. Regarding chemical reactions in liquid environments, the impact of temperature on the reaction rate is often outweighed by solubility constraints on reacting species concentrations.

If the volume averaging procedure introduced in section 2.2.2 is employed on the chemical reaction source terms, issues similar to the consideration of turbulence fluctuations arise as a consequence of the multiplicative combination of influencing factors. With the assumption of a uniform

reaction rate constant[3] λ, the exemplary transformation of an expression from equation (2.105) yields

$$\overline{\Psi}^{\mathrm{A}} = -\alpha\lambda\overline{Y^{\mathrm{A}}Y^{\mathrm{B}}} = -\alpha\lambda\left(\overline{Y}^{\mathrm{A}}\overline{Y}^{\mathrm{B}} + \overline{Y'^{\mathrm{A}}Y'^{\mathrm{B}}}\right). \tag{2.107}$$

It is not possible to evaluate the averaged correlation of SGS concentrations fluctuations $\overline{Y'^{\mathrm{A}}Y'^{\mathrm{B}}}$ from the transported variables $\overline{Y}^{\mathrm{A}}$ and $\overline{Y}^{\mathrm{B}}$ [4]. Thus, the alternative deduction of the chemical reaction source term in the form of a model approach is unavoidable, even in this simplistic exemplification. The consideration of local variations of λ and non-linearities with respect to species concentrations would additionally complicate the derivation of volume averaged expressions. For practicle engineering problems, the incorporation of chemical reaction phenomena in an Eulerian framework cannot be established without modeling considerations.

The selection of an adequate modeling approach depends on a comparison of relative reaction and mixing rates. Formally, this decisive relation is represented by the Damköhler number Da as

$$\mathrm{Da} = \frac{\tau_{mix}}{\tau_{chem}}, \tag{2.108}$$

with τ_{mix} and τ_{chem} denoting the characteristic time scales of species mixing and chemical reaction, respectively. Table 2.3 gives a rough outline of time scale value ranges in an industrial scale chemical reactor. According to this relation, reactive flow processes can be categorized as *slow chemistry*, *finite-rate chemistry* or *fast chemistry*.

Fox [79] describes the general approach to evaluating the characteristic chemical time scales of a reaction system by defining the corresponding Jacobian matrix as

$$\boldsymbol{\mathcal{J}} = \frac{\partial \boldsymbol{\Psi}}{\partial \boldsymbol{Y}}, \tag{2.109}$$

with $\boldsymbol{\Psi} = \begin{bmatrix}\Psi^{\mathrm{A}} & \Psi^{\mathrm{B}} & \cdots & \Psi^{\mathrm{R}}\end{bmatrix}^{\mathcal{T}}$ and $\boldsymbol{Y}^{X} = \begin{bmatrix}Y^{\mathrm{A}} & Y^{\mathrm{B}} & \cdots & Y^{\mathrm{R}}\end{bmatrix}^{\mathcal{T}}$.

[3] The simplification of a uniform reaction rate constant generally is invalid for practicle applications due to a strong dependency of λ on local temperatures (see (2.106)).

Chemical time scales	[s]	**Flow time scales**
	10^{3}	
	10^{2}	
slow chemistry	10^{1}	τ_{res}
	10^{0}	
	10^{-1}	τ_{mix}
finite-rate chemistry	10^{-2}	
	10^{-3}	
	10^{-4}	τ_{η}
	10^{-5}	
	10^{-6}	
fast chemistry	10^{-7}	
	10^{-8}	
	10^{-9}	

Table 2.3: Relation of chemical and fluid dynamic time scales in a typical plant scale chemical reactor (τ_{res} mean residence time, τ_{η} characteristic time scale of smallest turbulent eddies: Kolmogorov time scale) (adapted from [79])

From the eigenvalues Λ_i of this matrix, individual chemical time scales for the concerned species can be determined in the form of

$$\tau_{chem,i} = \frac{1}{|\Lambda_i|}, \tag{2.110}$$

where $\min(\tau_{chem,i})$ represents the decisive value for the chemical reaction system. If the one-step reaction system of expression (2.104) is considered, the evaluation of chemical time scales yields $\tau_{chem,1} = \left(-\frac{\partial \Psi^{\mathrm{A}}}{\partial Y^{\mathrm{A}}}\right)^{-1} = \frac{1}{\lambda Y^{\mathrm{B}}}$, $\tau_{chem,2} = \frac{1}{\lambda Y^{\mathrm{A}}}$ and $\tau_{chem,3} = 0$. The latter expression indicates that C is an inert species in the respective system of reactions.[4]

Several models have been developed for the evaluation of the characteristic time scale of turbulent mixing in the flow field [167] [179]. The arguably most prominent formulation regarding mixing processes in liquids was introduced by Corrsin [46]. He describes the time range for the reduction

[4] The Jacobian matrix for the considered chemical source terms reads $\boldsymbol{\mathcal{J}} = \begin{bmatrix} \frac{\partial \Psi^{\mathrm{A}}}{\partial Y^{\mathrm{A}}} & \frac{\partial \Psi^{\mathrm{A}}}{\partial Y^{\mathrm{B}}} & 0 \\ \frac{\partial \Psi^{\mathrm{B}}}{\partial Y^{\mathrm{A}}} & \frac{\partial \Psi^{\mathrm{B}}}{\partial Y^{\mathrm{B}}} & 0 \\ \frac{\partial \Psi^{C}}{\partial Y^{\mathrm{A}}} & \frac{\partial \Psi^{C}}{\partial Y^{\mathrm{B}}} & 0 \end{bmatrix}$

of species fluctuations from the domain dependent largest scales l_s over the Kolmogorov microscales l_η to the Batchelor length l_B as a combination of respective terms

$$\tau_{mix} = \underbrace{2\left(\frac{l_s^2}{\epsilon}\right)^{1/3}}_{l_s \to l_\eta} + \underbrace{\frac{1}{2}\left(\frac{\nu}{\epsilon}\right)^{1/2} \ln\left(\mathrm{Sc}\right)}_{l_\eta \to l_B}. \tag{2.111}$$

Depending on the categorization according to time scale considerations, inherently diverging approaches are commonly applied for the modeling of chemical reactions in an Eulerian context. To this end, the Damköhler number is used as an indicator for appropriate model selection and will consequently be employed for the systematic subdivision of the subsequent section on modeling approaches.

2.5.3 Modeling approaches

Hereinafter, several theories for the description of chemical reactions within an Eulerian numerical framework are introduced subject to a categorization with respect to the Damköhler number. In general, the models are not rigorously derived from filtered balance equations, but involve phenomenological simplifications or rest upon statistical conceptions. A more elaborate presentation of respective approaches is given by Fox [79] or Andersson et al. [4].

2.5.3.1 Slow chemistry (Da $\ll 1$)

If all chemical time scales are significantly larger than the characteristic time scale of turbulent mixing, it can be assumed that the species concentrations are already mixed down to the molecular level at the time of reaction. In this case, the *laminar chemistry model* can be applied which implies that SGS fluctuations of the species concentrations and temperature field can be neglected in the determination of the chemical source terms. Therefore, the simple correlation

$$\overline{\Psi}^{\mathrm{X}}\left(\lambda, Y^{\mathrm{A}}, Y^{\mathrm{B}}, \ldots, Y^{\mathrm{R}}\right) = \alpha\Psi^{\mathrm{X}}\left(\overline{\lambda}, \overline{Y}^{\mathrm{A}}, \overline{Y}^{\mathrm{B}} \ldots, \overline{Y}^{\mathrm{R}}\right) \tag{2.112}$$

is valid; or regarding the exemplary reaction of expression (2.104):

$$\overline{\Psi}^{\mathrm{A}} = -\alpha\lambda\left(\overline{Y}^{\mathrm{A}}\overline{Y}^{\mathrm{B}}\right). \tag{2.113}$$

2.5.3.2 Fast chemistry (Da $\gg 1$)

A high Damköhler number implies that occurring chemical reactions are fast in comparison to turbulent mixing rates. In this case, the reactive flow processes are mixing-limited. A reaction rate-based description of chemical source terms similar to equation (2.105) is inadequate, since the stiff system of equations would hinder the simultaneous evaluation of fluid dynamic and chemical processes in the flow. As a consequence, alternative approaches have been developed, of which several are based on the *mixture fraction theory*. This method can be applied for non-premixed reacting species and was originally established for combustion modeling of diffusion flames [203].

To give a concrete description of this approach, the simple chemical reaction expression (2.104) is generalized by the inclusion of generic stoichiometric coefficients as

$$\mathrm{j}^{\mathrm{A}}\mathrm{A} + \mathrm{j}^{\mathrm{B}}\mathrm{B} \longrightarrow \mathrm{j}^{\mathrm{C}}\mathrm{C}. \tag{2.114}$$

With the stoichiometric concentration ratio $\mathbb{S} = \frac{j^A}{j^B}$, the chemical source terms are related by $\Psi^{\mathrm{A}} = \mathbb{S}\Psi^{\mathrm{B}}$ and $\Psi^{C} = -\left(1-\mathbb{S}\right)\Psi^{\mathrm{A}}$. The definition of a parameter $Z = Y^{\mathrm{A}} - Y^{\mathrm{B}}/\mathbb{S}$ permits the formulation of the following transport equation:

$$\frac{\partial}{\partial t}Z + \nabla\cdot\left(Z\boldsymbol{u}\right) = -\nabla\cdot\left(\mathcal{D}\nabla Z\right). \tag{2.115}$$

In this way, an explicit evaluation of the chemical reaction source terms is avoided and the depiction of the reactive flow is reduced to the consideration of a passive scalar. It is possible to define alternative scalar parameters, from

which transport equations similar to (2.115) can be derived. The mixture fraction ξ is formulated by a normalization of Z as

$$\xi = \frac{j^{\mathrm{B}} Y^{\mathrm{A}} - j^{\mathrm{A}} Y^{\mathrm{B}} + j^{\mathrm{A}} Y_0^{\mathrm{B}}}{j^{\mathrm{B}} Y_0^{\mathrm{A}} + j^{\mathrm{A}} Y_0^{\mathrm{B}}}, \tag{2.116}$$

where Y_0^{A} and Y_0^{B} are the species concentrations in their premixed state, commonly representing different inlet streams. Thus, the value range of ξ is limited to $0 \leq \xi \leq 1$. If combustion processes are considered, the limiting values represent the concentration conditions at the inlets for fuel and oxidizer.

Formulation (2.116) is specifically favorable for fast irreversible reactions. In the ultimate case (*mixed-is-reacted* approach), the simultaneous presence of multiple reactants at a location in the flow field is assumed invalid ($Y^{\mathrm{B}} = 0$ if $Y^{\mathrm{A}} > 0$, and vise versa). Beyond that, a state has to be considered in which no reactants are present ($Y^{\mathrm{B}} = 0$, $Y^{\mathrm{A}} = 0$). It is defined by the stoichiometric mixture fraction ξ_{st} as

$$\xi_{st} = \frac{j^{\mathrm{A}} Y_0^{\mathrm{B}}}{j^{\mathrm{B}} Y_0^{\mathrm{A}} + j^{\mathrm{A}} Y_0^{\mathrm{B}}}. \tag{2.117}$$

With this parameter, expressions for the local instantaneous reactants concentrations can be deduced with respect to the assumption of infinitely fast chemistry. The consequent formulations read

$$Y^{\mathrm{B}} = Y_0^{\mathrm{B}} \left(1 - \frac{\xi}{\xi_{st}}\right); \; Y^{\mathrm{A}} = 0 \quad \text{if} \quad \xi < \xi_{st}, \tag{2.118}$$

$$Y^{\mathrm{A}} = Y_0^{\mathrm{B}} \, \mathbb{S} \left(\frac{\xi}{\xi_{st}} - 1\right); \; Y^{\mathrm{B}} = 0 \quad \text{if} \quad \xi > \xi_{st}. \tag{2.119}$$

The species concentration relations from equations (2.118) and (2.119) are graphically depicted in figure 2.12.

For the determination of volume averaged reactant concentrations ($\overline{Y}^{\mathrm{A}}$ and $\overline{Y}^{\mathrm{B}}$) a probability density function (PDF) $P(\xi)$ for the mixture fraction is

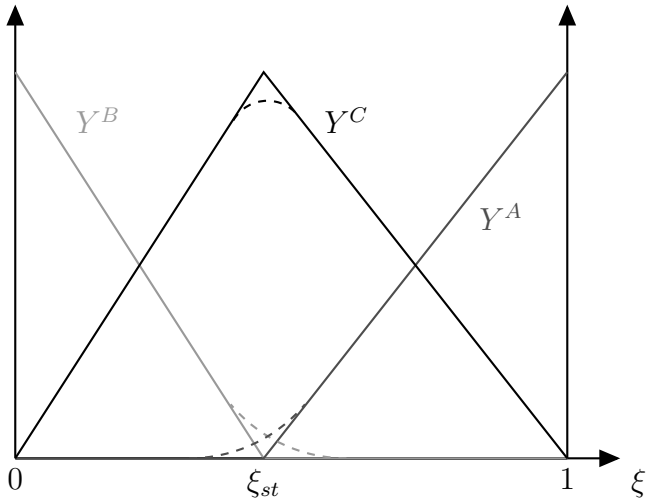

Figure 2.12: Sketched distributions of reactants (Y^A, Y^B) and product (Y^C) concentrations in case of infinitely fast chemistry (continuous line) and finite-rate conditions (dashed line) [32]

introduced in conjunction with an LES filtering procedure in analogy to (2.48):

$$\overline{P}(\xi, \boldsymbol{x}) = \int G(\boldsymbol{x}, \boldsymbol{x}') P(\xi, \boldsymbol{x}') \, \mathrm{d}\boldsymbol{x}'. \tag{2.120}$$

In an LES context, $\overline{P}(\xi, \boldsymbol{x})$ can be interpreted as probability of occurrence on a SGS level. The locally defined expression $P(\xi, \boldsymbol{x}')$ is commonly referred to as *fine-grain function*, whereas the LES parameter $\overline{P}(\xi, \boldsymbol{x})$ is termed *filtered density function* (FDF) or *large eddy PDF* (LEPDF) [25].

The combination of equations (2.119) and (2.120) yields a definition of the averaged species concentration of A as a function of $\overline{P}(\xi, \boldsymbol{x})$, given by

$$\overline{Y}^{\mathrm{A}} = \int_0^1 Y^{\mathrm{A}} \overline{P}(\xi) \, \mathrm{d}\xi = Y_0^{\mathrm{B}} \mathbb{S} \int_0^1 \left(\frac{\xi}{\xi_{st}} - 1 \right) \overline{P}(\xi) \, \mathrm{d}\xi. \tag{2.121}$$

In the commonly applied presumed PDF approach, a functional form of $\overline{P}$ is predefined with its parameters derived from the LES-filtered mixture fraction value $\overline{\xi}$ and a modeling approach for the associated SGS variance $\boldsymbol{G}_{tur}$ in the corresponding transport equation

$$\frac{\partial}{\partial t} \left(\alpha \rho \overline{\xi} \right) + \nabla \cdot \left(\alpha \rho \overline{\xi} \overline{\boldsymbol{u}} \right) + \nabla \cdot \left(\alpha \boldsymbol{G}_{tur} \right) = -\nabla \cdot \left(\alpha \rho \mathcal{D} \nabla \overline{\xi} \right), \tag{2.122}$$

with

$$\boldsymbol{G}_{tur} = \rho \left(\overline{\xi \boldsymbol{u}} - \overline{\xi}\,\overline{\boldsymbol{u}} \right). \tag{2.123}$$

As a summary, figure 2.13 illustrates the sequential steps for the determination of LES-filtered species concentrations in the mixture fraction approach. First, the input parameters for the mixture fraction transport equation (2.122) are generated by the numerical evaluation of the LES-filtered Navier-Stokes equations including accompanied turbulence modeling. The resulting averaged values of ξ are adopted to specify the respective PDF which in turn is used to calculate species concentrations according to equation (2.121).

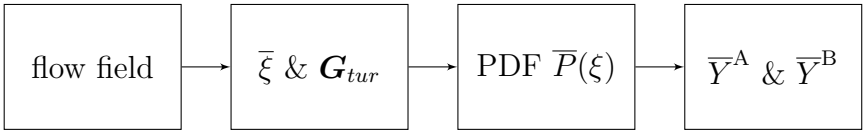

Figure 2.13: Schematic procedure for the mixture fraction approach for instantaneous reactions (adapted from [4])

Adapting the present procedure, more complex reaction schemes as well as equilibrium reactions can be described through the consideration of a passive scalar. More information on these modifications as well as a detailed deduction of generic governing equations for this method are outlined by Fox [79].

As an alternative to the mixture fraction method, the *eddy dissipation model* (EDM) [193] [139] is applicable for the numerical description of premixed or partially premixed fast reactions in the flow. This method is based on the conception of considered chemical reactions being completely describable by the characteristics of turbulent mixing. For the application of this approach, the following formulations are to be evaluated:

$$\Psi^{\mathrm{X}} = j^{\mathrm{X}} \mathbb{M}^{\mathrm{X}} C_{EDM,1}\, \rho\, \tau_{SGS}^{-1} \min_{\mathrm{R}} \left(\frac{Y^{\mathrm{R}}}{j^{\mathrm{R}} \mathbb{M}^{\mathrm{R}}} \right) \tag{2.124}$$

- According to equation (2.124), the concentration of the reaction-limiting reactant determines the evaluation of the source term. In a lean combustion, for example, the fuel concentration would be relevant, in the case of rich combustion the oxidizer concentration, respectively.

$$\Psi^{\mathrm{X}} = j^{\mathrm{X}}\mathbb{M}^{\mathrm{X}} C_{EDM,1} C_{EDM,2}\, \rho\, \tau_{SGS}^{-1} \frac{\sum_{\mathrm{P}} Y^{\mathrm{P}}}{\sum_{\mathrm{P}} j^{\mathrm{P}}\mathbb{M}^{\mathrm{P}}} \tag{2.125}$$

- Equation (2.125) is based on the idea that in case of premixed conditions, the reaction progress is potentially determined by the contacting of reaction products with the reactant flow. Thus, the sum of product concentrations $\sum_{\mathrm{P}} Y^{\mathrm{P}}$ is used for the calculation of the chemical source term.

According to the EDM, the minimum of equations (2.124) and (2.125) is eventually employed as source term in the corresponding species equation. The parameters $C_{EDM,1}$ and $C_{EDM,2}$ represent model constants which have to be adjusted to the particular problem within a wide range of potential values. As an essential influencing factor, the SGS turbulent time scale $\tau_{SGS} = \left|\overline{S}\right|$ is included in the LES form of the EDM to quantify the intensity of mixing processes. Alternatively, the turbulent time scale τ_{SGS} can be determined in analogy to the procedure for RANS models through according formulations for turbulent dissipation ϵ and SGS turbulent energy k_{SGS} ($\tau_{SGS} = k_{SGS}/\epsilon$) [73]. In order to extend the scope of this model, this approach was further developed in various forms. More detailed information on EDM and its adaptations can be found in literature by Peters [168] as well as by Cant & Mastorakos [32].

2.5.3.3 Finite-rate chemistry (Da $\approx$ 1)

While the consideration of reactive processes could be significantly simplified by appropriate assumptions in sections 2.5.3.1 and 2.5.3.2, an analogous approach is not possible for this category of reactive flows. The time scales of chemical reaction and turbulent mixing are of a comparable magnitude, thus, none of these two processes can be prioritized. As a consequence, statistical methods are primarily applied for an adequate LES modeling of the reactive flow. Based on the definition of the mixture fraction PDF in the preceding section, a similar expression can be formulated for the chemical source term in a more general manner:

$$\overline{\Psi}^{\mathrm{X}} = \int\int\int \ldots \int \Psi^{\mathrm{X}} \overline{P}\left(\lambda, Y^{\mathrm{A}}, Y^{\mathrm{B}}, \ldots, Y^{\mathrm{R}}\right) \mathrm{d}\lambda \, \mathrm{d}Y^{\mathrm{A}} \, \mathrm{d}Y^{\mathrm{B}} \ldots \mathrm{d}Y^{\mathrm{R}}. \quad (2.126)$$

In this case, all influencing parameters of the chemical source term are used as internal variables of the PDF. These generally include the reactants concentrations, as well as the reaction rate constant which in turn is usually a function of temperature. For determining LES-filtered PDF values, different procedures have been established:

Presumed Function PDF/FDF

If the functional form of the PDF is specified a priori, it is sufficient to formulate and evaluate transport equations for the first moments (mean, variance, ...) of this function in order to allow closure of the equation system for arbitrary combinations of the internal variables. Both the choice of a function type, as well as the modeling of LES-filtered terms in the transport equations, is associated with considerable uncertainty.

Transported PDF/FDF

This approach is based on the direct formulation of a transport equation for the multidimensional PDF $P\left(\lambda, Y^{\mathrm{A}}, Y^{\mathrm{B}}, \ldots, Y^{\mathrm{R}}\right)$. The definition of the associated LES-filtered convective term is restricted to coarsely simplifying model assumptions. To work around this issue, the internal variables of P can be supplemented by the flow velocity components ($P\left(\lambda, Y^{\mathrm{A}}, Y^{\mathrm{B}}, \ldots, Y^{\mathrm{R}}, \boldsymbol{u}\right)$). The formulation of LES governing equations for this configuration is accompanied by a considerable modeling effort as well. Alternatively, Monte Carlo methods are often resorted to for solving the transport equation in order to realize an efficient numerical evaluation even for high-dimensional PDFs.

Detailed information on the derivation and characteristics of statistical methods for chemical reaction modeling in a CFD context are provided by Pope [174] and Fox [79].

2.5.4 Multiphase reactive flow modeling

Regarding reactive flows in a multiphase environment, Ranade [179] distinguishes between three categories:

- The reaction zone is located in one of the phases, either in the bulk or close to the interface, e.g., various gas-liquid reactions.
- Interfacial reactions which occur on the phase boundaries, e.g., catalytic reactions.
- Single phase reactions with products forming another phase, e.g., crystallizations.

Bubble column reactors are intensively applied for both bulk and interfacial reactions, while this type of apparatus is rarely employed for reactive flows of the third category. Reactions occurring in the continuous phase of bubble column flows are initiated by absorption processes, which allow the migration of gaseous reactants into the liquid. As described in section 2.4.2, absorption phenomena depend on local flow conditions and fluid particle size relations. The latter influence is also essential to interfacial reactions in which the reactive area is determined by the magnitude of interfacial area in the flow. To accurately account for local phase boundary relations and bubble size spectra in an Euler-Euler context, a population balance equation with respect to fluid particle size or volume has to be included in the model setup. According formulations are introduced in the subsequent chapter.

3 Population balance

Different gas-liquid flow regimes occur in bubble column reactors depending on the superficial gas velocity and the size of the apparatus. While the bubble size is approximately constant for low gas flow rates, bubble breakup and coalescence phenomena gain significance in the heterogeneous regime which is characterized by higher superficial gas velocities. This operating condition is attractive for industrial applications due to enhanced mixing rates and increased gas throughput. For the highly dynamic heterogeneous flow field, predictions resulting from the evaluation of global parameters are limited in generality and validity. More detailed models are necessary for an adequate depiction of the flow characteristics. This includes the consideration of local bubble size evolution and its interaction with the two-phase hydrodynamics. [105] [57] [110]

In the scope of this chapter, the representation of the fluid particle size dynamics by means of a *population balance equation* (PBE) is explicated. Starting from the presentation of fundamentals of this approach, the general governing terms of the PBE are derived and specified for the investigated gas-liquid system. Subsequently, the inclusion of formal representations for continuous size evolution or particle interaction phenomena in the PBE framework is outlined. A general presentation of the numerical solving procedures of the PBE formulation and its integration into an Euler-Euler framework is given prior to the specification of the according configuration used in this work.

3.1 Population balance equation

In an Eulerian framework, polydispersity and particle interaction phenomena, e.g., breakup and coalescence, are described by the population balance equation (PBE). This transport equation for the local number density function (NDF) of fluid particles depicts the bubble size dynamics in gas-liquid flows. In this section, the principles of this method are introduced

in a generic context. The explication ranges from the definition of a general population balance equation to the derivation of the monovariate NDF considered in this work. More detailed information on all aspects related to the numerical description of polydisperse multiphase systems are comprehensively given by Marchisio & Fox [143].

3.1.1 Fundamentals and governing equations

In a population balance framework, disperse phase particles are identified by a certain number of considered properties, termed *coordinates* in this context. These coordinates are classified as either external or internal. Examples of external coordinates are spatial position or the instance of time, while internal coordinates can be of various nature, e.g., particle temperature, size or volume. If multiple dispersed particles have the identical set of coordinates, these are indistinguishable in the considered population balance framework. If only one internal coordinate is taken into account, the population balance is specified as *monovariate*, in contrast to the higher-dimensional *multivariate* case with numerous potential combinations of internal coordinates.

For the general derivation of the PBE, an internal-coordinate vector $\boldsymbol{\zeta} \equiv (\zeta_1, \zeta_2, \ldots)^{\mathcal{T}}$ is defined. With this, the number of dispersed particles in a generic volume $\mathrm{d}\boldsymbol{x} = (\mathrm{d}x_1, \mathrm{d}x_2, \mathrm{d}x_3)^{\mathcal{T}}$ featuring characteristics within the interval $\mathrm{d}\boldsymbol{\zeta}$ are described by

$$n\left(\boldsymbol{\zeta}; \boldsymbol{x}, t\right) \mathrm{d}\boldsymbol{x}\, \mathrm{d}\boldsymbol{\zeta}, \tag{3.1}$$

where n is the NDF subject to the set of internal coordinates $\boldsymbol{\zeta}$. In general, the NDF is assumed to represent the deterministic behavior of a large number of particles to ensure the smoothness of this function regarding external and internal coordinate space. The characteristics and limits of the relation between particle number and NDF are extensively discussed by Ramkrishna [178]. In this work, the population balance model is considered in line with the conventional continuum mechanical theory which implies the description of NDF dynamics in the form of a respective balance equation

$$\underbrace{\frac{\partial n\left(\boldsymbol{\zeta};\boldsymbol{x},t\right)}{\partial t}}_{\text{transient term}}+\underbrace{\nabla\cdot\left[n\left(\boldsymbol{\zeta};\boldsymbol{x},t\right)\boldsymbol{u}_p\right]}_{\text{convection term}}+\underbrace{\frac{\partial}{\partial\boldsymbol{\zeta}}\cdot\left[n\left(\boldsymbol{\zeta};\boldsymbol{x},t\right)\dot{\boldsymbol{\zeta}}\right]}_{\substack{\text{representation of}\\ \text{continuous processes}}}=\underbrace{h}_{\substack{\text{representation of}\\ \text{discontinuous processes}}}. \tag{3.2}$$

Equation (3.2) constitutes the population balance equation (PBE) in continuous form, while a subdivision of n according to internal coordinate intervals yields a discrete formulation. This differentiation of equation types with a focus on fluid particle populations is further outlined by Jakobsen [105], albeit denoting the variants *microscopic* and *macroscopic* PBE. The relation between PBE formulations and corresponding solving procedures is sketched in section 3.4 of this thesis.

The first term on the left hand side of equation (3.2) describes the temporal change of the NDF, whereas the second term represents its modification in virtue of convective particle transport in physical space. An evolution of the NDF due to continuous changes in one or multiple internal coordinates is depicted by the third term. In this context, $\dot{\boldsymbol{\zeta}}=\frac{\mathrm{d}\boldsymbol{\zeta}}{\mathrm{d}t}$ designates the internal-coordinate velocity comprised of individual internal coordinate variations as vector components. Discontinuous events altering the NDF are summarized in the source term h. In theory, the categorization between continuous and discontinuous phenomena is subject to the considered length and time scale relations. In view of the current application on polydisperse bubbly flows, this classification is evident: processes on a molecular level, e.g., absorption, are regarded as continuous, while discrete particle phenomena, e.g., bubble coalescence, are described as discontinuous events.

In case the particle velocity is incorporated as internal coordinate in the NDF, an alternative formulation is more suitable. Here, the transport equation for $n\left(\boldsymbol{\zeta},\boldsymbol{u}_p;\boldsymbol{x},t\right)$ is known as *generalized population balance equation* (GPBE) which reads

$$\begin{aligned}\frac{\partial n\left(\boldsymbol{\zeta},\boldsymbol{u}_p;\boldsymbol{x},t\right)}{\partial t}+\nabla\cdot\left[n\left(\boldsymbol{\zeta},\boldsymbol{u}_p;\boldsymbol{x},t\right)\boldsymbol{u}_p\right]+\frac{\partial}{\partial\boldsymbol{u}_p}\cdot\left[n\left(\boldsymbol{\zeta},\boldsymbol{u}_p;\boldsymbol{x},t\right)\boldsymbol{a}_p\right]\\ +\frac{\partial}{\partial\boldsymbol{\zeta}}\cdot\left[n\left(\boldsymbol{\zeta},\boldsymbol{u}_p;\boldsymbol{x},t\right)\dot{\boldsymbol{\zeta}}\right]=h.\end{aligned} \tag{3.3}$$

The third term on the left hand side of equation (3.3) is depicted separately from the remaining internal coordinate contributions (which are summarized in the fourth term), as it allows an analysis of particle kinetics. The continuous evolution of the NDF in particle velocity space, which is described in that term by $\boldsymbol{a}_p$, represents particle acceleration or body forces acting on a particle, e.g., gravity. With $\boldsymbol{u}_p$ as internal coordinate, the source term h specifically includes the representation of discrete changes in the particle velocity caused by collision processes, for example.

The analytical evaluation of equation (3.2) or (3.3) is limited to simplistic cases without practical relevance. For the numerical solution, specific methods have to be employed, of which several are introduced in section 3.4. However, even these procedures are bound to closure models for various terms, which need to be formulated with respect to the particulate system at hand. Specifics for the description of disperse gas-liquid flows are introduced in the subsequent sections.

3.1.2 Application to gas-liquid flows

In this work, population balance theory is used to describe the particulate character of the gaseous phase in bubble column hydrodynamics. Various internal coordinates can be used to formulate the NDF or, more specifically, *bubble number density function*. Potential features for the categorization of fluid particles are their thermodynamical, chemical or geometrical properties (e.g., enthalpy, species concentration or surface area). In addition, the particle velocity can be employed as internal coordinate with an accompanied formulation of the GPBE. Only very few examples of the definition of a multivariate PBE in the context of gas-liquid flows can be found in the literature (e.g., [28]). The specification of a monovariate population balance, with the bubble size or volume as single internal variable, is by far the most common configuration.

Following this concept, the bubble diameter D_p is considered as single internal coordinate in the remainder of this thesis. This specification consequently implies a monovariate NDF $n\left(D_p; \boldsymbol{x}, t\right)$, which reflects the polydisperse character of turbulent bubbly flows. As an additional assumption, all bubbles are regarded as spherical in the context of population

balance theory. This common simplification coincides well with gas-liquid flows featuring small sized bubbles, while minor discrepancies arise for higher values of particle Reynolds and Eötvös numbers (see figure 2.6). The prerequisite regarding sphericity of fluid particles does not apply to the Euler-Euler framework presented above, where the interfacial exchange may be specified with regard to deformable fluid particles.

3.2 Breakup and coalescence

The basic principles of breakup and coalescence modeling in the framework of a bubble size related PBE is presented in this segment. Following the introduction of conventional model formulations for discontinuous events in the PBE, their applicability to turbulent bubble column flows is discussed.

Marchisio & Fox [143] distinguish between three fundamental types of discrete processes affecting the population balance. With an association to dispersed gas-liquid flows, these categories can be introduced as:

- Zeroth-order point processes, exclusively determined by local continuous phase conditions (e.g., nucleation of bubbles)
- First-order point processes, describing the interaction of dispersed fluid particles with the liquid phase fluid dynamics (e.g., turbulence induced bubble breakup)
- Second-order point processes, representing discontinuous phenomena related to bubble-bubble interaction (e.g., bubble coalescence)

With the neglect of the first category, the consideration of discrete processes affecting the PBE is limited to the depiction of bubble coalescence and breakup in this study. Resulting effects on the PBE are collectively incorporated by the source term h in equation (3.2). For an adequate representation, a subdivision of this parameter according to the nature of the discontinuous event (i.e. coalescence $h_{\mathcal{C}}$, breakup $h_{\mathcal{B}}$) and its type of influence on the NDF is more suitable:

$$h\left(D_p\right) = h_{\mathcal{C}}\left(D_p\right) + h_{\mathcal{B}}\left(D_p\right) = b_{\mathcal{C}}\left(D_p\right) - d_{\mathcal{C}}\left(D_p\right) + b_{\mathcal{B}}\left(D_p\right) - d_{\mathcal{B}}\left(D_p\right). \quad (3.4)$$

- Coalescence birth term $b_{\mathcal{C}}(D_p)$: production rate of bubbles with diameter D_p due to coalescence of smaller fluid particles
- Coalescence death term $d_{\mathcal{C}}(D_p)$: destruction rate of bubbles with diameter D_p due to their coalescence with other particles
- Breakup birth term $b_{\mathcal{B}}(D_p)$: production rate of bubbles with diameter D_p due to breakup of bigger fluid particles
- Breakup death term $d_{\mathcal{B}}(D_p)$: destruction rate of bubbles with diameter D_p due to their breakup

Numerous model approaches have been proposed for the specification of each component of equation (3.4). Although different physical and fluid dynamic conditions and causalities in relation to fluid particle breakup and coalescence have been considered, the basic equation structure is similar in most cases. Commonly, the general expressions established by Ramkrishna [178] constitute the formal basis, which is extended and interpreted to specify model relations. In line with the bubble diameter-based formulation of the NDF $n(D_p; \boldsymbol{x}, t)$, these functions will subsequently be presented in the formulation subject to particle diameter ($b(D_p)$, $d(D_p)$). The derivation of these expressions from bubble volume-based functions is presented in appendix A.1.

The physical fundamentals of fluid particle breakup and coalescence modeling are outlined in the following, accompanied by exemplary model formulations specifically for turbulent bubbly flows. For further reading, Liao & Lucas [128] [129] give a very comprehensive overview of available approaches

3.2.1 Bubble coalescence modeling

Apart from a few exceptions, model approaches for the description of bubble coalescence are based on the conception of a three step mechanism. First, two bubbles collide, then coher and form a liquid film between them, draining out gradually. As a last step, the liquid layer eventually raptures to leave a single fluid particle. Generally, the coalescence of more than two bubbles is disregarded with reference to the low probability of a respective phenomenon.

Local differences in bubble motion induce relative velocities of fluid particles and consequently allow for their collision. In turbulent flows, multiple potential causes for local particle velocity inhomogeneities can be identified. Prince & Blanch [176] propose a cumulative consideration of collision phenomena due to turbulent fluctuations, buoyancy effects and laminar shear. Yet, further possible origins of collision processes have been reported [129]. Concerning turbulent bubbly flows, Chen [38] concludes that only turbulence induced collision and collision through wake entrainment are of interest in this context. With the unavailability of an adequate model for the latter phenomena and its subordinate importance, this work, as the vast majority of related studies, is limited to the consideration of turbulent bubble collisions.

The PBE source terms for aggregation phenomena are introduced in their size-specific form to account for bubble coalescence in the respective monovariate population balance:

$$b_{\mathcal{C}}(D_p) = \frac{D_p^2}{2} \int_0^{D_p} \frac{r_{\mathcal{C}}\left(\gamma_p, \left(D_p^3 - \gamma_p^3\right)^{1/3}\right)}{\left(D_p^3 - \gamma_p^3\right)^{2/3}} \, n(\gamma_p) \, n\left(\left(D_p^3 - \gamma_p^3\right)^{1/3}\right) \, \mathrm{d}\gamma_p, \quad (3.5)$$

$$d_{\mathcal{C}}(D_p) = n(D_p) \int_0^{\infty} r_{\mathcal{C}}(\gamma_p, D_p) \, n(\gamma_p) \, \mathrm{d}\gamma_p. \quad (3.6)$$

While several empirical correlations for the coalescence rate $r_{\mathcal{C}}$ as kernel function have been proposed in early studies, the subdivision into a collision frequency $\omega_{\mathcal{C}}$ and a coalescence probability $\mathcal{P}_{\mathcal{C}}$ is common to later publications (e.g., [176], [126]). The corresponding expression reads

$$r_{\mathcal{C}}\left(\gamma_p, D_p\right) = \omega_{\mathcal{C}}(\gamma_p, D_p) \mathcal{P}_{\mathcal{C}}(\gamma_p, D_p). \quad (3.7)$$

With the limitation to turbulence induced bubble collisions in the gas-liquid flow, an analogy to the random motion of molecules in the kinetic gas theory is commonly assumed. With this prerequisite, the collision frequency can be formulated as a combination of the potential collision area of impacting bubbles $A_{\mathcal{C}}$ and the approach velocity $\boldsymbol{u}_{p,rel}$. In general, the velocity of colliding fluid particles is equated to the velocity of equivalent turbulence

eddies with length scales similar to the bubble diameters [47]. The formal expression for this correlation yields

$$u_{p,rel}\left(\gamma_p, D_p\right) = \left(\left(u_{tur}(D_p)\right)^2 + \left(u_{tur}(\gamma_p)\right)^2\right)^{1/2}, \tag{3.8}$$

with

$$u_{tur}(D_p) = C_{\mathcal{C}}\left(\epsilon_c D_p\right)^{1/3}, \tag{3.9}$$

where $C_{\mathcal{C}}$ is a model constant. This concept is based on the assumption that the energy of smaller turbulence eddies is insufficient to effect bubble motion, while bigger eddies influence disperse phase movement on a larger scale without causing local relative velocities.

The area for bubble collision is specified as the circular face of potential bubble intersection as

$$A_{\mathcal{C}}\left(\gamma_p, D_p\right) = \frac{\pi}{4}\left(D_p + \gamma_p\right)^2. \tag{3.10}$$

Hence, the fluid particle collision frequency is given in the form of

$$\begin{aligned}\omega_{\mathcal{C}}\left(\gamma_p, D_p\right) &= A_{\mathcal{C}}\left(D_p, \gamma_p\right) u_{p,rel}\left(D_p, \gamma_p\right) \\ &= C_{\mathcal{C}}^{1/2}\frac{\pi}{4}\epsilon_c^{1/3}\left(D_p + \gamma_p\right)^2\left(D_p^{2/3} + \gamma_p^{2/3}\right)^{1/2}.\end{aligned} \tag{3.11}$$

Various values of $C_{\mathcal{C}}$ have been reported in different model approaches spanning a value range between 0.127 and 2 [129]. In order to clarify the rather ambiguous specification of this parameter, latest publications propose an evaluation with respect to volume fraction conditions and fluid particle distance [213].

According to the introduced sequential process of bubble coalescence, two fluid particles cohere prior to unification. Whether coalescence eventuates is determined by the relation between the time t_{drain} the separating liquid film needs to drain out and the contact time t_{cont} of respective fluid particles. Coulaloglou [48] expressed this relationship by

$$\mathcal{P}_{\mathcal{C}}\left(\gamma_p, D_p\right) = \exp\left(-\frac{t_{drain}\left(\gamma_p, D_p\right)}{t_{cont}\left(\gamma_p, D_p\right)}\right). \tag{3.12}$$

Based on phenomenological considerations, Chesters [42] formulated expressions for t_{drain} subject to fluid particle surface rigidity and mobility. Regarding gas bubbles, the approach for deformable particles with fully mobile interfaces is appropriate, which reads

$$t_{drain}\left(\gamma_p, D_p\right) = \frac{1}{2}\frac{\rho_c u_{p,rel} D_p^2}{\left(1+\vartheta\right)^2 \sigma}, \tag{3.13}$$

with $\vartheta = \frac{\min(\gamma_p, D_p)}{\max(\gamma_p, D_p)}$.

Luo [137] derived a correlation for the interaction time t_{cont} of dispersed gas in bubble column flows by making use of a kinetic energy conservation approach applied to a simplified parallel liquid film. These considerations yield

$$t_{cont}\left(\gamma_p, D_p\right) = \left(1+\vartheta\right)\left[\frac{\left(\frac{\rho_d}{\rho_c} + C_{VM}\right)}{3\left(1+\vartheta^2\right)\left(1+\vartheta^3\right)}\frac{\rho_c D_p^3}{\sigma}\right]^{1/2}. \tag{3.14}$$

With the combination of equations (3.13) and (3.14), the formal specification of the coalescence probability is obtained as

$$\mathcal{P}_{\mathcal{C}}\left(\gamma_p, D_p\right) = \exp\left(-\frac{\left[\frac{3}{4}\left(1+\vartheta^2\right)\left(1+\vartheta^3\right)\right]^{1/2}}{\left(\frac{\rho_d}{\rho_c} + C_{VM}\right)^{1/2}\left(1+\vartheta\right)^3}\mathrm{We}^{1/2}\right), \tag{3.15}$$

where the dimensionless Weber number $\mathrm{We} = \frac{\rho_c \min(\gamma_p, D_p) u_{p,rel}}{\sigma}$.

Although several of its underlying assumptions are repeatedly commented on as questionable [105], the present configuration for bubble coalescence modeling in turbulent gas-liquid flows is well established and by far the most frequently applied. However, a definite specification of the constant $C_{\mathcal{C}}$ has not been derived so far and the selected values may vary considerably.

3.2.2 Bubble breakup modeling

In comparison to the depiction of aggregation phenomena in the PBE, which is discussed in the preceding section, modeling approaches for fluid particle fragmentation are more diverse in the determination of causal physical processes and more complex in their mathematical formulation. The latter property specifically impedes on numerical solving procedures of the PBE and will be discussed as part 4.3 of the subsequent chapter.

The physical origin of dispersed fluid particle fragmentation is characterized by an interaction between external stresses on the interface, emanating from the continuous phase dynamics and counteracting interfacial effects. The latter influence is composed of surface stress due to surface tension and viscous stresses caused by fluid motion inside the bubble or drop. Both contributions work towards restoring the fluid particle shape, while continuous phase fluid dynamics potentially induce destabilizing alterations of the phase boundary. The spectrum of respective external effects is comprised of, without limitation, laminar shear, local shearing-off phenomena and turbulent fluctuations. In consistency with the considerations on bubble coalescence, exclusively effects from continuous phase turbulence are regarded as relevant in this work. This assumption is well established and justified with respect to turbulent gas-liquid flows in bubble columns.

The source terms for fluid particle fragmentation in the monovariate PBE introduced in equation (3.4) are specified as

$$b_{\mathcal{B}}(D_p) = \int_{D_p}^{\infty} r_{\mathcal{B}}(\gamma_p, D_p) n(\gamma_p)\, \mathrm{d}\gamma_p, \tag{3.16}$$

$$d_{\mathcal{B}}(D_p) = \int_{0}^{D_p} \frac{\gamma_p^3}{D_p^3} r_{\mathcal{B}}(D_p, \gamma_p)\, \mathrm{d}\gamma_p\, n(D_p). \tag{3.17}$$

Here, the death term $d_{\mathcal{B}}$ is expressed according to the comparatively general formulation by Lehr & Mewes [125]. For information on the transformation from the original volume-specific forms to the current expressions (3.16) and (3.17), the reader is again referred to appendix A.1.

The considered breakup models are based on the conception of fluctuating turbulence eddies impinging on the bubble surface and potentially causing fluid particle fragmentation. To allow for an adequate mathematical representation of this phenomenon, this perception is limited to binary breakup processes only. Analogous to the evaluation of the coalescence kernel function, the equivalent for breakage $r_{\mathcal{B}}(D_p, \gamma_p)$ can be determined from the combination of a collision frequency $\Omega_{\mathcal{B}}$ and a breakup probability $\mathcal{P}_{\mathcal{B}}$ as

$$r_{\mathcal{B}}\left(D_p, \gamma_p\right) = \int_{\phi_{min}}^{\phi_{max}} \Omega_{\mathcal{B}}\left(D_p, \phi\right) \mathcal{P}_{\mathcal{B}}\left(D_p, \gamma_p, \phi\right) \, \mathrm{d}\phi, \tag{3.18}$$

where $\Omega_{\mathcal{B}}\left(D_p, \phi\right)$ describes the bombardment rate of the regarded fluid particle with turbulence eddies of size ϕ and $\mathcal{P}_{\mathcal{B}}\left(D_p, \gamma_p, \phi\right)$ denotes the probability of its ensuing fragmentation into daughter bubbles of size γ_p and $\left(D_p^3 - \gamma_p^3\right)^{1/3}$, maintaining gas phase volume. The definition of integration limits ϕ_{min} and ϕ_{max} varies among model approaches [176] [138] [126]. These limits define the smallest and largest eddy dimensions to be relevant in this context. The impact of smaller eddies is regarded as insufficient to cause breakage while turbulent fluctuations on a larger scale induce fluid particle motion rather than fragmentation. Equation (3.18) is frequently modified to deduce a simpler correlation which reads

$$r_{\mathcal{B}}\left(D_p, \gamma_p\right) = F_{\mathcal{B}}\left(D_p\right) \beta_{\mathcal{B}}\left(D_p, \gamma_p\right), \tag{3.19}$$

where $F_{\mathcal{B}}\left(D_p\right)$ represents the breakup frequency of bubbles with diameter D_p and $\beta_{\mathcal{B}}\left(D_p, \gamma_p\right)$ is termed daughter bubble size distribution and describes the probability a bubble of size γ_p is formed by the fragmentation of a fluid particle with diameter D_p.

Even with the limitation to turbulence induced bubble breakup, numerous different interpretations of related physical phenomena have been reported in prevalent models [128]. The respective approaches are predominantly variant in the identification of the critical condition which eventually results in fluid particle separation. Three prominent models will be introduced briefly:

Model of Luo & Svendsen [138]

According to this model, bubble breakup eventuates if the kinetic energy of impacting turbulent eddies overcomes the additional surface energy caused by fragmentation. Using an energy balance with reference to the kinetic gas theory, Luo & Svendsen derive a model function for $\mathcal{P}_{\mathcal{B}}$, while the collision frequency $\Omega_{\mathcal{B}}$ is evaluated similarly to the coalescence equivalent $\omega_{\mathcal{C}}$ with fluid particle and turbulence eddies as collision partners. For simplicity, the resulting formulation for $r_{\mathcal{B}}$ is presented with respect to bubble volumes $\left(V_p = \frac{\pi}{6} D_p^3;\ \Theta_p = \frac{\pi}{6}\gamma_p^3 = \mathrm{f}\, V_p\right)$ as

$$r_{\mathcal{B}}\left(V_p, \mathrm{f}\, V_p\right) = 0.923\,(1-\alpha)\left(\frac{\epsilon}{D_p^2}\right)^{1/3} \int_{\varsigma_{min}}^{1} \frac{(1+\varsigma)^2}{\varsigma^{11/3}} \exp(-\chi)\ \mathrm{d}\varsigma, \quad (3.20)$$

with

$$\chi = \frac{12\left[\mathrm{f}^{2/3} + \left(1-\mathrm{f}^{2/3}\right) - 1\right]\sigma}{C_{\mathcal{C}}\rho_c \epsilon^{2/3} D_p^{5/3} \varsigma^{11/3}}, \quad (3.21)$$

where $\varsigma = \frac{\phi}{D_p}$ and f denotes the volume ratio of the smaller daughter bubble and the mother bubble. Evidently, the expression for breakup frequency $F_{\mathcal{B}}$ can be deduced from (3.20) by

$$F_{\mathcal{B}}\left(V_p\right) = \int_0^{0.5} r_{\mathcal{B}}\left(V_p, \mathrm{f}\, V_p\right)\ \mathrm{df}. \quad (3.22)$$

Model of Martínez-Bazán et al. [145][146]

The basic idea of this approach is comparable to Luo & Svendsen's model, except for the definition of the critical kinetic energy of turbulence to effect bubble breakup. In this case, the external stresses are contrasted with the interfacial stress from surface tension. In other words, bubble breakage occurs if enough deformation energy is introduced to outweigh retaining effects. In contrast to alternative approaches, Martínez-Bazán does not express this correlation in terms of collision frequency and fragmentation probability, but directly deduces a formulation for the breakup frequency $F_{\mathcal{B}}$ by making use of the assumed isotropic characteristic of turbulence. This yields

$$F_{\mathcal{B}}\left(V_p\right) = C_{MB}\frac{\left[C_{\mathcal{C}}\left(\epsilon D_p\right)^{2/3} - 12\frac{\sigma}{\rho_c D_p}\right]^{1/2}}{D_p}, \tag{3.23}$$

with the model constant $C_{MB} \equiv 0.25 \pm 0.03$ for air-water systems.

Model of Lehr et al. [126]

This model is based on a balance between the inertial force of the impinging turbulence eddy and the surface force of the smaller daughter bubble. With this concept, capillary effects are also taken into account, which prohibits the separation into very small bubbles, although energy considerations would not only allow but promote a respective fragmentation. The determination of the breakup probability is deduced from the force balance, while the collision frequency is formulated equivalently to Luo & Svendsen's method. The combination of both parameters yields

$$r_{\mathcal{B}}\left(V_p, \Theta_p\right) = 1.190 \int_{\phi_{min}}^{\phi_{max}} \frac{\sigma}{\rho_c \epsilon^{1/3} \gamma_p^4} \frac{\left(D_p + \phi\right)^2}{\phi^{13/3}} \exp\left(-\frac{2\sigma}{\rho_c \epsilon^{2/3} \phi^{2/3} \gamma_p}\right) \mathrm{d}\phi. \tag{3.24}$$

A rigorous derivation of the breakup frequency F from correlation (3.24) follows expression (3.22). Yet, Lehr et al. recognize the mathematical complexity of this procedure due to the occurring integral expressions and specify an approximated analytical solution. The resulting expression is specifically favorable for the PBE solving method applied in this study and its derivation and characteristics will be presented in section 4.3.

The introduction of appendant mathematical expressions for the daughter bubble size distributions β is omitted in favor of a graphical depiction of corresponding relations via figure 3.1. Respective functional forms can be ascribed to three distinct categories, commonly termed U-shaped 3.1a, bell-shaped (or inverted U-shaped) 3.1b and M-shaped 3.1c. These graphs exhibit the fundamentally different conceptions of bubble breakup phenomena by the introduced methods and indicate the complexity of finding an adequate mathematical description of fluid particle fragmentation

processes. Following the conclusions of the latest studies on this topic, an M-shaped daughter bubble size distribution is arguably most suitable for the depiction of bubble breakup in turbulent flows [212] [128].

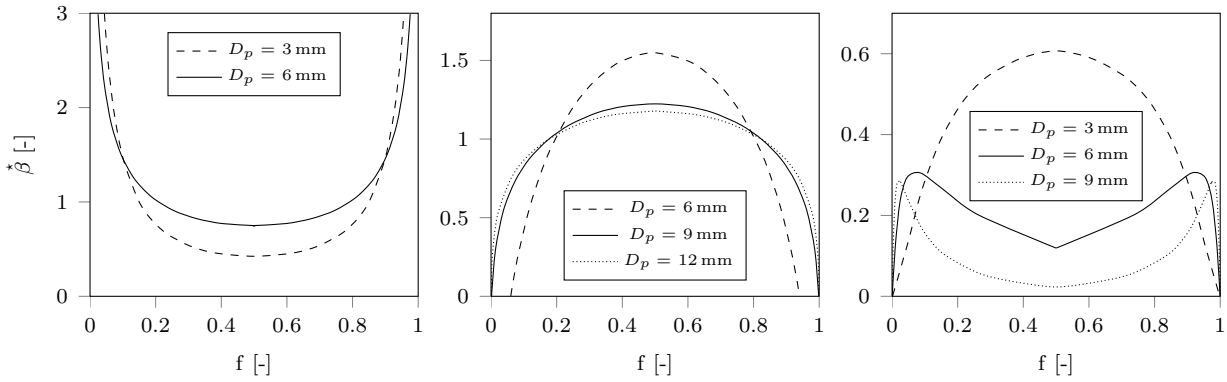

(a) Luo & Svendsen model **(b)** Martínez-Bazán et al. model **(c)** Lehr et al. model

Figure 3.1: Dimensionless daughter bubble size distributions $\overset{\star}{\beta}$ as a function of the daughter bubble to mother bubble volume ratio f for the introduced breakup models [128]

Although the fluid particle breakup model of Luo & Svendsen [138] is the most prominent approach, as it has been used in numerous published investigations (e.g., [40], [222], [209], [16]) and implemented in several commercial CFD tools (e.g., [6]), this model has been repeatedly and extensively criticized in the academic literature (e.g., [92], [212], [115]). The frequent application of this method may be explained partially by the absence of model parameters, which also applies for the approach of Lehr et al.. By contrast, two adjustable model constants are part of the formulation by Martínez-Bazán et al. with its application being bound to homogeneous isotropic turbulent flows [128]. Comparative studies of bubble breakup closures of Luo & Svendsen, and Martínez-Bazán et al. for bubble column flows do not come to a unanimous conclusion regarding model quality and applicability, which implies a rather situative validity of model concepts [41] [154].

From the discussion outlined above, it can be concluded that a comprehensive and physically sound model description of fluid particle breakup phenomena has not yet been developed. Thus, further efforts in terms of experimental and numerical investigations are required to this end [38] [5] [128]. Concerning bubble column flows, this statement is at least partially valid for bubble coalescence modeling as well. This is emphasized by

Jakobsen et al. [107] (referencing Duduković et al. [71]), who conclude to this regard: "The mechanisms of coalescence and breakage are far from being sufficiently understood yet".

3.3 Absorption

In contrast to the incorporation of bubble breakup and coalescence models, absorption processes in the gas-liquid flow are taken into account by a continuous event formulation in the PBE.[1] Regarding the monovariate diameter-based population balance considered here, the corresponding source term can be deduced form equation (3.2) as

$$\frac{\partial}{\partial D_p}\left[n\left(D_p\right)\dot{D}_p\right]. \tag{3.25}$$

The mathematical description of net mass transfer across the phase boundary of a fluid particle is formulated through an according mass balance. With reference to the species-specific expression (2.97), the balance equation reads

$$\frac{\mathrm{d}V_p}{\mathrm{d}t}\rho_d = -\sum_{\mathrm{X}} \mathcal{K}_c^{\mathrm{X}} A_p \rho_c \left(Y_{c,I}^{\mathrm{X}} - Y_c^{\mathrm{X}}\right), \tag{3.26}$$

where A_p is the fluid particle surface area. Assuming spherical particles $\left(\frac{\mathrm{d}V_p}{\mathrm{d}D_p} = \frac{A_p}{2}\right)$ yields

$$\dot{D}_p = \frac{\mathrm{d}D_p}{\mathrm{d}t} = -2\frac{\rho_c}{\rho_d}\sum_{\mathrm{X}} \mathcal{K}_c^{\mathrm{X}}\left(Y_{c,I}^{\mathrm{X}} - Y_c^{\mathrm{X}}\right). \tag{3.27}$$

Model expressions for the volumetric mass transfer coefficient $\mathcal{K}_c^{\mathrm{X}}$, particularly in association with gas-liquid flows, have been introduced previously in section 2.4.2.

[1] The complete dissolution of bubbles as a result of mass transfer, which represents a zeroth order discontinuous event, will not be approached in this work.

3.4 Population balance equation and CFD

The discretization with respect to external and internal coordinates of the continuous population balance formulation is the prerequisite for its numerical solution in association with the Euler-Euler multiphase flow model. The LES filtering procedure introduced above is applied to the spatial discretization of the present diameter-based monovariate PBE to give

$$\frac{\partial \overline{n}\left(D_p\right)}{\partial t} + \nabla \cdot \left[\overline{n}\left(D_p\right) \overline{\boldsymbol{u}}_n\left(D_p\right)\right] + \frac{\partial}{\partial D_p}\left[\overline{n}\left(D_p\right) \dot{\overline{D}}_p\right] = \overline{b}_{\mathcal{C}}\left(D_p\right) - \overline{d}_{\mathcal{C}}\left(D_p\right) + \overline{b}_{\mathcal{B}}\left(D_p\right) - \overline{d}_{\mathcal{B}}\left(D_p\right), \quad (3.28)$$

as SGS fluctuations of the NDF are commonly neglected.

A crucial aspect in the formulation of the PBE (3.28) is the definition of an adequate convection velocity $\overline{\boldsymbol{u}}_n$. In many cases, the assumption $\overline{\boldsymbol{u}}_n = \overline{\boldsymbol{u}}_d$ is made, although the convection velocity $\overline{\boldsymbol{u}}_d$ merely represents the dispersed phase volume motion in a purely two-fluid description. With this specification, the impact of convection on the PBE does not consider individual fluid particle kinetics, but is of an averaged nature. Consequently, variations in particle motion due to different internal coordinate values, specifically geometrical characteristics like size or volume, are not accounted for with this configuration. A respective model concept does not allow for the depiction of size-dependent segregation processes, for example. Being an important aspect of gas-liquid flow modeling, the consideration of local bubble velocity distributions in conjunction with the selected PBE solution approach is one of the methodical novelties of this work and is discussed in section 4.4.

The discretization of the PBE with regard to internal coordinates is explicated in the following. Therefore, an overview of available methods is given prior to a more detailed description of the quadrature method of moments, which constitutes the basis for the numerical model developed in this work. For the sake of simplicity the overbar to denote spatial averaged quantities, as well as the PBE source term for continuous processes affecting

the NDF $\left(\frac{\partial}{\partial D_p}\left[\overline{n}\left(D_p\right)\dot{\overline{D}}_p\right]\right)$ is neglected in the following subsections. This restriction to discrete events as PBE source terms allows for a simple description of discretization principles.

3.4.1 Method of classes

The arguably most natural approach to discretizing the PBE with respect to internal coordinates is the subdivision of the continuous NDF $n(\boldsymbol{\zeta})$ into numerous segments $n_i(\boldsymbol{\zeta}_i)$, corresponding to discrete intervals of $\boldsymbol{\zeta}$. An exemplary depiction of such an approximative representation of a diameter-based NDF is illustrated in figure 3.2. These subdivisions are commonly referred to as *classes* and allow a representation of the PBE as

$$\frac{\partial n_i}{\partial t} + \nabla \cdot (n_i \boldsymbol{u}_{n,i}) = b_{\mathcal{C},i} - d_{\mathcal{C},i} + b_{\mathcal{B},i} - d_{\mathcal{B},i}. \tag{3.29}$$

Since the classes are considered similarly to distinct dispersed phases with a corresponding set of Eulerian equations, the numerical effort multiplies accordingly. Regarding an NDF with respect to fluid particle size, this problem often is at least partially avoided by applying the *multiple-size group model* (MUSIG) by Lo [131]. He expresses the PBE (3.29) in mass conservative form for every particle size group and assumes a common velocity field, yielding

$$\frac{\partial \rho_d \alpha_d \varpi_i}{\partial t} + \nabla \cdot (\rho_d \alpha_d \varpi_i \boldsymbol{u}_d) = b_{\mathcal{C},\varpi,i} - d_{\mathcal{C},\varpi,i} + b_{\mathcal{B},\varpi,i} - d_{\mathcal{B},\varpi,i}. \tag{3.30}$$

Here, $\varpi_i = \frac{\alpha_{d,i}}{\alpha_d}$ denotes the dispersed phase volume fraction of fluid particles of size group n_i. The aspect of a common convection velocity is associated with the considerable model shortcomings addressed above, yet, it results in substantial reductions of computational costs. With this assumption towards particle kinetics, the application of this approach regarding gas-liquid flows is not only limited to "convection dominated bubbly flows or bubbles with small inertia", as stated by Liao [130], but also insufficient to capture the considerable influence of size depended interfacial momentum transfer.

As a further development of the original MUSIG method (later termed *homogeneous MUSIG model*) Krepper et al. [117] presented an adaption. They proposed the subsummation of several fluid particle size groups into velocity groups to define two levels of particle classification (see figure 3.2). With this approach, commonly referred to as *inhomogeneous MUSIG model*, the PBE reads

$$\frac{\partial \rho_d \alpha_{d,j} \varpi_i}{\partial t} + \nabla \cdot (\rho_d \alpha_{d,j} \varpi_i \boldsymbol{u}_{d,j}) = b_{\mathcal{C},\varpi,i} - d_{\mathcal{C},\varpi,i} + b_{\mathcal{B},\varpi,i} - d_{\mathcal{B},\varpi,i}, \tag{3.31}$$

where $\varpi_i = \frac{\alpha_{d,i}}{\alpha_{d,j}}$ and $\sum_j \alpha_{d,j} = \alpha_d$.

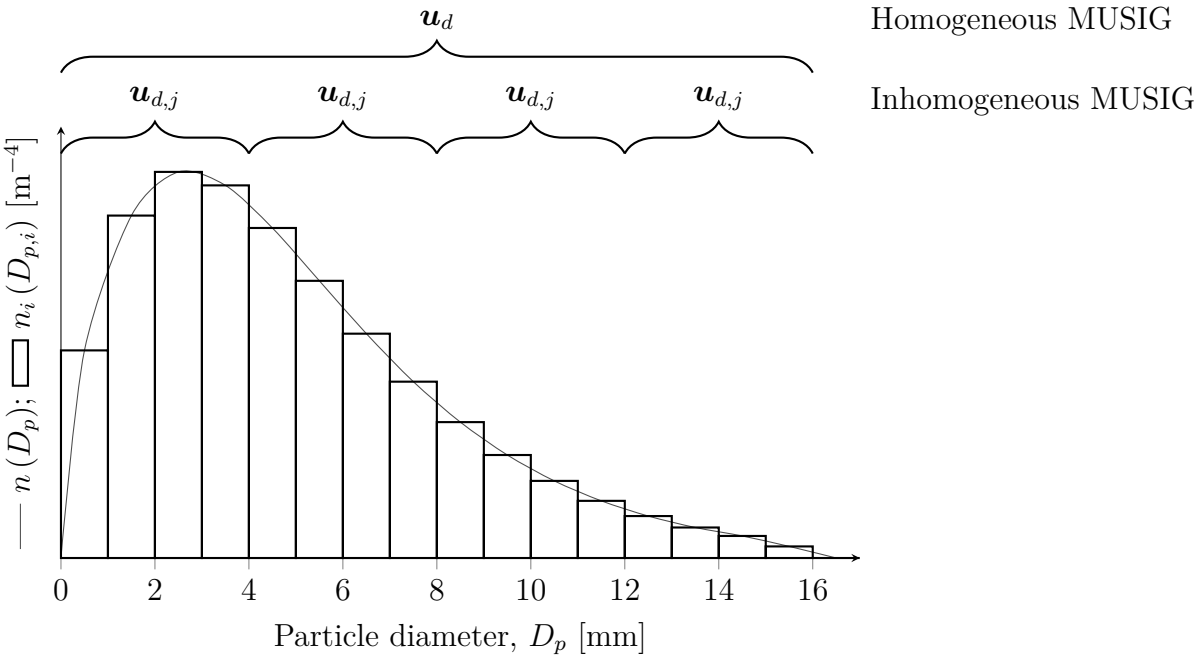

Figure 3.2: Method of classes, homogeneous and inhomogeneous MUSIG model representation of an exemplary diameter-based NDF $n\,(D_p)$

Depending on the number of velocity groups and the ratio to the number of particle size subgroups, the inhomogeneous MUSIG model compensates for the weaknesses of the prior formulation to some extent. It potentially allows for a more accurate depiction of fluid particle motion in association with an improved representation of particle interaction. Nevertheless, the advancement is strongly dependent on an appropriate classification of fluid particles and adequate closure formulations for particle interaction and

interfacial exchange. Still, all variants of classes methods are immanently accompanied by an extensive numerical effort in order to accurately depict polydisperse flows of practical interest.

The polydispersity of bubble column flows has frequently been described by approaches of the category method of classes (e.g., [30], [39], [221]). Bannari et al. [14] validated the numerical results of several classes method configurations against comparative data of experimental scale bubble column hydrodynamics. They came to the conclusion that 11 to 25 bubble size classes are necessary to give a decent representation of the dispersed gas-liquid flow. An according setup is computationally expensive and consequently hinders the analysis of bubble column flows on larger scales, even if considerable computational capabilities are available.

3.4.2 Method of moments

In view of the deficiencies of classes methods in the discretization of the particle NDF, alternative approaches have been developed in recent years. According theories abstract the PBE by using only specific characteristics of the NDF (i.e. the mathematical moments). Regarding their general definition, the multivariate NDF moments are evaluated by

$$M^{(k,l,\ldots,m)} = \int_0^\infty \ldots \int_0^\infty \int_0^\infty n\left(\boldsymbol{\zeta}\right) \zeta_1^k \zeta_2^l \ldots \zeta_i^m \,\mathrm{d}\zeta_1 \,\mathrm{d}\zeta_2 \ldots \,\mathrm{d}\zeta_i. \tag{3.32}$$

Thus, moments of the diameter-based NDF are formulated as

$$M^{(k)} = \int_0^\infty n\left(D_p\right) D_p^k \,\mathrm{d}D_p, \tag{3.33}$$

where the generic expression $M^{(k)}$ is referred to as *moment of order* k. The application of the according mathematical operation to the corresponding continuous PBE yields

$$\frac{\partial M^{(k)}}{\partial t} + \nabla \cdot \left(M^{(k)} \boldsymbol{u}^{(k)}\right) = b_{\mathcal{C}}^{(k)} - d_{\mathcal{C}}^{(k)} + b_{\mathcal{B}}^{(k)} - d_{\mathcal{B}}^{(k)}, \tag{3.34}$$

which is commonly denoted as *moment transport equation* (MTE). With the representation of the continuous NDF by a finite number of moments, some information on the exact function shape is lost, while characteristics of particular importance in an engineering context are captured by the set of moments. Equation (3.33) accompanied by the assumption of spherical particles allows for the following physical interpretation of lower order moments [35]:

- $M^{(0)}$: total number of particles (per unit volume)
- $M^{(1)}$: sum of particle diameter (per unit volume)
- $\pi M^{(2)}$: total surface area of particles (per unit volume)
- $\frac{\pi}{6} M^{(3)}$: total volume of particles (per unit volume); or the local volume fraction of the dispersed phase α_d

An analytical solution of the MTE is limited to academic cases with simplistic formulations for discontinuous processes as well as restrictions concerning initial and boundary conditions [100]. These simplified configurations do not correspond to practical problems with PBE characteristics as introduced in the preceding sections. In more realistic cases, a closure problem is inevitable and several approaches for its resolution are presented as part of this section.

To avoid the simplifying assumption of locally uniform particle motion, variant moment velocities $\boldsymbol{u}^{(k)}$ for different orders k of moments have to be considered in the MTE. Their theoretical definition for the conception of size-determined particle motion is given by

$$\boldsymbol{u}^{(k)} = \frac{\int_0^\infty \boldsymbol{u}_n(D_p) n(D_p) D_p^k \, \mathrm{d}D_p}{\int_0^\infty n(D_p) D_p^k \, \mathrm{d}D_p}, \tag{3.35}$$

which indicates that a practical evaluation is nontrivial. Explications on the relation of convection velocities of individual particles and NDF moments as well as the presentation of the approximative determination of $\boldsymbol{u}^{(k)}$ used in this study are introduced in chapter 4.4.

Another crucial point in the use of method of moments (MOM) for bubble column flows is the incorporation of accurate bubble coalescence and breakup formulations in the numerical framework without losing

computational efficiency or numerical stability. A further discussion on this aspect in conjunction with the selection and adaption of adequate formulations is outlined in section 4.3 of this thesis.

3.4.2.1 Presumed function method of moments (PMOM)

The closure problem related to the method of moments becomes manifest in the necessity to determine higher or non-normal order moments occurring in the MTE. One way of approaching this issue is the predefinition of the functional form of the NDF. In this way, the computation of a finite number of MTEs is sufficient to define the entire NDF and consequently allows for the evaluation of moments of arbitrary order. In this context, several functional forms of the NDF have been proposed, with beta- and gamma-functions being the most prominent. Regarding the latter function type, configurations with two or three parameters can be found in corresponding publications [214] [34] [35]. The NDF definition in the three-parameter variant is given by

$$n(D_p) = C_{\Gamma,1} \frac{D_2^{C_{\Gamma,3}-1} \exp\left(-\frac{D_p}{C_{\Gamma,2}}\right)}{C_{\Gamma,2}^{C_{\Gamma,3}} \Gamma(C_{\Gamma,3})}, \tag{3.36}$$

where the variables $C_{\Gamma,1}$, $C_{\Gamma,2}$ and $C_{\Gamma,3}$ are determined by three consecutive moments evaluated by respective MTEs. With this prerequisite, all NDF moments can be computed by

$$M^{(k)} = C_{\Gamma,1} \frac{\Gamma(C_{\Gamma,3}+k) C_{\Gamma,2}^k}{\Gamma(C_{\Gamma,3})}. \tag{3.37}$$

As the major disadvantage of this approach, the considered distributions need to be representable by the selected functional form. As an example, a gamma function type cannot be used to depict a multipeak NDF. This property may substantially limit potential applications, or necessitate the adjustment of NDFs to meet the function form specifications. This aspect of the PMOM, as well as further information on its formal derivation and examples of its application for gas-liquid flows, are comprehensively discussed by Carneiro [36].

3.4.2.2 Quadrature method of moments (QMOM)

In his pioneering work, McGraw [149] defined a solution to the moment closure problem that is based on a Gaussian quadrature approximation of a monovariate NDF. As a result of this procedure, the continuous distribution function subject to the internal coordinate is represented by a summation of Dirac delta functions. In this sense, the fundamental approach is comparable to the PMOM, albeit the QMOM is not limited to the depiction of distribution functions of a specific type. With the generic internal coordinate vector $\boldsymbol{\zeta}$, the representation of a multivariate NDF in a QMOM context is expressed as

$$\hat{n}\left(\boldsymbol{\zeta}\right) = \sum_{m=1}^{N_m} \dots \sum_{l=1}^{N_l} \sum_{k=1}^{N_k} w_{k,l,\dots,m}\, \delta\left(\zeta_1 - \hat{\zeta}_{1,k}\right)\, \delta\left(\zeta_2 - \hat{\zeta}_{2,l}\right) \dots\, \delta\left(\zeta_j - \hat{\zeta}_{j,m}\right), \tag{3.38}$$

where the quadrature parameters are denoted by w_i, representing the weights and $\hat{\zeta}_i$, representing the abscissas, respectively. For the monovariate, diameter-based distribution the according expression reads

$$\hat{n}\left(D_p\right) = \sum_{i=1}^{N_i} w_i\, \delta\left(D_p - \hat{D}_{p,i}\right), \tag{3.39}$$

which is exemplarily illustrated for $N_i = 3$ in figure 3.3.

The QMOM allows for an approximative evaluation of arbitrary order moments through

$$M^{(k)} = \int_0^\infty n\left(D_p\right) D_p^k \,\mathrm{d}D_p = \sum_{i=1}^{\infty} w_i \hat{D}_{p,i}^k \approx \sum_{i=1}^{N_i} w_i \hat{D}_{p,i}^k, \tag{3.40}$$

where equation (3.40) is exact in case $n\left(D_p\right)$ corresponds to a polynomial of degree $(2N_i - 1)$ or less. Otherwise, the accuracy of approximation depends on the number of quadrature parameters N_i as well as on the NDF characteristics [144] [43].

Several mathematical algorithms can be used for the determination of quadrature parameters, i.e. weights and abscissas, from the function mo-

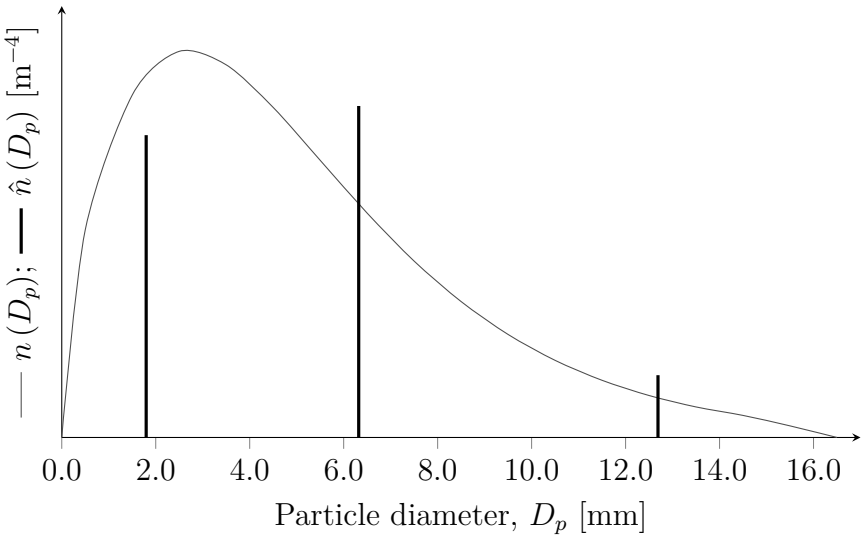

Figure 3.3: QMOM representation with three abscissas and weights of an exemplary diameter-based NDF $n\,(D_p)$

ments. These quadrature procedures are a central element of the QMOM and discussed as part of section 3.5 together with further information on QMOM characteristics, specifically regarding the model configuration considered in this work. The QMOM has frequently been applied for the representation of polydispersity in bubbly flows (e.g., [183], [169], [85]). In this context, several QMOM variants have been reported. They differ, e.g., in the number of considered moments or with respect to fluid particle interaction modeling. The configuration employed in this study is specified in the subsequent chapter.

Due to the properties of conventional quadrature procedures, the classical QMOM is restricted to the consideration of monovariate NDFs only. To this end, Yuan & Fox [226] developed an extension by introducing a conditional density function. This parameter defines a conditional relation of internal coordinates and therefore facilitates the computation of weights and abscissas for multivariate distributions. As a first step, the quadrature parameters of a primary internal coordinate are individually determined before dependencies on other coordinates are sequentially incorporated through subsequent adapted quadrature procedures. This method is generally referred to as *conditional quadrature method of moments* (CQMOM) and first applications of this theory to gas-liquid flows can be found in scientific journal publications [26] [170].

Another promising adaption of the QMOM, termed extended quadrature method of moments (EQMOM), has been reported recently [225]. This approach is based on the idea of introducing an additional parameter in the NDF representation to specify functions with finite support to approximate the distribution function, instead of resorting to Dirac delta functions. In this way, it is possible to reconstruct a smooth, non-negative NDF with an exact representation of the first $2N_i + 1$ moments [143].

3.4.2.3 Direct quadrature method of moments (DQMOM)

Given the mathematical complexity of quadrature procedures, the repeated determination of weights and abscissas from NDF moments is expensive in its computational realization and potentially compromises numerical stability. With the use of the DQMOM, this recursive evaluation is avoided by directly solving for transport equations of weights and abscissas. The consequent expressions read

$$\frac{\partial w_i}{\partial t} + \nabla \cdot (w_i \boldsymbol{u}_i) = h_{w,i}, \tag{3.41}$$

$$\frac{\partial \hat{D}_{p,i}}{\partial t} + \nabla \cdot \left(\hat{D}_{p,i} \boldsymbol{u}_i \right) = h_{\hat{D},i}, \tag{3.42}$$

where the source terms are determined by solving the following linear system of equations:

$$(1-k) \sum_{i=1}^{N_i} \hat{D}_{p,i}^{k} h_{w,i} + k \sum_{i=1}^{N_i} \hat{D}_{p,i}^{k-1} h_{\hat{D},i} = b_{\mathcal{C}}^{(k)} - d_{\mathcal{C}}^{(k)} + b_{\mathcal{B}}^{(k)} - d_{\mathcal{B}}^{(k)}. \tag{3.43}$$

In their original work, Marchisio & Fox [140] showed that this approach is applicable to both monovariate and multivariate distributions without the necessity of major adaptions. Besides the complexity of evaluating adequate source terms from equation (3.43), this method (in its original form) suffers from deficiencies regarding the conservation of NDF moments. As summarized by Buffo et al. [26], there are cases in which the DQMOM fails to correctly compute the evolution of NDF moments as a consequence

of spatial discontinuities of quadrature parameter fields and the absence of a diffusive term in equations (3.41) and (3.42). Yet, several applications of the DQMOM for the simulation of bubble column flows have been published, including the study by Selma et al. [186] who emphasized the beneficial properties of this method regarding computational costs.

As the majority of alternative quadrature-based methods of moments is related to one of the approaches presented above, their introduction will be omitted here and the reader is referred to the literature on sectional quadrature method of moments (SQMOM) [9], extended method of moments (EMOM) [75], et cetera.

The basic concepts of moments modeling in combination with an overview of approach variants were outlined in this section. As the QMOM is used as framework for the description of polydisperse bubble column hydrodynamics in this work, further explications regarding this theory in conjunction with its application to bubbly flows are given in chapter 3.5.

3.4.3 Interfacial area transport equation

As an alternative to the method of classes and moments methods with regard to the depiction of different fluid particle sizes in an Eulerian context, Kocamustafaogullari & Ishii [112] developed an approach based on the introduction of an additional conservation equation for the interfacial area. Consequently, this model is commonly referred to as *interfacial area transport equation* (IATE) or *interfacial area concentration equation* (IACE). In combination with the local dispersed phase volume fraction, the additional conserved variable allows for a very limited conception of prevailing fluid particle size conditions. In its original form, the respective theory predicts locally varying, monodisperse bubble sizes, but does not allow for a thorough conclusion on the characteristics of gas-liquid flow polydispersity. Several adaptions of this approach have been proposed to give a more detailed picture on local fluid particle sizes and shapes [95]. However, the description of bubble size dynamics in turbulent bubbly flows including fluid particle interaction is possible only to a very limited extent with this simplified approach. Nevertheless, some examples can be found

in literature in which the IATE approach was used for bubble column flow simulations (e.g., [93]).

3.5 Description of the QMOM

Based on the brief introduction of this approach in subsection 3.4.2.2, the description of the quadrature method of moments is further extended to provide a thorough depiction of this method's derivation and principles. As part of this presentation, the *product difference algorithm* is introduced, which determines the quadrature parameters from the transported moments. Subsequently, the QMOM governing equations for the characterization of continuous and discontinuous events in the PBE are deduced.

The QMOM is predicated on the Gaussian quadrature to approximate arbitrary moments of the diameter-based NDF as

$$M^{(k)} = \int_0^\infty n\left(D_p\right) D_p^k \, \mathrm{d}D_p \approx \sum_{i=1}^{N_i} w_i \hat{D}_{p,i}^k. \tag{3.44}$$

In the context of quadrature theory, the associated NDF $n(D_p)$ is regarded as weight function that has to fulfill the following requirements: positivity in the entire integration interval, existence of function moments of arbitrary order k [82]. These prerequisites are met, since all aspects are immanent characteristics of any valid NDF.

3.5.1 Quadrature procedure

As the central part of the QMOM, the quadrature procedure or inversion algorithm allows the computation of quadrature parameters from function moments. In theory, this evaluation is achieved by the solution of the following non-linear system of equations:

$$
\begin{aligned}
M^{(0)} &= \sum_{i=1}^{N_i} w_i, \\
M^{(1)} &= \sum_{i=1}^{N_i} w_i D_p, \\
&\vdots \\
M^{(2N_i-2)} &= \sum_{i=1}^{N_i} w_i D_p^{2N-2}, \\
M^{(2N_i-1)} &= \sum_{i=1}^{N_i} w_i D_p^{2N-1}.
\end{aligned}
\tag{3.45}
$$

Marchisio & Fox [143] advise against this direct procedure due to poor convergence behavior and advantageous alternatives. These are based on the consideration of orthogonal polynomials, characterized by

$$
\langle \mathrm{P}_i, \mathrm{P}_j \rangle = \int_0^\infty n(D_p) \mathrm{P}_i(D_p) \mathrm{P}_j(D_p) \, \mathrm{d}D_p \begin{cases} = 0 & \text{for } i \neq j \\ > 0 & \text{for } i = j \end{cases}. \tag{3.46}
$$

A Gaussian quadrature is defined if the roots of the orthogonal polynomials correspond to the abscissas $\hat{D}_p$ of the QMOM representation of $n(D_p)$ [61]. Assessing the leading coefficient of these orthogonal polynomials to be unity ($\mathrm{P}_i = D^i + \ldots$), they satisfy a recurrence formula as

$$
\mathrm{P}_i(D_p) = (D_p - C_{a,i}) \, \mathrm{P}_{i-1}(D_p) - C_{b,i}^2 \mathrm{P}_{i-2}(D_p) \quad \text{with} \quad i = 1, 2, \ldots \, , \tag{3.47}
$$

where the coefficients

$$
C_{a,i} = \frac{\langle D_p \mathrm{P}_{i-1}, \mathrm{P}_{i-1} \rangle}{\langle \mathrm{P}_{i-1}, \mathrm{P}_{i-1} \rangle} \quad \text{with} \quad i = 1, 2, \ldots \, , \tag{3.48}
$$

$$
C_{b,i}^2 = \frac{\langle \mathrm{P}_{i-1}, \mathrm{P}_{i-1} \rangle}{\langle \mathrm{P}_{i-2}, \mathrm{P}_{i-2} \rangle} \quad \text{with} \quad i = 2, 3, \ldots \, , \tag{3.49}
$$

and $\mathrm{P}_{-1} = 0$, $\mathrm{P}_0 = 1$, $C_{b,1} = 1$. This correlation can be expressed in matrix form:

$$\boldsymbol{C}\mathbf{p}(D_p) = D_p\mathbf{p}(D_p) + \mathbf{r}(D_p), \tag{3.50}$$

where

$$\boldsymbol{C} = \begin{pmatrix} C_{a,1} & 1 & & & \\ C_{b,2}^2 & C_{a,2} & 1 & & \\ & \ddots & \ddots & \ddots & \\ & & C_{b,N_i-1}^2 & C_{a,N_i-1} & 1 \\ & & & C_{b,N_i}^2 & C_{a,N_i} \end{pmatrix} \tag{3.51}$$

and

$$\mathbf{p}(D_p) = (\mathrm{P}_0(D_p), \ldots, \mathrm{P}_{N_i-1}(D_p))^{\mathcal{T}}, \qquad \mathbf{r}(D_p) = (0, \ldots, 0, -\mathrm{P}_{N_i}(D_p))^{\mathcal{T}}. \tag{3.52}$$

From the relation

$$\mathrm{P}_{N_i}(\hat{D}_p) = 0 \quad \Leftrightarrow \quad \boldsymbol{C}\mathbf{p}(\hat{D}_p) = \hat{D}_p\mathbf{p}(\hat{D}_p), \tag{3.53}$$

it is evident that the zeros of P_{N_i}, which represent the quadrature abscissas, coincide with the eigenvalues of $\boldsymbol{C}$. By scaling $\boldsymbol{C}$ with a diagonal matrix $\boldsymbol{D}_c = \mathrm{diag}\,(C_{c,1}, \ldots, C_{c,N_i})$ where $C_{c,1} = 1$ and $C_{c,i} = \frac{C_{c,i-1}}{C_{b,i}}$, correlation (3.53) is transformed into the symmetric eigenvalue problem $\breve{\boldsymbol{C}}\breve{\mathbf{p}} = D_p\breve{\mathbf{p}}$ with $\breve{\mathbf{p}} = \boldsymbol{D}_c\mathbf{p}$ and $\breve{\boldsymbol{C}} = \boldsymbol{D}_c\mathbf{C}\boldsymbol{D}_c^{\mathcal{T}}$ to give

$$\breve{\boldsymbol{C}} = \begin{pmatrix} C_{a,1} & C_{b,2} & & & \\ C_{b,2} & C_{a,2} & C_{b,2} & & \\ & \ddots & \ddots & \ddots & \\ & & C_{b,N_i-1} & C_{a,N_i-1} & C_{b,N_i} \\ & & & C_{b,N_i} & C_{a,N_i} \end{pmatrix}. \tag{3.54}$$

The matrix transformation restores the respective eigenvalues and allows their simple determination. A number of approaches have been published,

which allow for an efficient calculation of matrix coefficients C_a and C_b. Also applied in this work, the *product difference (PD) algorithm* constitutes the most prominent method and is outlined in appendix A.2. Yet, some researchers classified its numerical stability as suboptimal, specifically for a high number of QMOM abscissas, which has led to the promotion of alternatives [108] [143].

The evaluation of quadrature weights is defined by

$$w_i = v_{i,1}^2 M^{(0)}, \tag{3.55}$$

where $v_{i,1}$ is the first component of the normalized eigenvector of $\breve{\boldsymbol{C}}$ associated with the eigenvalue $\hat{D}_{p,i}$. A reconstruction of the underlying mathematical considerations for this relation is outlined in appendix A.3.

3.5.2 Breakup and Coalescence

As discussed in section 3.4.2, the QMOM is incorporated to overcome the closure problem associated with the application of moment methods on realistic particulate systems. The complication related to equation closure emerges from mathematically complex source term correlations. Specifically, expressions for fluid particle breakup and coalescence necessitate the application of additional model considerations such as QMOM. The transformation of corresponding source terms into a moments context prior to the formulation in terms of quadrature parameters is presented in the following, predicated on the explanations of Marchisio et al. [141].

The formulations (3.5) and (3.6), describing coalescence phenomena in the continuous, monovariate PBE, are adapted to represent MTE equivalents by

$$\begin{aligned} b_{\mathcal{C}}^{(k)} &= \int_0^\infty D_p^k b_{\mathcal{C}}(D_p)\,\mathrm{d}D_p \\ &= \frac{1}{2}\int_0^\infty n(\gamma_p)\int_0^\infty r_{\mathcal{C}}\left(\gamma_p,\breve{\gamma}_p\right)\left(\breve{\gamma}_p^3+\gamma_p^3\right)^{1/3} n\left(\breve{\gamma}_p\right)\,\mathrm{d}\breve{\gamma}_p\,\mathrm{d}D_p, \end{aligned} \tag{3.56}$$

with $\breve{\gamma}_p^3 = D_p^3 - \gamma^3$ and

$$d_{\mathcal{C}}^{(k)} = \int_0^\infty D_p^k d_{\mathcal{C}}(D_p)\,\mathrm{d}D_p = \int_0^\infty D_p^k n(D_p) \int_0^\infty r_{\mathcal{C}}(\gamma_p, D_p)\, n(\gamma_p)\,\mathrm{d}\gamma_p\,\mathrm{d}D_p. \tag{3.57}$$

The discretization of source terms $b_{\mathcal{C}}^{(k)}$ and $d_{\mathcal{C}}^{(k)}$ by the quadrature representation (3.44) yields a transformation of integral expressions to summations subject to abscissas $\hat{D}_{p,i}$ and weights w_i:

$$b_{\mathcal{C}}^{(k)} \approx \frac{1}{2} \sum_i w_i \sum_j w_j \left(\hat{D}_{p,i}^3 + \hat{D}_{p,j}^3\right)^{k/3} r_{\mathcal{C}}\left(\hat{D}_{p,i}, \hat{D}_{p,j}\right), \tag{3.58}$$

$$d_{\mathcal{C}}^{(k)} \approx \sum_i \hat{D}_{p,i}^3 w_i \sum_j w_j r_{\mathcal{C}}\left(\hat{D}_{p,i}, \hat{D}_{p,j}\right). \tag{3.59}$$

An equivalent transformation procedure is conducted for the PBE fragmentation source terms (3.16) and (3.17) where the breakup kernel function $r_{\mathcal{B}}(\gamma_p, D_p)$ is expressed by the breakup frequency $F_{\mathcal{B}}(D_p)$ and the daughter bubble size distribution $\beta_{\mathcal{B}}(D_p, \gamma_p)$ to give

$$b_{\mathcal{B}}^{(k)} = \int_0^\infty D_p^k b_{\mathcal{B}}(D_p)\,\mathrm{d}D_p = \int_0^\infty D_p^k \int_0^\infty \beta_{\mathcal{B}}(\gamma_p, D_p) F_{\mathcal{B}}(D_p) n(\gamma_p)\,\mathrm{d}\gamma_p\,\mathrm{d}D_p, \tag{3.60}$$

$$d_{\mathcal{B}}^{(k)} = \int_0^\infty D_p^k d_{\mathcal{B}}(D_p)\,\mathrm{d}D_p = \int_0^\infty D_p^{k-3} F_{\mathcal{B}}(D_p) n(D_p) \int_0^\infty \gamma_p^3 \beta_{\mathcal{B}}(D_p, \gamma_p)\,\mathrm{d}\gamma_p\,\mathrm{d}D_p. \tag{3.61}$$

The conversion in terms of a quadrature procedure yields

$$b_{\mathcal{B}}^{(k)} \approx \sum_i F_{\mathcal{B}}(\hat{D}_{p,i}) w_i \grave{B}_i, \tag{3.62}$$

with $\grave{B}_i = \int_0^{\hat{D}_{p,i}} \gamma_p^k \beta_{\mathcal{B}}(\hat{D}_{p,i}, \gamma_p)\,\mathrm{d}\gamma_p \underbrace{=}_{\text{(A.5)}} \int_0^{\hat{D}_{p,i}} \gamma_p^{k+2} \frac{\pi}{2} \beta'_{\mathcal{B}}\left(\frac{\pi}{6}\hat{D}_{p,i}^3, \frac{\pi}{6}\gamma_p^3\right)\mathrm{d}\gamma_p,$

$$d_{\mathcal{B}}^{(k)} \approx \sum_i \hat{D}_{p,i}^{k-3} F_{\mathcal{B}}(\hat{D}_{p,i}) w_i \acute{B}_i, \tag{3.63}$$

with $\acute{B}_i = \int_0^{\hat{D}_{p,i}} \gamma_p^3 \beta_{\mathcal{B}}(\hat{D}_{p,i}, \gamma_p)\, \mathrm{d}\gamma_p \underbrace{=}_{(A.5)} \int_0^{\hat{D}_{p,i}} \gamma_p^5 \frac{\pi}{2} \beta'_{\mathcal{B}} \left(\frac{\pi}{6} \hat{D}_{p,i}^3, \frac{\pi}{6} \gamma_p^3 \right) \mathrm{d}\gamma_p.$

The integral expressions in $\grave{B}_i$ and $\acute{B}_i$ cannot be evaluated by making use of QMOM properties, because they do not involve the NDF as weight function. These formulations do not correspond to the quadrature definition (3.44) and must be solved separately. For $k = 3$ the birth and death rates cancel each other out. Thus, the volumetric transport of the disperse phase is not influenced by the bubble interaction processes.

3.5.3 Absorption

Besides the source terms for discontinuous events in the PBE, absorption phenomena are accounted for in this work. In population balance theory, the resulting modifications of the NDF are classified as continuous processes and their transformation into a moments, respectively, a QMOM context is outlined in this section.

Starting point is the absorption expression for the diameter-based NDF introduced in equation (3.25). It is converted into a MTE term using the rule of integration by parts:

$$\int_0^\infty D_p^k \frac{\partial}{\partial D_p} \left[n\left(D_p\right) \dot{D}_p \right] \mathrm{d}D_p = \left[D_p^k n\left(D_p\right) \dot{D}_p \right] \Big|_{D_p=0}^{D_p=\infty} - \int_0^\infty \frac{\partial D_p^k}{\partial D_p} n\left(D_p\right) \dot{D}_p \, \mathrm{d}D_p. \quad (3.64)$$

While the first term on the right side is zero for the upper integration limit ($D_p = \infty$)[2], the consideration of $D_p = 0$ yields

$$\left[D_p^k n\left(D_p\right) \dot{D}_p \right] \Big|_{D_p=0} = \begin{cases} n\left(0\right) \dot{D}_p \big|_{D_p=0} & \text{if } k = 0 \\ 0 & \text{if } k > 0 \end{cases}. \quad (3.65)$$

For $\dot{D}_p \big|_{D_p=0} > 0$, expression (3.65) represents the nucleation rate of particles, for example, in crystallization processes. The consideration of

[2] For $D_p \to \infty$, $n\left(D_p\right)$ tends to zero faster than $D_p^k \dot{D}_p$ tends to infinity [143].

particle dissolution or droplet evaporation implicates $\dot{D}_p\big|_{D_p=0} < 0$. In these cases, the evaluation of term (3.65) is complex, as the described phenomena are a function of local particle size conditions [143] [90]. Since bubble dissolution plays an insignificant role for the gas-liquid system considered in the current study, expression (3.65) is entirely omitted here. This simplification is in line with similar investigations on bubbly flows (e.g., [26]) and allows a formulation of equation (3.64) as

$$\int_0^\infty D_p^k \frac{\partial}{\partial D_p} \left[n\left(D_p\right) \dot{D}_p \right] \, \mathrm{d}D_p = -k \int_0^\infty D_p^{k-1} n\left(D_p\right) \dot{D}_p \, \mathrm{d}D_p. \tag{3.66}$$

In case $\dot{D}_p$ is not a function of D_p, this term can be expressed as

$$k \int_0^\infty D_p^{k-1} n\left(D_p\right) \dot{D}_p \, \mathrm{d}D_p = k M^{(k-1)} \dot{D}_p \tag{3.67}$$

and does not hinder the closure of the MTE in conventional form. Otherwise, this correlation is to be expressed in terms of quadrature parameters, yielding

$$k \int_0^\infty D_p^{k-1} n\left(D_p\right) \dot{D}_p \, \mathrm{d}D_p \approx k \sum_i w_i \hat{D}_{p,i}^{k-1} \dot{D}_p(\hat{D}_{p,i}), \tag{3.68}$$

which allows for the solution in a QMOM framework. With the prefactor k in equations (3.67) and (3.68), these terms are omitted for the consideration of the zeroth moment. This implies that the number of fluid particles remains unchanged by respective correlations, which coincides with the properties of the described absorption phenomena.

4 Moments model

Based on the preceding introduction of fundamentals for the considered modeling approach, the adaptions and extensions developed in this work are presented in this chapter. To ensure the applicability of the resulting moments model for the accurate depiction of industrial bubble column flows, major modifications as well as novel approaches are incorporated. The adaptions include a numerically robust algorithm for moment conversion and correction, an adequate representation of bubble interaction phenomena and the consideration of size-specific bubble motion. In addition, a description referring to the implementation of the model in an existing CFD framework is part of this chapter.

4.1 Model framework

In this section, the mathematical basis of the present model is summarized referencing corresponding explications which were introduced in preceding chapters. The presentation of model fundamentals includes the Euler-Euler governing equations, the applied turbulence model and the considered interfacial forces. This recapitulating overview constitutes the basis for subsequently introduced model adaptions and extensions.

As a starting point, the governing equations for the numerical model are re-presented:

Mass balance equation

Equation (2.31) exhibits the volume averaged Euler-Euler mass balance equation in the considered form, which reads

$$\frac{\partial}{\partial t}\left(\alpha_k \rho_k\right) + \nabla \cdot \left(\alpha_k \rho_k \overline{\boldsymbol{u}}_k\right) = \Gamma_k. \tag{4.1}$$

Only the dispersed phase volume fraction ($k \equiv d$) is solved for since $\alpha_d + \alpha_c = 1$. The mass transfer source term Γ_d is evaluated according to equation (2.97) as

$$\Gamma_d = \sum_{\mathrm{X}} \Gamma_d^{\mathrm{X}} = -\sum_{\mathrm{X}} \mathcal{K}_c^{\mathrm{X}} a_p \rho_c \left(\mathcal{H}^{\mathrm{X}} \overline{Y}_d^{\mathrm{X}} \frac{\rho_d}{\rho_c} - \overline{Y}_c^{\mathrm{X}} \right), \tag{4.2}$$

with the volume-specific net bubble surface $a_p = \frac{6\alpha_d}{D_p}$ and the Sherwood correlation (2.100) by Glaeser [86] to determine the volumetric mass transfer coefficient $\mathcal{K}_c$ by

$$\mathrm{Sh}^{\mathrm{X}} = \frac{\mathcal{K}_c^{\mathrm{X}} D_p}{\mathcal{D}_c^{\mathrm{X}}} = 2 + 0.015\,\mathrm{Re}_p^{0.89} \left(\mathrm{Sc}_c^{\mathrm{X}}\right)^{0.7}. \tag{4.3}$$

Momentum balance equation

From equations (2.58) and (2.60), the phase generic Euler-Euler momentum conservation equation results in

$$\begin{aligned} \frac{\partial}{\partial t}\left(\alpha_k \rho_k \overline{\boldsymbol{u}}_k\right) + \nabla \cdot \left(\alpha_k \rho_k \overline{\boldsymbol{u}}_k \overline{\boldsymbol{u}}_k\right) = \\ \nabla \cdot \left[\alpha_k \mu_{k,eff} \left(\nabla \cdot \overline{\boldsymbol{u}}_k + \left(\nabla \cdot \overline{\boldsymbol{u}}_k\right)^{\mathcal{T}} - \frac{2}{3} \overline{\boldsymbol{u}}_k \boldsymbol{I} \right)\right] - \\ \alpha_k \nabla \overline{p} + \left(\alpha_k \rho_k \boldsymbol{g}\right) + \Gamma_k \overline{\boldsymbol{u}}_k + \boldsymbol{M}_{k,GD}, \end{aligned} \tag{4.4}$$

with $\mu_{c,eff} = \mu_c + \mu_{c,tur}$. The turbulent contribution is defined by an LES Smagorinsky approach, introduced in section 2.3.1, to give

$$\mu_{c,tur} = \rho_c (C_S \Delta_{tur})^2 \left|\overline{\boldsymbol{S}}_c\right|, \tag{4.5}$$

where $C_S = 0.1$. The dispersed phase effective viscosity is determined by $\mu_{d,eff} = \frac{\rho_d}{\rho_c} \mu_{c,eff}$ as proposed by Jakobsen [106] and introduced in equation (2.59).

As contributions to the generalized drag term $\boldsymbol{M}_{k,GD}$, drag, lift and virtual mass forces are taken into account in this study. Corresponding formulations are specified as follows:

Drag force

With the combination of equations (2.67), (2.68) and (2.70), the general expression for the drag force contribution on the momentum equation yields

$$\boldsymbol{M}_D = \frac{3}{4}\frac{C_D}{D_p}\rho_c\alpha_d \left|\overline{\boldsymbol{u}}_d - \overline{\boldsymbol{u}}_c\right| \left(\overline{\boldsymbol{u}}_d - \overline{\boldsymbol{u}}_c\right), \tag{4.6}$$

where the simplified Ishii-Zuber formulation (2.80) is used to determine the drag coefficient as

$$C_D = \frac{2}{3}\sqrt{\mathrm{Eo}}. \tag{4.7}$$

This arguably is the prevailing model for the description of fluid particle drag in bubble column flows (e.g., see the summary of simulation configurations by Tabib et al. [197]). It should be emphasized here that the combination of equations (4.6) and (4.7) results in a depiction of drag effects on the momentum conservation that is independent of fluid particle size. Hence, exclusively the gas volume fraction couples local dispersed phase characteristics with drag force specifics.

While the drag coefficient correlation by Ishii & Zuber, as presented in equation (4.7), as well as the resulting force on a single particle $\boldsymbol{F}_D$ is a function of fluid particle size, this dependency is compensated with the incorporation of this drag model into an Eulerian framework. The corresponding relation can be explained by the definition of the Eulerian source terms as volume-specific formulations (see section 2.4.1). Hence, the volume averaged impact of drag effects $\boldsymbol{M}_D$ does not feature a dependency on fluid particle size, although the drag force acting on an individual fluid particle is formulated subject to its diameter.

Lift force

The source term regarding lift force effects is presented in expression (2.84) and reads

$$\boldsymbol{M}_L = C_L \alpha_d \rho_c \left(\overline{\boldsymbol{u}}_d - \overline{\boldsymbol{u}}_c\right) \times \nabla \times \overline{\boldsymbol{u}}_c. \tag{4.8}$$

Two configurations for the computation of the lift force coefficient are applied here. Either a constant coefficient of $C_L = 0.5$ is assumed or alternatively the Tomiyama model, introduced in section 2.4.1.2, is incorporated to specify

$$C_L = \begin{cases} \min\left[0.228 \tanh\left(0.121 \mathrm{Re}_p\right), f\left(\mathrm{Eo}_h\right)\right] & \text{if } \mathrm{Eo}_h < 4 \\ f\left(\mathrm{Eo}_h\right) & \text{if } 4 \leq \mathrm{Eo}_h \leq 10 \\ -0.27 & \text{if } \mathrm{Eo}_h > 10 \end{cases}. \tag{4.9}$$

Virtual Mass force

The impact of virtual mass force effects on the Euler-Euler momentum balance reads

$$\boldsymbol{M}_{VM} = C_{VM} \alpha_d \rho_c \left(\frac{\mathrm{D}\overline{\boldsymbol{u}}_d}{\mathrm{D}t} - \frac{\mathrm{D}\overline{\boldsymbol{u}}_c}{\mathrm{D}t}\right), \tag{4.10}$$

as introduced in equation (2.90). For the appendant coefficient, a constant value of $C_{VM} = 0.5$ is selected as commonly specified for bubble column simulations.

Chemical species balance equation

In case absorption phenomena in the gas-liquid environment are considered, the hydrodynamic model is complemented by respective species flow fields. As chemical reactions are disregarded in the scope of this work, the conservation equation of a generic species X associated with phase k is deduced from expression (2.66) as

$$\frac{\partial}{\partial t}\left(\alpha_k \rho_k \overline{Y}_k^{\mathrm{X}}\right) + \nabla \cdot \left(\alpha_k \rho_k \overline{Y}_k^{\mathrm{X}} \overline{\boldsymbol{u}}_k\right) = \nabla \cdot \left(\alpha_k \mathcal{D}_{k,eff} \nabla \overline{Y}_k^{\mathrm{X}}\right) + \Gamma_k^{\mathrm{X}}. \tag{4.11}$$

Absorption phenomena are represented assuming that the gaseous phase constantly consists of one chemical species only. With $Y_d^{\mathrm{X}} = 1$ equation (4.11) reduces to the dispersed phase continuity equation (4.1), thus, solely the continuous phase species field is accounted for. In this context, the effective species diffusion is comprised of a molecular and a turbulent contribution ($\mathcal{D}_{c,eff}^{\mathrm{X}} = \mathcal{D}_c^{\mathrm{X}} + \mathcal{D}_{c,tur}$). In line with the LES Smagorinsky approach, $\mathcal{D}_{c,tur} = \frac{2(C_S \Delta_{tur})^2}{\mathrm{Sc}_{tur}} \left|\overline{\boldsymbol{S}}_c\right|$ with $\mathrm{Sc}_{tur} = 0.7$.

Moment transport equation

The MTE is introduced in the form of equation (3.34), which is expanded by the source term (3.66) if absorption is taken into account. In this case the MTE reads

$$\frac{\partial M^{(k)}}{\partial t} + \nabla \cdot \left(M^{(k)} \overline{\boldsymbol{u}}^{(k)}\right) - k \int_0^\infty D_p^{k-1} n\left(D_p\right) \dot{D}_p \, \mathrm{d}D_p = b_{\mathcal{C}}^{(k)} - d_{\mathcal{C}}^{(k)} + b_{\mathcal{B}}^{(k)} - d_{\mathcal{B}}^{(k)}, \tag{4.12}$$

where $\dot{D}_p$ is specified by formulation (3.27) as

$$\dot{D}_p = -2 \frac{\rho_c}{\rho_d} \sum_{\mathrm{X}} \mathcal{K}_c^{\mathrm{X}} \left(\mathcal{H}^{\mathrm{X}} \frac{\rho_d}{\rho_c} - \overline{Y}_c^{\mathrm{X}} \right). \tag{4.13}$$

The presentation of source term specifics for bubble breakup and coalescence formulations is omitted here, since a concise overview is given in section 3.5.2 and a discussion on model details follows as part 4.3 of this chapter.

4.2 Incorporation of the QMOM

4.2.1 Conversion of Euler-Euler governing equations

The combination of the QMOM with the Euler-Euler approach is specified in this section. While the formulation of MTE source terms in a QMOM context is straightforward, as outlined in passages 3.5.2 and 3.5.3, a corresponding conversion of the Euler-Euler equations for mass, momentum and species conservation requires additional considerations. Instead of the

assumption of a constant bubble diameter, the transport equation source terms are to be formulated subject to a local spectrum of bubble sizes. Formally, this can be achieved by expressing the dispersed phase volume fraction in terms of the bubble diameter NDF as

$$\alpha_d = n(D_p)\frac{\pi D_p^3}{6}\Delta D_p \tag{4.14}$$

prior to an integration of the conservation equations over the diameter spectrum (with $\Delta D_p \rightarrow \mathrm{d}D_p$)[34]. The resulting continuity equation for the dispersed phase volume fraction reads

$$\frac{\partial}{\partial t}\left(\frac{\pi}{6}M^{(3)}\rho_d\right) + \nabla\cdot\left(\frac{\pi}{6}M^{(3)}\rho_d\overline{\boldsymbol{u}}^{(3)}\right) = \\ -\int_0^\infty \mathcal{K}_c^{\mathrm{X}} n(D_p) D_p^2 \pi \rho_c \left(\mathcal{H}^{\mathrm{X}}\frac{\rho_d}{\rho_c} - \overline{Y}_c^{\mathrm{X}}\right)\mathrm{d}D_p. \tag{4.15}$$

Equation terms which initially do not feature a dependency on fluid particle size are reconverted into their original form by $\alpha_d = \frac{\pi}{6}M^{(3)}$ while a formulation in terms of NDF moments or QMOM parameters is facilitated otherwise. Although considered as bubble size dependent, the dispersed phase velocity is disregarded in the transformation procedure since its conception as a volume averaged quantity is consistent througout the equation conversion ($\overline{\boldsymbol{u}}_d = \overline{\boldsymbol{u}}^{(3)}$). With these prerequisites equation (4.15) can be expressed as

$$\frac{\partial}{\partial t}\left(\alpha_d\rho_d\right) + \nabla\cdot\left(\alpha_d\rho_d\overline{\boldsymbol{u}}_d\right) = -\int_0^\infty \mathcal{K}_c^{\mathrm{X}} n(D_p) D_p^2 \pi \rho_c \left(\mathcal{H}^{\mathrm{X}}\frac{\rho_d}{\rho_c} - \overline{Y}_c^{\mathrm{X}}\right)\mathrm{d}D_p. \tag{4.16}$$

In general, a mathematically complex dependency of the volumetric mass transfer coefficient on the bubble size ($\mathcal{K}_c^{\mathrm{X}}(D_p)$) has to be assumed, which necessitates the formulation of the mass transfer expression in terms of quadrature parameters, to give

$$\frac{\partial}{\partial t}\left(\alpha_d\rho_d\right) + \nabla\cdot\left(\alpha_d\rho_d\overline{\boldsymbol{u}}_d\right) = -\pi\rho_c\left(\mathcal{H}^{\mathrm{X}}\frac{\rho_d}{\rho_c} - \overline{Y}_c^{\mathrm{X}}\right)\sum_{i=1}^{N_i} w_i \mathcal{K}_c^{\mathrm{X}}(\hat{D}_{p,i})\hat{D}_{p,i}^2. \tag{4.17}$$

An equivalent conversion procedure is conducted for the momentum and chemical species conservation equations, which results in adapted formulations for mass and momentum transfer source terms. While the transformation of Γ_k was introduced above in equation (4.17), the generalized drag term modification yields

$$\begin{aligned}\boldsymbol{M}_{k,GD} = &\int_0^\infty \frac{3}{4}\frac{g\,|\rho_c-\rho_d|}{\sigma}\rho_c n(D_p)\frac{\pi D_p^3}{6}\,|\overline{\boldsymbol{u}}_d-\overline{\boldsymbol{u}}_c|\,(\overline{\boldsymbol{u}}_d-\overline{\boldsymbol{u}}_c)\,\mathrm{d}D_p\\ &+\int_0^\infty C_L n(D_p)\frac{\pi D_p^3}{6}\rho_c\,(\overline{\boldsymbol{u}}_d-\overline{\boldsymbol{u}}_c)\times\nabla\times\overline{\boldsymbol{u}}_c\,\mathrm{d}D_p\\ &+\int_0^\infty 0.5\,n(D_p)\frac{\pi D_p^3}{6}\rho_c\left(\frac{\mathrm{D}\overline{\boldsymbol{u}}_d}{\mathrm{D}t}-\frac{\mathrm{D}\overline{\boldsymbol{u}}_c}{\mathrm{D}t}\right)\mathrm{d}D_p.\end{aligned} \tag{4.18}$$

With the selection of the Ishii-Zuber model as correlation for the drag coefficient, the drag force source term in the Eulerian momentum equation $\boldsymbol{M}_{k,D}$ is independent of bubble size and is consequently unchanged by the equation transformation. While this characteristic also applies to the virtual mass force formulation, the lift force term potentially is altered if the Tomiyama approach (4.9) is used. Thus, the general expression subject to quadrature parameters reads

$$\boldsymbol{M}_{k,GD} = \boldsymbol{M}_{k,D}+\frac{\pi}{6}\rho_c\,(\overline{\boldsymbol{u}}_d-\overline{\boldsymbol{u}}_c)\times\nabla\times\overline{\boldsymbol{u}}_c\sum_{i=1}^{N_i}C_L(\hat{D}_p)w_i\hat{D}_p^3+\boldsymbol{M}_{k,VM}. \tag{4.19}$$

4.2.2 Disperse phase continuity equation and the MTE

In section 3.4.2 physical equivalences of NDF moments were introduced. Making use of the compatibility of the dispersed phase volume fraction and the third order moment, the associated transport equations are interchangeably linked via $\alpha = \frac{6}{\pi}M^{(3)}$. As a consequence, solely one of these conservation equations has to be solved for in the numerical model. The interrelation of both formulations is outlined in the sequel.

Since the source terms for bubble breakup and coalescence cancel each other out (see 3.5.2), the third order moment transport equation is deduced from expression (4.12) as

$$\frac{\partial M^{(3)}}{\partial t} + \nabla \cdot \left(M^{(3)} \overline{\boldsymbol{u}}^{(3)} \right) = -3 \int_0^\infty D_p^2 n\left(D_p\right) \dot{D}_p \, \mathrm{d}D_p. \tag{4.20}$$

With the incorporation of equation (4.13) and the consideration of the correspondence of $M^{(3)}$ to α_d, this correlation can be expressed by

$$\frac{\partial}{\partial t}\left(\alpha_d \rho_d\right) + \nabla \cdot \left(\alpha_d \rho_d \overline{\boldsymbol{u}}_d\right) = -\int_0^\infty \mathcal{K}_c^{\mathrm{X}} n(D_p) D_p^2 \pi \rho_c \left(\mathcal{H}^{\mathrm{X}} \frac{\rho_d}{\rho_c} - \overline{Y}_c^{\mathrm{X}} \right) \mathrm{d}D_p, \tag{4.21}$$

which is identical to formulation (4.16).

4.2.3 Invalid moments and moment correction

The spatio-temporal development of the constituent NDF moments is described individually by the corresponding transport equations (4.12). Although a set of moments is mathematically coupled as it physically represents different characteristics of the same distribution function, this relation may be altered due to the individual numerical transport of each moment. As a result, invalid combinations of moments may occur, which do not represent a physical NDF. In case QMOM functionalities are incorporated to close the system of equations, corrupted sets of moments prohibit the determination of appropriate quadrature parameters using, e.g., the PD algorithm.

Invalid moment combinations can be identified by the Hankel-Hadamard determinants, which define the following constraints for the validity of an arbitrary set of moments:

$$\begin{vmatrix} M^{(k)} & M^{(k+1)} & \cdots & M^{(k+l)} \\ M^{(k+1)} & M^{(k+1)} & \cdots & M^{(k+l+1)} \\ \vdots & \vdots & \ddots & \vdots \\ M^{(k+l)} & M^{(k+l+1)} & \cdots & M^{(k+2l)} \end{vmatrix} \geq 0, \tag{4.22}$$

where $k = 0, 1, \ldots, 2l+1$ and $l \geq 0$ [189].

It is aimed at correcting invalid sets of moments by assigning minimal changes to the individual moment values. For this purpose, McGraw [148] proposed the *minimum square gradient algorithm*, an iterative procedure based on the convexity requirement of $\ln\left(M^{(k)}\right)$ as a function of k . For the first four moments $\left(M^{(0)},\ldots,M^{(3)}\right)$ this relation equals the Hankel-Hadamard determinants for $k = 0, 1$ and $l = 1$ as

$$M^{(k)}M^{(k-2)} \geq \left(M^{(k-1)}\right)^2 . \tag{4.23}$$

In addition, this constraint is fulfilled for any physically consistent moment combination of consecutive order. However, in this general case, the convexity requirement only represents a necessary condition for moments validity, the sufficient requirement is given by expression (4.22).

McGraw's algorithm sequentially identifies and adapts specific moments to fulfill the convexity condition with minimal intrusion. By evaluating the Hankel-Hadamard determinants, additional correction steps may be initiated to eventually yield valid sets of moments. The corresponding modification procedure is briefly outlined in appendix A.4.1. For invalid NDFs which are virtually monodisperse, this procedure either fails to correct the set of moments in an acceptable number of iterations or the successful conversion is entirely prevented due to numerical inaccuracies. A mathematical reflection of this issue is outlined in appendix A.4.2.

For such cases, an alternative correction method is applied based on the approach by Wright et al. [219]. This algorithm conditions the log-normal distribution to constitute the functional form of the NDF, which is thus defined by

$$n(D_p) = C_{LN,1}\frac{\exp\left(\frac{-\ln(D_p - C_{LN,2})}{2C_{LN,3}^2}\right)}{D_p C_{LN,3}\sqrt{2\pi}}. \tag{4.24}$$

The corresponding NDF moments are evaluated from

$$M^{(k)} = C_{LN,1}\exp\left(kC_{LN,2} + \frac{k^2 C_{LN,3}^2}{2}\right), \tag{4.25}$$

where $C_{LN,1} \equiv M^{(0)}$, $C_{LN,2}$ denotes the distribution mean and $C_{LN,3}$ represents the standard deviation.

The arithmetic means of two log-normal distribution moments, determined from equation (4.25), are used to compute the corrected set of moments. In each case, the parameters $C_{LN,1}$, $C_{LN,2}$ and $C_{LN,3}$ of these log-normal functions are respectively evaluated from three low-order moments ($M^{(0)}$, $M^{(1)}$, $M^{(3)}$ and $M^{(0)}$, $M^{(2)}$, $M^{(3)}$). As $M^{(0)}$ and $M^{(3)}$ are adopted for the determination of both distribution functions, the consistency of respective variables (and their physical equivalents) is assured.

In practice, a maximum number of iterations[1] for the minimum square gradient algorithm is defined to yield a valid set of moments. If a physically consistent combination is not reached within this limit, the respective moments are evaluated by the log-normal approach. Since the affected distributions, i.e. virtually monodisperse NDFs, can be described very accurately by log-normal functions, this method proved to be both efficient and exact throughout the simulations. An analysis of moment modifications due to this hybrid correction procedure is presented in section 5.2 together with other simulation results. A depiction of the entire moment correction procedure is illustrated in the form of a flowchart in figure 4.1. A similar setup of the two introduced correction methods was successfully used for an alternative application by Petitti et al. [169].

Besides the discussed moment correction procedure, the introduction of minimum moment values necessitates the conditional modification of moment combinations. To prevent the occurrence of non-positive moment values, which would impede the determination of quadrature parameters and ultimately lead to instabilities in the numerical processing, a lower limit for moment values is defined. It is specified by a minimum local gas volume fraction of $\alpha_{d,min} = 10^{-5}$, which proved to be insignificant for mass conservativity relations yet sufficient to ensure numerical stability. In case this limit is undercut, the respective local dispersed phase fraction is reset to $\alpha_{d,min}$ with the NDF specifications at the gas inlet. This bounding procedure was tested extensively and the current configuration does not yield a noticeable alteration of numerical results.

[1] Although McGraw [148] reports that one or two passes through the algorithm should arguably be sufficient to correct regular distributions, a limiting number of 10 to 15 iterations proved to be both accurate and numerically efficient.

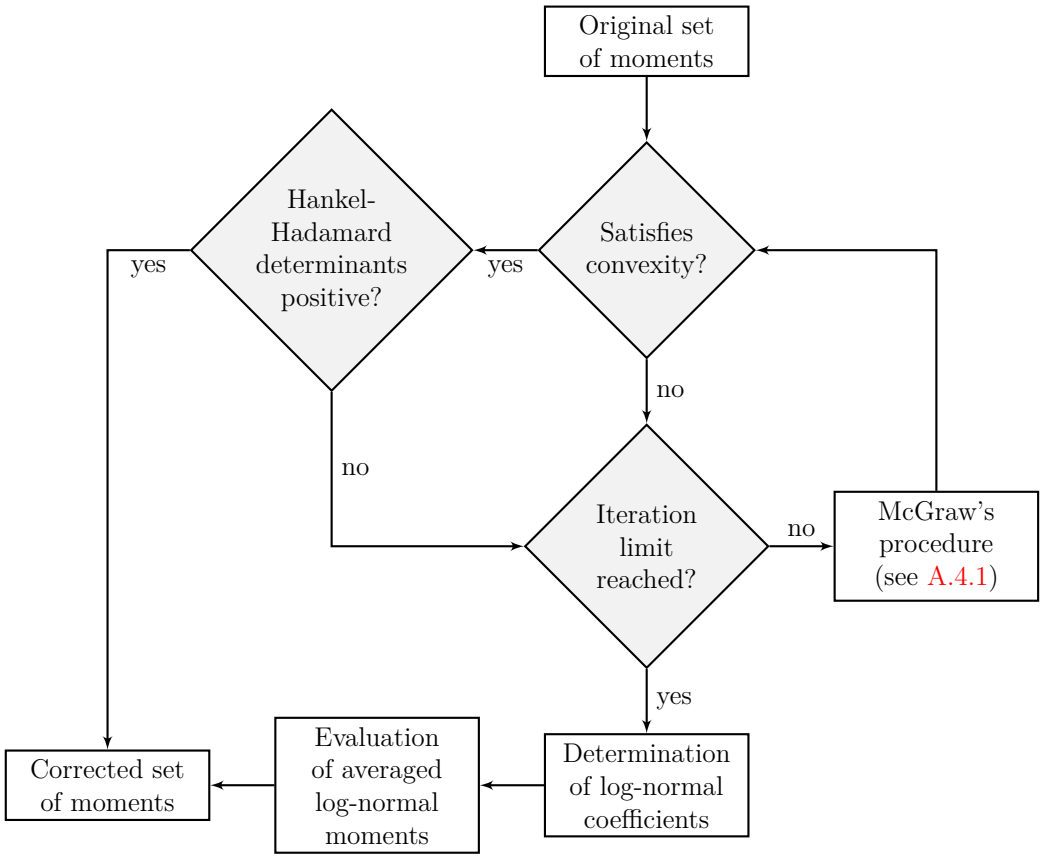

Figure 4.1: Flowchart of the incorporated procedure for correcting invalid sets of moments

4.3 Depiction of bubble breakup and coalescence

With the incorporation of conventional bubble breakup and coalescence formulations, which are presented in section 3.2, into the QMOM framework several aspects have to be taken into account. Besides the accurate description of population balance modifications, adequate for the regarded two-phase flow conditions, efficiency in the numerical realization of the approach is to be assured. The latter criterion can be satisfied by the selection of appropriate model formulations and their according adoption, in spite of the mathematical complexity of common breakup and coalescence theories. To this end, a combination of methods is implemented in the current numerical model to obtain an efficient numerical evaluation without jeopardizing accuracy in the depiction of the respective phenomena. This setup represents a novelty in the context of a QMOM and was introduced first in Acher et al. [1].

The QMOM expressions for fluid particle aggregation (3.58) and (3.59) indicate that model formulations for the bubble coalescence rate $r_{\mathcal{C}}$ can be directly incorporated without implicating additional complexities in the numerical calculation. Instead of the diameters of interacting fluid particles, the quadrature abscissas constitute the input variables for the evaluation of these parameters. With the coalescence kernel function $r_{\mathcal{C}}$ being determined by the product of the collision frequency $\omega_{\mathcal{C}}$ and the coalescence probability $\mathcal{P}_{\mathcal{C}}$ from expression (3.11) and (3.15), the respective QMOM source terms applied in the current model are obtained as

$$b_{\mathcal{C}}^{(k)} = \frac{\pi}{8} C_{\mathcal{C}}^{1/2} \epsilon_c^{1/3} \sum_i w_i \sum_j w_j \left(\hat{D}_{p,i}^3 + \hat{D}_{p,j}^3\right)^{k/3} \left(\hat{D}_{p,i} + \hat{D}_{p,j}\right)^2 \left(\hat{D}_{p,i}^{2/3} + \hat{D}_{p,j}^{2/3}\right)^{1/2} \times \exp\left(-\frac{\left[\frac{3}{4}\left(1+\vartheta^2\right)\left(1+\vartheta^3\right)\right]^{1/2}}{\left(\frac{\rho_d}{\rho_c} + C_{VM}\right)^{1/2}\left(1+\vartheta\right)^3} \mathrm{We}^{1/2}\right), \quad (4.26)$$

$$d_{\mathcal{C}}^{(k)} = \frac{\pi}{4} C_{\mathcal{C}}^{1/2} \epsilon_c^{1/3} \sum_i \hat{D}_{p,i}^3 w_i \sum_j w_j \left(\hat{D}_{p,i} + \hat{D}_{p,j}\right)^2 \left(\hat{D}_{p,i}^{2/3} + \hat{D}_{p,j}^{2/3}\right)^{1/2} \times \exp\left(-\frac{\left[\frac{3}{4}\left(1+\vartheta^2\right)\left(1+\vartheta^3\right)\right]^{1/2}}{\left(\frac{\rho_d}{\rho_c} + C_{VM}\right)^{1/2}\left(1+\vartheta\right)^3} \mathrm{We}^{1/2}\right), \quad (4.27)$$

with $\vartheta = \frac{\min\left(\hat{D}_{p,i}, \hat{D}_{p,j}\right)}{\max\left(\hat{D}_{p,i}, \hat{D}_{p,j}\right)}$ and $\mathrm{We} = \frac{\rho_c \min\left(\hat{D}_{p,i}, \hat{D}_{p,j}\right) u_{p,rel}}{\sigma}$.

Regarding the depiction of bubble breakup phenomena in a QMOM framework, the incorporation of a conventional model formulation is considerably more complex. As depicted in the delineation of QMOM fragmentation source terms (3.62) and (3.63), an additional integration operation is required to evaluate the parameters $\acute{B}_i$ and $\grave{B}_i$. Respective correlations cannot be simplified by an expression in terms of quadrature parameters and consequently represent a potential drawback to numerical efficiency. This is specifically relevant if the daughter bubble size distribution $\beta_{\mathcal{B}}$ in the integrand features an integral expression as well.

In section 3.2.2 three conventional approaches for the description of fluid particle fragmentation phenomena were introduced in their general for-

mulation for a continuous NDF. The model of Martínez-Bazán et al. is not considered further in this work due to the mentioned assumption regarding turbulence isotropy and the dependency on additional model parameters. Concerning the application of a population balance theory for the description of polydisperse bubbly flows, the model of Luo & Svendsen arguably represents the most prominent breakup formulation. In this method, the daughter bubble size distribution is deduced from the breakup kernel function $r_{\mathcal{B}}$, defined in equation (3.20), as

$$\beta_{\mathcal{B}}\left(V_p, \mathrm{f}\, V_p\right) = \frac{r_{\mathcal{B}}\left(V_p, \mathrm{f}\, V_p\right)}{F_{\mathcal{B}}\left(V_p\right)} = \frac{\displaystyle\int_{\varsigma_{min}}^{1} \frac{\left(1+\varsigma\right)^2}{\varsigma^{11/3}} \exp(-\chi)\, \mathrm{d}\varsigma}{\displaystyle\int_0^{0.5} \int_{\varsigma_{min}}^{1} \frac{\left(1+\varsigma\right)^2}{\varsigma^{11/3}} \exp(-\chi)\, \mathrm{d}\varsigma\, \mathrm{df}}. \tag{4.28}$$

While the accurate numerical evaluation of equation (4.28) itself is challenging, a respective incorporation into the QMOM framework via the expressions (3.62) and (3.63) necessitates a numerical realization which is computationally expensive and rather unstable. Even if advanced methods are used to evaluate the multidimensional integral expressions, associated with high computational costs, major inaccuracies may potentially occur due to critical function extrema at the integration domain boundaries. As this bubble breakup formulation evidently is unsuitable for the application in a QMOM context, the model of Lehr et al. is implemented in this work. While the mathematical structure of the original correlations is similar to the model of Luo & Svendsen (see equation (3.24)), Lehr et al. [126] provide an approximation based on the definition of following dimensionless coefficients for length $\overset{\star}{l}$ and time $\overset{\star}{t}$:

$$\overset{\star}{l} = \left(\frac{\sigma}{\rho_c}\right)^{3/5} \frac{1}{\epsilon_c^{2/5}}; \qquad \overset{\star}{t} = \left(\frac{\sigma}{\rho_c}\right)^{2/5} \frac{1}{\epsilon_c^{3/5}}. \tag{4.29}$$

With these prerequisites, the equation variables are expressed in dimensionless form ($\overset{\star}{D}_p = D_p/\overset{\star}{l}$, $\overset{\star}{\gamma}_p = \gamma_p/\overset{\star}{l}$,$\overset{\star}{V}_p = V_p/\overset{\star}{l}^3$, $\overset{\star}{\Theta}_p = \Theta_p/\overset{\star}{l}^3$, $\overset{\star}{F}_{\mathcal{B}} = F_{\mathcal{B}}\overset{\star}{t}$, $\overset{\star}{\beta} = \beta\overset{\star}{l}^3$), which allows for a mathematically simple formulation of approximated model correlations as

$$F_{\mathcal{B}}(D_p) = \frac{\overset{\star}{F}_{\mathcal{B}}(\overset{\star}{D}_p)}{\overset{\star}{t}} = \frac{1}{\overset{\star}{t}}\left[\frac{1}{2}\overset{\star}{D}_p^{5/3}\exp\left(-\frac{\sqrt{2}}{\overset{\star}{D}_p^3}\right)\right] \tag{4.30}$$

for the breakup frequency and

$$\beta'_{\mathcal{B}}(V_p,\Theta_p) = \frac{\overset{\star}{\beta}'_{\mathcal{B}}\left(\overset{\star}{V}_p,\overset{\star}{\Theta}_p\right)}{\overset{\star}{l}^3} = \frac{1}{\overset{\star}{l}^3}\left[\frac{6}{\pi^{3/2}\overset{\star}{\gamma}_p^3}\frac{\exp\left(-\frac{9}{4}\left[\ln\left(2^{2/5}\overset{\star}{\gamma}_p\right)\right]^2\right)}{\left(1+\operatorname{erf}\left[\frac{3}{2}\ln\left(2^{1/15}\overset{\star}{D}_p\right)\right]\right)}\right] \tag{4.31}$$

describing the daughter bubble size distribution as piecewise defined function, where

$$\begin{aligned} \beta'_{\mathcal{B}}(V_p,\Theta_p) &\quad \text{for} \quad 0 \le \Theta_p \le V_p/2 \\ \beta'_{\mathcal{B}}(V_p,\Theta_p) = \beta'_{\mathcal{B}}(V_p,V_p-\Theta_p) &\quad \text{for} \quad V_p/2 \le \Theta_p \le V_p \end{aligned}. \tag{4.32}$$

In contrast to the aforementioned Luo & Svendson approach, the incorporation of the simplified equations (4.30) and (4.31) into the QMOM formulations (3.62) and (3.63) reduces the mathematical complexity to a one-dimensional integral expression for each source term. With respect to the quadrature parameters, the corresponding correlation for $\grave{B}_i$ reads

$$\begin{aligned} \grave{B}_i = &\int_0^{\sqrt[3]{\frac{\hat{D}_{p,i}^3}{2}}} \gamma_p^{k-1}\frac{3}{\pi^{1/2}}\frac{\exp\left(-\frac{9}{4}\left[\ln\left(\frac{2^{2/5}}{\overset{\star}{l}}\gamma_p\right)\right]^2\right)}{\left(1+\operatorname{erf}\left[\frac{3}{2}\ln\left(\frac{2^{1/15}}{\overset{\star}{l}}\hat{D}_{p,i}\right)\right]\right)}\,\mathrm{d}\gamma_p \\ &+\int_{\sqrt[3]{\frac{\hat{D}_{p,i}^3}{2}}}^{\hat{D}_{p,i}}\frac{\gamma_p^{k+2}}{\hat{D}_{p,i}^3-\gamma_p^3}\frac{3}{\pi^{1/2}}\frac{\exp\left(-\frac{9}{4}\left[\ln\left(\frac{2^{2/5}}{\overset{\star}{l}}\left(\hat{D}_{p,i}^3-\gamma_p^3\right)^{1/3}\right)\right]^2\right)}{\left(1+\operatorname{erf}\left[\frac{3}{2}\ln\left(\frac{2^{1/15}}{\overset{\star}{l}}\hat{D}_{p,i}\right)\right]\right)}\,\mathrm{d}\gamma_p. \end{aligned} \tag{4.33}$$

For the first summand on the right hand side an antiderivative can be formulated as

$$\grave{\underset{\sim}{B}}_i(\gamma_p) = \int \gamma_p^{k-1} \underset{\sim}{C}_1 \exp\left(-\frac{9}{4}\left[\ln\left(\underset{\sim}{C}_2\gamma_p\right)\right]^2\right) \mathrm{d}\gamma_p$$
$$= \frac{\underset{\sim}{C}_1 \exp\left(\frac{k^2}{9}\right)\sqrt{2}\,\mathrm{erf}\left(\frac{-2\,k+9\ln(\underset{\sim}{C}_2\,\gamma_p)}{6}\right)}{3\,\underset{\sim}{C}_2^k} + \text{const}, \quad (4.34)$$

with $\underset{\sim}{C}_1 = \frac{3}{\pi^{1/2}} \frac{1}{\left(1+\mathrm{erf}\left[\frac{3}{2}\ln\left(\frac{2^{1/15}}{\overset{\star}{l}}\hat{D}_{p,i}\right)\right]\right)}$ and $\underset{\sim}{C}_2 = \frac{2^{2/5}}{\overset{\star}{l}}$ to eventually result in

$$\grave{B}_i = \grave{\underset{\sim}{B}}_i\left(\left(\frac{1}{2}\hat{D}_{p,i}^3\right)^{1/3}\right) - \grave{\underset{\sim}{B}}_i(0)$$
$$+ \int_{\sqrt[3]{\frac{\hat{D}_{p,i}^3}{2}}}^{\hat{D}_{p,i}} \frac{\gamma_p^{k+2}}{\hat{D}_{p,i}^3 - \gamma_p^3} \frac{3}{\pi^{1/2}} \underset{\sim}{C}_1 \exp\left(-\frac{9}{4}\left[\ln\left(\frac{2^{2/5}}{\overset{\star}{l}}\underset{\sim}{C}_2\left(\hat{D}_{p,i}^3 - \gamma_p^3\right)^{1/3}\right)\right]^2\right) \mathrm{d}\gamma_p. \quad (4.35)$$

Since the formulation for $\acute{B}_i$ represents a special case of $\grave{B}_i$ for $k = 3$ an individual presentation is omitted here.

With the exception of $\grave{B}_i$ and $\acute{B}_i$ all terms of the current QMOM breakup and coalescence configuration are expressed as algebraic formulations dependent on flow properties and the quadrature parameters only. This setup proved to be both exact in the computation of complex model correlations and computationally efficient in the associated numerical realization.

4.4 Relaxation time approach

An important and challenging aspect in the modeling of polydisperse flows with moment methods is the consideration of the size-dependency of particle motion through appropriate evaluation of moment velocities. In the most general *polykinetic* case, velocities of individual particles within one control volume may differ from each other, even if they are equal in size. This local particle velocity spectrum is represented in certain moment methods by incorporating the particle velocity components as internal variables in the moment setup (e.g., [226], [80]).

In the present work, a more restrictive situation is considered: this concept allows for size-specific particle motion, assuming that particles of identical size also have locally identical velocities. This perception is commonly referred to as *polycelerity*. Although not fully general, important effects like segregation due to size-dependent inter-phase momentum exchange can be captured in the MOM context through non-identical moment transport velocities without an extensive modification of the moment method. In line with this concept, Carneiro et al. [35] presented a model using the size-dependency of particle relaxation times to deduce corresponding constituent moment velocities. While this approach was incorporated into a PMOM setup, its application in a QMOM framework is outlined in Acher et al. [1] and is presented in detail in this thesis.

Regarding the numerical description of polydisperse gas-liquid flows with moment methods, it has been a common approach to assume all moment velocities to be identical to the Eulerian dispersed phase velocity (e.g., [169], [183]):

$$\boldsymbol{u}^{(k)} = \boldsymbol{u}_d. \tag{4.36}$$

As an alternative to this simplification, a more extensive model is applied and analyzed in the scope of this work. The theoretical definition of moment transport velocities for the assumption of a purely size-dependent spectrum of the local fluid particle velocities, i.e. polycelerity, is introduced in equation (3.35) and re-presented here for convenience:

$$\boldsymbol{u}^{(k)} = \frac{1}{M^{(k)}} \int_0^\infty \boldsymbol{u}_n(D_p) n(D_p) D_p^k \, \mathrm{d}D_p. \tag{4.37}$$

The current approach for the determination of constituent moment transport velocities is based on the ideas of the *equilibrium Eulerian method* by Ferry & Balachandar [76] [77]. With this alternative to the classical Eulerian concept, the particle velocity is formulated in terms of a first order expansion around the continuous phase velocity subject to its relaxation time.

Unlike the previous description of particle dynamics in an Eulerian context, the depiction within a Lagrangian framework constitutes the starting

point for the formal deduction of the current evaluation procedure of individual moment velocities. While Maxey & Riley [147] present an equation of individual particle motion including the consideration of various interfacial momentum exchange terms, the limitation of this concept to the representation of drag relations yields

$$\frac{\mathrm{d}\boldsymbol{u}_p}{\mathrm{d}t} = \tau\left(\boldsymbol{u}_c - \boldsymbol{u}_p\right), \tag{4.38}$$

where the particle relaxation time τ characterizes the response time scale of dispersed particle motion to an adaption of the surrounding continuous flow field. Deduced from these considerations, a formal expansion of the particle velocity $\boldsymbol{u}_p$ around an arbitrary velocity $\mathring{\boldsymbol{u}}$, corresponding to a relaxation time $\mathring{\tau}$, reads

$$\boldsymbol{u}_p = \mathring{\boldsymbol{u}} + \left(\tau - \mathring{\tau}\right) \left.\frac{\mathrm{d}\boldsymbol{u}_p}{\mathrm{d}\tau}\right|_{\mathring{\tau}} + \mathcal{O}\left(\tau^2\right). \tag{4.39}$$

The simplification to a first order expression with $\mathring{\tau} = 0$ yields

$$\boldsymbol{u}_p = \boldsymbol{u}_c + \tau \left.\frac{\mathrm{d}\boldsymbol{u}_p}{\mathrm{d}\tau}\right|_{\mathring{\tau}=0}, \tag{4.40}$$

with $\mathring{\boldsymbol{u}}|_{\mathring{\tau}=0} = \boldsymbol{u}_c$. Introducing a reference relaxation time τ_0 with the associated velocity $\boldsymbol{u}_0$, the derivative $\left.\frac{\mathrm{d}\boldsymbol{u}_p}{\mathrm{d}\tau}\right|_{\mathring{\tau}=0}$ can be evaluated by

$$\left.\frac{\mathrm{d}\boldsymbol{u}_p}{\mathrm{d}\tau}\right|_{\mathring{\tau}=0} = \frac{\boldsymbol{u}_0 - \boldsymbol{u}_c}{\tau_0}, \tag{4.41}$$

where τ_0 has to be sufficiently small to assure validity of this linear approximation. To transform this approach into the moment context, the respective integration procedure (4.37) is applied to the preceding expressions to give

$$\frac{1}{M^{(k)}} \int_0^\infty \boldsymbol{u}_n(D_p) n(D_p) D_p^k \,\mathrm{d}D_p = \boldsymbol{u}^{(k)} \approx \boldsymbol{u}_c + \frac{\tau^{(k)}}{\tau_0}\left(\boldsymbol{u}_0 - \boldsymbol{u}_c\right). \tag{4.42}$$

This formulation corresponds to an evaluation of the moment transport velocity $\boldsymbol{u}^{(k)}$ by a linear interpolation between the continuous phase velocity $\boldsymbol{u}_c$ and the reference velocity $\boldsymbol{u}_0$ (see figure 4.2). In line with the findings of Bollweg et al. [20], the current method is exclusively used for an interpolative evaluation, not for the extrapolation beyond $\boldsymbol{u}_0$.

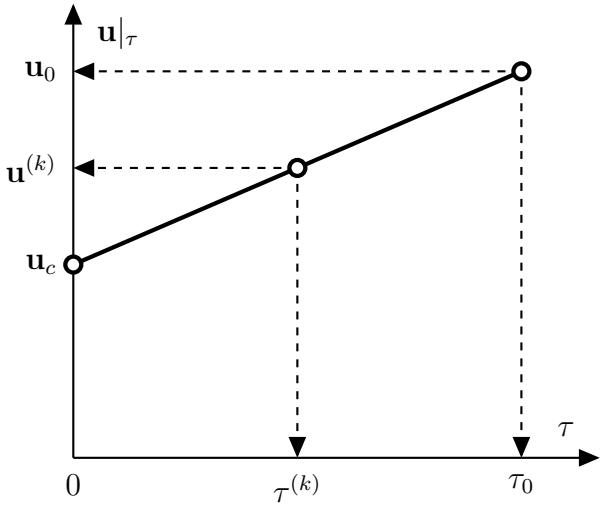

Figure 4.2: Schematic representation of the relaxation time approach: linear interpolation between the continuous phase velocity $\boldsymbol{u}_c$ and the reference velocity $\boldsymbol{u}_0$ to determine moment velocities $\mathbf{u}^{(k)}$ [35]

Since the third moment is transported similarly to the volume-averaged dispersed phase ($\boldsymbol{u}^{(3)} = \boldsymbol{u}_d$), $\boldsymbol{u}_d$ is selected as reference velocity and can be determined from the dispersed phase momentum equation (4.4). Hence, an according adaption of equation (4.42) yields

$$\boldsymbol{u}^{(k)} \approx \boldsymbol{u}_c + \frac{\tau^{(k)}}{\tau^{(3)}} \left(\boldsymbol{u}_d - \boldsymbol{u}_c \right). \tag{4.43}$$

Equation (4.43) constitutes the final form of the relaxation time approach which is hereof referred to as RTA, while the simplified model with identical moment velocities (see equation (4.36)) is denoted by IMV.

Analogous to the previous applications of this concept in a PMOM framework (e.g., [35], [60]), the formulation for Stokes flow is applied to determine the particle relaxation times as

$$\tau = \frac{\rho_d D_p^2}{18 \mu_c}. \tag{4.44}$$

The transformation to the moment context consequently yields

$$\tau^{(k)} = \frac{\rho_d}{18\mu_c} \frac{M^{(k+2)}}{M^{(k)}}. \tag{4.45}$$

The Stokes drag correlation allows for a numerically stable and efficient computation of moment velocities, but the application of this formulation for bubble column hydrodynamics is suboptimal. An adaption of the RTA based on the Schiller-Naumann correlation, as outlined in appendix A.5, does not improve the depiction of distorted bubble drag relations and is accompanied by numerical instabilities. The incorporation of a more adequate drag correlation is desired for future work. In contrast to the volume specific representation of the dispersed phase drag relations in the Euler-Euler framework, the considered relaxation times are determined from individual particle kinetics. Therefore, the incorporation of different drag models for the RTA and Euler-Euler formulations is well justified.

The fundamental ideas of the RTA can be used to extend the respective concept in order to simultaneously account for alternative interfacial forces. A potential approach which concurrently describes the effects of size-dependent drag and lift force correlations on the bubble size NDF is sketched in appendix A.6.

4.5 Implementation in *OpenFOAM*

Built in a `C++` environment, *OpenFOAM* constitutes an open-source code library which is specifically useful to solve for scalar or vector variable transport equations in a two or three-dimensional context. Hence, *OpenFOAM* can be used as a modular program package for various CFD problems and is an optimal software tool to extend or adapt predeveloped CFD solvers for specific applications. Carneiro et al. [33] used the Euler-Euler finite volume solver *twoPhaseEulerFoam* as a basis for the implementation of PMOM functionalities, which were further extended by Dems et al. [60]. The fundamental implementation principles of the *OpenFOAM* Euler-Euler solver remain unchanged in the course of these modifications and can be found in the comprehensive discussion by Rusche [181].

By adopting and extending the existing code, the QMOM framework with the described moments conversion and correction algorithms is established on top of the Euler-Euler base structure of the numerical model. The sequential solving procedure for the present approach is depicted in the form of a flow chart in figure 4.3. To allow for an efficient solution of the QMOM procedure, corresponding sections of the solver are summarized in a separate code class, which is called from the standard Euler-Euler environment. As part of this structure, the fluid particle breakup and coalescence functionalities are established as a distinct code module, which can be added as an option. Likewise, the RTA implementation allows for an optional activation of this feature, while the MTE configuration resorts to an IMV setup otherwise.

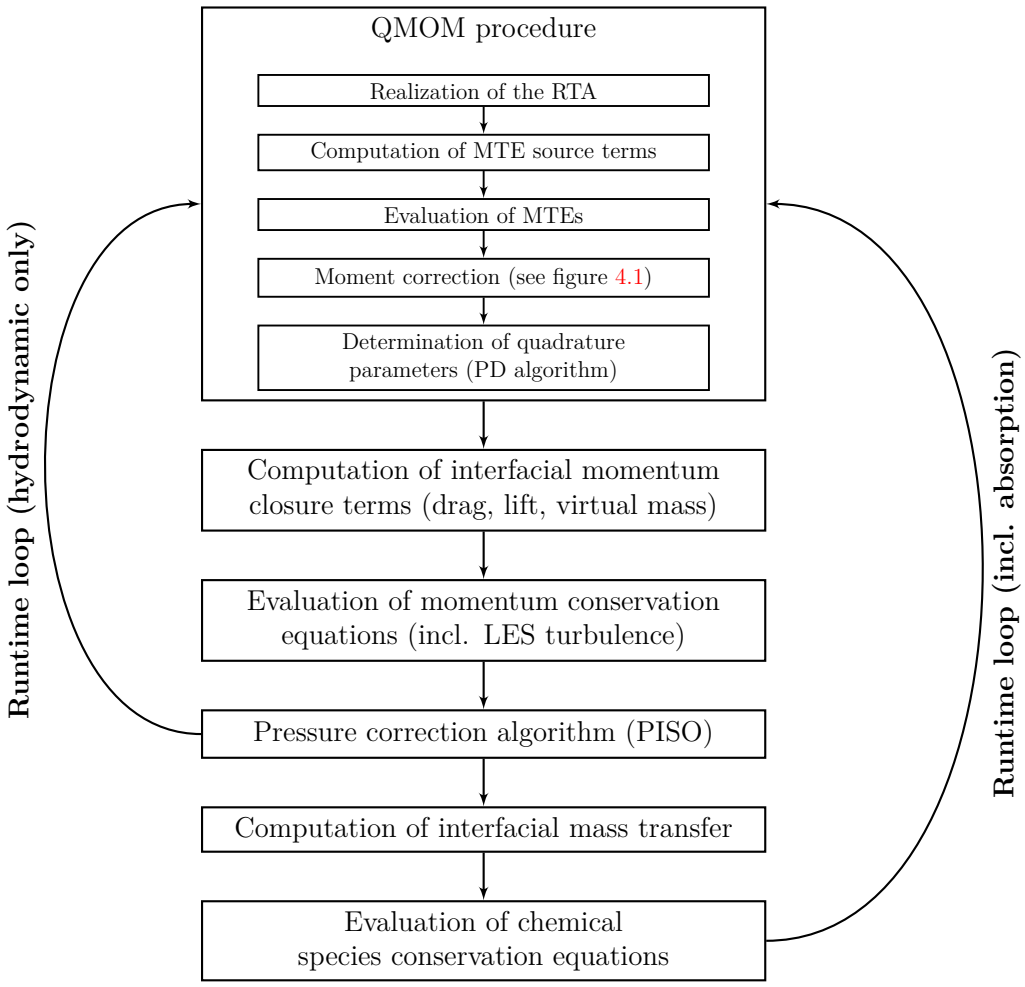

Figure 4.3: Sequential solution procedure for the current Euler-Euler moments model

Although the MTE source terms representing discontinuous events, i.e. bubble coalescence and breakup, are deduced to yield comparably simple mathematical correlations, one-dimensional integral expressions have to be evaluated in order to compute respective formulations (see section 4.3). To accurately and efficiently determine these correlations through an adaptive integration procedure, corresponding libraries of the *GNU Scientific Library* (GSL) are incorporated in the *OpenFOAM* environment and utilized as part of the code structure for breakup and coalescence formulations.

As indicated in the solution procedure illustration in figure 4.3, two solver variants have been developed. While the incorporation of chemical species balance equations in conjunction with corresponding source term correlations is omitted for exclusively hydrodynamic studies, respective formulations are included in case absorption phenomena are analyzed as well. Although the code complexity is substantially increased in the latter case, the addition in terms of computational time is inconsiderable as even complex transport equations are solved efficiently by the *OpenFOAM* algorithms.

As the main implementation strategy for code modifications and extensions conducted in the scope of this work, the incorporation of model functionalities is established on the premise of using as much of the *OpenFOAM* classes, functions and coding structure as possible. A key element in this effort represents the frequent application of indicator fields. These auxiliary scalar fields, with entries being either zero or one, allow for a locally conditional execution of algorithms by simple algebraic field operations, which are provided by the standard *OpenFOAM* code package.

5 Model validation and simulation results

5.1 Validation of the hydrodynamic model

The simulation results of the present model with regard to bubble column hydrodynamics are compared against experimental and numerical findings in this segment. Two test case configurations are considered. In subsection 5.1.1, a validation case with an experimental scale bubble column geometry of square cross-section is introduced prior to the presentation and analysis of simulation results. This investigation is complemented by the validation of the numerical model against experimental findings from a bubble column configuration with a circular cross-section. The respective results are discussed in part 5.1.2 of this chapter.

The experimental analysis of local bubble size distributions in bubble column flows necessitates the application of advanced measurement techniques. Due to the limited penetration depth of optical measurement methods, one often resorts to quasi two-dimensional bubble column geometries for according studies. The gas-liquid flow dynamics in a corresponding experimental setup varies substantially from the situation in industrial scale apparatuses. The boundaries, located closely together, hinder the development of radial, meandering or spiral motions of the gas-liquid flow. Sources for detailed experimental data on bubble size distributions in a genuine three-dimensional bubble column are rare, thus, additional experimental investigations on bubble column hydrodynamics are desired for future validations.

5.1.1 Results for square cross-sectional bubble column

Parts of the following validation of the hydrodynamic numerical model against experimental and numerical findings concerning a bubble column configuration with square cross-section were presented similarly in Acher et al. [1] [3].

5.1.1.1 Test case description and numerical setup

The experimental scale bubble column used as validation case in this work was first investigated by Deen et al. [58] for experimental and numerical studies of the two-phase flow field. Subsequently, various Euler-Euler and Euler-Lagrange based models (e.g., [227], [195]) were validated against their findings. The majority of these simulations are based on the assumption of a uniform bubble size. By applying advanced optical measurement techniques, Hansen [93] analyzes local bubble size distributions with this experimental setup. Additionally, he simulates the dynamic bubble size behavior by adding an interfacial area transportation equation (IATE) model to an Euler-Euler framework, incorporating the approaches of Wu et al. [220] (IATE Wu) and Moilanen et al. [156] (IATE Moi.) for bubble breakup and coalescence in the IATE formulation. Since these studies allow for a comparison of the local bubble size spectrum, the experimental and numerical results of Hansen [93] are used for the validation of the present numerical model.

The bubble column used as a test domain has a square cross-section (0.15 m × 0.15 m) and a height of 0.45 m (see figure 5.1a). The square gas sparger (0.0375 m × 0.0375 m) is concentric with the bottom of the bubble column and is modeled as a perforated plate with a porosity of 2.47%. All simulations describe a water/air system at room temperature where initially the entire column is filled with liquid. The air bubbles enter the bubble column through the sparger with a diameter of 4 mm as documented by Deen et al. [58]. Figure 5.1a shows the simulation domain including the horizontal evaluation line $\boldsymbol{H}$ (0.25 m centrally above the sparger) and the vertical centerline $\boldsymbol{V}$. For the analysis of bubble size distributions, Hansen [93] primarily used area-averaged data from the measurement plane $\boldsymbol{P}$ (0.15 m × 0.12 m) with its center at a distance of 0.25 m from the gas inlet.

The numerical grid, as taken from Hansen [93], consists of 46080 equal-sized hexahedral cells depicted in figure 5.1b. Considering the inlet bubble size, the spatial resolution meets the Milelli criterion (see section 2.3). Ničeno et al. [162] and Sungkorn et al. [195] successfully employed a finer numerical mesh for the simulation of the current test case with a filter width being only 20 to 25% larger than the presumed fluid particle size. This criterion is fulfilled in all current simulations for the vast majority of

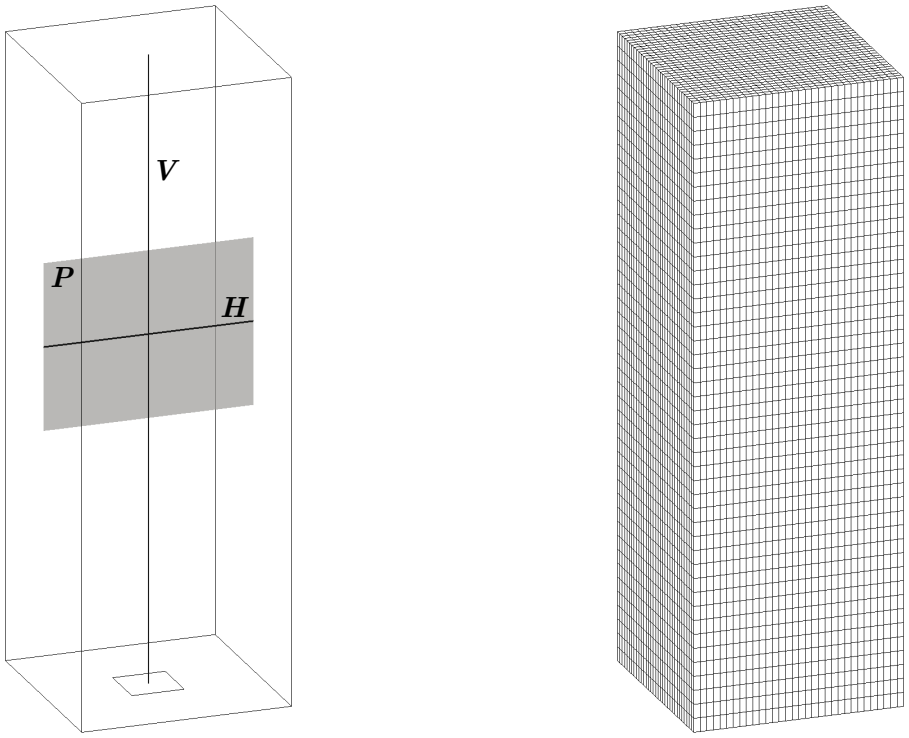

(a) Domain geometry, measurement lines (***H***, ***V***) and plane ***P***

(b) Numerical mesh

Figure 5.1: Illustration of bubble column test case configuration with square cross-section

bubble sizes, based on measurements of the experimental as well as of the numerical bubble size distributions.

This validation study concentrates on the case with a superficial gas velocity of $u_{d,sf} = 4.9\,\mathrm{mm/s}$. To further scrutinize local bubble size distributions, the results of two additional cases with superficial gas velocities of $3.2\,\mathrm{mm/s}$ and $6.6\,\mathrm{mm/s}$ are evaluated. The simulated time for each case is $350\,\mathrm{s}$, where time-averaged data is taken from the last $150\,\mathrm{s}$.

A summary of boundary condition specifications and numerical schemes for the transported flow variables is listed in table 5.1. A small tolerance is allowed concerning the definition of moment inlet conditions to ensure the validity of the selected combination of moments, which does not impair the consistency of implemented boundary conditions with respective experimental investigations. In line with recent publications (e.g., [29]),

first order schemes are employed for the evaluation of MTE formulations. In this manner, the corruption of moments sets due to individual numerical processing of moments is kept to a minimum.

Variable	Inlet	Outlet	Walls	Scheme
Gas volume fraction α_d	0.0247	Zero gradient	Zero gradient	1st order upwind
Moments $M^{(k)}$	$M^{(k)}/M^{(k-1)} =$ 4 mm($\pm$0.003 mm)	Zero gradient	Zero gradient	1st order upwind
Gas velocity $\boldsymbol{u}_d$	Depends on $u_{d,sf}$	Zero gradient with backflow	No slip	Lim. 2nd order upwind
Liquid velocity $\boldsymbol{u}_c$	0.0 m/s	Zero gradient with backflow	No slip	Lim. 2nd order upwind
Pressure p	Zero gradient	Fixed value for outflow; fixed total pressure for inflow	Zero gradient	1st order upwind

Table 5.1: Simulation boundary conditions and numerical schemes for the square cross-sectional bubble column test case

The Ishii-Zuber drag correlation and the specification of constant coefficients for lift[1] and virtual mass force formulations ($C_L = 0.5$, $C_{VM} = 0.5$) constitute the adopted configuration for the Eulerian momentum exchange modeling (see chapter 4). An equivalent configuration of interfacial force models is used by Hansen [93] to obtain his numerical findings. For the coalescence coefficient in the fluid particle interaction formulation, a value of $C_{\mathcal{C}} = 2$ is specified for the current simulations.

5.1.1.2 Gas-liquid flow results

The investigated bubble column flow represents a highly transient two-phase system. Figure 5.2a shows a snapshot of the gas volume fraction distribution at the simulated time of 200 s, whereas figure 5.3a represents the corresponding velocity field for the liquid phase. The interaction with the continuous phase decelerates the incoming stream of gas, which causes a region of comparatively high volumetric gas content ($\alpha_d \approx 0.1$) above the sparger. The ascending disperse phase remains compact below the

[1] Preliminary results showed that an adoption of the Tomiyama lift force model in the current simulation setup did not significantly alter the QMOM findings. However, it led to a reduction of numerical stability for this validation case of Hansen, which prevented the evaluation of representative time-averaged results.

axial position close to the level of the evaluation plane $\boldsymbol{P}$ and fluctuates with a small range. Downstream, the bubble plume breaks up until the gas is spread throughout the entire bubble column cross-section. A highly dynamic interaction between the gas and liquid flow is present in this region. The liquid phase velocity field is dominated by vortices of a wide size spectrum randomly changing form and position over time. A similar flow behavior is also shown in simulation results by Zhang et al. [227] and reported from experimental investigations by Deen et al. [58].

In contrast to the dynamic appearance of the instantaneous pictures, the time-averaged representations in figures 5.2b and 5.3b show a steady symmetric pattern. The ascending gas flow is averaged to a slightly diverging plume, while the liquid velocity field forms the characteristic recirculation pattern. These illustrations indicate that the time-averaging interval chosen in line with Hansen [93] yields valid data for the subsequent analysis.

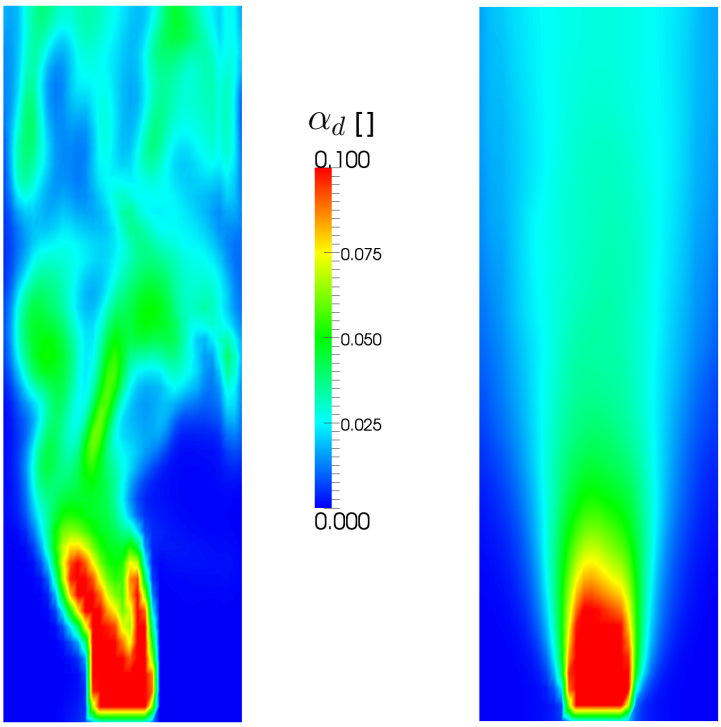

(a) Instantaneous flow field

(b) Time-averaged flow field (200 s – 350 s)

Figure 5.2: Contour plots of the gas volume fraction α_d on a vertical cutting plane at column center

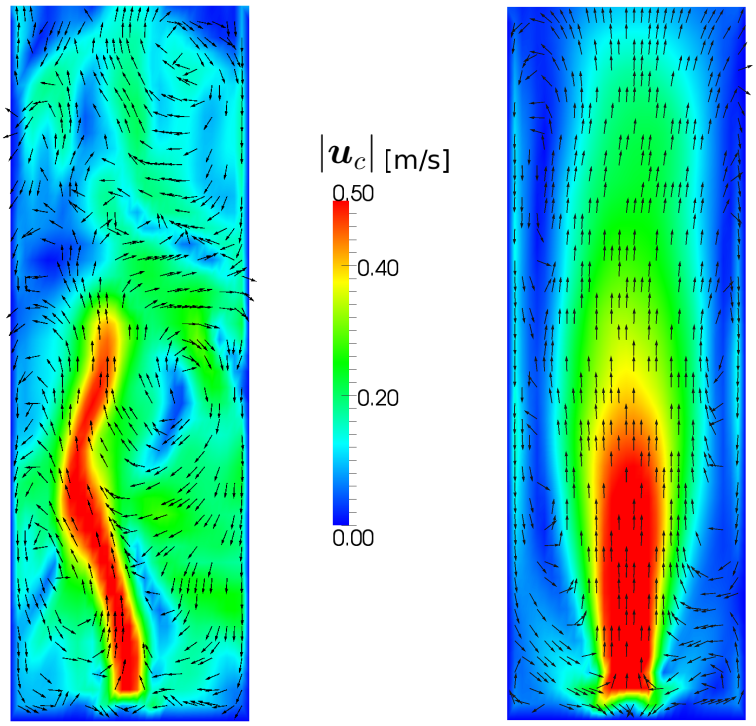

(a) Instantaneous flow field

(b) Time-averaged flow field (200 s – 350 s)

Figure 5.3: Contour plots of the liquid velocity magnitude $|\boldsymbol{u}_c|$ and unscaled velocity vectors on a vertical cutting plane at the column center

Figure 5.4 shows the time-averaged axial gas velocity along the horizontal centerline $\boldsymbol{H}$ of the column. The QMOM simulation results are in good agreement with the comparative numerical and experimental data. The decay of velocity at the column walls is not depicted in detail in the comparative data due to the lack of monitoring points in that area. The axial velocity is zero for both phases on the walls because of the non-slip boundary condition.

The peak values of the distribution of the averaged liquid axial velocity along $\boldsymbol{H}$ do not agree for the data considered. As shown in figure 5.5 the QMOM simulation results are below Hansen's numerical and experimental findings for the center part of the domain. Since the drag formulation is similar for all simulations, this difference can be explained by the analogous variance of peak values for the axial gas phase velocity profile (see figure 5.4).

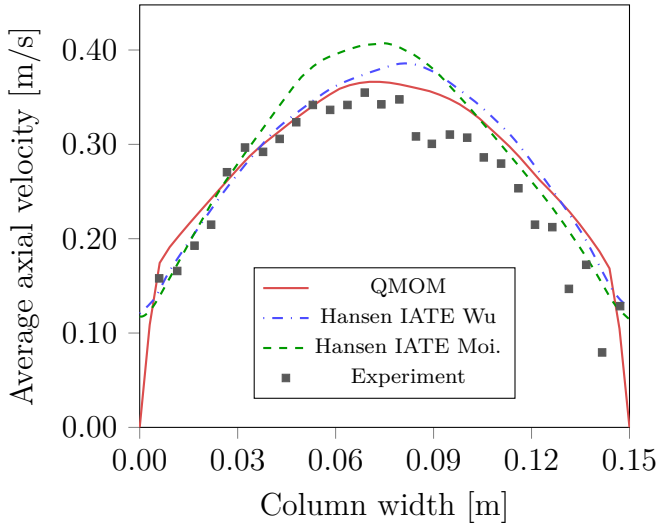

Figure 5.4: Time-averaged axial gas velocity along the horizontal centerline ***H*** of the column; QMOM simulation results compared with experimental and numerical data from Hansen [93]

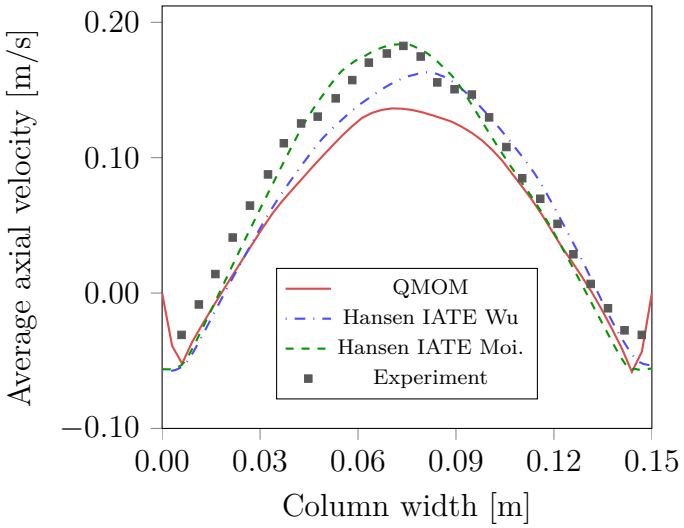

Figure 5.5: Time-averaged axial liquid velocity along the horizontal centerline ***H*** of the column; QMOM simulation results compared with experimental and numerical data from Hansen [93]

The slower upward motion of the liquid phase results in a moderate attenuation of the axial velocity fluctuations in comparison to the respective experimental and numerical data. Figure 5.6 depicts the corresponding data along the horizontal centerline $\boldsymbol{H}$. While there is an offset between the QMOM simulation results and the comparative data, the approximately flat trend throughout the column cross-section is well captured. In analogy to the continuous phase velocity values, its fluctuations cease close to the wall due to the non-slip boundary condition.

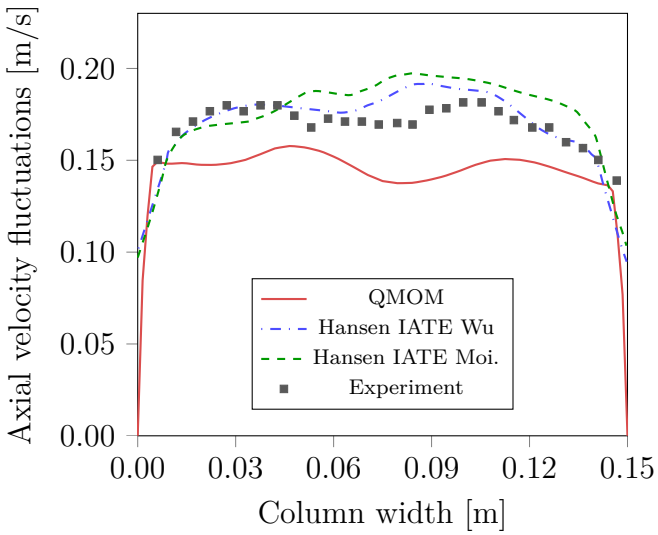

Figure 5.6: Time-averaged axial liquid velocity fluctuations along the horizontal centerline $\boldsymbol{H}$ of the column; QMOM simulation results compared with experimental and numerical data from Hansen [93]

Figure 5.7 shows the radial fluctuations of the liquid velocity along $\boldsymbol{H}$. The numerical results of IATE and QMOM simulations are in good agreement with the experimental values. From the comparison with the axial liquid velocity fluctuations (see figure 5.6), Deen et al. [58] concluded that the assumption of isotropic turbulence used in standard RANS models is not applicable in this case. The accurate representation of turbulence in the two-phase flow field by the solver is of special importance, since the turbulence dissipation rate significantly influences the bubble breakup and coalescence models and hence the bubble size distribution.

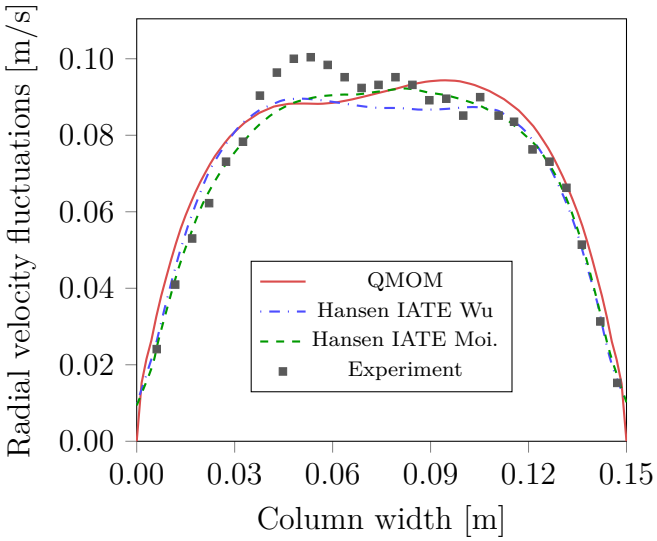

Figure 5.7: Time-averaged radial liquid velocity fluctuations along the horizontal centerline $\boldsymbol{H}$ of the column; QMOM simulation results compared with experimental and numerical data from Hansen [93]

5.1.1.3 Analysis of bubble size distribution

For the analysis of bubble size relations on $\boldsymbol{P}$, a comparison between the experimental values of different representative bubble diameters and the corresponding simulation results is depicted in figure 5.8. In addition to the results of the simulation case with a superficial gas velocity of $u_{d,sf} = 4.9\,\mathrm{mm/s}$, the numerical data for $u_{d,sf} = 3.2\,\mathrm{mm/s}$ and $u_{d,sf} = 6.6\,\mathrm{mm/s}$ are evaluated. Representative bubble diameter formulations are defined by respective moment relations $\left(D_{p,ij} = \left(M^{(i)}/M^{(j)}\right)^{1/(i-j)}\right.$; e.g., Sauter diameter $\left.D_{p,32} = M^{(3)}/M^{(2)}\right)$, while the standard deviation (std. dev.) is evaluated by $\sqrt{\left(M^{(2)}/M^{(0)}\right) - \left(M^{(1)}/M^{(0)}\right)^2}$.

As illustrated in figure 5.8, simulation values for all representative bubble diameters are in good agreement with the corresponding experimental data. The analysis of bubble sizes yields similar results for the three superficial gas velocities. This can be ascribed to the relatively low gas throughput, which does not give reason to expect significant variation of bubble interaction intensity. Due to the comparably high dispersed phase volume fractions in proximity to the gas inlet, the majority of bubble interaction phenomena

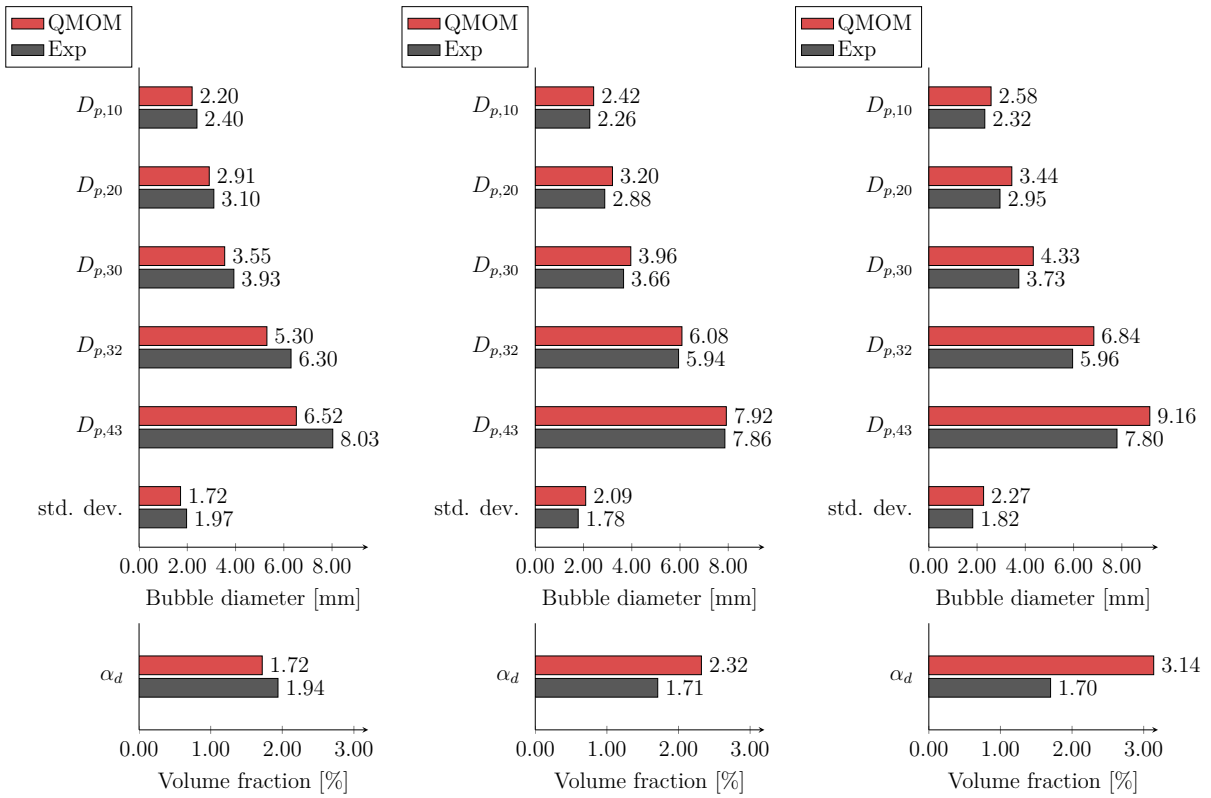

(a) Superficial gas velocity $u_{d,sf} = 3.2\,\mathrm{mm/s}$

(b) Superficial gas velocity $u_{d,sf} = 4.9\,\mathrm{mm/s}$

(c) Superficial gas velocity $u_{d,sf} = 6.6\,\mathrm{mm/s}$

Figure 5.8: Results for representative bubble diameters and gas volume fraction area-averaged over plane $\boldsymbol{P}$; QMOM simulation results compared with experimental data from Hansen [93]

occur in this flow region, before the gas is being spread throughout the entire bubble cross-section while ascending.

The aim of the experimental investigations of Hansen [93] was to measure local bubble sizes as accurately as possible. Using latest optical measurement techniques, he analyzed approximately 10^5 bubbles in each run to generate statistically definite experimental results regarding dispersed phase size relations. This emphasizes the quality of the experimental validation data concerning local bubble size distributions. The dispersed phase volume fraction is deduced from these findings accompanied by a high absolute measurement error for the present low gas fraction values. This is a plausible explanation for the significant deviation of the simulation results with the experimental findings regarding dispersed phase volume fractions, especially in the case with a superficial gas velocity $u_{d,sf} = 6.6\,\mathrm{mm/s}$.

Apart from the analysis of moment relations by representative bubble diameters, the experimental results of Hansen [93] allow for a validation of bubble size distributions by transforming the computed moment values into continuous function form. To this end, a log-normal distribution is presumed as basic function type and the three parameters $C_{LN,1}$,$C_{LN,2}$ and $C_{LN,3}$ are calculated according to equation (4.25). Taking into account the shape of the experimentally found bubble size distributions depicted in the histograms of figure 5.9, this rather simple reconstruction procedure is arguably sufficient for the considered cases. Since the low-order moments and their physical equivalents represent the most significant characteristics for the dispersed phase flow, the log-normal function is evaluated using $\left(M^{(0)}, M^{(1)}, M^{(2)}\right)$ (LogNorm012), $\left(M^{(0)}, M^{(1)}, M^{(3)}\right)$ (LogNorm013) and $\left(M^{(0)}, M^{(2)}, M^{(3)}\right)$ (LogNorm023). In order to compare the resulting continuous representations of the bubble size distributions to the experimental findings, mathematical moments are calculated from the discrete histogram values and are used to depict the experimental results in terms of the corresponding log-normal functions as well.

Applying this consideration, the QMOM findings for the bubble size distribution functions depicted in figure 5.9 are in good agreement with the corresponding experimental data. This analysis yields similar relations between the numerical and comparative experimental data for all regarded superficial gas velocities. A comparison of the bubble size spectrum with the numerical data from Hansen [93] is not possible, since the IATE model does not allow the prediction of the entire function profile. Instead, the Sauter diameter $D_{p,32}$ as representative bubble size can be deduced from the IATE variables.

In addition to the investigation of area-averaged bubble size distributions on the evaluation plane $\boldsymbol{P}$, Hansen [93] measured bubble sizes at five distinct locations (focus plane $0.02\,\mathrm{m} \times 0.02\,\mathrm{m}$) in the flow field. The position of the corresponding points (Center, Bottom, Top, Left, Right) on $\boldsymbol{P}$ are illustrated in figure 5.10. The experimental analysis is limited to the evaluation of $D_{p,10}$, $D_{p,32}$ and the standard deviation. This set of values corresponds to a rather limited representation of the number density function, but allows for a qualitative validation of the local numerical results. Respective local measurements for the bubble Sauter diameter are used to augment the subsequent comparison of QMOM and IATE results

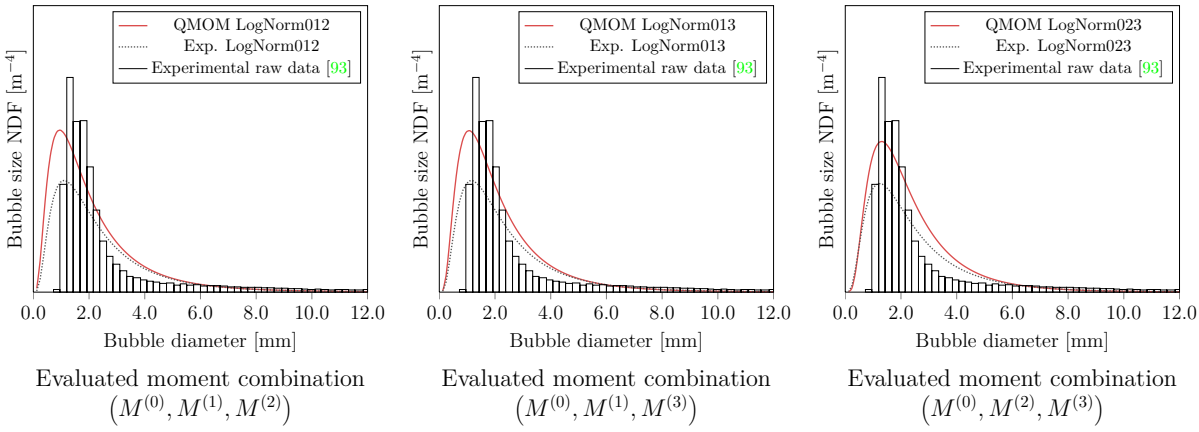

(a) Superficial gas velocity $u_{d,sf} = 3.2\,\mathrm{mm/s}$

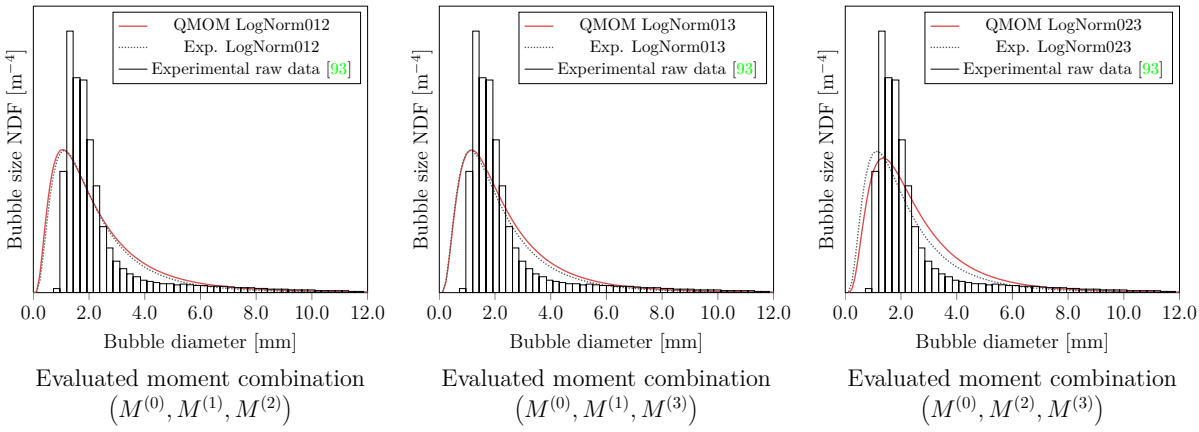

(b) Superficial gas velocity $u_{d,sf} = 4.9\,\mathrm{mm/s}$

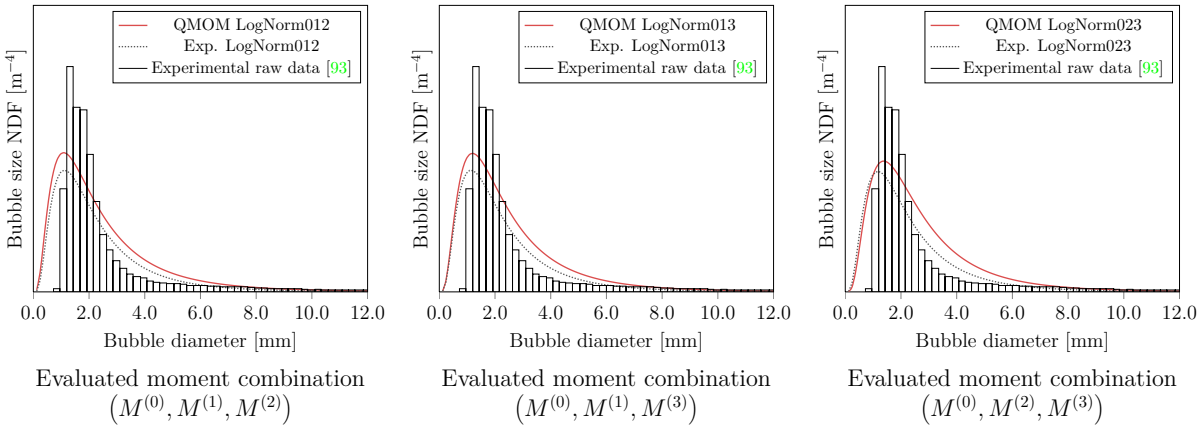

(c) Superficial gas velocity $u_{d,sf} = 6.6\,\mathrm{mm/s}$

Figure 5.9: Discrete and continuous bubble size distribution functions from QMOM simulation results and comparative experimental data area-averaged over plane $\boldsymbol{P}$

located along the horizontal and vertical evaluation line. An extended analysis of bubble size relations at the specified locations is presented as part of section 5.2.

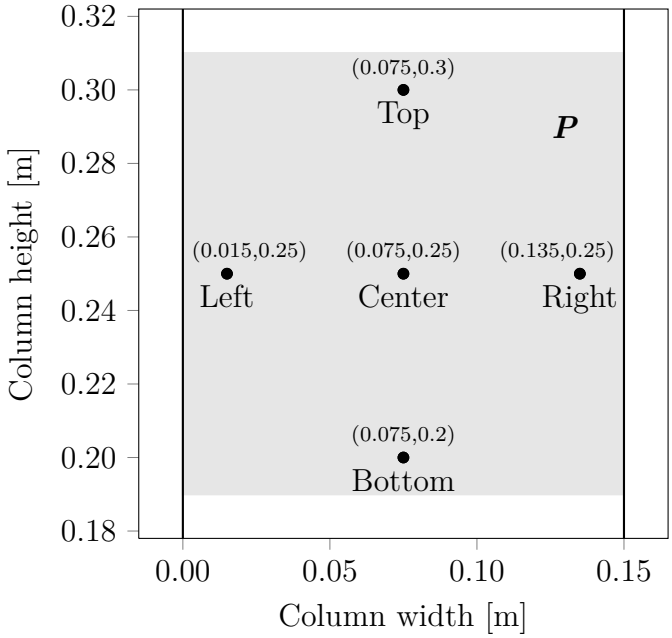

Figure 5.10: Positions of local bubble size evaluation locations on plane ***P***

Figure 5.11a shows the Sauter diameter distribution along the horizontal centerline ***H*** of the column considering the experimental and numerical results of Hansen, as well as the determined QMOM values for the case with a superficial gas velocity of $u_{d,sf} = 4.9\,\mathrm{mm/s}$. While the QMOM results are in the range of the experimental values over the whole column width, large differences to the IATE data can be identified, particularly close to the walls. QMOM's high diameter values in that area seem to be in line with the experimental results, although more data points would be needed for a definite conclusion. Similar statements can be made for the test case analysis with superficial gas velocities $u_{d,sf} = 3.2\,\mathrm{mm/s}$ and $u_{d,sf} = 6.6\,\mathrm{mm/s}$ (see figures 5.11b and 5.11c). The QMOM simulation results capture the shape of the diameter profile significantly better than the IATE models and with reasonable agreement with the absolute values.

Hansen also numerically analyzed the Sauter diameter profile along the vertical centerline ***V***. Unfortunately, only the IATE results for sampling positions with a distance of more than 0.15 m from the sparger were published. A plot of the experimental and numerical findings along ***V*** for

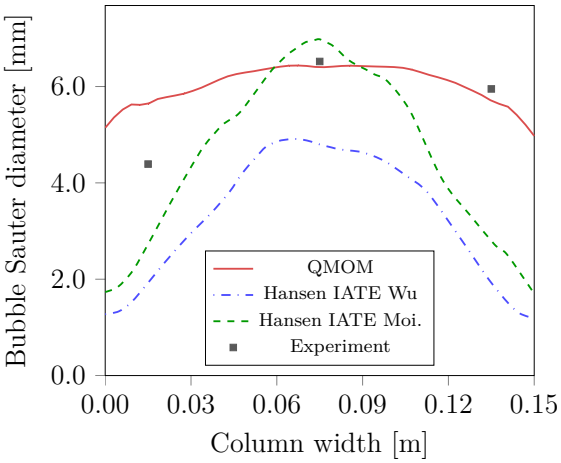

(a) Superficial gas velocity $u_{d,sf} = 4.9\,\mathrm{mm/s}$

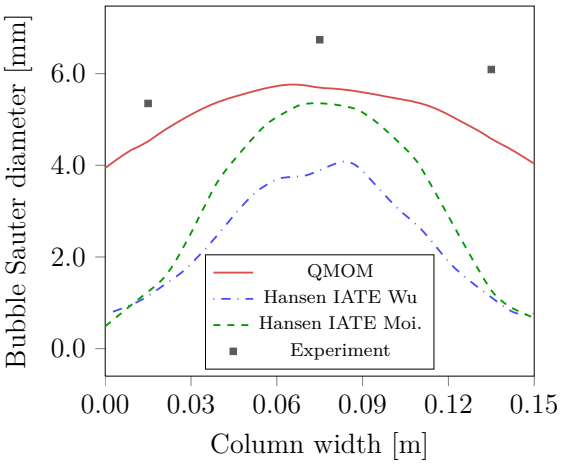

(b) Superficial gas velocity $u_{d,sf} = 3.2\,\mathrm{mm/s}$

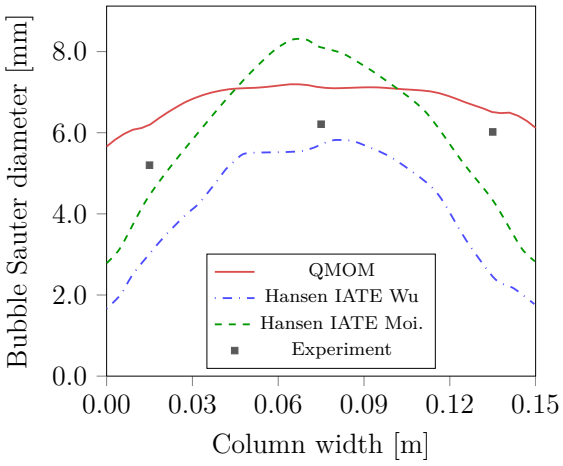

(c) Superficial gas velocity $u_{d,sf} = 6.6\,\mathrm{mm/s}$

Figure 5.11: Sauter diameter profile along the horizontal evaluation line $\boldsymbol{H}$; QMOM simulation results compared with experimental and numerical data from Hansen [93]

the main case with a gas superficial velocity of $u_{d,sf} = 4.9\,\mathrm{mm/s}$ shows significant differences between the IATE and the QMOM results (see figure 5.12a). Both IATE models predict a considerable increase of the bubble size within the bottom 0.15 m of the bubble column, followed by a breakup dominated region, before the diameter value stabilizes. In contrast, the QMOM results indicate a less significant effect of the coalescence processes above the gas sparger and a smooth increase of bubble size further along the vertical centerline $\boldsymbol{V}$.

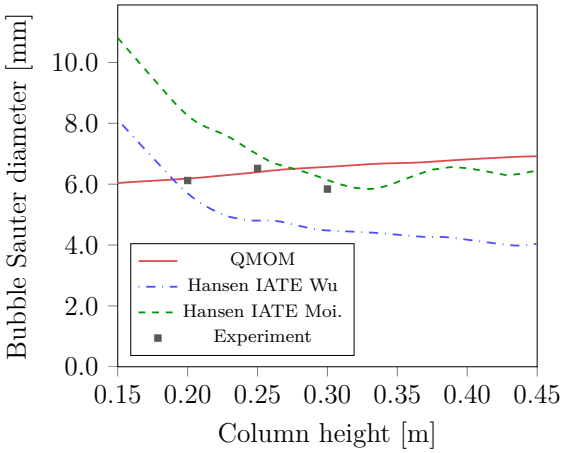

(a) Superficial gas velocity $u_{d,sf} = 4.9\,\mathrm{mm/s}$

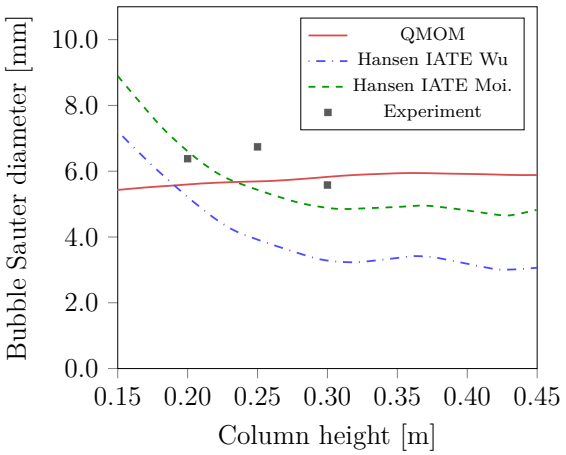

(b) Superficial gas velocity $u_{d,sf} = 3.2\,\mathrm{mm/s}$

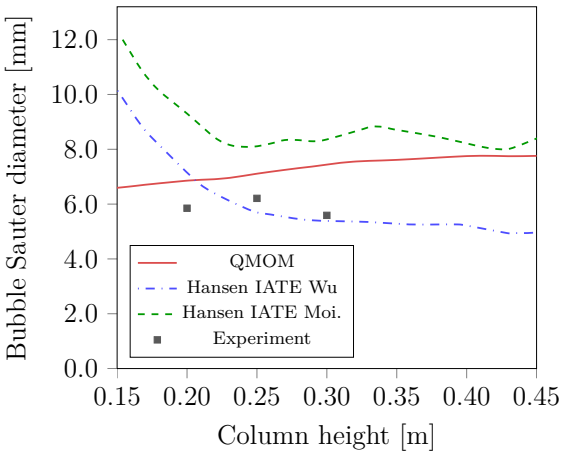

(c) Superficial gas velocity $u_{d,sf} = 6.6\,\mathrm{mm/s}$

Figure 5.12: Sauter diameter profile along the vertical centerline $\boldsymbol{V}$; QMOM simulation results compared with experimental and numerical data from Hansen [93]

For the main test case, shown in figure 5.12a, all simulation results are in range with the experimental values. Because of the very limited data set from the experimental studies, a conclusive evaluation of the different numerical approaches is not possible. Unfortunately, the analysis of the corresponding results for the test cases with superficial gas velocities of $u_{d,sf} = 3.2\,\mathrm{mm/s}$ and $u_{d,sf} = 6.6\,\mathrm{mm/s}$ does not clarify this point (see figures 5.12b and 5.12c). The qualitative and quantitative depiction of the diameter distribution along $\boldsymbol{V}$ is very similar to the main test case.

5.1.2 Results for circular cross-sectional bubble column

As an additional validation case, the gas-liquid flow of an air-water system in a circular cross-sectional bubble column is analyzed. The considered test case was originally used by Bhole et al. [17] to experimentally investigate bubble column hydrodynamics via laser Doppler anemometer measurements. Subsequently, their findings have been employed as comparative data for numerous numerical studies (e.g., [16], [197]). The presentation of the respective experimental data by Bhole et al. [16] is taken as a basis for the following validation study.

The test case geometry, depicted in figure 5.13a, consists of a circular column of 0.15 m diameter and a height of 0.9 m. In contrast to the preceding validation case configuration, the gas inlet sparger takes up the entire column cross-section and a significantly higher superficial gas velocity of $u_{p,sf} = 20\,\mathrm{mm/s}$ is investigated. With the corresponding gas throughput, the current setup features hydrodynamic specifications which are more likely to coincide with values from industrial applications. In line with Bhole et al. [16], a constant bubble size is assumed at the gas inlet which is determined by the correlation of Miyahara et al. [155]. With respect to the current sparger characteristics, this evaluation yields an inlet bubble diameter of $D_p = 8.81\,\mathrm{mm}$. A constant gas volume fraction of $\alpha_d = 0.5$ is imposed at the gas inlet, analogous to the simulation configuration of Buffo et al. [29]. Apart from these modifications, the remaining numerical specifications are consistent with the setup presented in table 5.1.

As depicted in illustrations 5.13b and 5.13c, the simulation domain is spacially discretized by a numerical mesh of 13000 hexagonal cells. With respect to the experimental values of local fluid particle size conditions, the resulting ratio of computational grid size to bubble diameter is similar to the relations specified in the proceeding study. Although the spatial resolution may locally fail to meet the Milelli criterion (see section 2.3), mesh size conditions as proposed by Ničeno et al. [162] and Sungkorn et al. [195] are generally satisfied.

Similar to the two-phase flow pattern in the square cross-sectional bubble column, the current gas-liquid hydrodynamics are characterized by transient vortices of different sizes and orientations, yielding a highly dynamic bubbly

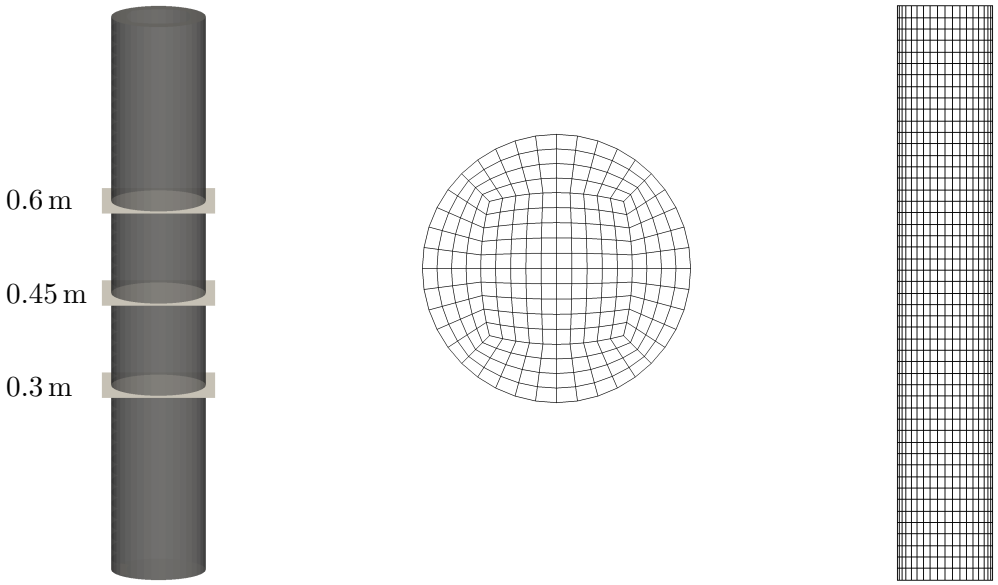

(a) Simulation domain and evaluation heights **(b)** Numerical mesh on cross-section **(c)** Numerical mesh along column height

Figure 5.13: Geometry, numerical grid and evaluation locations of the bubble column test case with circular cross-section

flow. Validation data are derived from numerical results time-averaged over a period of 200 s (simulation time 200 s – 400 s). To allow for a comparison with equivalent experimental values, the simulation results are evaluated as radial profiles of fluid dynamic quantities at column heights of 0.3 m, 0.45 m and 0.6 m as illustrated in figure 5.13a.

In their numerical studies of the current test case, Bhole et al. [16] analyzed the impact of different lift force models on the simulation findings. They report of fundamentally variant hydrodynamic characteristics, depending on the selected lift force formulation and argue that the Tomiyama model is most suitable for this kind of configuration. This conclusion is supported by the current numerical investigations. Using the previous Euler-Euler setup for interfacial momentum exchange (Ishii-Zuber drag model, $C_L = 0.5$, $C_{VM} = 0.5$) results in the development of a stable or metastable recirculation region above the gas inlet (see figure 5.14a). This flow pattern hinders the appearance of radial-symmetric validation data even for long averaging periods, jeopardizes numerical stability and dominates gas-liquid flow characteristics. With the adoption of the Tomiyama lift force model,

the highly transient hydrodynamic pattern develops as depicted in figure 5.14b and described by Tabib et al. [197].

As they observe a substantial overprediction of bubble diameters for the current test case using conventional model formulations, Bhole et al. [16] propose an adaption of the bubble coalescence model. Likewise, Chen et al. [39] [41] report similar deficiencies in the depiction of bubble size relations with common fluid particle breakup and coalescence formulations. In their studies, considering a circular cross-sectional bubble column configuration of similar dimensions, they propose a multiplication of the fragmentation rate by an arbitrarily determined factor of 10 to compensate for bubble size overprediction. If the bubble interaction terms used in the previous test case ($C_{\mathcal{C}} = 2.0$) are applied for this study without modification, bubble diameter values are 20% to 50% above the experimental findings. With the adaption of the coalescence coefficient to $C_{\mathcal{C}} = 0.127$, which represents the minimum of the reported value range [129], the simulation results concerning bubble size are in good agreement with comparative experimental data as discussed in the following presentation of the validation study results.

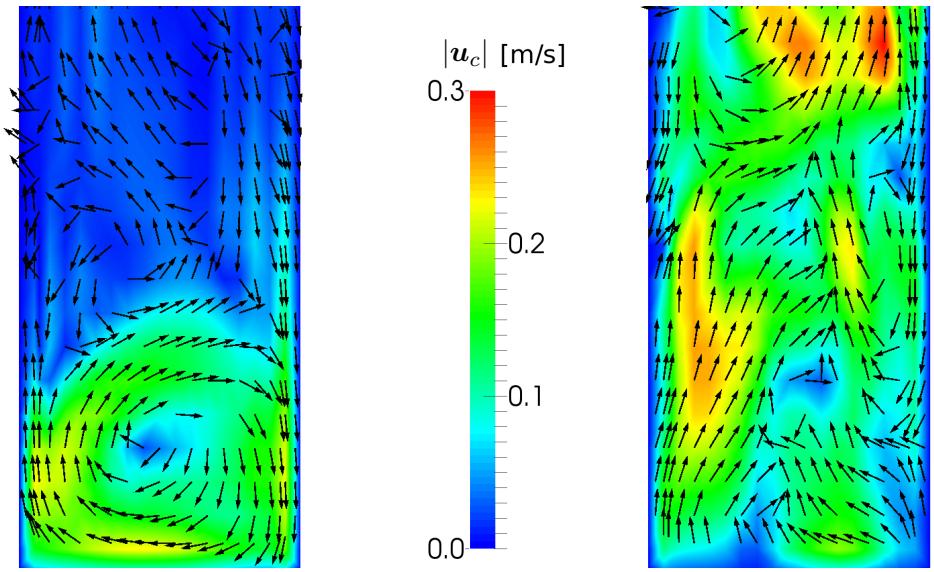

(a) Lift force coefficient $C_L = 0.5$ **(b)** Tomiyama lift force model

Figure 5.14: Instantaneous liquid velocity magnitude $|\boldsymbol{u}_c|$ and unscaled velocity vectors on a central cutting plane at the lower third of the column

Figure 5.15 depicts the experimental and numerical data regarding the axial liquid velocity as radial profiles at the aformentioned evaluation heights. The QMOM results correspond well to the validation values in all three considered cases. While the peak values at the column center are slightly below the experimental findings, the numerical results closer to the boundaries tend to overpredict experimentally determined velocities. The current mesh size does not allow for a detailed depiction of fluid dynamic conditions at the column wall, yet the recirculating motion of liquid in that area is captured well.

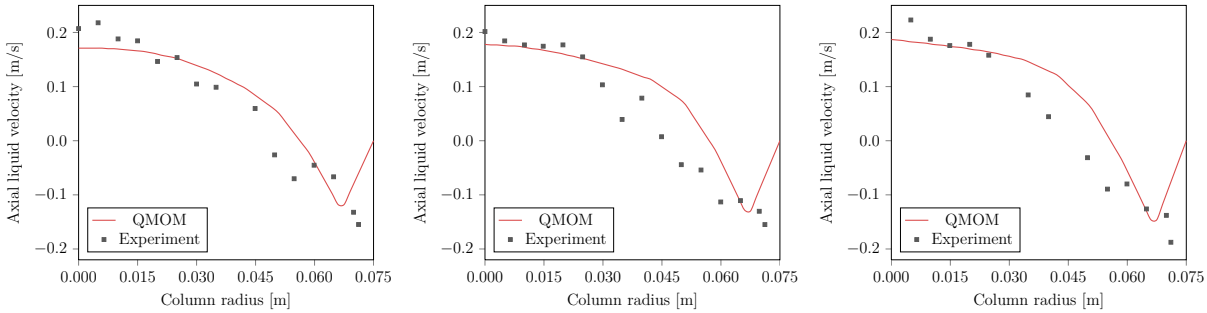

(a) Column height 0.3 m (b) Column height 0.45 m (c) Column height 0.6 m

Figure 5.15: Time-averaged radial profiles of the axial liquid velocity (200 s – 400 s); QMOM simulation results compared with experimental data from Bhole et al. [16]

Unfortunately, the literature sources for the validation data on local bubble size relations do not specify which representative diameter (e.g., D_{32}, D_{10}) is analyzed in their studies [17] [16]. Hence, exclusively qualitative conclusions can be drawn from the comparison with local bubble size distribution characteristics of QMOM findings. While, at a column height of 0.3 m, the representative bubble diameters from simulation results are significantly higher than corresponding experimental data, a generally good agreement can be assessed for the evaluation locations on higher levels (see figure 5.16). The numerical results indicate that the effects of bubble breakup and coalescence models compensate one another for most of the simulation domain and yield approximately constant size distributions at all evaluation positions. In the experimental study, a corresponding state of equilibrium for the diameter relations of ascending bubbles is reached above 0.3 m column height.

As depicted in figure 5.17, the analysis of gas volume fraction values yields similar results for the three locations in the domain. Close to the column

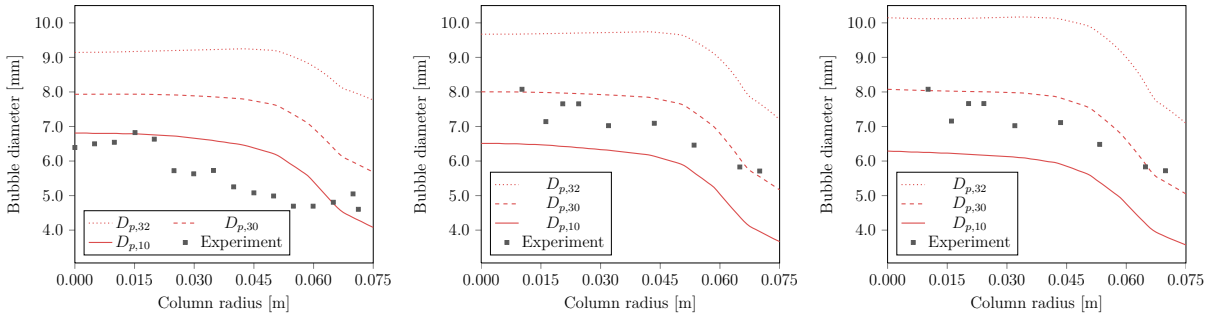

(a) Column height 0.3 m (b) Column height 0.45 m (c) Column height 0.6 m

Figure 5.16: Time-averaged radial profiles of representative bubble diameters (200 s – 400 s); QMOM simulation results compared with experimental data from Bhole et al. [16]

walls, the QMOM findings correspond well to the validation data, while the simulation values substantially underpredict the gas content at the column center. The correlation of this underprediction with the positions of highest bubble diameter values arguably indicates a deficient representation of drag forces with regard to corresponding bubble size conditions. Applying an alternative drag model, the simulation results of Bhole et al. [16] follow the experimental data on the volumetric gas fraction more closely.

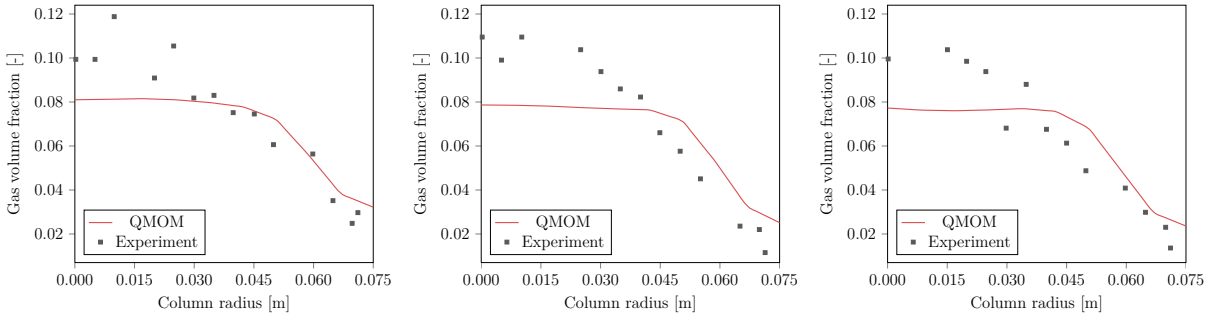

(a) Column height 0.3 m (b) Column height 0.45 m (c) Column height 0.6 m

Figure 5.17: Time-averaged radial profiles of dispersed phase volume fraction (200 s – 400 s); QMOM simulation results compared with experimental data from Bhole et al. [16]

5.2 Analysis of polycelerity

The current numerical model makes it possible to analyze the effect of a size-dependent particle velocity formulation (RTA) on the simulation results in comparison to the assumption of locally uniform bubble motion

(IMV). To this end, the square cross-sectional bubble column test case introduced in segment 5.1.1.1 was simulated with two corresponding QMOM configurations of the Euler-Euler solver. The respective numerical results concerning local bubble size distributions in case of the application of the RTA are presented in section 5.1.1.3. By extending this validation of RTA simulation data against experimental findings, the numerical results of both moment velocity models are contrasted. To this end, differences in local bubble size distributions are illustrated and analyzed.

Since the interfacial forces are independent of the bubble size for the selected formulations for drag (Ishii-Zuber model), lift ($C_L = 0.5$) and virtual mass ($C_{VM} = 0.5$), the moment velocity formulation does not influence the hydrodynamic representation by the Eulerian framework, but effects the bubble size distribution results only. Apart from minor deviations due to the finite averaging period of the dynamic flow field, the resulting hydrodynamic values are identical for both simulation setups and section 5.1.1.2 exhibits an according validation against experimental data of the concerned test case. Hence, an explicit examination of gas and liquid velocity conditions for the IMV simulation is omitted here. A corresponding analysis can be found in Acher et al. [2] which additionally features parts of the following comparative study of moment velocity models.

The inclusion of IMV simulation results concerning the representative diameter values on $\boldsymbol{P}$ into the respective analysis depicted in figure 5.8 allows for a comparison of both simulation types (see figure 5.18). As shown above, the RTA simulation findings correspond well with the experimental validation data. If the RTA is not incorporated, evaluated representative bubble diameters ($D_{p,10}, D_{p,20}, D_{p,30}$) are substantially larger for all considered cases. This correlation is further analyzed and interpreted through a continuous representation of bubble size relations on $\boldsymbol{P}$.

Figure 5.19 exhibits good agreement of all predicted bubble size distributions from simulations applying the RTA with the experimental findings. As already indicated by the corresponding representative bubble diameters, neglecting the RTA in the present QMOM model leads to major deviations of experimental and numerical results. Compared to the experimental findings, the peak values of the log-normal functions are at diameter values more than twice as large and the content of bubbles with diameters below

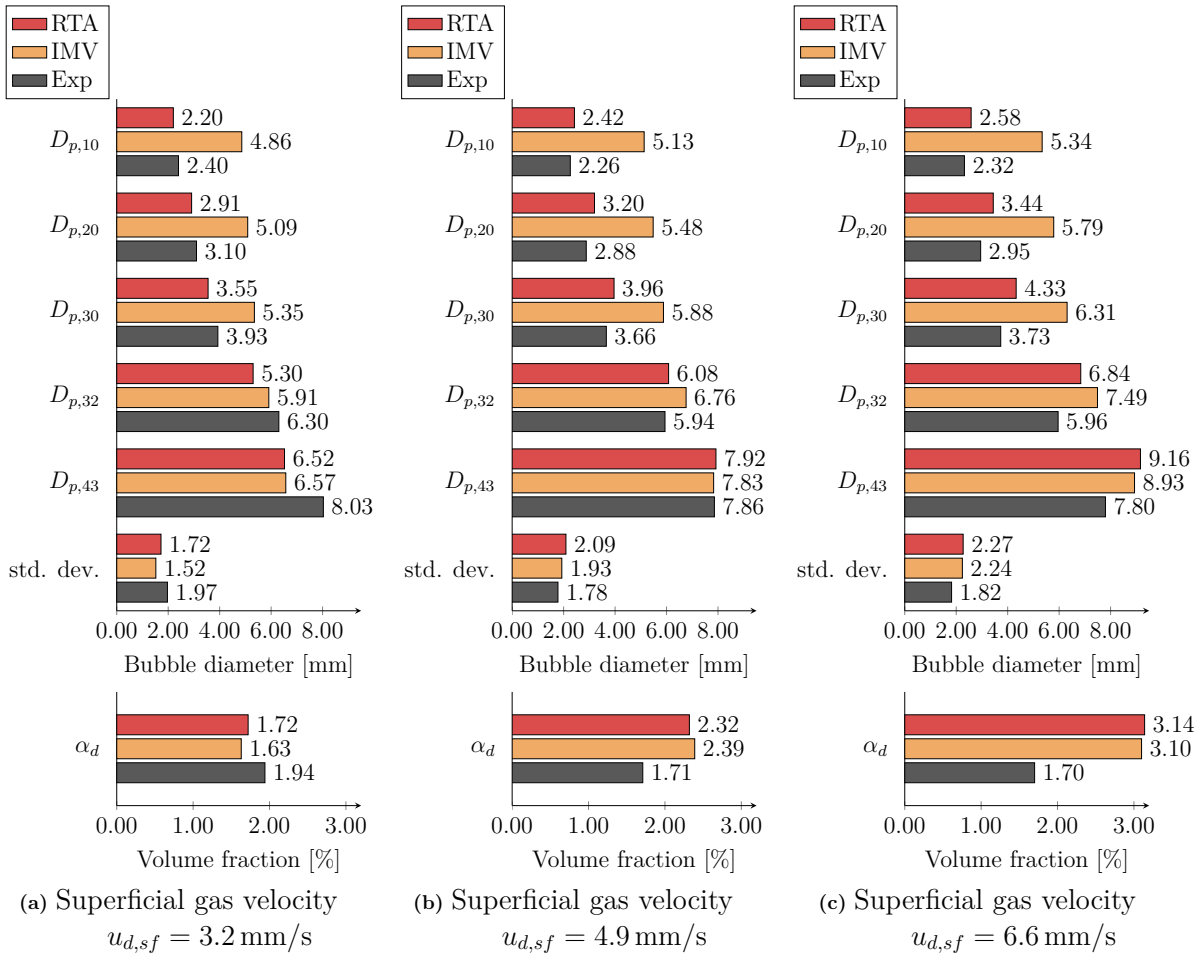

(a) Superficial gas velocity $u_{d,sf} = 3.2\,\mathrm{mm/s}$

(b) Superficial gas velocity $u_{d,sf} = 4.9\,\mathrm{mm/s}$

(c) Superficial gas velocity $u_{d,sf} = 6.6\,\mathrm{mm/s}$

Figure 5.18: Representative bubble diameters and gas volume fraction area-averaged over plane $\boldsymbol{P}$; QMOM simulation results with identical moment velocities (IMV) and applying the relaxation time approach (RTA) compared with experimental data from Hansen [93]

2 mm is marginal. Due to the increased contribution of larger bubbles to the dispersed phase volume fraction, the number density function represents a comparably flat curve throughout the diameter range.

The poor results for the bubble size distributions, that is observed if all moments are convected with identical velocities, can be explained by the insufficient representation of the bubble size-dependent fluid particle flow patterns. While the path of larger bubbles is influenced by the liquid flow field on large scales only, smaller bubbles follow the continuous phase more faithfully. In areas of recirculating liquid phase, small bubbles will follow the vortices or even get trapped for a short period of time. This leads to an increase in residence time of small bubbles in the corresponding flow

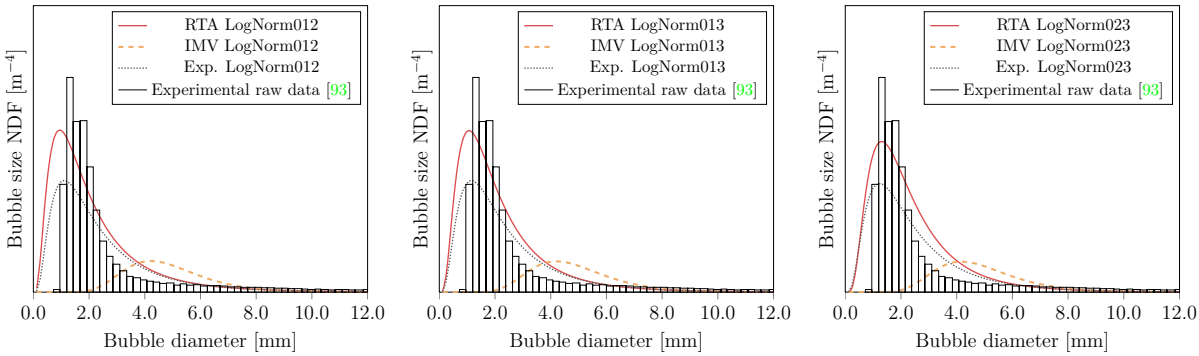

Evaluated moment combination $\left(M^{(0)}, M^{(1)}, M^{(2)}\right)$ | Evaluated moment combination $\left(M^{(0)}, M^{(1)}, M^{(3)}\right)$ | Evaluated moment combination $\left(M^{(0)}, M^{(2)}, M^{(3)}\right)$

(a) Superficial gas velocity $u_{d,sf} = 3.2\,\mathrm{mm/s}$

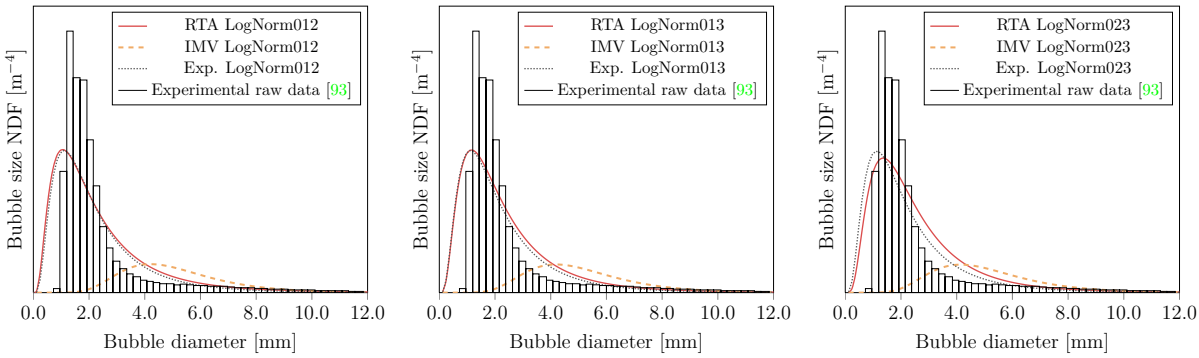

Evaluated moment combination $\left(M^{(0)}, M^{(1)}, M^{(2)}\right)$ | Evaluated moment combination $\left(M^{(0)}, M^{(1)}, M^{(3)}\right)$ | Evaluated moment combination $\left(M^{(0)}, M^{(2)}, M^{(3)}\right)$

(b) Superficial gas velocity $u_{d,sf} = 4.9\,\mathrm{mm/s}$

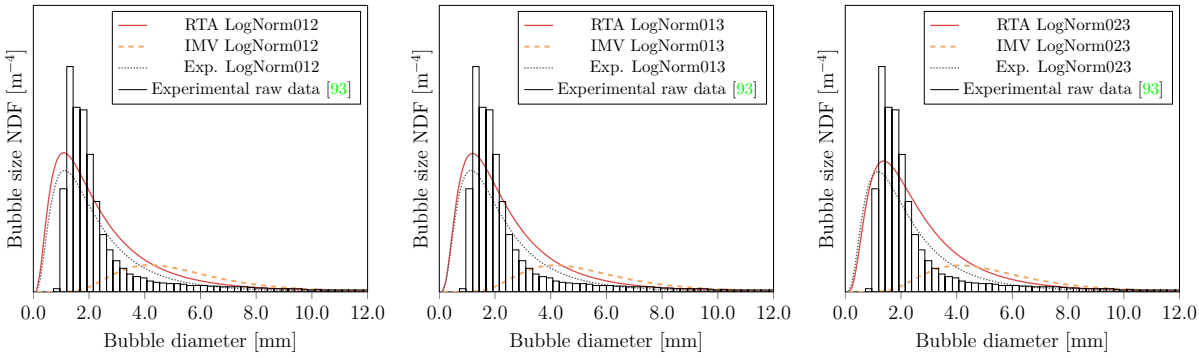

Evaluated moment combination $\left(M^{(0)}, M^{(1)}, M^{(2)}\right)$ | Evaluated moment combination $\left(M^{(0)}, M^{(1)}, M^{(3)}\right)$ | Evaluated moment combination $\left(M^{(0)}, M^{(2)}, M^{(3)}\right)$

(c) Superficial gas velocity $u_{d,sf} = 6.6\,\mathrm{mm/s}$

Figure 5.19: Discrete and continuous bubble size distribution functions from QMOM simulation results (RTA and IMV) and comparative experimental data area-averaged over plane ***P***

regions. Figure 5.20 shows a fluid vortex and the Sauter diameter ($D_{p,32}$) contours in its proximity. The circulating flow field leads to a size-dependent separation of the bubbles in the downflow region on the left. Smaller bubbles accumulate in the wall region, whereas larger bubbles remain in the center.

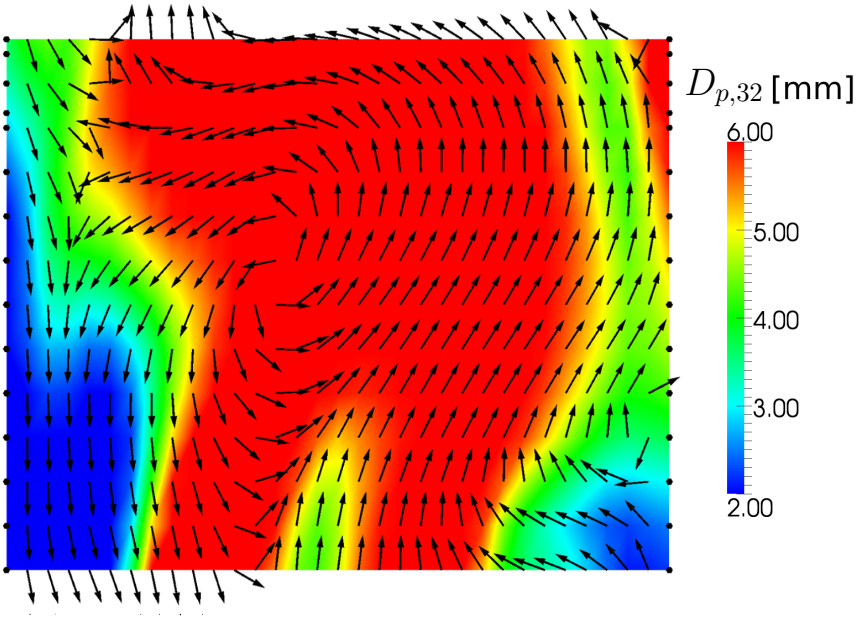

Figure 5.20: Contour plot of the instantaneous Sauter diameter ($D_{p,32}$) field and unscaled liquid velocity vectors on plane ***P***

At distinct positions on ***P***, specified by depiction 5.10, local numerical and experimental representative diameters for the studied superficial gas velocities are illustrated in figure 5.21. Similar conclusions can be drawn from the comparison of the corresponding results for all three gas throughput rates. While the RTA results are in range of the experimental findings for the representative diameter $D_{p,10}$, severe deviations to the alternative numerical data are clearly recognizable. This tendency corresponds to the discussed area-averaged findings and indicates that the percentage of small bubbles is underestimated. Regarding the remaining representative diameters, the quality of the corresponding numerical results is comparable, though the simulations including the RTA yield a better agreement with the comparative experimental data for higher gas flow rates.

In all cases, the experimental values indicate the trend of bubble sizes along the column width. Smaller bubbles accumulate at the column walls, whereas the bubble size distributions at the center are dominated by large bubbles.

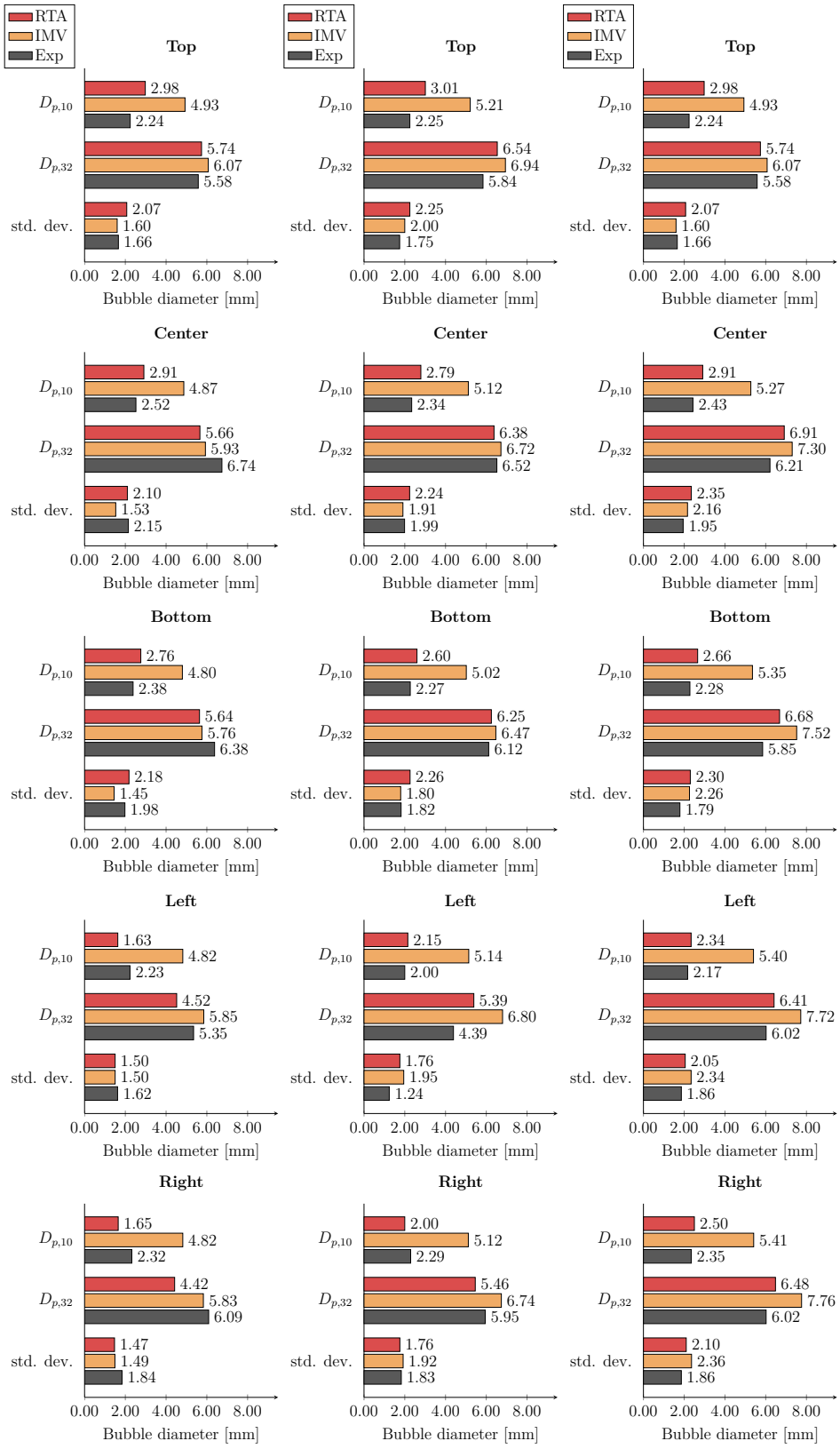

(a) Superficial gas velocity $u_{d,sf} = 3.2\,\mathrm{mm/s}$

(b) Superficial gas velocity $u_{d,sf} = 4.9\,\mathrm{mm/s}$

(c) Superficial gas velocity $u_{d,sf} = 6.6\,\mathrm{mm/s}$

Figure 5.21: Results for representative bubble diameters at distinct positions on ***P***

This deviation is captured accordingly by all RTA simulations. In contrast, the numerical data with identical moment velocities is characterized by a flat trend along the column width or even by a minimum of the bubble size in the center.

To demonstrate the influence of the moments correction algorithm described in section 4.2.3, figure 5.22 exemplarily depicts the time-averaged relative moment modifications $\theta^{(k)} = \Delta M^{(k)}/M^{(k)}$ for k=3 as a consequence of moment correction. The flow region close to the gas inlet is susceptible to moment correction, since minor numerical inaccuracies are sufficient to yield invalid sets of moments for virtually monodisperse distributions. Illustration 5.22b also shows that the simulation including the RTA is more commonly subject to moment correction, albeit with marginal relative moment modifications. This increased rate of moment correction can be ascribed to the additional option of moment variance due to the moment velocity formulation.

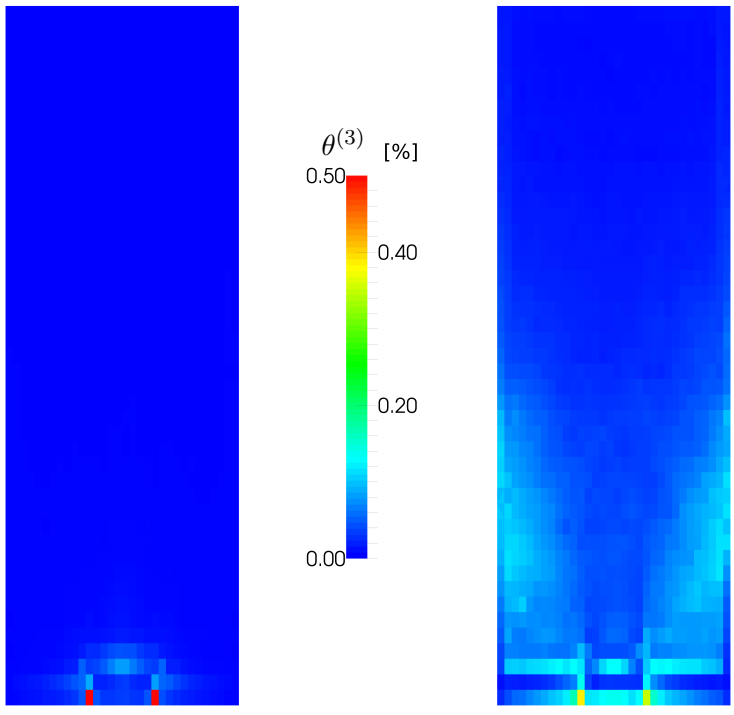

(a) Identical moment velocities (IMV)

(b) Relaxation time approach (RTA)

Figure 5.22: Contour plots of the time-averaged relative moment corrections for the third moment $M^{(3)}$ on a vertical cutting plane at column center (200 s – 350 s)

The maximum values of $\theta^{(k)}$ in the computational domain for all incorporated moments are listed in table 5.2. For both moment velocity formulations all time-averaged corrections of moments are significantly below 1% and consequently may not substantially influence the final results concerning local bubble size distributions. Since the dispersed phase is convected through the column and released at the outlet, the modification of moments due to the correction algorithm does not accumulate in the domain. Concerning the dispersed phase volume fraction, moment correction yields a time-averaged offset in gas throughput from inlet to outlet of maximum 3%.

Moment velocity formulation	$M^{(0)}$	$M^{(1)}$	$M^{(2)}$	$M^{(3)}$	$M^{(4)}$	$M^{(5)}$
Relaxation time approach (RTA)	0.31%	0.15%	0.17%	0.39%	0.05%	0.17%
Identical moment velocities (IMV)	0.03%	0.01%	0.01%	0.65%	0.03%	0.01%

Table 5.2: Maximum domain-wide values of time-averaged relative moment corrections $\theta^{(k)}$ (200 s - 350 s)

5.3 Simulation of interfacial mass transfer

The incorporation of chemical species transport equations including appropriate source terms for interfacial exchange phenomena allows the depiction of absorption processes in gas-liquid flows. Since an adequate representation of the bubble column hydrodynamics in the square cross-sectional bubble column test case is ensured by the model validation (see 5.1.1), further studies concerning the interfacial mass transfer are conducted with this configuration. The corresponding simulation results are analyzed and compared with analogous numerical findings from literature sources. To this end, the Euler-Euler investigation of mass transfer phenomena for this test case by Zhang et al. [229] [228] is used for comparison. Besides this study, Darmana et al. [52] analyzed equivalent processes for the current bubble column setup applying an Euler-Lagrange model.

For all current numerical studies, the dispersion of CO_2 bubbles in pure water constitutes the considered gas-liquid system with properties[2] analo-

[2] Gas:$\rho_d = 1.98\,\mathrm{kg/m^3}$, $\mu_d = 1.812 \times 10^{-5}\,\mathrm{kg/ms}$; Liq.:$\rho_c = 1.0 \times 10^3\,\mathrm{kg/m^3}$, $\mu_c = 1.0 \times 10^{-3}\,\mathrm{kg/ms}$; $\sigma = 7.275 \times 10^{-2}\,\mathrm{N/m}$, $\mathcal{D}_c^{CO_2} = 1.699 \times 10^{-9}\,\mathrm{m^2/s}$

gous to the specifications by Zhang et al. [229]. As a simplification, this species combination is represented assuming purity of the gaseous phase ($Y_d^{CO_2} = 1$) throughout the simulation. Consequently, the respective CO_2 concentration equation reduces to the dispersed phase continuity formulation (see subsection 4.1) and the hydrodynamic model is extended by a balance equation for $Y_c^{CO_2}$ only. Initialized as zero, the respective scalar mass fraction field is solved with a limited second order upwind scheme and all boundary conditions are defined as zero gradient. For the determination of the interfacial mass transfer, the Sherwood correlation by Glaeser [86] is incorporated as outlined in section 4.1.

The remaining model setup is similar to the main validation case presented in section 5.1.1. This applies to the domain geometry and the spatial discretization (see figure 5.1) as well as to the simulation boundary conditions and numerical schemes stated in table 5.1. Furthermore, the identical set of models for the Eulerian representation of interfacial momentum exchange (Ishii-Zuber drag model, $C_L = 0.5$, $C_{VM} = 0.5$) and fluid particle interaction ($C_C = 2$) is used. The simulation domain is initially filled with pure water before the CO_2 enters the bubble column with a superficial gas velocity of $u_{d,sf} = 4.9\,\text{mm/s}$ and a monodisperse inlet bubble size of 4 mm.

As part of the following numerical investigation, the impact of different model functionalities on the simulation results concerning interfacial mass transfer is studied. Therefore, a variety of simulation configurations are considered, which are introduced in table 5.3. With *Sim 1* the absorption processes exclusively affect local gas volume fractions, while the bubble size remains constant ($D_p = 4\,\text{mm}$). Configurations *Sim 2* and *Sim 3* allow for a modification of bubble sizes as a result of absorption phenomena only. The additional consideration of bubble breakup and coalescence events is part of simulation cases *Sim 4* and *Sim 5*.

Concerning the analysis of absorption phenomena, Zhang et al. [229] considered two simulation configurations: an Euler-Euler model with the definition of a constant bubble size (similar to *Sim 1*) and a model extension in terms of a bubble number density equation to allow for variable fluid particle sizes. The *bubble number density model* (BNDM) is characterized by the incorporation of a transport equation for the volume-specific number of fluid particles. Considering the physical equivalents of

Simulations	Bubble size distribution	Moment transport velocity	Bubble interaction
Sim 1	Constant bubble size	-	-
Sim 2	QMOM	IMV	-
Sim 3	QMOM	RTA	-
Sim 4	QMOM	IMV	Breakup and Coalescence
Sim 5	QMOM	RTA	Breakup and Coalescence

Table 5.3: Simulation cases for the numerical study of interfacial mass transfer

NDF moments, this formulation coincides with the MTE for $M^{(0)}$. In combination with the dispersed phase continuity equation, it allows the calculation of a representative bubble diameter and gives a very limited depiction of local bubble size conditions. Since Zhang et al. [229] use the Eulerian convection velocity for the bubble number density equation, the BNDM simulation setup can be regarded as similar to case *Sim 2* but with an inferior representation of bubble size relations and alternative submodels for interfacial momentum exchange.

This resemblance is reflected by the numerical results regarding bubble size profiles along a horizontal and vertical evaluation line as illustrated in figure 5.23. Both plots show that simulation case *Sim 2* and the BNDM yield very similar numerical results. If a size-dependent particle velocity is considered via the RTA (*Sim 3*), bubble sizes are generally below the alternative findings. This phenomenon coincides well with the conception of simulated fluid particle motion being more susceptible to deflection by the liquid flow if the RTA is applied (see figure 5.20). As a consequence, specifically smaller bubbles will follow fluid vertices more faithfully and therefore have an increased residence time. This is associated with a longer absorption period and an enhanced shrinking of respective fluid particles.

Looking at figure 5.23b, the significance of this effect can be related to the column height. At the lower part of the domain, the ascending stream of bubbles is compact and not exposed to strong recirculating liquid motions. At a column height of 0.15 m to 0.2 m the plume breaks up and disperses the gas bubbles throughout the domain cross-section. Here, the size-dependent consideration of fluid particle motion takes effect and ultimatelly yields a reduction of the Sauter diameter.

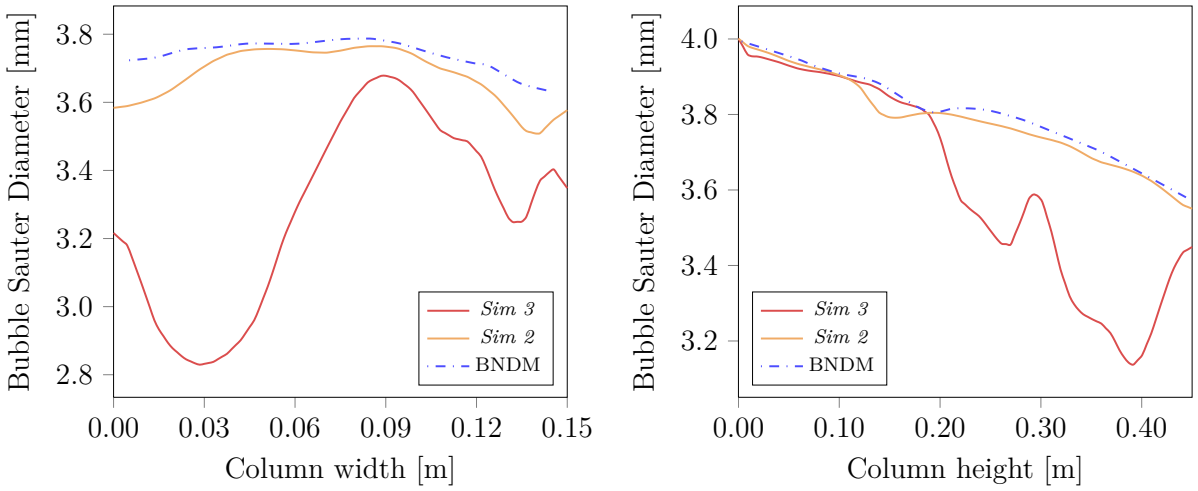

(a) Horizontal centerline at 0.284 m column height

(b) Vertical centerline of the column

Figure 5.23: Instantaneous bubble Sauter diameter profiles (time = 25 s); Comparison of two similar approaches (*Sim 2* (QMOM, IMV, no coalescence and breakup) and bubble number density model (BNDM) of Zhang et al. [229]) with results of simulation *Sim 3* (QMOM, RTA, no coalescence and breakup)

The similarity of QMOM results applying an IMV approach (*Sim 2*) and the BNDM data can also be identified from the comparison of illustrations presented in figure 5.24. There, contour plots of bubble Sauter diameter values on a central cutting plane are depicted for three different simulation times. While the size reduction of ascending bubbles due to interfacial mass transfer is strongest at early stages of the simulation, it exhibits a decline with the gradually increasing aqueous CO_2 concentration. As a result of converging concentration levels in gas and liquid, the interfacial mass transfer is attenuated and the impact of absorption processes on bubble sizes is less significant. The sequential illustrations of bubble size relations in both the QMOM and BNDM simulation capture this correlation with great resemblance.

The impact of moment velocity models on the depiction of absorption phenomena by the numerical simulation can be analyzed through a comparison of respective dissolved CO_2 concentration fields. Figure 5.25 exhibits contour plots of the instantaneous CO_2 concentrations for simulation times 25 s, 50 s and 75 s. While the range of concentration values is on a similar level at the starting phase of simulations, the results gradually diverge from each other as the absorption rate with the application of the RTA is considerably higher compared with the IMV simulations.

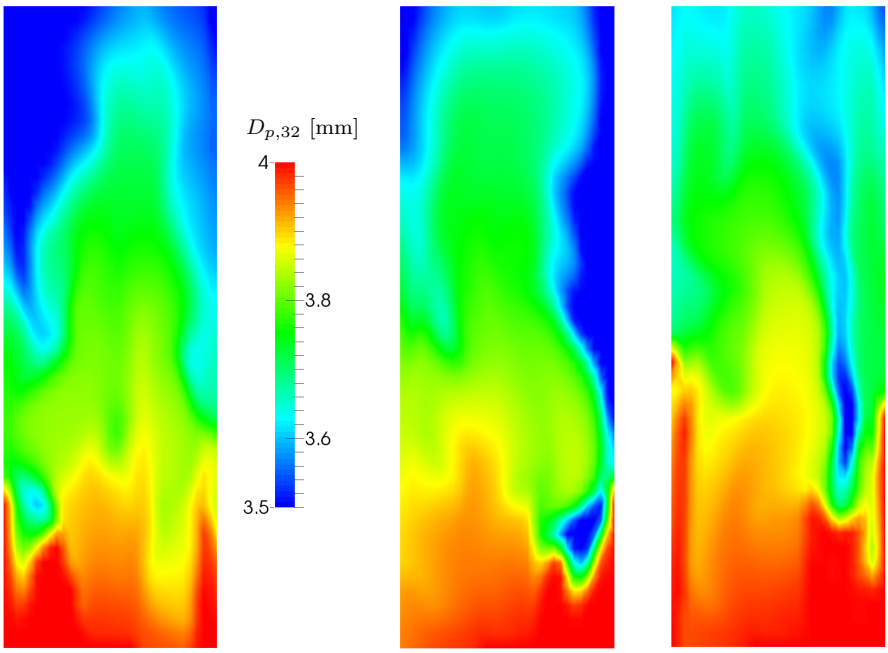

(a) Results of simulation *Sim 2* (QMOM, IMV, no coalescence and breakup)

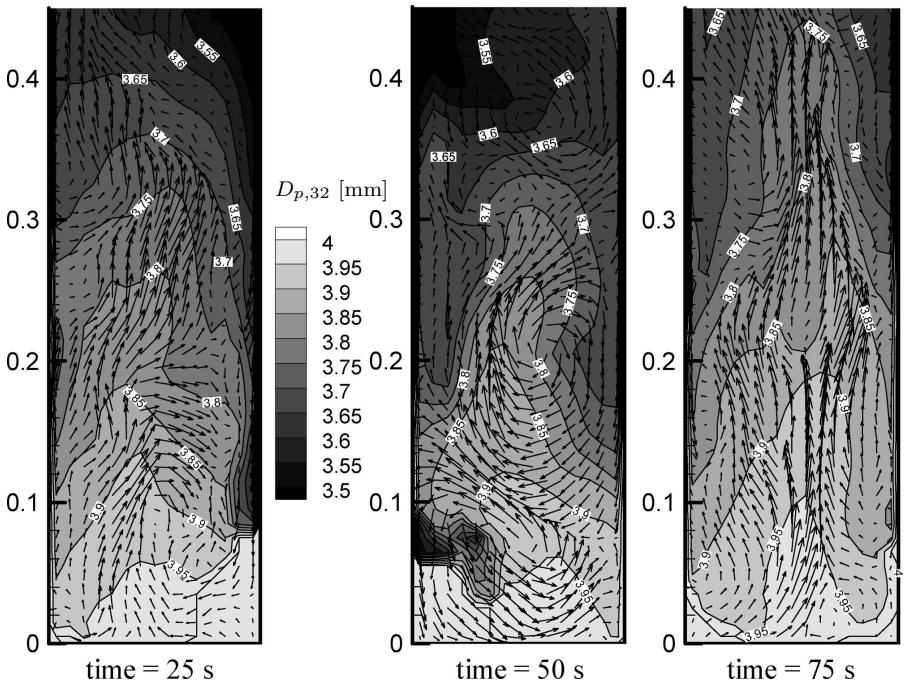

(b) Numerical comparative data (BNDM) [229]

Figure 5.24: Contour plots of the instantaneous bubble Sauter diameter values on a vertical cutting plane at column center

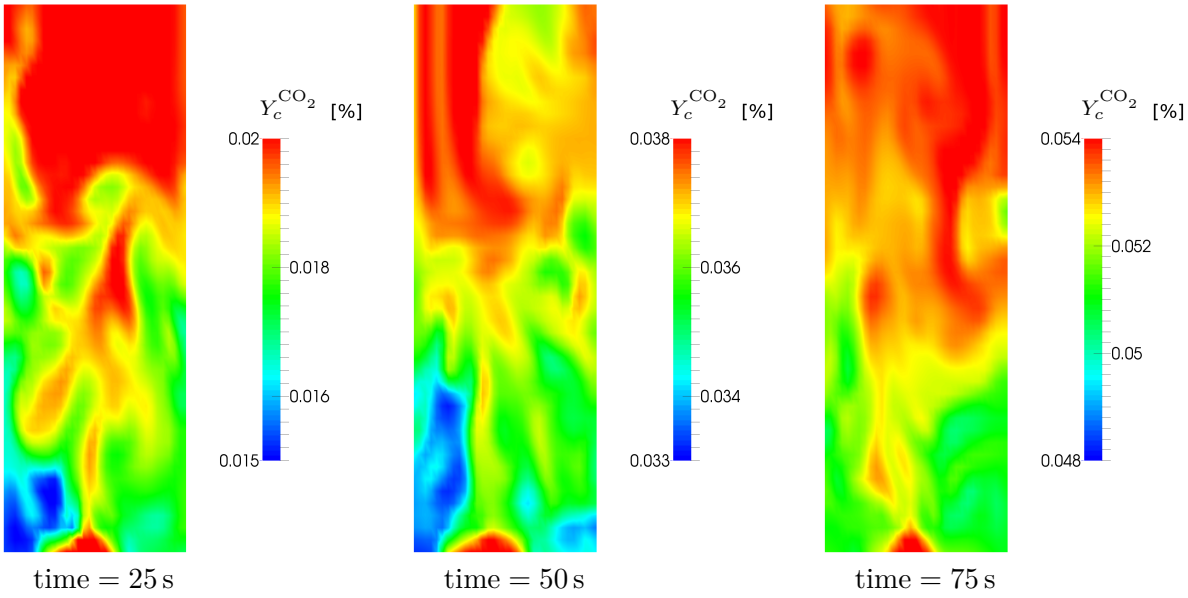

(a) Results of simulation *Sim 3* (QMOM, RTA, no coalescence and breakup)

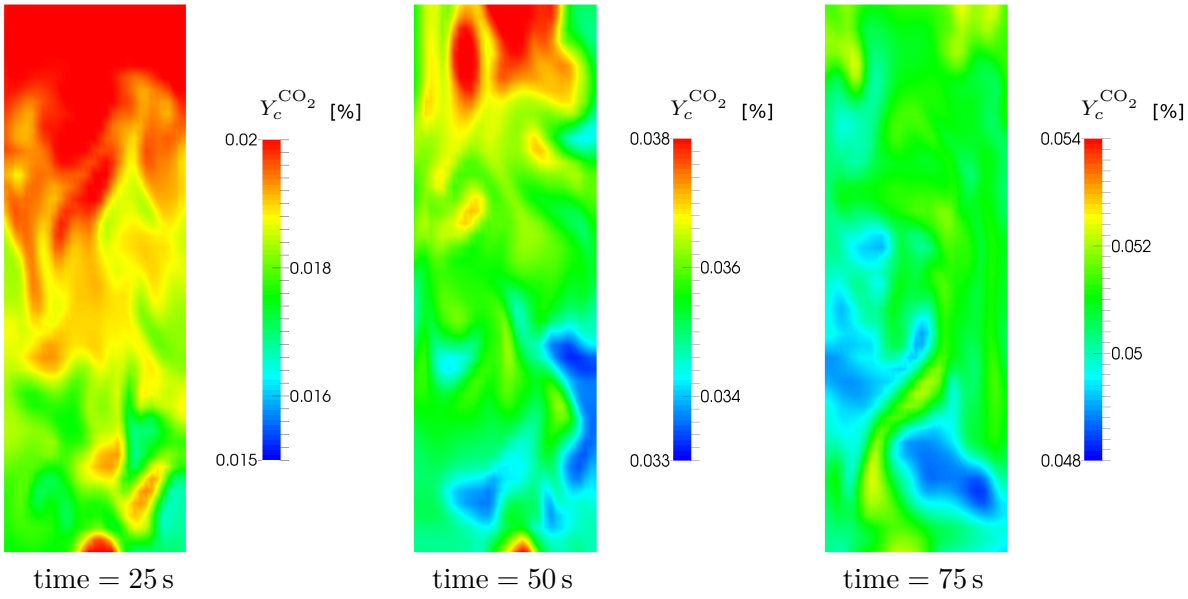

(b) Results of simulation *Sim 2* (QMOM, IMV, no coalescence and breakup)

Figure 5.25: Contour plots of the instantaneous CO_2 concentrations on a vertical cutting plane at column center

Generally, a narrow value range of local instantaneous CO_2 concentration in the domain can be assessed from figure 5.25, which indicates a rather homogeneous absorption process despite differences in local gas volume fractions and bubble size relations. The high intensity of liquid flow dynamics and turbulence accounts for a rapid leveling of concentration inhomogeneities, leaving only a minor general increase of dissolved CO_2 concentrations from the sparger to the column outlet.

Figure 5.26 shows the evolution of the domain-wide normalized dissolved CO_2 concentration for all conducted simulations as well as for the comparative data from Zhang et al. [229]. With the consideration of bubble size modifications in consequence of interfacial mass transfer an increase of absorption effects compared to the constant bubble case is observed for both numerical models. Smaller bubbles are associated with higher values for the volume-specific interfacial area and consequently enhance mass transfer processes. In contrast to the gradually growing difference of respective concentration levels in current simulations *Sim 1* and *Sim 2*, Zhang et al. predict a steep increase of dissolved CO_2 concentration at early BNDM simulation stages followed by a trend similar to the relations with constant bubble size. Figure 5.26a additionally depicts the aforementioned intensification of simulated absorption phenomena with the incorporation of the RTA. The resulting increase of the normalized concentration level compared with IMV findings is similar to the difference between *Sim 2* and *Sim 1* results.

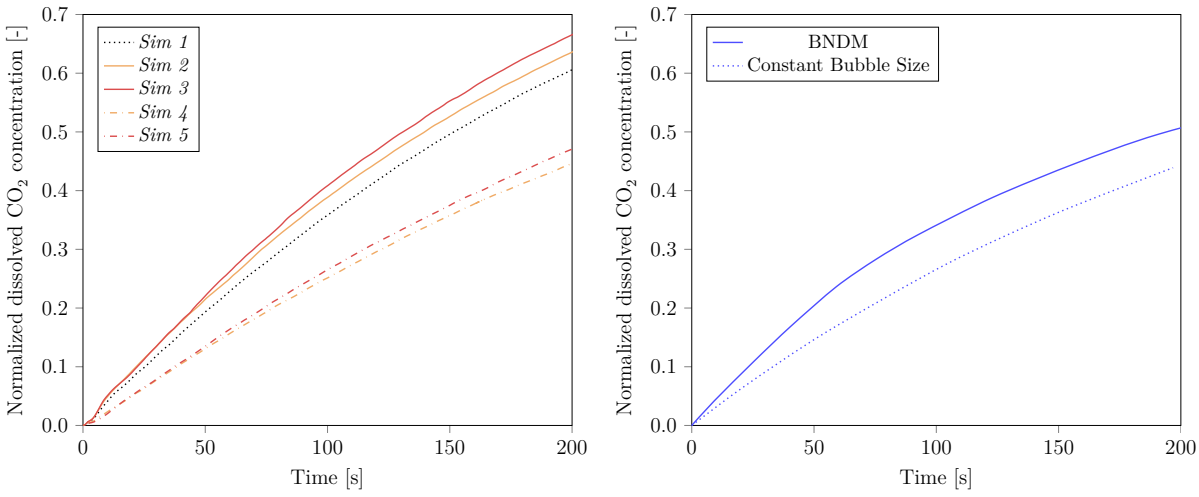

(a) QMOM simulation results (see table 5.3)

(b) Numerical comparative data [229]

Figure 5.26: Evolution of the normalized dissolved CO_2 concentration in the domain

An additional consideration of bubble breakup and coalescence yields results of dissolved CO_2 concentrations significantly below the alternative numerical findings. In spite of the slightly different fluid properties, the incorporation of fluid particle interaction models results in similar bubble size relations as for the air-water system presented in section 5.1.1.3. The impact of absorption processes on the simulated bubble size conditions is of subordinate importance. Respective bubble Sauter diameter values of 5 mm to 7 mm are accountable for the attenuated absorption of CO_2 compared with simulation results neglecting fluid particle interaction.

In figure 5.26, the quantitative discrepancies between current simulation results and comparative numerical data arguably originate from non-identical Eulerian model formulations for interfacial momentum exchange. While the lift force correlation applied by Zhang et al. [229] coincides with the current configuration, their simulations incorporate alternative drag and virtual mass force models by Tomiyama [200]. A comparative investigation of different model combinations for momentum and mass exchange formulations with the current model is desired, but must be left for future work.

6 Conclusions and Outlook

A numerical model has been developed for the accurate and computationally efficient description of polydisperse bubble column flows. With the current approach, it is possible to consider gas-liquid flow conditions in apparatuses of industrial relevance, with respect to geometrical scale as well as regarding fluid properties and operating conditions. The model functionalities allow for a depiction of prevailing hydrodynamic characteristics and enable the representation of the highly transient two-phase flow dynamics. In addition, the introduced numerical method has been extended in order to capture absorption phenomena in the gas-liquid environment, which determine the overall mass transfer capabilities of the apparatus.

An Euler-Euler two-fluid framework with appropriate submodels for the representation of interfacial exchange of momentum and mass constitutes the methodical basis of the developed solver. In this context, the effects of drag, lift and virtual mass forces are taken into account, which govern the interrelation of gas and liquid flow dynamics. Turbulence in the flow field is considered through an LES approach, which is specifically configured for the current application on bubbly flows. In this way, the dynamic behavior of the two-phase flow is captured accurately as opposed to a time-averaged attenuated representation in RANS formulations. The evaluation of transient turbulence characteristics provides the basis for the adequate prediction of local bubble-bubble and bubble-fluid interaction.

In order to account for local bubble size distributions, population balance theory is applied in combination with the two-fluid approach. With the incorporation of a method of moments formulation, this configuration is able to depict the polydisperse character of bubble column hydrodynamics with comparably low additional computational demand. The physical validity of moment sets is assured through a correction algorithm, which is tailored to adapt individual moment values with minimal intrusion. It resorts to one of two basic moment correction procedures depending on the prevailing bubble size distribution characteristics.

Closure of the moment transport equations is attained by making use of a quadrature approximation for source terms of high mathematical complexity. The current quadrature method of moments features appropriate bubble coalescence and breakup formulations to obtain an efficient evaluation without jeopardizing accuracy in the representation of the respective phenomena. The local size specific bubble motion is considered by individual moment transport velocities, which are evaluated through a numerically efficient approach. Based on the relation of size dependent bubble relaxation times, formulations for constituent moment velocities are derived and incorporated in the QMOM setup. The resulting numerical model is implemented by adapting and extending an existing CFD solver from the open-source software package *OpenFOAM*.

A validation study of the hydrodynamic model has been conducted using comparative experimental and numerical results for the two-phase flow in a square as well as in a circular cross-sectional bubble column domain. The respective findings demonstrate the capability of the present approach to accurately predict the gas and liquid flow fields and capture local bubble size relations considerably well. A quantitative comparison of the bubble size spectrum with the experimental results is carried out based on representative bubble diameters as well as regarding continuous representations of the bubble size distributions.

An additional study focuses on the effect of different moment transport velocity formulations on local bubble size relations. While the applied relaxation time approach yields simulation results which correspond well to respective experimental findings, the values from simplified considerations with identical moment velocities deviate substantially. Without the RTA, the tendency of smaller bubbles to accumulate in near-wall regions is not depicted, which results in an underrepresentation of these bubble sizes in corresponding distributions.

This deficient description of local bubble size relations consequently affects the representation of absorption phenomena in the two-phase flow. These correlations have been analyzed in an additional investigation regarding local and global flow characteristics influenced by gas absorption. To this end, several model configurations have been considered and their numerical results are presented in comparison. In this context, the impact of interfacial

mass transfer on bubble sizes has been investigated regarding spacial distribution as well as with respect to temporal evolution. Differences in the accumulation of the dissolved chemical species have been analyzed via illustrations of the instantaneous concentration field and in the form of normalized global concentration levels. The study results exhibit a moderate increase of absorption processes in case the adaption of bubble sizes due to mass transfer is included. This tendency is intensified if non-uniformity of moment velocities is taken into account by incorporating the RTA. With the consideration of bubble breakup and coalescence phenomena comes a significant decrease of absorption effects due to the general increase of bubble sizes. With regard to the considered bubble column flows, these numerical results indicate a subordinate importance of mass transfer effects on bubble size relations compared to bubble interaction phenomena.

Due to the complexity of respective measurement techniques, experimental investigations considering two-phase flow characteristics and specifically local bubble size distributions in bubble column flows are rare. To obtain this experimental data in a simplified manner, several corresponding studies resort to quasi two-dimensional bubble column geometries. These experimental setups are substantially different from industrial scale apparatuses, as the boundaries hinder the appearance of characteristic motions of the gas-liquid flow in these domains. To further scrutinize numerical results of gas-liquid flow models, an enhanced experimental research effort in this field is desired. With a broader spectrum of potential validation data, the quality and applicability of submodels for interfacial momentum exchange or fluid particle interaction could be adequately evaluated.

As discussed in section 2.4, various correlations have been proposed to account for interfacial forces such as drag, lift or virtual mass in an Euler-Euler context. With regard to the simulation of bubble column flows, numerous configurations of momentum exchange formulations have been used in published investigations. The concerning model specifications differ in terms of considered phenomena as well as their respective correlations. The closure formulations incorporated in the current work coincide with the majority of comparable investigations. Yet, additional studies with the application of alternative submodels could be used to evaluate the universality of the developed numerical approach regarding the considered gas-liquid flow conditions.

The relaxation time approach for the determination of individual moment transport velocities (see section 4.4) is based on the conception of solid particle movement under Stokes flow conditions. This drag correlation allows for a numerically stable and efficient computation of moment velocities, yet its application to bubble column hydrodynamics is suboptimal. The analysis of alternative formulations resulting in the incorporation of a more adequate drag correlation is desired for future work.

References

[1] T. Acher, P. Dems, S. Lenz, C. Gobert, and W. Polifke. Validation of a quadrature method of moments for polydisperse flow in bubble columns including poly-celerity, breakup and coalescence. In *International Conference on Multiphase Flow, Jeju, Korea*, 2013.

[2] T. Acher, P. Dems, S. Lenz, C. Gobert, and W. Polifke. A moment velocity model for the simulation of bubble column flows with a quadrature method of moments. *submitted to Chemical Engineering & Technology*, 2014.

[3] T. Acher, P. Dems, S. Lenz, C. Gobert, and W. Polifke. A quadrature method of moments for polydisperse flow in bubble columns including poly-celerity, breakup and coalescence. *The Journal of Computational Multiphase Flows*, in press, 2014.

[4] B. Andersson, R. Andersson, L. Håkansson, M. Mortensen, R. Sudiyo, and B. Van Wachem. Computational fluid dynamics for engineers. Cambridge University Press, 2012.

[5] R. Andersson and B. Andersson. Modeling the breakup of fluid particles in turbulent flows. *AIChE Journal*, 52(6):2031–2038, 2006.

[6] Ansys FLUENT V14.5 Population balance module manual. ANSYS, Inc., October 2012.

[7] S. P. Antal, R. T. Lahey Jr, and J. E. Flaherty. Analysis of phase distribution in fully developed laminar bubbly two-phase flow. *International Journal of Multiphase Flow*, 17(5):635–652, 1991.

[8] R. Aris. Vectors, tensors and the basic equations of fluid mechanics. Prentice-Hall, Englewood Cliffs, NJ, 1962.

[9] M. M. Attarakih, C. Drumm, and H.-J. Bart. Solution of the population balance equation using the sectional quadrature method of moments (SQMOM). *Chemical Engineering Science*, 64(4):742 – 752, 2009.

[10] T. R. Auton. The lift force on a spherical body in a rotational flow. *Journal of Fluid Mechanics*, 183:199–218, 1987.

[11] B. Azzopardi, D. Zhao, Y. Yan, H. Morvan, R. F. Mudde, and S. Lo. Hydrodynamics of gas-liquid reactors: normal operation and upset conditions. John Wiley & Sons, New York, 2011.

[12] H. D. Baehr and K. Stephan. Heat and mass transfer. Springer, Berlin, 2006.

[13] W. Bai, N. G. Deen, and J. A. M. Kuipers. Numerical analysis of the effect of gas sparging on bubble column hydrodynamics. *Industrial & Engineering Chemistry Research*, 50(8):4320–4328, 2011.

[14] R. Bannari, F. Kerdouss, B. Selma, A. Bannari, and P. Proulx. Three-dimensional mathematical modeling of dispersed two-phase flow using class method of population balance in bubble columns. *Computers & Chemical Engineering*, 32(12):3224 – 3237, 2008.

[15] K. Bech. Dynamic simulation of a 2D bubble column. *Chemical Engineering Science*, 60(19):5294–5304, 2005.

[16] M. R. Bhole, J. B. Joshi, and D. Ramkrishna. CFD simulation of bubble columns incorporating population balance modeling. *Chemical Engineering Science*, 63(8):2267–2282, 2008.

[17] M. R. Bhole, S. Roy, and J. B. Joshi. Laser doppler anemometer measurements in bubble column: effect of sparger. *Industrial & Engineering Chemistry Research*, 45(26):9201–9207, 2006.

[18] R. B. Bird, W. E. Stewart, and E. N. Lightfoot. Transport phenomena. John Wiley & Sons, New York, 2002.

[19] M. Blažej, G. M. Cartland Glover, S. C. Generalis, and J. Markoš. Gas–liquid simulation of an airlift bubble column reactor. *Chemical Engineering and Processing: Process Intensification*, 43(2):137–144, 2004.

[20] P. Bollweg, A. Kaufmann, and W. Polifke. Derivation and application of a poly-celerid method for poly-dispersed two-phase flows. In *6th International Conference on Multiphase Flow, Leipzig, Germany*, 2007.

[21] S. Bove. Computational fluid dynamics of gas-liquid flows including bubble population balances. PhD thesis, Esbjerg Institute of Technology, Aalborg University, 2005.

[22] S. Bove, T. Solberg, and B. H. Hjertager. Numerical aspects of bubble column simulations. *International Journal of Chemical Reactor Engineering*, 2(A1):1–22, 2004.

[23] H. Brauer. Particle/fluid transport processes. *Fortschrittsberichte der Verfahrenstechnik*, 17:61–98, 1979.

[24] C. E. Brennen. Fundamentals of multiphase flow. Cambridge University Press, 2005.

[25] T. Broeckhoven. Large eddy simulation of turbulent combustion: Numerical study and applications. PhD thesis, Vrije Universiteit Brussel, 2007.

[26] A. Buffo, M. Vanni, D. L. Marchisio, and R. O. Fox. Multivariate quadrature-based moments methods for turbulent polydisperse gas-liquid systems. *International Journal of Multiphase Flow*, 50:41–57, 2013.

[27] A. Buffo. Multivariate population balance for turbulent gas-liquid flows. PhD thesis, Politecnico di Torino, 2012.

[28] A. Buffo, M. Vanni, and D. L. Marchisio. Multidimensional population balance model for the simulation of turbulent gas–liquid systems in stirred tank reactors. *Chemical Engineering Science*, 70:31–44, 2012.

[29] A. Buffo, D. L. Marchisio, M. Vanni, and P. Renze. Simulation of polydisperse multiphase systems using population balances and example application to bubbly flows. *Chemical Engineering Research and Design*, 91(10):1859–1875, 2013.

[30] V. V. Buwa and V. V. Ranade. Dynamics of gas–liquid flow in a rectangular bubble column: experiments and single/multi-group CFD simulations. *Chemical Engineering Science*, 57(22):4715–4736, 2002.

[31] E. M. Cachaza, M. E. Díaz, F. J. Montes, and M. A. Galán. Simultaneous computational fluid dynamics (CFD) simulation of

the hydrodynamics and mass transfer in a partially aerated bubble column. *Industrial & Engineering Chemistry Research*, 48(18):8685–8696, 2009.

[32] R. S. Cant and E. Mastorakos. An introduction to turbulent reacting flows. Imperial College Press, 2008.

[33] J. N. E. Carneiro, V. Kaufmann, and W. Polifke. Implementation of a moments model in OpenFOAM for polydispersed multiphase flows. In *Open Source CFD International Conference, Berlin, Germany*, 2008.

[34] J. N. E. Carneiro, V. Kaufmann, and W. Polifke. Numerical simulation of droplet dispersion and evaporation with a moments-based CFD model. In *COBEM, Gramado, Brazil*, 2009.

[35] J. N. E. Carneiro, P. Dems, V. Kaufmann, and W. Polifke. Eulerian simulations of polydisperse flows using a moments model with a relaxation approach for the moment transport velocities fluidized and circulating fluidized beds. In *7th International Conference on Multiphase Flow, Tampa, FL*. 2010.

[36] J. N. E. Carneiro. Development of a presumed function method of moments with application to polydisperse sprays. PhD thesis, Technische Universität München, 2011.

[37] J. Chahed, V. Roig, and L. Masbernat. Eulerian–Eulerian two-fluid model for turbulent gas–liquid bubbly flows. *International Journal of Multiphase Flow*, 29(1):23–49, 2003.

[38] P. Chen. Modeling the fluid dynamics of bubble column flows. PhD thesis, Washington University, 2004.

[39] P. Chen, J. Sanyal, and M. Dudukovic. CFD modeling of bubble columns flows: implementation of population balance. *Chemical Engineering Science*, 59(22-23):5201 – 5207, 2004.

[40] P. Chen, M. P. Duduković, and J. Sanyal. Three-dimensional simulation of bubble column flows with bubble coalescence and breakup. *AIChE Journal*, 51(3):696–712, 2005.

[41] P. Chen, J. Sanyal, and M. Duduković. Numerical simulation of bubble columns flows: effect of different breakup and coalescence closures. *Chemical Engineering Science*, 60(4):1085 – 1101, 2005.

[42] A. K. Chesters. The modelling of coalescence processes in fluid-liquid dispersions: a review of current understanding. *Chemical Engineering Research & Design*, 69(A4):259–270, 1991.

[43] D.-F. Choi. Simulation von Mehrphasenströmungen mit einer Multi-Fluid-Methode. PhD thesis, Technische Universität Darmstadt, 2010.

[44] R. Clift, J. R. Grace, and M. E. Weber. Bubbles, drops, and particles. Academic Press, 1978.

[45] R. Collins. The effect of a containing cylindrical boundary on the velocity of a large gas bubble in a liquid. *Journal of Fluid Mechanics*, 28(01):97–112, 1967.

[46] S. Corrsin. The isotropic turbulent mixer: Part ii. arbitrary schmidt number. *AIChE Journal*, 10(6):870–877, 1964.

[47] C. A. Coulaloglou and L. L. Tavlarides. Description of interaction processes in agitated liquid-liquid dispersions. *Chemical Engineering Science*, 32(11):1289–1297, 1977.

[48] C. A. Coulaloglou. Dispersed phase interactions in an agitated flow vessel. PhD thesis, Illinois Institute of Technology, 1979.

[49] C. T. Crowe, J. D. Schwarzkopf, M. Sommerfeld, and Y. Tsuji. Multiphase flows with droplets and particles, second edition. CRC Press, 2012.

[50] E. L. Cussler. Diffusion: mass transfer in fluid systems. Cambridge University Press, 2009.

[51] P. V. Danckwerts. Significance of liquid-film coefficients in gas absorption. *Industrial & Engineering Chemistry*, 43(6):1460–1467, 1951.

[52] D. Darmana, N. G. Deen, and J. A. M. Kuipers. Detailed modeling of hydrodynamics, mass transfer and chemical reactions in a bubble column using a discrete bubble model. *Chemical Engineering Science*, 60(12):3383–3404, 2005.

[53] D. Darmana, N. G. Deen, J. A. M. Kuipers, W. K. Harteveld, and R. F. Mudde. Numerical study of homogeneous bubbly flow: influence of the inlet conditions to the hydrodynamic behavior. *International Journal of Multiphase Flow*, 35(12):1077–1099, 2009.

[54] D. Darmana. On the multiscale modelling of hydrodynamics, mass transfer and chemical reactions in bubble columns. PhD thesis, University of Twente, 2006.

[55] D. Darmana, N. G. Deen, and J. A. M. Kuipers. Modeling of mass transfer and chemical reactions in a bubble column reactor using a discrete bubble model. In *5th International Conference on Multiphase Flow, Yokohama, Japan*, 2004.

[56] W.-D. Deckwer and R. W. Field. Bubble column reactors. Wiley Chichester, 1992.

[57] W.-D. Deckwer, Y. Louisi, A. Zaidi, and M. Ralek. Hydrodynamic properties of the Fischer-Tropsch slurry process. *Industrial & Engineering Chemistry Process Design and Development*, 19(4):699–708, 1980.

[58] N. G. Deen, T. Solberg, and B. H. Hjertager. Large eddy simulation of the gas–liquid flow in a square cross-sectioned bubble column. *Chemical Engineering Science*, 56(21):6341–6349, 2001.

[59] E. Delnoij. Fluid dynamics of gas-liquid bubble columns. PhD thesis, Universiteit Twente, 1999.

[60] P. Dems, N. E. Carneiro, and W. Polifke. Large eddy simulation of particle-laden swirling flow with a presumed function method of moments. In *8th International Conference on CFD in Oil & Gas Metallurgical and Process Industries, Trondheim, Norway*, 2011.

[61] P. Deuflhard, F. Bornemann, and A. Hohmann. Numerische Mathematik, Band 1. De Gruyter, 2002.

[62] M. T. Dhotre, B. Niceno, and B. L. Smith. Large eddy simulation of a bubble column using dynamic sub-grid scale model. *Chemical Engineering Journal*, 136(2):337–348, 2008.

[63] M. T. Dhotre, N. G. Deen, B. Niceno, Z. Khan, and J. B. Joshi. Large eddy simulation for dispersed bubbly flows: a review. *International Journal of Chemical Engineering*, 2013, 2013.

[64] M. E. Díaz, A. Iranzo, D. Cuadra, R. Barbero, F. J. Montes, and M. A. Galán. Numerical simulation of the gas–liquid flow in a laboratory scale bubble column: influence of bubble size distribution and non-drag forces. *Chemical Engineering Journal*, 139(2):363–379, 2008.

[65] M. E. Díaz, F. J. Montes, and M. A. Galán. Influence of the lift force closures on the numerical simulation of bubble plumes in a rectangular bubble column. *Chemical Engineering Science*, 64(5):930–944, 2009.

[66] W. Dijkhuizen, I. Roghair, M. Van Sint Annaland, and J. A. M. Kuipers. DNS of gas bubbles behaviour using an improved 3D front tracking model–Drag force on isolated bubbles and comparison with experiments. *Chemical Engineering Science*, 65(4):1415–1426, 2010.

[67] D. Drew, L. Cheng, and R. T. Lahey Jr. The analysis of virtual mass effects in two-phase flow. *International Journal of Multiphase Flow*, 5 (4):233–242, 1979.

[68] D. A. Drew. Mathematical modeling of two-phase flow. *Annual Review of Fluid Mechanics*, 15(1):261–291, 1983.

[69] D. A. Drew and R. T. Lahey Jr. The virtual mass and lift force on a sphere in rotating and straining inviscid flow. *International Journal of Multiphase Flow*, 13(1):113–121, 1987.

[70] D. A. Drew and S. L. Passman. Theory of multicomponent fluids. Springer, 1999.

[71] M. P. Duduković, F. Larachi, and P. L. Mills. Multiphase reactors–revisited. *Chemical Engineering Science*, 54(13):1975–1995, 1999.

[72] T. M. Eidson. Numerical simulation of the turbulent Rayleigh–Bénard problem using subgrid modelling. *Journal of Fluid Mechanics*, 158(1): 245–268, 1985.

[73] H. A. E.-R. El-Asrag. Large eddy simulation subgrid model for soot prediction. PhD thesis, Georgia Institute of Technology, 2007.

[74] S. Elghobashi. On predicting particle-laden turbulent flows. *Applied Scientific Research*, 52(4):309–329, 1994.

[75] A. Falola, A. Borissova, and X. Z. Wang. Extended method of moment for general population balance models including size dependent growth rate, aggregation and breakage kernels. *Computers & Chemical Engineering*, 56:1–11, 2013.

[76] J. Ferry and S. Balachandar. A fast Eulerian method for disperse two-phase flow. *International Journal of Multiphase Flow*, 27(7):1199 – 1226, 2001.

[77] J. Ferry and S. Balachandar. Equilibrium expansion for the Eulerian velocity of small particles. *Powder Technology*, 125(2):131–139, 2002.

[78] J. H. Ferziger and M. Perić. Computational methods for fluid dynamics. Springer Berlin, 1996.

[79] R. O. Fox. Computational models for turbulent reacting flows. Cambridge University Press, 2003.

[80] R. O. Fox. Higher-order quadrature-based moment methods for kinetic equations. *Journal of Computational Physics*, 228(20):7771 – 7791, 2009.

[81] T. Frank, J. Shi, and A. D. Burns. Validation of Eulerian multiphase flow models for nuclear safety application. In *Third International Symposium on Two-Phase Modelling and Experimentation, Pisa, Italy*, 2004.

[82] W. Gautschi. Orthogonal polynomials: computation and approximation. Oxford University Press, 2004.

[83] M. Germano, U. Piomelli, P. Moin, and W. H. Cabot. A dynamic subgrid-scale eddy viscosity model. *Physics of Fluids A: Fluid Dynamics (1989-1993)*, 3(7):1760–1765, 1991.

[84] J. A. Geurst. Virtual mass in two-phase bubbly flow. *Physica A: Statistical Mechanics and its Applications*, 129(2):233–261, 1985.

[85] J. Gimbun, C. D. Rielly, and Z. K. Nagy. Modelling of mass transfer in gas–liquid stirred tanks agitated by rushton turbine and CD-6 impeller: a scale-up study. *Chemical Engineering Research and Design*, 87(4):437–451, 2009.

[86] H. Glaeser. Berechnung des Impuls- und Stofftransportes durch die Grenzfläche einer formveränderlichen Blase. PhD thesis, TU Berlin, 1976.

[87] R. G. Gordon. Error bounds in equilibrium statistical mechanics. *Journal of Mathematical Physics*, 9:655–663, 1968.

[88] J. R. Grace. Shapes and velocities of bubbles rising in infinite liquids. *Trans. Inst. Chem. Eng.*, 51(2):116–120, 1973.

[89] J. R. Grace, T. Wairegi, and T. H. Nguyen. Shapes and velocities of single drops and bubbles moving freely through immiscible liquids. *Trans. Inst. Chem. Eng*, 54(3):167–173, 1976.

[90] R. Grosch, H. Briesen, W. Marquardt, and M. Wulkow. Generalization and numerical investigation of QMOM. *AIChE Journal*, 53(1):207–227, 2007.

[91] A. Gupta and S. Roy. Euler–Euler simulation of bubbly flow in a rectangular bubble column: Experimental validation with radioactive particle tracking. *Chemical Engineering Journal*, 225:818–836, 2013.

[92] L. Hagesaether, H. A. Jakobsen, and H. F. Svendsen. A model for turbulent binary breakup of dispersed fluid particles. *Chemical Engineering Science*, 57(16):3251–3267, 2002.

[93] R. Hansen. Computational and experimental study of bubble size in bubble columns. PhD thesis, Aalborg University, 2009.

[94] F. H. Harlow and A. A. Amsden. Numerical calculation of multiphase fluid flow. *Journal of Computational Physics*, 17(1):19–52, 1975.

[95] T. Hibiki and M. Ishii. Two-group interfacial area transport equations at bubbly-to-slug flow transition. *Nuclear Engineering and Design*, 202(1):39–76, 2000.

[96] T. Hibiki and M. Ishii. Lift force in bubbly flow systems. *Chemical Engineering Science*, 62(22):6457–6474, 2007.

[97] R. Higbie. The rate of absorption of a pure gas into still liquid during short periods of exposure. *American Institute of Chemical Engineers*, 31:365–389, 1935.

[98] C. W. Hirt and B. D. Nichols. Volume of fluid (VOF) method for the dynamics of free boundaries. *Journal of Computational Physics*, 39 (1):201–225, 1981.

[99] B. H. Hjertager. Multi-fluid CFD analysis of chemical reactors. In *Multiphase Reacting Flows: Modelling and Simulation*, pages 125–179. Springer, 2007.

[100] H. M. Hulburt and S. Katz. Some problems in particle technology: A statistical mechanical formulation. *Chemical Engineering Science*, 19 (8):555–574, 1964.

[101] M. Ishii. Thermo-fluid dynamic theory of two-phase flow. *Paris, Eyrolles*, 22:275, 1975.

[102] M. Ishii and K. Mishima. Two-fluid model and hydrodynamic constitutive relations. *Nuclear Engineering and Design*, 82(2):107–126, 1984.

[103] M. Ishii and T. Hibiki. Thermo-fluid dynamics of two-phase flow. Springer, 2011.

[104] M. Ishii and N. Zuber. Drag coefficient and relative velocity in bubbly, droplet or particulate flows. *AIChE Journal*, 25(5):843–855, 1979.

[105] H. A. Jakobsen. Chemical reactor modeling: multiphase reactive flows. Springer, 2008.

[106] H. A. Jakobsen, , S. Grevskott, and H. F. Svendsen. Modeling of vertical bubble-driven flows. *Industrial & Engineering Chemistry Research*, 36(10):4052–4074, 1997.

[107] H. A. Jakobsen, H. Lindborg, and C. A. Dorao. Modeling of bubble column reactors: Progress and limitations. *Industrial & Engineering Chemistry Research*, 44(14):5107–5151, 2005.

[108] V. John and F. Thein. On the efficiency and robustness of the core routine of the quadrature method of moments (QMOM). *Chemical Engineering Science*, 75:327–333, 2012.

[109] W. P. Jones and M. Wille. Large-eddy simulation of a plane jet in a cross-flow. *International Journal of Heat and Fluid Flow*, 17(3): 296–306, 1996.

[110] N. Kantarci, F. Borak, and K. O. Ulgen. Bubble column reactors. *Process Biochemistry*, 40(7):2263–2283, 2005.

[111] I. Kataoka and A. Serizawa. Basic equations of turbulence in gas-liquid two-phase flow. *International Journal of Multiphase Flow*, 15 (5):843–855, 1989.

[112] G. Kocamustafaogullari and M. Ishii. Foundation of the interfacial area transport equation and its closure relations. *International Journal of Heat and Mass Transfer*, 38(3):481–493, 1995.

[113] N. I. Kolev. Multiphase flow dynamics 1: Fundamentals. Multiphase Flow Dynamics. Springer London, Limited, 2007.

[114] N. I. Kolev. Multiphase flow dynamics 4: Turbulence, gas adsorption and release, diesel fuel properties. Multiphase Flow Dynamics. Springer Berlin Heidelberg, 2012.

[115] M. Kostoglou and A. J. Karabelas. Toward a unified framework for the derivation of breakage functions based on the statistical theory of turbulence. *Chemical Engineering Science*, 60(23):6584–6595, 2005.

[116] M. Kraume. Transportvorgänge in der Verfahrenstechnik. Springer, 2004.

[117] E. Krepper, D. Lucas, T. Frank, H.-M. Prasser, and P. J. Zwart. The inhomogeneous MUSIG model for the simulation of polydispersed flows. *Nuclear Engineering and Design*, 238(7):1690–1702, 2008.

[118] R. Krishna and J. M. Van Baten. Eulerian simulations of bubble columns operating at elevated pressures in the churn turbulent flow regime. *Chemical Engineering Science*, 56(21):6249–6258, 2001.

[119] R. T. Lahey Jr. The analysis of phase separation and phase distribution phenomena using two-fluid models. *Nuclear Engineering and Design*, 122(1):17–40, 1990.

[120] R. T. Lahey Jr, M. Lopez de Bertodano, and O. C. Jones Jr. Phase distribution in complex geometry conduits. *Nuclear Engineering and Design*, 141(1):177–201, 1993.

[121] H. Lamb. Hydrodynamics. Cambridge University Press, 1993.

[122] J. C. Lamont and D. S. Scott. An eddy cell model of mass transfer into the surface of a turbulent liquid. *AIChE Journal*, 16(4):513–519, 1970.

[123] M. Lance and J. Bataille. Turbulence in the liquid phase of a uniform bubbly air–water flow. *Journal of Fluid Mechanics*, 222:95–118, 1991.

[124] Y. M. Lau, I. Roghair, N. G. Deen, M. Van Sint Annaland, and J. A. M. Kuipers. Numerical investigation of the drag closure for bubbles in bubble swarms. *Chemical Engineering Science*, 66(14): 3309–3316, 2011.

[125] F. Lehr and D. Mewes. A transport equation for the interfacial area density applied to bubble columns. *Chemical Engineering Science*, 56 (3):1159–1166, 2001.

[126] F. Lehr, M. Millies, and D. Mewes. Bubble-size distributions and flow fields in bubble columns. *AIChE Journal*, 48(11):2426–2443, 2002.

[127] O. Levenspiel. Chemical reaction engineering. *Industrial & Engineering Chemistry Research*, 38(11):4140–4143, 1999.

[128] Y. Liao and D. Lucas. A literature review of theoretical models for drop and bubble breakup in turbulent dispersions. *Chemical Engineering Science*, 64(15):3389–3406, 2009.

[129] Y. Liao and D. Lucas. A literature review on mechanisms and models for the coalescence process of fluid particles. *Chemical Engineering Science*, 65(10):2851–2864, 2010.

[130] Y. Liao. Development and validation of models for bubble coalescence and breakup. PhD thesis, Dresden University of Technology, 2013.

[131] S. Lo. Application of the MUSIG model to bubbly flows. Technical report, AEAT-1096, AEA Technology, 1996.

[132] M. Lopez de Bertodano, R. T. Lahey, and O. C. Jones. Development of a k-ε model for bubbly two-phase flow. *Journal of Fluids Engineering*, 116(1):128–134, 1994.

[133] M. A. Lopez de Bertodano. Two fluid model for two-phase turbulent jets. *Nuclear Engineering and Design*, 179(1):65–74, 1998.

[134] E. Loth. Numerical approaches for motion of dispersed particles, droplets and bubbles. *Progress in Energy and Combustion Science*, 26(3):161–223, 2000.

[135] D. Lucas, E. Krepper, and H.-M. Prasser. Use of models for lift, wall and turbulent dispersion forces acting on bubbles for poly-disperse flows. *Chemical Engineering Science*, 62(15):4146–4157, 2007.

[136] D. Lucas and E. Krepper. CFD models for polydispersed bubbly flows. Forschungszentrum Dresden-Rossendorf, 2007.

[137] H. Luo. Coalescence, breakup and liquid circulation in bubble column reactors. PhD thesis, NTH Trondheim, 1993.

[138] H. Luo and H. F. Svendsen. Theoretical model for drop and bubble breakup in turbulent dispersions. *AIChE Journal*, 42(5):1225–1233, 1996.

[139] B. F. Magnussen and B. H. Hjertager. On mathematical modeling of turbulent combustion with special emphasis on soot formation and combustion. In *Symposium (International) on Combustion, Pittsburgh, PA*, pages 719–729. Elsevier, 1977.

[140] D. L. Marchisio and R. O. Fox. Solution of population balance equations using the direct quadrature method of moments. *Journal of Aerosol Science*, 36(1):43–73, 2005.

[141] D. L. Marchisio, R. Dennis Vigil, and R. O. Fox. Implementation of the quadrature method of moments in CFD codes for aggregation–breakage problems. *Chemical Engineering Science*, 58(15):3337–3351, 2003.

[142] D. L. Marchisio. Quadrature method of moments for poly-disperse flows. In *Multiphase Reacting Flows: Modelling and Simulation*, pages 41–77. Springer, 2007.

[143] D. L. Marchisio and R. O. Fox. Computational models for polydisperse particulate and multiphase systems. Cambridge University Press, 2013.

[144] D. L. Marchisio, R. D. Vigil, and R. O. Fox. Quadrature method of moments for aggregation–breakage processes. *Journal of Colloid and Interface Science*, 258(2):322–334, 2003.

[145] C. Martínez-Bazán, J. L. Montanes, and J. C. Lasheras. On the breakup of an air bubble injected into a fully developed turbulent flow. Part 1. Breakup frequency. *Journal of Fluid Mechanics*, 401: 157–182, 1999.

[146] C. Martínez-Bazán, J. L. Montanes, and J. C. Lasheras. On the breakup of an air bubble injected into a fully developed turbulent flow. Part 2. Size PDF of the resulting daughter bubbles. *Journal of Fluid Mechanics*, 401:183–207, 1999.

[147] M. R. Maxey and J. J. Riley. Equation of motion for a small rigid sphere in a nonuniform flow. *Physics of Fluids*, 26:883, 1983.

[148] R. McGraw. Correcting moment sequences for errors associated with advective transport, 2006. URL http://www.ecd.bnl.gov/pubs/momentcorrection_mcgraw2006.pdf. Last visited 8th May 2014.

[149] R. McGraw. Description of aerosol dynamics by the quadrature method of moments. *Aerosol Science and Technology*, 27(2):255–265, 1997.

[150] H. D. Mendelson. The prediction of bubble terminal velocities from wave theory. *AIChE Journal*, 13(2):250–253, 1967.

[151] G. V. Messa. Two fluid model for solid liquid flows in pipeline systems. PhD thesis, Politecnico di Milano, Italy, 2013.

[152] M. Milelli, B. L. Smith, and D. Lakehal. Large-eddy simulation of turbulent shear flows laden with bubbles. *ERCOFTAC SERIES*, 8: 461–470, 2001.

[153] M. Milelli. A numerical analysis of confined turbulent bubble plumes. PhD thesis, Swiss Federal Institute of Technology Zurich, 2002.

[154] J. F. Mitre, R. S. M. Takahashi, C. P. R. Jr., and P. L. C. Lage. Analysis of breakage and coalescence models for bubble columns. *Chemical Engineering Science*, 65(23):6089 – 6100, 2010.

[155] T. Miyahara, Y. Matsuba, and T. Takahashi. Size of bubbles generated from perforated plates. *Kagaku Kogaku Ronbunshu*, 8(1): 13–17, 1982.

[156] P. Moilanen, M. Laakkonen, O. Visuri, V. Alopaeus, and J. Aittamaa. Modelling mass transfer in an aerated 0.2 m^3 vessel agitated by rushton, phasejet and combijet impellers. *Chemical Engineering Journal*, 142(1):95–108, 2008.

[157] P. Moin and J. Kim. Numerical investigation of turbulent channel flow. *Journal of Fluid Mechanics*, 118:341–377, 1982.

[158] F. J. Moraga, A. E. Larreteguy, D. A. Drew, and R. T. Lahey Jr. Assessment of turbulent dispersion models for bubbly flows in the low Stokes number limit. *International Journal of Multiphase Flow*, 29 (4):655–673, 2003.

[159] S. A. Morsi and A. J. Alexander. An investigation of particle trajectories in two-phase flow systems. *Journal of Fluid Mechanics*, 55(02):193–208, 1972.

[160] R. F. Mudde and O. Simonin. Two-and three-dimensional simulations of a bubble plume using a two-fluid model. *Chemical Engineering Science*, 54(21):5061–5069, 1999.

[161] B. Ničeno, M. Boucker, and B. L. Smith. Euler-Euler large eddy simulation (EELES) of a square cross-sectional bubble column using the NURESIM CFD platform. In *The 12th International Topical Meeting on Nuclear Reactor Thermal Hydraulics (NURETH-12), Pittsburgh, PA*, 2007.

[162] B. Ničeno, M. Boucker, and B. L. Smith. Euler-Euler large eddy simulation of a square cross-sectional bubble column using the Neptune–CFD code. *Science and Technology of Nuclear Installations*, 2009, 2008.

[163] B. Ničeno, M. T. Dhotre, and N. G. Deen. One-equation sub-grid scale (SGS) modelling for Euler–Euler large eddy simulation (EELES) of dispersed bubbly flow. *Chemical Engineering Science*, 63(15):3923–3931, 2008.

[164] R. I. Nigmatulin. Spatial averaging in the mechanics of heterogeneous and dispersed systems. *International Journal of Multiphase Flow*, 5 (5):353–385, 1979.

[165] E. Olmos, C. Gentric, C. Vial, G. Wild, and N. Midoux. Numerical simulation of multiphase flow in bubble column reactors. influence of bubble coalescence and break-up. *Chemical Engineering Science*, 56 (21):6359–6365, 2001.

[166] S. Osher and J. A. Sethian. Fronts propagating with curvature-dependent speed: algorithms based on Hamilton-Jacobi formulations. *Journal of Computational Physics*, 79(1):12–49, 1988.

[167] E. L. Paul, V. Atiemo-Obeng, and S. M. Kresta. Handbook of industrial mixing: science and practice. John Wiley & Sons, 2004.

[168] N. Peters. Turbulent combustion. Cambridge University Press, 2000.

[169] M. Petitti, A. Nasuti, D. L. Marchisio, M. Vanni, G. Baldi, N. Mancini, and F. Podenzani. Bubble size distribution modeling in stirred gas-liquid reactors with QMOM augmented by a new correction algorithm. *AIChE Journal*, 56(1):36–53, 2010.

[170] M. Petitti, M. Vanni, D. L. Marchisio, A. Buffo, and F. Podenzani. Simulation of coalescence, break-up and mass transfer in a gas-liquid stirred tank with CQMOM. *Chemical Engineering Journal*, 2013.

[171] D. Pfleger and S. Becker. Modelling and simulation of the dynamic flow behaviour in a bubble column. *Chemical Engineering Science*, 56 (4):1737 – 1747, 2001.

[172] D. Pfleger, S. Gomes, N. Gilbert, and H.-G. Wagner. Hydrodynamic simulations of laboratory scale bubble columns fundamental studies of the Eulerian–Eulerian modelling approach. *Chemical Engineering Science*, 54(21):5091–5099, 1999.

[173] H. Pitsch and H. Steiner. Large-eddy simulation of a turbulent piloted methane/air diffusion flame (Sandia flame D). *Physics of Fluids*, 12: 2541, 2000.

[174] S. B. Pope. PDF methods for turbulent reactive flows. *Progress in Energy and Combustion Science*, 11(2):119–192, 1985.

[175] S. B. Pope. Turbulent flows. Cambridge University Press, 2000.

[176] M. J. Prince and H. W. Blanch. Bubble coalescence and break-up in air-sparged bubble columns. *AIChE Journal*, 36(10):1485–1499, 1990.

[177] A. Prosperetti and G. Tryggvason. Computational methods for multiphase flow. Cambridge University Press, 2007.

[178] D. Ramkrishna. Population balances: theory and applications to particulate systems in engineering. Elsevier, 2000.

[179] V. V. Ranade. Computational flow modeling for chemical reactor engineering. Academic Press, 2002.

[180] I. Roghair, Y. M. Lau, N. G. Deen, H. M. Slagter, M. W. Baltussen, M. Van Sint Annaland, and J. A. M. Kuipers. On the drag force of bubbles in bubble swarms at intermediate and high Reynolds numbers. *Chemical Engineering Science*, 66(14):3204–3211, 2011.

[181] H. Rusche. Computational fluid dynamics of dispersed two-phase flows at high phase fractions. PhD thesis, Imperial College London (University of London), 2003.

[182] R. Rzehak and E. Krepper. CFD modeling of bubble-induced turbulence. *International Journal of Multiphase Flow*, 55:138–155, 2013.

[183] J. Sanyal, S. Vásquez, S. Roy, and M. P. Duduković. Numerical simulation of gas–liquid dynamics in cylindrical bubble column reactors. *Chemical Engineering Science*, 54(21):5071–5083, 1999.

[184] Y. Sato and K. Sekoguchi. Liquid velocity distribution in two-phase bubble flow. *International Journal of Multiphase Flow*, 2(1):79–95, 1975.

[185] L. Schiller and A. Naumann. Über die grundlegenden Berechnungen bei der Schwerkraftaufbereitung. *Zeitschrift des Vereines deutscher Ingenieure*, 77:318–320, 1933.

[186] B. Selma, R. Bannari, and P. Proulx. Simulation of bubbly flows: comparison between direct quadrature method of moments (DQMOM) and method of classes (CM). *Chemical Engineering Science*, 65(6): 1925 – 1941, 2010.

[187] J. A. Sethian. Level set methods and fast marching methods: evolving interfaces in computational geometry, fluid mechanics, computer vision, and materials science. Cambridge University Press, 1999.

[188] Y. T. Shah, B. G. Kelkar, S. P. Godbole, and W.-D. Deckwer. Design parameters estimations for bubble column reactors. *AIChE Journal*, 28(3):353–379, 1982.

[189] J. A. Shohat and J. D. Tamarkin. The problem of moments. American Mathematical Society, 1943.

[190] M. Simonnet, C. Gentric, E. Olmos, and N. Midoux. Experimental determination of the drag coefficient in a swarm of bubbles. *Chemical Engineering Science*, 62(3):858–866, 2007.

[191] W. A. Sirignano. Fluid dynamics and transport of droplets and sprays. Cambridge University Press, 2010.

[192] J. Smagorinsky. General circulation experiments with the primitive equations: I. the basic experiment. *Monthly Weather Review*, 91(3): 99–164, 1963.

[193] D. B. Spalding. Mixing and chemical reaction in steady confined turbulent flames. In *Symposium (International) on Combustion, Pittsburgh, PA*, pages 649–657. Elsevier, 1971.

[194] G. G. Stokes. On the effect of the internal friction of fluids on the motion of pendulums. Pitt Press, 1851.

[195] R. Sungkorn, J. J. Derksen, and J. G. Khinast. Modeling of turbulent gas–liquid bubbly flows using stochastic Lagrangian model and lattice-Boltzmann scheme. *Chemical Engineering Science*, 66(12):2745–2757, 2011.

[196] M. V. Tabib and P. Schwarz. Quantifying sub-grid scale (SGS) turbulent dispersion force and its effect using one-equation SGS large eddy simulation (LES) model in a gas–liquid and a liquid–liquid system. *Chemical Engineering Science*, 66(14):3071–3086, 2011.

[197] M. V. Tabib, S. A. Roy, and J. B. Joshi. CFD simulation of bubble column–an analysis of interphase forces and turbulence models. *Chemical Engineering Journal*, 139(3):589–614, 2008.

[198] P. J. Thomas. On the influence of the basset history force on the motion of a particle through a fluid. *Physics of Fluids A: Fluid Dynamics (1989-1993)*, 4(9):2090–2093, 1992.

[199] A. Tomiyama. Struggle with computational bubble dynamics. In *3rd International Conference on Multiphase Flow, Lyon, France*, 1998.

[200] A. Tomiyama. Drag, lift and virtual mass force acting on a single bubble. In *3rd International Symposium on Two-Phase Flow Modelling and Experimentation, Pisa, Italy*, 2004.

[201] A. Tomiyama, I. Kataoka, I. Zun, and T. Sakaguchi. Drag coefficients of single bubbles under normal and micro gravity conditions. *JSME International Journal. Series B, Fluids and Thermal Engineering*, 41 (2):472–479, 1998.

[202] A. Tomiyama, H. Tamai, I. Zun, and S. Hosokawa. Transverse migration of single bubbles in simple shear flows. *Chemical Engineering Science*, 57(11):1849–1858, 2002.

[203] H. L. Toor. The non-premixed reaction $A + B \rightarrow$ products. In *Turbulence in Mixing Operations*. Academic Press New York, 1975.

[204] A.-K. Tornberg. Interface tracking methods with application to multiphase flows. PhD thesis, Royal Institute of Technology Stockholm, 2000.

[205] A. A. Troshko and Y. A. Hassan. A two-equation turbulence model of turbulent bubbly flows. *International Journal of Multiphase Flow*, 27(11):1965–2000, 2001.

[206] G. Tryggvason and R. Scardovelli. Direct numerical simulations of gas-liquid multiphase flows. Cambridge University Press, 2011.

[207] M. Ungarish. Hydrodynamics of suspensions: fundamentals of centrifugal and gravity separation. Springer-Verlag New York, 1993.

[208] S. O. Unverdi and G. Tryggvason. A front-tracking method for viscous, incompressible, multi-fluid flows. *Journal of Computational Physics*, 100(1):25–37, 1992.

[209] E. I. V. van den Hengel, N. G. Deen, and J. A. M. Kuipers. Application of coalescence and breakup models in a discrete bubble model for bubble columns. *Industrial & Engineering Chemistry Research*, 44 (14):5233–5245, 2005.

[210] S. Van der Hoeven, B. Boersma, and D. Roekaerts. Large eddy simulation of turbulent non-premixed jet flames with a high order numerical method. In *Advanced Computational Methods in Science and Engineering*, pages 269–287. Springer, 2010.

[211] M. van Sint Annaland, N. G. Deen, and J. A. M. Kuipers. Multi-level modelling of dispersed gas-liquid two-phase flows. In *Bubbly Flows*, pages 139–157. Springer, 2004.

[212] T. Wang, J. Wang, and Y. Jin. A novel theoretical breakup kernel function for bubbles/droplets in a turbulent flow. *Chemical Engineering Science*, 58(20):4629–4637, 2003.

[213] T. Wang, J. Wang, and Y. Jin. A CFD-PBM coupled model for gas-liquid flows. *AIChE Journal*, 52(1):125–140, 2006.

[214] A. Watkins. The application of gamma and beta number size distribution to the modelling of sprays. In *20th Annual Conf. of ILASS-Europe, Orleans, France*, 2005.

[215] R. M. Wellek, A. K. Agrawal, and A. H. P. Skelland. Shape of liquid drops moving in liquid media. *AIChE Journal*, 12(5):854–862, 1966.

[216] D. Wiemann. Numerisches Berechnen der Strömungs- und Konzentrationsfelder in zwei- und dreiphasig betriebenen Blasensäulen. Cuvillier Verlag, 2005.

[217] D. C. Wilcox. Turbulence modeling for CFD. DCW Industries La Canada, CA, 1998.

[218] M. Wörner. A compact introduction to the numerical modeling of multiphase flows. Forschungszentrum Karlsruhe, 2003.

[219] D. L. Wright, R. McGraw, and D. E. Rosner. Bivariate extension of the quadrature method of moments for modeling simultaneous coagulation and sintering of particle populations. *Journal of Colloid and Interface Science*, 236(2):242–251, 2001.

[220] Q. Wu, S. Kim, M. Ishii, and S. G. Beus. One-group interfacial area transport in vertical bubbly flow. *International Journal of Heat and Mass Transfer*, 41(8):1103–1112, 1998.

[221] C. Xing, T. Wang, and J. Wang. Experimental study and numerical simulation with a coupled CFD–PBM model of the effect of liquid viscosity in a bubble column. *Chemical Engineering Science*, 95:313–322, 2013.

[222] G. H. Yeoh and J. Y. Tu. Thermal-hydrodynamic modeling of bubbly flows with heat and mass transfer. *AIChE Journal*, 51(1):8–27, 2005.

[223] G. H. Yeoh and J. Tu. Computational techniques for multiphase flows. Elsevier, 2009.

[224] D. You and P. Moin. A dynamic global-coefficient subgrid-scale eddy-viscosity model for large-eddy simulation in complex geometries. *Physics of Fluids (1994-present)*, 19(6):065110, 2007.

[225] C. Yuan, F. Laurent, and R. O. Fox. An extended quadrature method of moments for population balance equations. *Journal of Aerosol Science*, 51:1–23, 2012.

[226] C. Yuan and R. O. Fox. Conditional quadrature method of moments for kinetic equations. *Journal of Computational Physics*, 230(22): 8216–8246, 2011.

[227] D. Zhang, N. G. Deen, and J. A. M. Kuipers. Numerical simulation of the dynamic flow behavior in a bubble column: a study of closures for turbulence and interface forces. *Chemical Engineering Science*, 61 (23):7593 – 7608, 2006.

[228] D. Zhang. Eulerian modeling of reactive gas-liquid flow in a bubble column. PhD thesis, University of Twente, 2007.

[229] D. Zhang, N. G. Deen, and J. A. M. Kuipers. Euler-Euler modeling of flow, mass transfer, and chemical reaction in a bubble column. *Industrial & Engineering Chemistry Research*, 48(1):47–57, 2009.

[230] N. Zuber. Average volumetric concentration in two-phase flow systems. *Journal of Heat Transfer*, 87:453–464, 1965.

A Appendix

A.1 Transformation of discontinuous PBE source terms

For the depiction of polydispersity in terms of a monovariate PBE, the particle volume V_p is often preferred to the diameter D_p as single internal variable. In case solely discontinuous processes in the population balance are accounted for, the resulting PBE for the NDF $n'(V_p)$ reads

$$\frac{\partial n'(V_p)}{\partial t} + \nabla \cdot [n'(V_p)\,\boldsymbol{u}_p] = b'_{\mathcal{C}}(V_p) - d'_{\mathcal{C}}(V_p) + b'_{\mathcal{B}}(V_p) - d'_{\mathcal{B}}(V_p)\,. \tag{A.1}$$

The following transformation of PBE source terms to diameter-based expressions is predicated on the explanations of Marchisio et al. [144]. Given their definition, the following relation between the considered forms of NDFs can be deduced for spherical particles:

$$n'(V_p)\,\mathrm{d}V_p = n'\left(\frac{\pi}{6}D_p^3\right)\frac{\pi}{2}D_p^2\mathrm{d}D_p = n(D_p)\,\mathrm{d}D_p. \tag{A.2}$$

Furthermore, it must be noted that coalescence kernel function $r_{\mathcal{C}}$ and the breakup frequency F are intensive properties, which implies

$$r'_{\mathcal{C}}(\Theta, V_p) = r'_{\mathcal{C}}\left(\frac{\pi}{6}\gamma_p^3, \frac{\pi}{6}D_p^3\right) = r_{\mathcal{C}}(\gamma_p, D_p) \tag{A.3}$$

and, respectively,

$$F'_{\mathcal{B}}(V_p) = F'_{\mathcal{B}}\left(\frac{\pi}{6}D_p^3\right) = F_{\mathcal{B}}(D_p)\,. \tag{A.4}$$

In contrast,

$$\beta'_{\mathcal{B}}\left(\Theta_p, V_p\right) = \beta'_{\mathcal{B}}\left(\frac{\pi}{6}\gamma_p^3, \frac{\pi}{6}D_p^3\right) = \frac{2}{\pi D_p^2}\beta_{\mathcal{B}}\left(\gamma, D_p\right) \tag{A.5}$$

applies for the daughter bubble size distribution β.

With these prerequisites, the following transformations for the birth and death terms can be formulated:

- Coalescence birth term $b_{\mathcal{C}}$:

$$b'_{\mathcal{C}}\left(V_p\right) = \frac{1}{2}\int_0^{V_p} r'_{\mathcal{C}}\left(\Theta_p, V_p - \Theta_p\right) n'\left(V_p - \Theta_p\right) n'\left(\Theta_p\right)\, \mathrm{d}\Theta_p, \tag{A.6}$$

$$\begin{aligned} b'_{\mathcal{C}}\left(\frac{\pi}{6}D_p^3\right) &= \frac{1}{2}\int_0^{D_p} r_{\mathcal{C}}\left(\gamma_p, \left(D_p^3 - \gamma_p^3\right)^{1/3}\right) n'\left(\frac{\pi}{6}D_p^3 - \frac{\pi}{6}\gamma_p^3\right) n\left(\gamma_p\right)\, \mathrm{d}\gamma_p = \\ &\frac{1}{2}\int_0^{D_p} r_{\mathcal{C}}\left(\gamma_p, \left(D_p^3 - \gamma_p^3\right)^{1/3}\right) \frac{n\left(\left(D_p^3 - \gamma_p^3\right)^{1/3}\right)}{\frac{\pi}{2}\left(D_p^3 - \gamma_p^3\right)^{2/3}} n\left(\gamma_p\right)\, \mathrm{d}\gamma_p, \end{aligned} \tag{A.7}$$

$$b_{\mathcal{C}}(D_p) = \frac{D_p^2}{2}\int_0^{D_p} \frac{r_{\mathcal{C}}\left(\gamma_p, \left(D_p^3 - \gamma_p^3\right)^{1/3}\right)}{\left(D_p^3 - \gamma_p^3\right)^{2/3}}\, n(\gamma_p)\, n\left(\left(D_p^3 - \gamma_p^3\right)^{1/3}\right)\, \mathrm{d}\gamma_p, \tag{A.8}$$

with $b'_{\mathcal{C}}\left(V_p\right) = b'_{\mathcal{C}}\left(\frac{\pi}{6}D_p^3\right) = \frac{\pi}{2}D_p^2 b_{\mathcal{C}}\left(D_p\right)$.

- Coalescence death term $d_{\mathcal{C}}$:

$$d'_{\mathcal{C}}\left(V_p\right) = n'\left(V_p\right)\int_0^{\infty} r'_{\mathcal{C}}\left(\Theta_p, V_p\right) n'\left(\Theta_p\right)\, \mathrm{d}\Theta_p, \tag{A.9}$$

$$d'_{\mathcal{C}}\left(\frac{\pi}{6}D_p^3\right) = n'\left(\frac{\pi}{6}D_p^3\right)\int_0^{\infty} r'_{\mathcal{C}}\left(\frac{\pi}{6}\gamma_p^3, \frac{\pi}{6}D_p^3\right) n\left(\gamma_p\right)\, \mathrm{d}\gamma_p, \tag{A.10}$$

$$d_{\mathcal{C}}(D_p) = n(D_p)\int_0^{\infty} r_{\mathcal{C}}(\gamma_p, D_p)\, n(\gamma_p)\, \mathrm{d}\gamma_p, \tag{A.11}$$

with $d'_{\mathcal{C}}\left(V_p\right) = d'_{\mathcal{C}}\left(\frac{\pi}{6}D_p^3\right) = \frac{\pi}{2}D_p^2 d_{\mathcal{C}}\left(D_p\right)$.

- Breakup birth term $b_{\mathcal{B}}$:

$$b'_{\mathcal{B}}(V_p) = \int_{V_p}^{\infty} F'_{\mathcal{B}}(\Theta_p)\,\beta'_{\mathcal{B}}(\Theta_p, V_p)\,n'(\Theta_p)\,\mathrm{d}\Theta_p, \tag{A.12}$$

$$b'_{\mathcal{B}}\left(\frac{\pi}{6}D_p^3\right) = \int_{D_p}^{\infty} F'_{\mathcal{B}}\left(\frac{\pi}{6}D_p^3\right)\beta'_{\mathcal{B}}\left(\frac{\pi}{6}\gamma_p^3, \frac{\pi}{6}D_p^3\right)n(\gamma_p)\,\mathrm{d}\gamma_p, \tag{A.13}$$

$$b_{\mathcal{B}}(D_p) = \int_{D_p}^{\infty} F_{\mathcal{B}}(D_p)\,\beta_{\mathcal{B}}(\gamma_p, D_p)\,n(\gamma_p)\,\mathrm{d}\gamma_p, \tag{A.14}$$

  with $b'_{\mathcal{B}}(V_p) = b'_{\mathcal{B}}\left(\frac{\pi}{6}D_p^3\right) = \frac{\pi}{2}D_p^2 b_{\mathcal{B}}(D_p)$.

- Breakup death term $d_{\mathcal{B}}$:

$$d'_{\mathcal{B}}(V_p) = \int_0^{V_p} \frac{\Theta_p}{V_p}\beta'_{\mathcal{B}}(V_p, \Theta_p)\,\mathrm{d}\Theta_p\,F'_{\mathcal{B}}(V_p)\,n'(V_p), \tag{A.15}$$

$$d'_{\mathcal{B}}\left(\frac{\pi}{6}D_p^3\right) = \int_0^{D_p} \frac{\gamma_p^3}{D_p^3}\beta'_{\mathcal{B}}\left(\frac{\pi}{6}D_p^3, \frac{\pi}{3}\gamma_p^3\right)\frac{\pi}{2}\gamma_p^2\,\mathrm{d}\gamma_p\,F'_{\mathcal{B}}\left(\frac{\pi}{6}D_p^3\right)n'\left(\frac{\pi}{6}D_p^3\right) = \int_0^{D_p} \frac{\gamma_p^3}{D_p^3}\beta_{\mathcal{B}}(D_p, \gamma_p)\,\mathrm{d}\gamma_p\,F'_{\mathcal{B}}\left(\frac{\pi}{6}D_p^3\right)n'\left(\frac{\pi}{6}D_p^3\right), \tag{A.16}$$

$$d_{\mathcal{B}}(D_p) = \int_0^{D_p} \frac{\gamma_p^3}{D_p^3}\beta_{\mathcal{B}}(D_p, \gamma_p)\,\mathrm{d}\gamma_p\,F'_{\mathcal{B}}(D_p)\,n(D_p), \tag{A.17}$$

  with $d'_{\mathcal{B}}(V_p) = d'_{\mathcal{B}}\left(\frac{\pi}{6}D_p^3\right) = \frac{\pi}{2}D_p^2 d_{\mathcal{B}}(D_p)$.

A.2 Product difference algorithm

The PD algorithm, introduced by Gordon [87], is used to evaluate the coefficients $C_{a,i}$ and $C_{b,i}$ of the recurrence formula, which in turn define the Gaussian quadrature abscissas and weights (see section 3.5.1). For information beyond the following brief summary of this approach the reader can turn to Marchisio and Fox [143], John and Thein [108] or Marchisio [142].

As a preliminary step, the matrix $\boldsymbol{A}$ is defined with entries $A_{i,j}$ specified by

$$
\begin{aligned}
A_{i,1} &= \begin{cases} 1 & \text{for } i = 1 \\ 0 & \text{for } i \neq 1 \end{cases} && \text{with } i = 1, \ldots, 2N_i + 1 \,, \\
A_{i,2} &= (-1)^{i-1} \frac{M^{(i-1)}}{M^{(0)}} && \text{with } i = 1, \ldots, 2N_i \,, \\
A_{i,j} &= A_{1,j-1} A_{i+1,j-2} - A_{1,j-2} A_{i+1,j-1} && \begin{matrix} \text{with } i = 1, \ldots, 2N_i + 2 - j \\ \text{and } j = 3, \ldots, 2N_i + 1 \end{matrix} \,.
\end{aligned}
\tag{A.18}
$$

From this matrix the polynomial coefficients are evaluated by

$$
\begin{aligned}
C_{a,i} &= \begin{cases} \varrho_2 & \text{with } i = 1 \\ \varrho_{2i} + \varrho_{2i-1} & \text{with } i = 2, \ldots, N_i \end{cases} \,, \\
C_{b,i+1} &= \sqrt{-\varrho_{2i+1} \varrho_{2i}} \quad \text{with } i = 1, \ldots, N_i - 1 \,,
\end{aligned}
\tag{A.19}
$$

where

$$
\varrho_i = \frac{A_{1,i+1}}{A_{1,i} A_{1,i-1}} \quad \text{with } i = 2, \ldots, 2N_i. \tag{A.20}
$$

Examples:

PD algorithm:

$$
C_{a,1} = \frac{M^{(1)}}{M^{(0)}}. \tag{A.21}
$$

Recurrence formula:

$$
C_{a,1} = \frac{\langle D_p \mathrm{P}_0, \mathrm{P}_0 \rangle}{\langle \mathrm{P}_0, \mathrm{P}_0 \rangle} = \frac{\int_0^\infty D_p n(D_p) \, \mathrm{d}D_p}{\int_0^\infty n(D_p) \, \mathrm{d}D_p} = \frac{M^{(1)}}{M^{(0)}} \tag{A.22}
$$

$$
\Rightarrow \quad \mathrm{P}_1(D_p) = D_p - \frac{M^{(1)}}{M^{(0)}}. \tag{A.23}
$$

PD algorithm:

$$C_{b,2} = \left(\frac{M^{(2)} M^{(0)} - \left(M^{(1)}\right)^2}{M^{(0)} M^{(1)}} \frac{M^{(1)}}{M^{(0)}} \right)^{1/2} = \left(\frac{M^{(2)} M^{(0)} - \left(M^{(1)}\right)^2}{\left(M^{(0)}\right)^2} \right)^{1/2}. \tag{A.24}$$

Recurrence formula:

$$C_{b,2} = \left(\frac{\langle \mathrm{P}_1, \mathrm{P}_1 \rangle}{\langle \mathrm{P}_0, \mathrm{P}_0 \rangle} \right)^{1/2} = \left(\frac{\int_0^\infty \left(D_p^2 - 2 D_p \frac{M^{(1)}}{M^{(0)}} + \left(\frac{M^{(1)}}{M^{(0)}} \right)^2 \right) n(D_p) \, \mathrm{d}D_p}{\int_0^\infty n(D_p) \, \mathrm{d}D_p} \right)^{1/2}$$
$$= \left(\frac{M^{(2)} M^{(0)} - \left(M^{(1)}\right)^2}{\left(M^{(0)}\right)^2} \right)^{1/2}, \tag{A.25}$$

et cetera.

A.3 Fundamentals of the determination of quadrature weights

The QMOM quadrature weights are evaluated by equation (3.55) which is re-presented here for convenience:

$$w_i = v_{i,1}^2 M^{(0)}. \tag{A.26}$$

Here, $v_{i,1}$ is the first component of the normalized eigenvector of $\breve{\boldsymbol{C}}$ associated with the eigenvalue $\hat{D}_{p,i}$. This relation can be reconstructed by considering

$$\langle 1, \mathrm{P}_j \rangle = \sum_{i=1}^{N_i} w_i \mathrm{P}_j = \begin{cases} 0 & \text{for } j = 1, \ldots, N_i \\ M^{(0)} & \text{for } j = 0 \end{cases}. \tag{A.27}$$

Hence,

$$\breve{\mathbf{P}}\,[w_1,\ldots,w_{N_i}]^{\mathcal{T}} = M^{(0)}\,[1,0,\ldots]^{\mathcal{T}} = M^{(0)}\boldsymbol{e}_1, \tag{A.28}$$

with the matrix $\breve{\mathbf{P}}$ comprised of eigenvectors $\breve{\mathbf{P}} = \left[\breve{\mathbf{p}}(\hat{D}_{p,1}),\ldots,\breve{\mathbf{p}}(\hat{D}_{p,N_i})\right]$. By defining $\breve{\mathbf{P}}_{\aleph}$ which represents the orthogonal matrix with normalized eigenvectors of $\breve{\boldsymbol{C}}$ as columns ($\breve{\mathbf{P}}_{\aleph}^{\mathcal{T}}\breve{\boldsymbol{C}}\breve{\mathbf{P}}_{\aleph} = \mathrm{diag}(\hat{D}_{p,i},\ldots,\hat{D}_{p,N_i})$), it yields

$$\boldsymbol{v}_i = \breve{\mathbf{P}}_{\aleph}\boldsymbol{e}_i = v_{i,1}\breve{\mathbf{p}}(\hat{D}_{p,i}) \quad \Rightarrow \quad \breve{\mathbf{P}}_{\aleph} = \breve{\mathbf{P}}\boldsymbol{D}_v, \tag{A.29}$$

with $\boldsymbol{D}_v = \mathrm{diag}(v_{1,1},\ldots,v_{N_i,1})$. And finally the relation for w_i reads

$$w_i = M^{(0)}\boldsymbol{e}_i^{\mathcal{T}}\breve{\mathbf{P}}\boldsymbol{e}_1 = M^{(0)}\boldsymbol{e}_i^{\mathcal{T}}\breve{\mathbf{P}}_{\aleph}\boldsymbol{D}_v^{\mathcal{T}}\boldsymbol{e}_1 = M^{(0)}v_{i,1}^2. \tag{A.30}$$

A.4 Minimum square gradient algorithm

A.4.1 Fundamental procedure

A detailed explication of this conversion procedure including exemplary moment combinations is presented by McGraw [148] or Petitti et al. [169]. The following summary aims to provide the fundamental idea of this algorithm.

Starting point of the *minimum square gradient algorithm* is the determination of a difference table with $\ln\left(M^{(k)}\right)$ being the first column entries as depicted in table A.1.

$\ln\left(M^{(k)}\right)$	$\mathfrak{D}_1$	$\mathfrak{D}_2$	$\mathfrak{D}_3 \equiv \boldsymbol{a}$	…
$\ln\left(M^{(0)}\right)$	$\mathfrak{D}_{1,1} = \ln\left(M^{(1)}\right) - \ln\left(M^{(0)}\right)$	$\mathfrak{D}_{2,1} = \mathfrak{D}_{1,2} - \mathfrak{D}_{1,1}$	$a_1 = \mathfrak{D}_{2,2} - \mathfrak{D}_{2,1}$	…
$\ln\left(M^{(1)}\right)$	$\mathfrak{D}_{1,2} = \ln\left(M^{(2)}\right) - \ln\left(M^{(1)}\right)$	$\mathfrak{D}_{2,2} = \mathfrak{D}_{1,3} - \mathfrak{D}_{1,2}$	$a_2 = \mathfrak{D}_{2,3} - \mathfrak{D}_{2,2}$	…
$\ln\left(M^{(2)}\right)$	$\mathfrak{D}_{1,3} = \ln\left(M^{(3)}\right) - \ln\left(M^{(2)}\right)$	$\mathfrak{D}_{2,3} = \mathfrak{D}_{1,4} - \mathfrak{D}_{1,3}$	$a_3 = \mathfrak{D}_{2,4} - \mathfrak{D}_{2,3}$	…
⋮	⋮	⋮	⋮	

Table A.1: Difference table subject to $\ln\left(M^{(k)}\right)$

Using this table, compliance of moment combinations with the convexity criterion is verified by non-negativity of third column entries ($\mathfrak{D}_{2,1}, \mathfrak{D}_{2,2}, \ldots$).

If the relation of $\ln\left(M^{(k)}\right)$ and k is of quadratic form, fourth column entries equal zero and consequently yield $|\boldsymbol{a}|^2 = 0$. The moment correction procedure is based on the minimization of $|\boldsymbol{a}|^2$ via

$$\boldsymbol{a}_{new} = \boldsymbol{a}_{old} + \ln\left(\mathfrak{C}_k \boldsymbol{b}_k\right), \tag{A.31}$$

where $\boldsymbol{b}_k$ represents the response vector which characterizes the impact of a unit increment of $\ln\left(M^{(k)}\right)$ on $\boldsymbol{a}$. In case the first six moments $(M^{(0)}, \ldots, M^{(5)})$ are considered, this concept can be depicted by a vector modification as illustrated in figure A.1

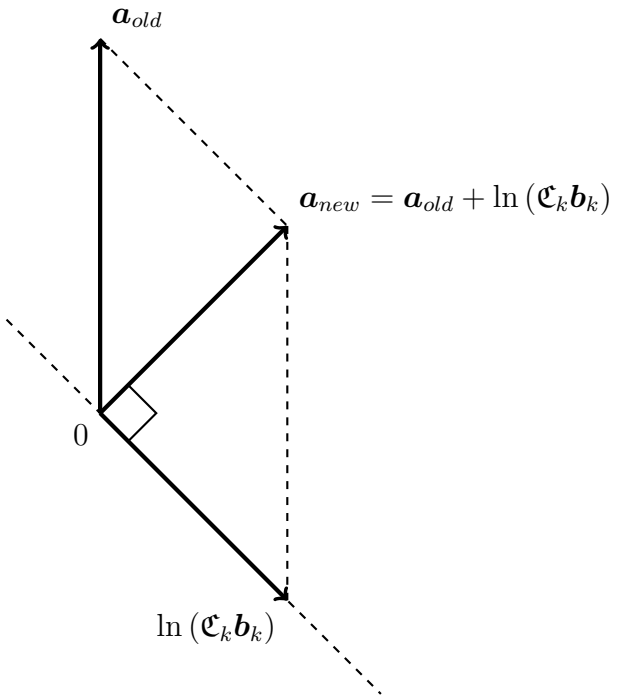

Figure A.1: Illustration of the minimum square gradient correction procedure in the form of a vector operation [149]

By assigning orthogonality between $\boldsymbol{a}_{new}$ and $\boldsymbol{b}_k$ the adaption is ensured to be of minimal extent and is described by

$$\left(\boldsymbol{a}_{old} + \ln\left(\mathfrak{C}_k \boldsymbol{b}_k\right)\right) \cdot \boldsymbol{b}_k = 0, \tag{A.32}$$

which results in the definition of the modification factor $\mathfrak{C}_k$ as

$$\mathfrak{C}_k = \exp\left(-\cos\left(\boldsymbol{a}_{old}, \boldsymbol{b}_k\right)\frac{|\boldsymbol{a}_{old}|}{|\boldsymbol{b}_k|}\right) = \exp\left(-\frac{(\boldsymbol{a}_{old}\cdot\boldsymbol{b}_k)}{|\boldsymbol{b}_k|^2}\right). \tag{A.33}$$

With equation (A.31) this consequently yields

$$|\boldsymbol{a}_{new}|^2 = |\boldsymbol{a}_{old}|^2\left[1-\cos^2\left(\boldsymbol{a}_{old}, \boldsymbol{b}_k\right)\right]. \tag{A.34}$$

The moment $M^{(k^*)}$ to be modified is identified by the largest value for $\cos^2\left(\boldsymbol{a}_{old}, \boldsymbol{b}_k\right)$ in order to optimally rectify smoothness of $\ln\left(M^{(k)}\right)$ as a function of k. Thus, the corrected moment value is determined by

$$\ln\left(M_{new}^{(k^*)}\right) = \ln\left(M_{old}^{(k^*)}\right) + \ln\left(\mathfrak{C}_k*\right). \tag{A.35}$$

If the resulting set of moments does not fulfill the convexity criterion or fails the superordinate Hankel-Hadamard requirement (4.22), the correction procedure sequentially proceeds minimizing $|\boldsymbol{a}|^2$ until eventually a valid moment combination is attained.

A.4.2 Virtually monodisperse distributions

Number density functions which practically represent monodisperse distributions are characterized by a relation of consecutive function moments as

$$\frac{M^{(k+1)}}{M^{(k)}} \approx \frac{M^{(k)}}{M^{(k-1)}}. \tag{A.36}$$

With the consideration of an extended formulation of the third column entries $\mathfrak{D}_{2,k}$ of table A.1 as

$$\begin{aligned}\mathfrak{D}_{2,k} &= \left[\ln\left(M^{(k+1)}\right) - \ln\left(M^{(k)}\right)\right] - \left[\ln\left(M^{(k)}\right) - \ln\left(M^{(k-1)}\right)\right] \\ &= \ln\left(\frac{M^{(k+1)}}{M^{(k)}}\right) - \ln\left(\frac{M^{(k)}}{M^{(k-1)}}\right),\end{aligned} \tag{A.37}$$

it becomes evident that $\mathfrak{D}_{2,k} \approx 0$ for the regarded functional form. Hence, the identification of an invalid set of moments is dependent on minor changes of $\mathfrak{D}_{2,k}$ or can even be influenced by numerical inaccuracies.

With $\mathfrak{D}_{2,k} \approx 0$ follows $a_k \approx 0$ which complicates the accurate evaluation of equation (A.33) to find the exact value of $\mathfrak{C}_k \approx 1$. This in turn impinges on the precise moment correction in correlation (A.35). Thus, the determination of a valid moment combination for virtually monodisperse distributions by the *minimum square gradient algorithm* either results in a mathematically inefficient procedure or is prevented due to numerical inaccuracies.

A.5 RTA with Schiller-Naumann drag correlation

The drag relations of dispersed spherical particles are accurately represented by the Stokes model in case of low relative velocities to the continuous phase flow ($\mathrm{Re}_p < 1$), while the formulation of Schiller & Naumann depicts the respective phenomena for moderate to high particle Reynolds numbers ($0.1 < \mathrm{Re}_p < 1000$). Combining the general definition of the particle relaxation time

$$\tau = \frac{4}{3}\frac{\rho_d D_p}{\rho_c C_D \left|(\boldsymbol{u}_c - \boldsymbol{u}_p)\right|}, \tag{A.38}$$

with the C_D-correlation of the Schiller-Naumann approach yields

$$\tau = \min\left(\frac{\rho_d D_p^2}{18\nu_c\rho_c}\,\frac{1}{1+0.15\,\mathrm{Re}_p^{0.687}}, \frac{4}{3}\frac{\rho_d D_p}{0.44\rho_c\left|\boldsymbol{u}_d - \boldsymbol{u}_c\right|}\right). \tag{A.39}$$

A.5.1 QMOM formulation

An evaluation of equation (A.39) in a QMOM framework is straightforward as the quadrature parameters are adopted to determine the particle relaxation time in a moments context as

$$\tau^{(k)} = \frac{1}{M^{(k)}} \int_0^\infty \tau(D_p)\, D_p^k\, n(D_p)\, \mathrm{d}D_p \approx \frac{1}{M^{(k)}} \sum_{i=1}^{N_i} \tau(D_{p,i})\, D_{p,i}^k\, w_i. \tag{A.40}$$

A.5.2 Approximation by series expansion

If the closure procedure of the MTE does not resort to a quadrature approximation of the NDF (e.g., PMOM), $\tau^{(k)}$ can be approximated by a series expansion. To this end, expression (A.39) is reformulated to give

$$\tau = \min \left(\underbrace{\frac{\rho_d}{2.7 \nu_c^{0.313} \rho_c u_{rel}^{0.687}} \; \frac{D_p^2}{\frac{1}{0.15}\left(\frac{\nu_c}{u_{rel}}\right)^{0.687} + D_p^{0.687}}}_{\tau_1}, \underbrace{\frac{4}{3} \frac{\rho_d D_p}{0.44 \rho_c u_{rel}}}_{\tau_2} \right). \tag{A.41}$$

with $u_{rel} = |\boldsymbol{u}_d - \boldsymbol{u}_c|$. The transformation of τ_1 into a moments context yields

$$\tau_1^{(k)} = \frac{1}{M^{(k)}} \int_0^\infty \left(\mathfrak{A} \, \frac{D_p^2}{\mathfrak{B} + D_p^{0.687}} \right) n(D_p)\, D_p^k\, \mathrm{d}D_p, \tag{A.42}$$

where $\mathfrak{A} = \frac{\rho_d}{2.7 \nu_c^{0.313} \rho_c u_{rel}^{0.687}}$ and $\mathfrak{B} = \frac{1}{0.15}\left(\frac{\nu_c}{u_{rel}}\right)^{0.687}$. For the approximative determination of $\tau_1^{(k)}$, a series expansion for τ_1 is conducted around $\mathfrak{B} = 0$ to result in

$$\tau_1 \approx \mathfrak{A} D_p^{1.313} - \mathfrak{A}\mathfrak{B} D_p^{0.626} + \mathfrak{A}\mathfrak{B}^2 D_p^{-0.061}. \tag{A.43}$$

The consideration of the quadratic term in equation (A.43) is necessary to prevent the occurrence of negative relaxation time values in case of small particle Reynolds numbers. Thus, the approximation for $\tau_1^{(k)}$ reads

$$\tau_1^{(k)} \approx \mathfrak{A} \frac{M^{(k+1.313)}}{M^{(k)}} - \mathfrak{A}\mathfrak{B} \frac{M^{(k+0.626)}}{M^{(k)}} + \mathfrak{A}\mathfrak{B}^2 \frac{M^{(k-0.061)}}{M^{(k)}}. \tag{A.44}$$

Regarding the upper limit τ_2 of the Schiller-Naumann relaxation time correlation (A.41), the equivalent in terms of a MOM formulation is obtained as

$$\tau_2^{(k)} = \frac{4}{3}\frac{\rho_d}{0.44\,\rho_c u_{rel}}\frac{M^{(k+1)}}{M^{(k)}}. \tag{A.45}$$

With the approximate formulation (A.43), the drag correlation of Schiller & Naumann does not convert to the Stokes model anymore for low particle Reynolds numbers. The incorporation of the Stokes moment relaxation time introduced in expression (4.45) into the minimum function of the Schiller-Naumann correlation restores this transition. Thus, the resulting correlation for $\tau^{(k)}$ is given by

$$\tau^{(k)} = \min\left(\frac{\rho_d}{18\mu_c}\frac{M^{(k+2)}}{M^{(k)}}, \tau_1^{(k)}, \tau_2^{(k)}\right). \tag{A.46}$$

A.6 Towards an extension of the RTA to account for lift force effects

The RTA as outlined in section 4.4 is based on an expansion of the particle velocity $\boldsymbol{u}_p$ around the continuous phase velocity $\boldsymbol{u}_c$ subject to the particle relaxation time τ. The consequent formulation is introduced in expression (4.40) and subsequently used to deduce the moment transport velocity correlation as stated in equation (4.43) and re-presented here for convenience:

$$\boldsymbol{u}^{(k)} \approx \boldsymbol{u}_c + \frac{\tau^{(k)}}{\tau_0}\left(\boldsymbol{u}_0 - \boldsymbol{u}_c\right) = \boldsymbol{u}_c + \frac{\tau^{(k)}}{\tau^{(3)}}\boldsymbol{u}_{rel}. \tag{A.47}$$

This concept corresponds to an evaluation of $\boldsymbol{u}^{(k)}$ by a linear interpolation along $\boldsymbol{u}_{rel}$, a deflection normal to this direction is neglected.

A.6.1 Impact of lift force

Regarding bubbly flows, lift force effects, as introduced in section 2.4.1.2, are arguably the main reason for an impact on fluid particle motion in a direction deviant to $\boldsymbol{u}_{rel}$. With the assumption that the particle velocity component in the direction of action of the lift force $\left(\boldsymbol{u}_p^{\perp} = \left(\boldsymbol{u}_p \cdot \frac{\boldsymbol{F}_L}{|\boldsymbol{F}_L|}\right)\frac{\boldsymbol{F}_l}{|\boldsymbol{F}_l|} \Rightarrow \boldsymbol{u}_p^{\perp} \perp \boldsymbol{u}_{rel}\right)$ is not influenced by any other phenomena, an expansion subject to the lift coefficient C_L can be formulated analogously to the previous RTA as

$$\left.\frac{\mathrm{d}\boldsymbol{u}_p^{\perp}}{\mathrm{d}t}\right|_{C_L} = \underbrace{\left.\frac{\mathrm{d}\boldsymbol{u}_p^{\perp}}{\mathrm{d}t}\right|_{C_L=0}}_{=0} + C_L \frac{\left.\frac{\mathrm{d}\boldsymbol{u}_p^{\perp}}{\mathrm{d}t}\right|_{C_{L,0}} - 0}{C_{L,0} - 0}. \tag{A.48}$$

Consequently, $\frac{\mathrm{d}\boldsymbol{u}_p^{\perp}}{\mathrm{d}t}$ is a linear function of the lift coefficient:

$$\frac{\mathrm{d}\boldsymbol{u}_p^{\perp}}{\mathrm{d}t} = \frac{C_L}{C_{L,0}} \left.\frac{\mathrm{d}\boldsymbol{u}_p^{\perp}}{\mathrm{d}t}\right|_{C_{L,0}}. \tag{A.49}$$

A simple first order discretization in time yields

$$\Delta\boldsymbol{u}_p^{\perp} = \left(\boldsymbol{u}_p - \boldsymbol{u}_p^{old}\right)^{\perp} = \frac{C_L}{C_{L,0}} \Delta\, \boldsymbol{u}_p^{\perp}|_{C_{L,0}}. \tag{A.50}$$

A.6.2 Extension of the RTA

The RTA as presented in section 4.4 is limited to the consideration of effects on the particle velocity in relative velocity direction. A particle size-dependent force normal to this direction (e.g., Tomiyama lift force) disagrees with this conception. In case of the simultaneous consideration of drag and lift force effects, expressions (4.40) and (A.50) can be combined to yield

$$\boldsymbol{u}_p = \underbrace{\boldsymbol{u}_c + \frac{\tau}{\tau_0}\boldsymbol{u}_{rel}}_{(a)} + \underbrace{\frac{\tau}{\tau_0}}_{(d)} \left(\underbrace{-\Delta\, \boldsymbol{u}_p^{\perp}\big|_{C_{L,0}}}_{(b)} + \underbrace{\frac{C_L}{C_{L,0}} \Delta\, \boldsymbol{u}_p^{\perp}\big|_{C_{L,0}}}_{(c)} \right). \tag{A.51}$$

(a) Previous formulation; Implicitly includes deflection of reference particle normal to $\boldsymbol{u}_{rel}$

(b) Deflection of reference particle normal to $\boldsymbol{u}_{rel}$ is subtracted to allow for an unimpaired linear interpolation according to (A.50)

(c) Linearly interpolated contribution of the lift force is added to the particle velocity evaluation

(d) As the lift force is a linear function of both the lift coefficient and the reference particle velocity $\boldsymbol{u}_0$, this prefactor is appropriate

Three examples for the determination of the particle velocity by the extended RTA are illustrated in figure A.2 and several characteristics of equation (A.51) are presented thereafter.

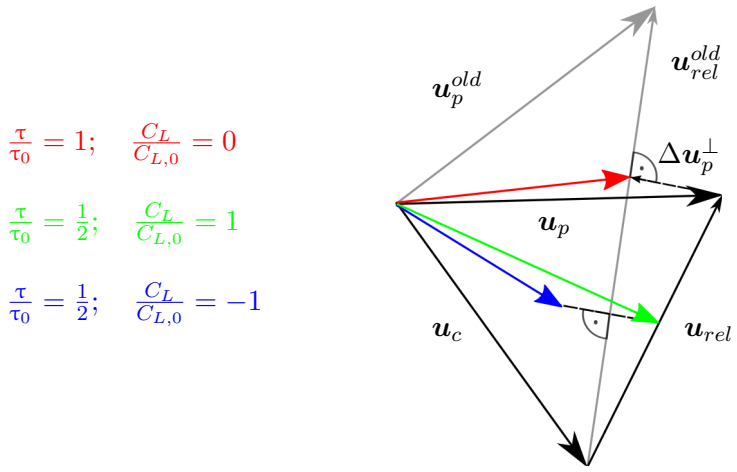

Figure A.2: Sketch of exemplary determinations of particle velocities with the extended relaxation time approach

- $\boldsymbol{u}_p = \boldsymbol{u}_c$ for $\tau = 0$
- $\boldsymbol{u}_p = \boldsymbol{u}_d$ for $\tau = \tau_0$ und $C_L = C_{L,0}$

- If C_L is independent of particle size ($\frac{C_L}{C_{L,0}} = 1$), correlation (A.51) converts to the previous RTA

Transferred into the moments context equation (A.51) reads

$$\boldsymbol{u}^{(k)} = \boldsymbol{u}_c + \frac{\tau^{(k)}}{\tau_d}\boldsymbol{u}_{rel} + \frac{\tau^{(k)}}{\tau_d}\left(\frac{C_L^{(k)}}{C_{L,d}} - 1\right)\Delta\, \boldsymbol{u}_p^{\perp}\big|_{C_{L,d}}\,. \tag{A.52}$$